Université Fédérale

Toulouse Midi-Pyrénées

THÈSE

En vue de l'obtention du

DOCTORAT DE L'UNIVERSITÉ DE TOULOUSE

Délivré par :

Institut Supérieur de l'Aéronautique et de l'Espace

Présentée et soutenue par :
Khairol Amali BIN AHMAD

le jeudi 11 juin 2015

Titre :

Surveillance de la fiabilité du positionnement par satellite (GNSS) pour les applications de véhicules terrestres dans les milieux urbains

Reliability Monitoring of GNSS Aided Positioning for Land Vehicle Applications in Urban Environments

---

École doctorale et discipline ou spécialité :

ED MITT : Réseaux, télécom, système et architecture

Unité de recherche :

Équipe d'accueil ISAE-ONERA SCANR

Directeur(s) de Thèse :

M. Christophe MACABIAU (directeur de thèse)
M. Mohamed SAHMOUDI (co-directeur de thèse)

Jury :

M. Michel BOUSQUET - Président
M. David BÉTAILLE
M. Philippe BONNIFAIT
M. Roland CHAPUIS
M. Maan EL-BADAOUI EL-NAJJAR - Rapporteur
M. Bernd EISSFELLER - Rapporteur
M. Christophe MACABIAU - Directeur de thèse
M. Mohamed SAHMOUDI - Co-directeur de thèse

Abstract

This thesis addresses the challenges in reliability monitoring of GNSS aided navigation for land vehicle applications in urban environments. The main objective of this research is to develop methods of trusted positioning using GNSS measurements and confidence measures for the user in constrained urban environments. In the first part of the thesis, the NLOS errors in urban settings are characterized by means of a 3D model of the urban surrounding. In an environment with limited number of visible satellites, excluding degraded signals could result in not having enough number of acceptable measurements for a position fix or adversely affect the satellites geometry. Using a GNSS simulator together with the 3D model, NLOS signals are identified and their biases are predicted. From this prediction, NLOS signals are corrected and used to improve the accuracy and integrity of the estimated positions. For the second part of the thesis, the work proposes a reliability monitoring technique in the range domain for urban environment using a trusted velocity sensor. The approach takes on pseudorange (PR) prediction using hybridization with other sensors. Single odometer and a gyro are used to obtain a reference position for reliability checking of GNSS pseudorange. By using the hybrid approach, residuals are generated and test statistic are calculated, and tested against a threshold. A few forms of residuals were derived based on several observables, namely the PR, the range rate and the velocity. Finally, the research developed a novel experimental scheme in integrity monitoring for positioning in urban environment. Working directly in the position domain, Horizontal Position Errors (HPE) are characterized using generalized Pareto Distribution. Then, a test statistic is derived based on position residuals which CDF are mapped or inflated to match the characterized overbounding position error CDF. By monitoring the test statistic against a specific threshold, the positioning integrity and continuity are met at a certain level of confidence. In addition, the Horizontal Protection Level (HPL) computation using a composite approach has also been analysed.

Acknowledgements

I would like to express my sincere gratitude to those who have helped me in whatever ways along my journey to complete this thesis. I especially wish to acknowledge my two supervisors, Dr. Christophe Macabiau and Dr. Mohamed Sahmoudi, whom I am forever indebted, for making this research possible. Thank you both for the supervision, guidance and mentoring throughout the studies and also for the encouragement and providing insightful comments which are beneficial for the progress of the thesis.

I would like to extend my thanks also to the jury members who have taken their time to review the thesis and shared their vast knowledge and experience in providing their comments and recommendations.

My gratitude also goes to the colleagues and staffs of DEOS - Aude, Syed, Paulo, Cheng, Azeddine, Remy, Nabil, Quintin, Benoît, Gael and others, - who in one way or another give me the sense of companionship and comradery that I am not alone in the struggle.

And last but not least, to my beloved family - who had accompanied me with perseverance along this arduous journey till the end.

Contents

List of Figures

List of Tables

Abbreviations

AAIM	aircraft autonomous integrity monitoring
ABAS	Aircraft Based Augmentation System
ABS	Antilock Braking System
ADAS	Advance Driver Assistance System
A-GNSS	Assisted GNSS
AL	Alert Limit
AOA	angle of arrival
AR	autoregressive
CDF	cumulative distribution function
CP	carrier-phase
DIA	Detection, Identification and Adaptation
DOP	dilution of precision
DP	Doppler
DR	Dead Reckoning
ECA	error characterization approach
ECEF	Earth-Centered, Earth-Fixed
EKF	Extended Kalman Filter
ENU	East-North-Up
ERP	Electronic Road Pricing
ESP	Electronic Stability Program
FDE	Fault Detection and Exclusion
GBAS	Ground Based Augmentation System
GIS	geographic information system
GLONASS	GLObal NAvigation Satellite System
GNSS	Global Navigation Satellite System

GPD	generalized Pareto distribution
GPS	Global Positioning System
GPU	graphic processing unit
GT	Global Test
HPE	horizontal position error
HPL	Horizontal Protection Level
HTL	Horizontal Trust Level
IBPL	Isotropy Based Protection Level
ICAO	International Civil Aviation Organization
IMU	inertial measurement unit
INS	Inertial Navigation System
ITS	Intelligent Transport System
KF	Kalman Filter
LBS	location-based-service
LHCP	left-handed circular polarization
LOS	line-of-sight
LSR	Least Square Residual
LT	Local Test
MEMS	Micro Electro-Mechanical Systems
MM	map-matching
MP	multipath
MRA	measurement rejection approach
MSS	maximum solution of separation
NLOS	non-line-of-sight
PAYD	pay-as-you-drive
PF	Particle Filter
PL	Protection Level
PLL	Phase Lock Loop
PR	pseudorange
PVT	position, velocity and timing
RAIM	receiver autonomous integrity monitoring
RF	radio-frequency
RHCP	right-handed circular polarization

RISS	Reduced Inertial Sensor System
RUC	road-user-charging
SBAS	Satellite Based Augmentation System
SNR	signal-to-noise-ratio
SPS	Standard Positioning Service
SSE	sum of the squared errors
TTA	Time to Alert
UERE	User Range Equivalent Error
UKF	Unscented Kalman Filter
VPL	Vertical Protection Level
WLS	Weighted Least-Square

RÉSUMÉ DES TRAVAUX EN FRANÇAIS

Introduction

Les services des systèmes globaux de positionnement par satellite (GNSS) pour les applications terrestres sont devenus très utiles et populaires que son marché devrait croître encore d'une façon exponentielle les années à venir. Les applications terrestres actuelles avec de nombreuse services potentielles couvrent une large gamme d'applications telles que le tarification basée sur la localisation, "pay-as-you-drive" (PAYD), la tarification routière, le suivi de voiture spécifique (les courses, les assurances, les criminels, etc.) et rapports de géolocalisation. En outre, les applications pour le système d'assistance au conducteur (ADAS) comme le suivi de la voie, l'évitement de collision etc. font également l'utilisation du système de positionnement par GNSS.

Dans ces applications terrestres, le récepteur GNSS est généralement un sous-système qui permet de calculer la position, la vitesse et l'heure (PVT) qui seront utilisées comme entrées ultérieures par le module suivant dans le système global de l'application. En fait, le GNSS n'est pas la seule technologie incluse dans le module de positionnement lorsque une solution hybride est mis en œuvre. Dans ce cas, la technologie GNSS est complétée par d'autres capteurs, par exemple inertiel ou odométrie, afin d'améliorer les performances de la solution PVT. En raison de ces dispositions, il est nécessaire de choisir un type de récepteur approprié et de connaître ses performances minimales de sorte que l'exigence des applications finales au niveau de l'utilisateur sera atteinte. A cet effet, la caractérisation de l'erreur de positionnement est nécessaire pour fournir à l'utilisateur final, avec le niveau de confiance requis par son application, une solution GNSS qui respecte les exigences techniques. Comme un bon nombre des services impliquent des engagements financiers, juridiques et potentiellement des répercussions de sécurité de la vie, ces applications doivent se conformer avec les exigences de sécurité et de fiabilité.

De nombreux facteurs affectent la performance finale d'un récepteur GNSS. Certains d'entre eux sont liés à la qualité intrinsèque du récepteur et de son antenne (sensibilité, la qualité du traitement du signal, la résilience aux interférences et de brouillage, etc.), tandis que certains sont liés aux couches atmosphériques travercées par les signaux GNSS et enfin certains sont lié à l'environnement de réception du récepteur. L'environnement de réception locale (masquage, multi-trajets, diffraction, etc.), y compris la dynamique des objets mobiles a des effets décisifs sur la qualité du signal résultants de la dégradation subie ce qui implique une dégradation des performances de positionnement du récepteur. En effet, avec l'émergence et l'innovation de nouvelles applications terrestres, la plupart des exigences et des défis sur leurs performances proviennent des milieux urbains où les besoins de traitement des signaux reçus sont beaucoup plus complexes que dans les environnements à ciel ouvert.

Une localisation fiable par GNSS est difficile à atteindre dans les zones urbaines denses parce que dans ces environnements les signaux satellites sont souvent masqués ou réfléchis par les bâtiments et les objets environnants le récepteur, qui faussent les mesures et biaisent la position calculée. Les signaux réfractés et réfléchis reçus avec le signal direct peut entraîner des erreurs de positionnement de dix mètres d'ordre, et des centaines de mètres d'erreur de positionnement peuvent être présents quand les signaux reçus en la configuration non-line-of-sight (NLOS). Comme ces problèmes empêchent ou ralentissent l'adoption du GNSS dans les applications qui nécessitent une haute disponibilité de service ou un bon niveau de confiance dans l'information PVT pour une utilisation dans des environnements urbains, des solutions efficaces et opportunes sont très recherchées. Pour toutes ces raisons, nous avons choisi de travailler sur le contrôle de la fiabilité du positionnement GNSS pour les applications de véhicules terrestres dans les milieux urbains.

Positionnement par satellite

Un récepteur GNSS calcule la pseudo-distance (PR) à partir d'un satellite sur la base de l'estimation du temps de propagation du signal de satellite multiplié par la vitesse de la lumière. Dans la pratique, les récepteurs GNSS ne sont pas synchronisés avec le temps GNSS. Par conséquent, la PR est basée sur la durée de transition du signal et de la différence de temps entre l'horloge du récepteur et celle du satellite.

Les mesures de PR réelles sont également affectés par diverses erreurs de propagation et du système et d'environnement. En tenant compte de ces bruits et des erreurs, la PR peut être représentée par l'équation [3] suivante:

$$\rho_i = d_i + c.dt_r - c.dt_s + I_i + T_i + \epsilon_i \tag{1}$$

où

- d_i est la distance en ligne droite entre le récepteur et le satellite
- $c.dt_i$ est le décalage de l'horloge du satellite
- $c.dt_r$ est le décalage de l'horloge du récepteur
- I_i est le retard ionosphérique
- T_i est le retard troposphérique
- ϵ_i représente le bruit du récepteur, les multi-trajets et NLOS

En milieu urbain, l'erreur dans ϵ_i est dominé par les multi-trajets et NLOS qui dépendent de l'environnement local et qui sont de caractère non-gaussien, non stationnaire et peuvent être temporellement corrélés. Par conséquent, les biais multi-trajets et NLOS sont très difficiles à estimer et en effet font un sujet ciblé dans cette thèse.

Une fois les PR sont mesurées, on obtient un ensemble d'équations non linéaires à quatre inconnues, appelé l'équation de navigation. Dans un système de coordonnées cartésiennes,

$$\rho_i = d_i + c.dt_r \tag{2}$$

où

$$d_i = \sqrt{(x_i - x)^2 + (y_i - y)^2 + (z_i - z)^2} \tag{3}$$

Au moins quatre mesures de PR sont nécessaires pour estimer les 4 inconnues (x, y, z et dt_r). Les positions des satellites sont calculées en utilisant les paramètres de Kepler démodulés obtenus à partir d'un message de navigation par satellite. La position est calculée et ensuite transformée en un système de coordonnées en longitude, latitude et altitude ellipsoïdale. Le système le plus couramment utilisé est de coordonnées WGS84

(World Geodetic System 1984) [4]. Le modèle de mesures standard liant les measures PR, données dans le vecteur Z, du vecteur d'état à estimer, X, est donné par:

$$\mathbf{Z} = \mathbf{HX} + \varepsilon \tag{4}$$

En utilisant les mesures de PR, plusieurs algorithmes différents peuvent être utilisés pour calculer diverses solutions, par exemple; position, biais d'horloge, la vitesse, le temps et l'accélération. Les algorithmes de navigation les plus couramment utilisés sont les moindres carrés pondérés et le filtre de Kalman. Outre les mesures de PR, la solution de navigation peut également exploiter d'autres mesures GNSS comme des mesures de l'effet Doppler (DR) ou des mesures de la phase des porteuses (CP) pour lisser la solution dans le domaine de mesures ou dans le domaine de la position. Les méthodes de lissage existantes utilisent les CP et DR pour profiter de la caractéristique de haute précision de la CP et de la DR, afin d'améliorer la précision de la PVT [5, 6].

Contrôle de l'intégrité

Dans le domain de l'aviation civile, le contrôle de l'intégrité est souvent accompli par les techniques de contrôle autonome de l'intégrité par le récepteur (RAIM) qui utilisent les algorithmes de détection et d'exclusion des défauts (FDE) pour rejeter les valeurs aberrantes à partir des données mesurées et aussi par les systèmes d'augmentation comme l'augmentation basée sur des systèmes sol (GBAS) et l'augmentation basée sur des satellites (SBAS) qui transmettent des informations d'intégrité aux avions pour calculer le niveau de protection (PL) associée à un risque d'intégrité. Ces techniques sont conçues pour les applications aéronautiques dans un contexte avec assez de redondance des données, des normes de performance matures pour chaque phase de la navigation sont disponibles, les erreurs de mesure et de position sont modélisées par une distribution gaussienne et un seul défaut est attendu à un instant du traitement.

Les algorithmes d'intégrité de positionnement et de surveillance de la fiabilité sont généralement basés sur l'inférence statistique et des tests d'hypothèses. Vu que l'erreur réelle de la position ne peut pas être connue ou mesurée en temps réel, RAIM calcule un paramètre scalaire mesurable qui fournit des informations sur les erreurs de mesure de pseudo-distance (qui peut être lié à l'erreur de position). Ce paramètre mesurable

est appelée statistique de test. C'est une variable aléatoire de distribution connue. Par exemple, dans Least Square RAIM, la statistique de test est calculée à partir de résidus de pseudodistance (PR), qui sont la différence entre le PR mesuré et le PR dérivé de la solution de navigation estimée. Dans RAIM, la détection de défaut est obtenue en comparant une statistique de test contre un seuil de détection. Pour la mise en œuvre en milieu urbain, la statistique de test doit être formulée pour détecter les erreurs dans les mesures aberrantes comme provenant de NLOS et des effets multi-trajets. La difficulté est de pouvoir caractériser la statistique de test dans ce type d'environnement non gaussiens.

Dans l'approche SBAS, chaque fois que le PL surveillée est inférieure à la limite d'alerte (AL), le positionnement est considéré comme étant dans la condition d'intégrité. Cependant, pour les applications terrestres en particulier en milieu urbain, l'adaptation directe ou simple de contrôle de l'intégrité de l'approche de l'aviation civile n'est pas possible en raison des caractéristiques de dégradation du signal. En raison de circonstances posées par les milieux urbains, les approches développées pour les environnements à ciel ouvert ne sont pas efficaces pour assurer la fiabilité de positionnement dans des environnements restreints. Le principal défi dans ces environnements difficiles en milieu urbain est la difficulté d'avoir un modèle fiable des mesures reçues, l'outil de base pour la plupart des méthodes d'analyse des performances et d'intégrité, comme dans le cas des applications de l'aviation civile.

Contributions Scientifiques de la Thèse

NLOS: caractérisation en milieu urbain à l'aide d'un modèle 3D

Dans la première partie de la thése, les erreurs NLOS en milieu urbain sont caractérisées par un modèle 3D de l'environnement urbain. Dans un environnement avec un nombre limité de satellites visibles, l'exclusion des signaux dégradés pourrait entraîner ne pas avoir assez de mesures acceptables pour une solution de position ou nuire à la géométrie des satellites. En utilisant un simulateur GNSS avec le modèle 3D, les signaux NLOS sont identifiés et leurs biais sont estimés. Grâce à cette prédiction, les signaux NLOS sont corrigés et utilisés pour améliorer l'exactitude et l'intégrité des positions estimées.

A cet effet, ce travail combine le modèle de variance sigma-ε avec un saut de moyenne (biais NLOS) pour modéliser les erreurs de pseudodistances. Tout d'abord, un modèle 3D de l'environnement est utilisé pour détecter l'état de réception NLOS et de prédire le biais NLOS liées au phénomène de retard excès. Pour un positionnement fiable, un ajustement de la variance des PR en LOS basé sur les valeurs du C/No est mis en œuvre. En outre, le biais est soustrait des NLOS PR lors de l'étape de trilatération du calcul de la position. Les biaises NLOS ont été obtenus à priori pour chaque satellite en mesurant la différence entre les PR mesurées et les PR référencées lorsque l'état de réception est déterminé en situation NLOS par le modèle 3D. La performance du système proposé est évaluée à l'aide des données réelles et comparée à un filtre de Kalman standard sans les informations aidant du simulateur 3D.

Prédiction des conditions des signaux GNSS via un modèle 3D

Dans ce travail, le logiciel SE-NAV [7] est utilisé pour prédire la réception du signal des systèmes GNSS comme le GPS dans des scènes virtuelles 3D de zones urbaines connues. La propagation de signaux est basée sur un algorithme de traçage de rayon qui calcule les effets de masquage et de multi-trajets. SE-NAV utilise l'optique géométrique pour calculer les rayons réfléchis, diffractés et transmis. Basé sur ces multiples rayons qui atteignent le récepteur, l'état de réception LOS ou NLOS d'un satellite est fourni. Afin de caractériser les biais a priori, la position des satellites et le récepteur doivent être connus. Les positions des satellites sont calculées sur la base des données d'éphémérides alors que les positions le long de la trajectoire sont obtenues à partir du récepteur.

Nous précisons que le modèle 3D représente seulement une approximation de la réalité de la propagation et que la reconstruction parfaite des signaux réels reçus reste très difficile. Tout d'abord, il existe une variabilité non quantifié de la vie réelle de l'environnement qui entoure le récepteur par rapport à la représentation virtuelle de l'environnement statique de réception. Par exemple, il y a des objets non-permanents tels que les véhicules et les personnes qui peuvent affecter la propagation du signal, mais ne sont pas inclus dans le modèle 3D. Au fil du temps, même le feuillage de la végétation change et ainsi les attributs de surface du bâtiment. En fait, pour acquérir la modélisation de la précision des structures et des matériaux de construction en termes de leurs effets sur les signaux GNSS est en soi une tâche difficile.

La complexité de la propagation du signal électromagnétique pose encore une autre contrainte sur le modèle 3D. Les modèles déterministes basés sur l'optique géométrique (GO) et la théorie uniforme de la diffraction (UTD) exigent des informations géométrique et morphologique détaillée sur l'environnement de propagation. Dans les scénarios urbains, la propagation des rayons est affectée par de multiples interactions avec les diffuseurs. Chaque fois qu'un rayon est modélisée avec une réflexion ou diffraction, il y a une erreur associée à la prédiction du modèle en raison de la représentation inexacte de propriétés du matériau ou les dimensions des objets dans l'environnement. Pour les rayons qui sont modélisés par de multiples réflexions, ces erreurs ont tendance à s'accumuler, ce qui rend les prédictions du modèle encore moins précis. En outre, l'effet de l'antenne réelle et le modèle du récepteur sur le signal reçu, le plus souvent, sont indisponibles pour être inclus dans le modèle 3D. Tout cela introduit des erreurs dans la prédiction de la PR par un modèle 3D.

Pour toutes les raisons ci-dessus, dans le travail de [8], les auteurs ont étudié la validité de l'aide d'un modèle de simulation 3D GNSS, en particulier la capacité de SE-NAV de prédire les biais des mesures de PR. De la comparaison entre les biais de la PR mesurée à l'aide de la position de référence et les biais prédites en utilisant le modèle SE-NAV 3D, l'étude a conclut que les erreurs de PR simulées sont tout à fait compatibles avec les veritables erreurs avec une correspondance qui peut atteindre 80% pour certains recépteurs.

En dehors de prédire l'état de réception, le modèle 3D est également utilisé pour prédire le biais statistique NLOS, qui peut être utilisé pour la correction de la PR. Dans ce cas, la différence entre la valeur du biais simulé et du biais NLOS mesuré affectera la qualité de la position finale calculée. Le biais NLOS mesuré est calculé à partir de la différence entre la PR mesurée et la PR réfrencée lorsque l'état de réception est dèterminé en NLOS par SE-NAV. Le biais NLOS prédit est obtenu à partir du retard de trajet du signal calculé par SE-NAV en utilisant les estimations de position calculées par le récepteur lorsque l'état de réception est déterminé en NLOS par SE-NAV.

Chaque fois qu'il y a de nombreuses composantes réfléchies d'un signal, SE-NAV fournit les retards des trajets multiples. Dans le cas d'un signal LOS, la valeur du retard de la composante directe du signal est fourni en 0. Dans le cas d'une réception NLOS, toutes les composantes du signal devraient arriver en retard puisqu'il n'y a aucune composante

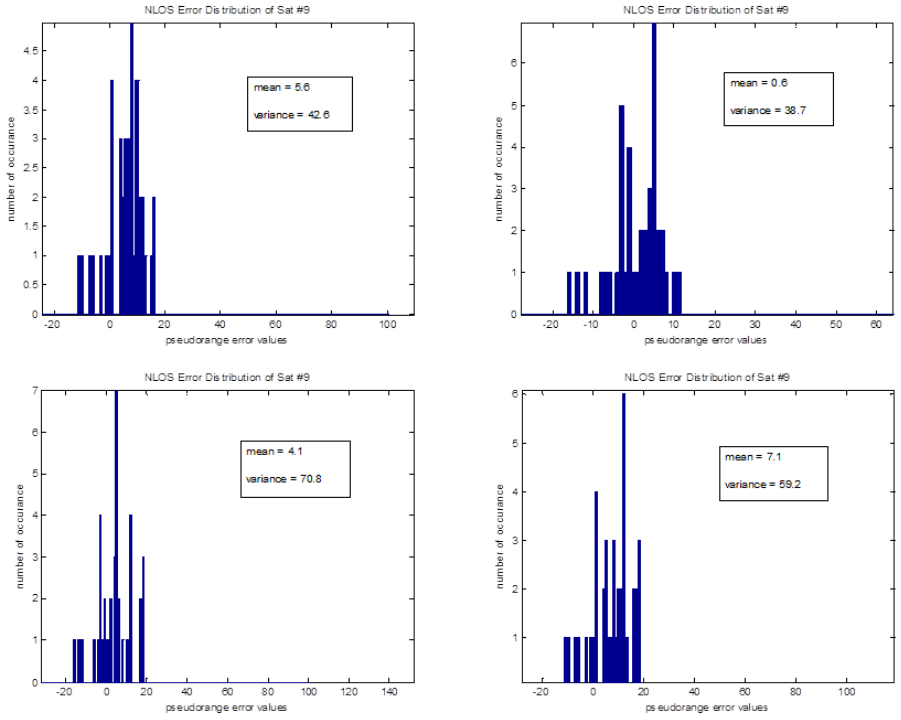

FIGURE 1: Distributions d'erreur de PR en milieu urbain (le Capitole, Toulouse) obtenues à partir d'un même satellite dans diverses périodes de 40 secondes

directe du signal. Dans ce travail, quand il y a plus d'un trajet réfléchi dans le cas NLOS, une hypothèse optimiste est choisie au moment de décider de la valeur du biais prévu à la réception NLOS. Il est supposé que le récepteur va acquérir la composante non-direct avec le plus court délais, car il est fort probable que la composante qui correspond au plus court délai aura la plus grande puissance, à savoir la moins atténuée quand elle arrive sur le récepteur et donc celle qui affecte plus le traitement de récepteur.

L'approche proposée pour le positionnement avec des signaux NLOS

Au cours d'une fenêtre d'observation relativement longue, l'erreur de mesure NLOS peut être modèlisée par une distribution non gaussienne et peut être approximée par un mélange de distributions gaussiennes [9]. Cependant, pour une courte fenêtre d'observation, l'approche la plus courante consiste à modéliser l'erreur de pseudodistances par une distribution gaussienne avec une moyenne non-nulle et une variance adaptive [10], comme illustré dans la figure 4.5. Ici, les distributions d'erreur du même satellite sont présentées sur différentes 40 secondes fenêtres où on peut observer les variations de la moyenne et de la variance. Dans le cas NLOS, la présence de signaux réfléchis introduit seulement un saut sur la valeur moyenne en raison de la distance supplémentaire. Dans le cas d'un

trajet LOS dégradé, une variation supplémentaire est présentée comme une augmentation de l'incertitude sur le trajet direct. En conséquence, ces effets du bruit du signal LOS dégradé et le biais NLOS sur l'erreur des mesures de PR sont modélisés séparément.

Pour le cas de la réception en LOS avec un multitrajet dégradé, la mise en œuvre du modèle de la variance basée sur le rapport signal-sur-bruit, dit SIGMA-ε, permettrait d'améliorer la précision de positionnement dans l'environnement urbain [11, 12]. La matrice de covariance de l'observation peut être réalisé sous la forme $\mathbf{R} = diag(\sigma_1^2, \sigma_2^2, \ldots, \sigma_k^2)$ où

$$\sigma_k^2 = a + b.10^{\frac{-C/No}{10}} \tag{5}$$

et σ_k^2 est la variance de la k^{eme} observation. Les constantes a et b sont déterminés en fonction de l'environnement et de l'équipement de l'utilisateur, qui peut être calculées à priori hors ligne à l'aide des erreurs de mesures des PR et leur C/No sur une certaine époque.

Pour chaque satellite, la pseudodistance ρ_k peut être exprimée par,

$$\rho_k = d_k + c.dt_k^{sat} + c.dt_k^{rcv} + atmo_k + m_k + \epsilon_k \tag{6}$$

avec $c.dt$ représente décalage d'horloge (par satellite ou récepteur), $atmo$ représente à la fois les retards ionosphériques et troposphériques. Le terme m_k est le retard de propagation par multitrajets tandis que ϵ_k représente le bruit du récepteur. En milieu urbain, m_k est la principale contributrice de l'erreur et pourrait représenter des conditions LOS/NLOS mixtes. Une fois les troposphériques, ionosphériques et horloge erreurs sont compensées, le modèle est réduit à l'expression suivante,

$$\rho_k = d_k + m_k + \epsilon_k \tag{7}$$

Pour illustrer plus en détail les conditions LOS/NLOS dans la propagation par multitrajets, nous pouvons réécrire l'équation comme [13]:

$$\rho_k = d_k + m_k + b_k w_k \tag{8}$$

où

$$m_k = \begin{cases} 0, \text{ en condition LOS} \\ m_{NLOS}, \text{ en condition NLOS} \end{cases} \tag{9}$$

$$b_k = \begin{cases} \sigma, \text{ en condition LOS} \\ \sqrt{\sigma^2 + \sigma_{NLOS}^2}, \text{ en condition NLOS} \end{cases} \tag{10}$$

et w_k est la moyenne nulle du bruit blanc gaussien $\mathcal{N}(0,1)$. En d'autres termes, le terme NLOS est caractérisé par sa moyenne, m_{NLOS}, et sa variance, σ_{NLOS}^2. Ainsi, dans le cas du NLOS, pour corriger la pseudo-distance du biais de NLOS, la mesure affectée devient

$$\rho_k' = \rho_k - m_{NLOS} = d_k + b_k w_k \tag{11}$$

et

$$b_k = \sqrt{\sigma^2 + \sigma_{NLOS}^2} \tag{12}$$

Le biais estimé en utilisant le modèle 3D est soustrait des PR qui sont utilisées dans l'estimation de la PVT par un filtre de Kalman étendu. L'équation d'état peut être fournie par:

$$\mathbf{X_{k+1}} = \mathbf{F}\mathbf{X_k} + \mathbf{v_k} \tag{13}$$

où $\mathbf{X}$ est le vecteur d'état, $\mathbf{F}$ est la matrice de transition d'état et $\mathbf{v}$ est le bruit de processus de distribution gaussienne de moyenne nul.

En supposant un modèle de vitesse presque constante, le vecteur d'état cosidéré est:

$$\mathbf{X_k} = [p_k, \dot{p}_k, ct_k, \dot{ct}_k]^T \tag{14}$$

où p_k est le x_k, y_k, z_k coordonnées de position, $\dot{p}_k$ sont les vitesses, ct_k est le biais d'horloge et $\dot{ct}_k$ est la dérive d'horloge.

La matrice de transition d'état est donné par:

$$\mathbf{F} = \begin{bmatrix} \mathbf{I} & T_s\mathbf{I} & 0 & 0 \\ 0 & \mathbf{I} & 0 & 0 \\ 0 & 0 & 1 & T_s \\ 0 & 0 & 0 & 1 \end{bmatrix} \tag{15}$$

où $\mathbf{I}$ est la matrice d'identité 3×3 et T_s est la période d'échantillonnage.

Le bruit de processus en temps discret est donné par:

$$\mathbf{v_k} \sim \mathcal{N}(0, diag(\mathbf{Q_1}, \mathbf{Q_2})) \tag{16}$$

où

$$\mathbf{Q_1} = \begin{bmatrix} \frac{T_s^3}{3}\sigma_a^2\mathbf{I} & \frac{T_s^2}{2}\sigma_a^2\mathbf{I} \\ \frac{T_s^2}{2}\sigma_a^2\mathbf{I} & T_s\mathbf{I} \end{bmatrix} \tag{17}$$

et

$$\mathbf{Q_2} = \begin{bmatrix} \sigma_b^2 T_s + \frac{T_s^3}{3}\sigma_d^2 & \frac{T_s^2}{2}\sigma_d^2 \\ \frac{T_s^2}{2}\sigma_d^2 & T_s\sigma_d^2 \end{bmatrix} \tag{18}$$

La variance du biais d'horloge σ_b^2 et la variance de la dérive d'horloge σ_d^2 dépendent de la qualité du récepteur, tandis que la variance de l'accélération σ_a^2 dépend du mouvement du récepteur.

Si la PR mesurée est prévue en tant que signal LOS, sa covariance est adaptée selon l'équation 4.1. Si la mesure est prédit la réception NLOS, le biais NLOS m_{NLOS} est prédit à partir de SE-NAV où il fournit la distance retardée du 'ray tracing' NLOS par rapport à la distance en ligne droite entre le satellite et le récepteur. Ensuite, le biais est soustrait de la mesure de la PR et la variance du NLOS σ_{NLOS}^2 est incluse dans la covariance comme décrit par les équations 4.4 et 4.7. Par conséquent, l'équation d'observation peut être formulée sous la forme,

$$\mathbf{z_k} = \mathbf{h}(\mathbf{X_k}) + \mathbf{m_k} + \mathbf{b_k}\mathbf{w_k} \tag{19}$$

où $\mathbf{h}$ décrit la dépendance non-linéaire des observations en fonction de l'état. La covariance d'observation est,

$$\mathbf{b_k}\mathbf{w_k} \sim \mathcal{N}(0, \mathbf{R}) \tag{20}$$

où $\mathbf{R}$ dépend de la condition LOS/NLOS de l'état de réception de la mesure PR.

Résultats et analyse

Afin de mettre en œuvre le modèle SIGMA-ε de la variance comme dans l'équation 4.1, les valeurs des paramètres a et b devront être déterminés en ajustant l'écart-type $\sigma_k = \sqrt{a + b.10^{\frac{C/No}{10}}}$ d'erreurs absolues des pseudodistances en fonction des valeurs du C/No. Figure 4.7 montre un exemple de la courbe obtenue et le tableau 4.1 liste tous

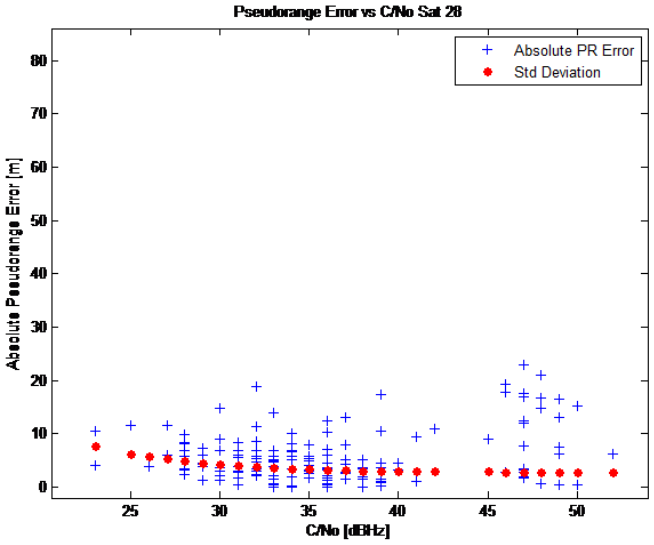

FIGURE 2: Erreurs de Pseudodistances en fonction de C/No

les a et b valeurs déterminées par satellite visible lors de la collecte de données. Il a été observé que pour plusieurs satellites, il y a des valeurs négatives de la constante b, ce qui indique une dégradation de sigma pour C/No. Cette situation confirme la question de la difficulté d'utiliser uniquement C/No tant qu'indicateur de la qualité de la mesure dans les environnements urbains en particulier avec ce court données. La réception de signaux GNSS dans les environnements urbains sont dégradés par multitrajets et NLOS, donc il est possible pour un signal réfléchi d'avoir une valeur C/No élevée.

La prédiction LOS/NLOS par SE-NAV est comparée à la valeur C/No des mesures PRs. Les C/No de valeurs de seuil de 40, 38 et 30 dB-Hz sont utilisées pour cette comparaison. On peut voir dans le tableau 4.2 que le seuil $<$ 40 dB-Hz a le plus d'accord entre la prédiction SE-NAV et le critère du C/No. Ces valeurs C/No peuvent également être comparés avec l'angle d'élévation des satellites (figure 4.8) puisque les signaux des satellites de basse altitude sont plus susceptibles d'être reçu comme NLOS en milieu urbain par rapport à ceux avec une altitude plus élevée. Dans le tableau 4.2, pour les satellites dotés de moins de 26^o élévation, la prédiction LOS/NLOS par SE-NAV est parfaitement en accord avec la métrique du C/No. Autrement dit, la prédiction de la réception LOS/NLOS par le modèle 3D est plus semblable à la prédiction basée sur C/No lorsque l'élévation des satellites est basse par opposition quand l'élévation du satellite est plus élevé.

La figure 4.12 compare les erreurs de position 2D entre l'estimation de position avec

Sat #	Number of samples	*a*	*b*
5	164	164	-1×10^4
8	127	115	1×10^4
9	152	127	3336
10	132	171	2×10^4
15	165	136	-1×10^4
17	24	325	1339
18	114	48	2×10^4
24	18	982	- 4649
26	161	55	-1×10^4
27	155	29	-7603
28	162	8	1×10^4

TABLE 1: Liste des paramètres du modèle de la variance (C/No) obtenu par ajustement de la courbe des erreurs de PR absolues

Sat PRN, Elevation	Threshold < 40 dB-Hz	Threshold < 38 dB-Hz	Threshold < 30 dB-Hz
5, 35°	61 %	45 %	2 %
8, 26°	98 %	95 %	48 %
9, 26°	89 %	87 %	54 %
10, 12°	86 %	82 %	75 %
15, 65°	64 %	47 %	5 %
17, 9°	100 %	100 %	62 %
18, 17°	100 %	100 %	72 %
24, 4°	100 %	100 %	100 %
26, 43°	91 %	80 %	14 %
27, 40°	94 %	93 %	38 %
28, 48°	93 %	83 %	15 %
Total	**89 %**	**83 %**	**44 %**

TABLE 2: La conformité entre la prédiction SE-NAV LOS/NLOS et le critère basé sur le C/No

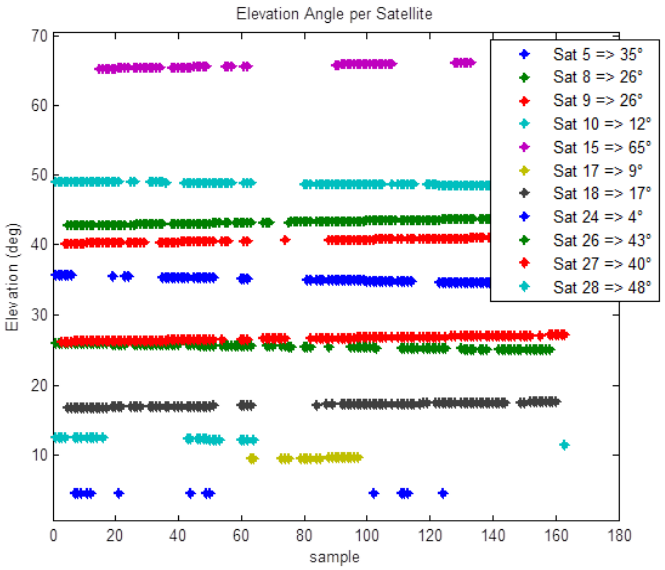

FIGURE 3: L'angle d'élévation par satellite

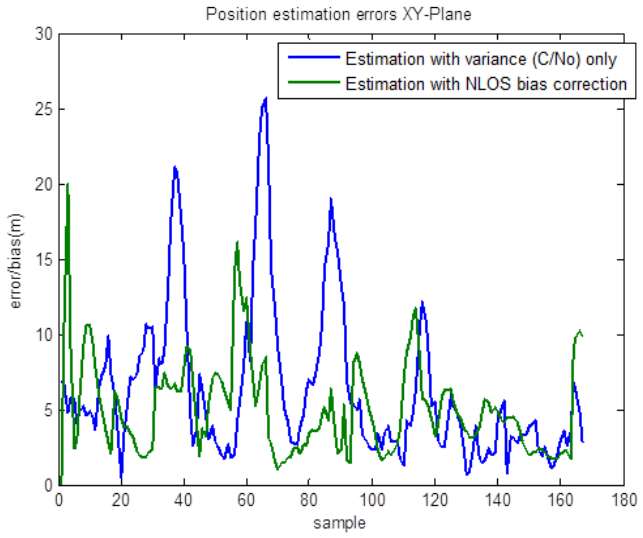

FIGURE 4: Erreur d'estimations de position dans le plan X-Y

correction du biais NLOS et estimation de position en utilisant le C/No modèle de variance (sans tenir compte LOS/NLOS réception). On peut voir que l'estimation avec correction du biais NLOS était généralement meilleur que l'estimation de position en utilisant seulement le C/No,via le modèle de la variance. L'estimation avec correction du biais a été en mesure de réduire les grandes erreurs qui existent dans l'estimation, plus que dans le cas avec le modèle de la variance (autour de la 37ème, 66ème et 87ème échantillons) basée sur le C/No.

La figure 4.13 montre la comparaison du biais mesurée contre le biais prédit pour les

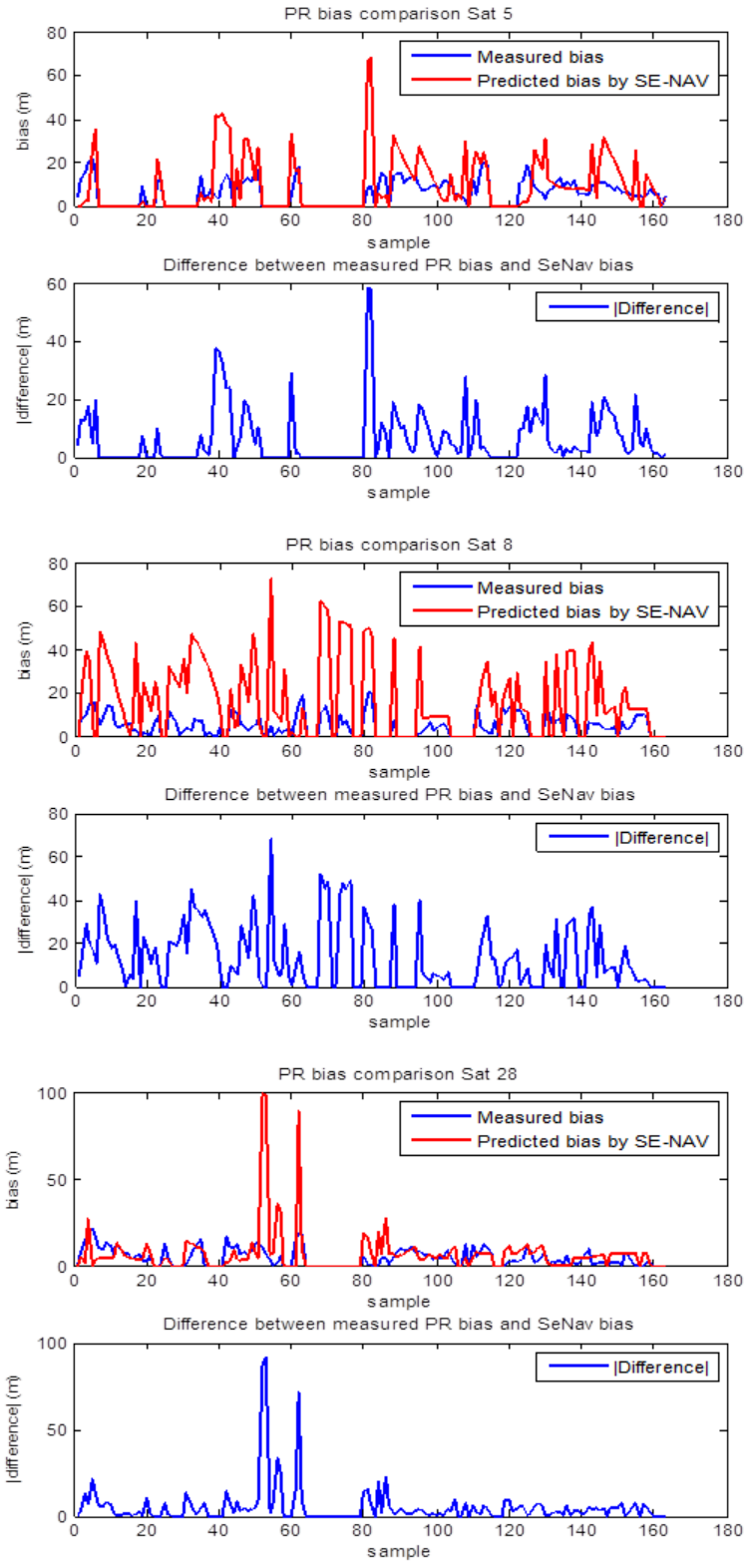

FIGURE 5: Comparaison des biais NLOS mesurés contre les biais prédits

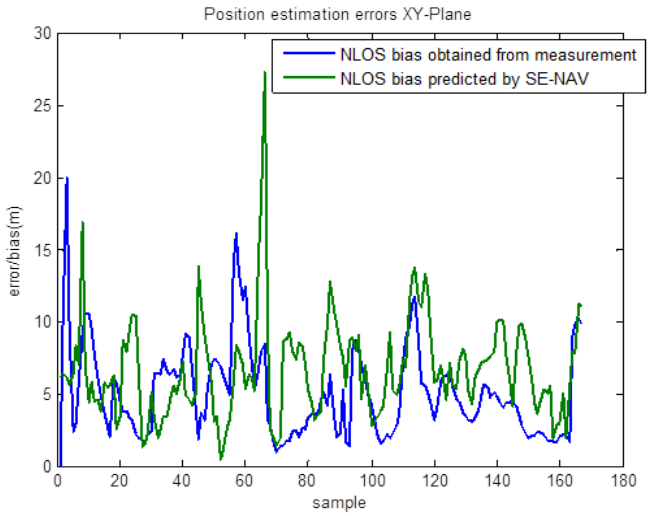

FIGURE 6: Les erreurs de position - biais NLOS mesurés contre le biais NLOS prédit par SE-NAV

satellites 5, 8 et 28. La comparaison montre que bien qu'il y ait une certaine similitude dans les profils, les valeurs des biais sont très différents entre eux. Autres recherches pourraient être poursuivie afin d'améliorer le prédiction de biais NLOS par le modèle 3D. Malgré la différence entre leurs valeurs de biais, leurs performances de positionnement dans le plan X-Y (figure 4.14) sont assez semblables en général. Cet effet est dû à la projection des biais de distance dans le domaine de position qui est également influencée par la géométrie de la constellation des satellites. La différence des biais de mesure et prédits peut également être impacté par d'autres objets réels dans les environs du récepteur qui ne sont pas pris en compte dans le modèle 3D (voiture et personnes de passage, arbre, etc).

La capacité du modèle 3D pour prédire LOS/NLOS est encourageant en comparaison avec d'autres indicateurs tels que C/No et l'angle d'élévation par satellite. D'autre part, la capacité du modèle 3D à prédire le biais NLOS a été jugé modeste et non concluante pour les données traitées, relativement de courte durée. Plus de recherches et des analyses sont nécessaires pour valider la qualité des prédictions par modèle 3D. De même, quand les biais prédits ont été utilisés pour les corrections de PR dans l'estimation de position, les résultats ont montré que les erreurs de positionnement sont généralement presque similaires à celles calculées en utilisant le biais mesuré calculé à partir de la trajectoire de référence. Même si la prédiction n'est pas parfaite, les incertitudes associées sont absorbées par le filtre de Kalman et donc le modèle 3D donne des informations utiles.

Par conséquent, en terme de la prédiction de biais, d'autres techniques d'exploiter mieux les informations 3D doivent être développées.

Fiabilité de la mesure par prédiction de pseudodistances en utilisant une approche hybride

Dans la deuxième partie de la thèse, nous avons proposé une technique de surveillance de la fiabilité dans le domaine des mesures GNSS pour l'environnement urbain en utilisant un capteur de vitesse fiable. Dans cette approche, nous calculons une prédiction des pseudodistances (PR) par hybridation avec d'autres capteurs. Un odomètre et gyroscope sont utilisés pour obtenir une position de référence pour la vérification de la fiabilité de la pseudodistance. En utilisant l'approche hybride, les résidus sont générés pour former une statistique de test qui est testée contre un seuil. Quelques formes de résidus ont été calculées sur la base de plusieurs observables, qui sont la PR, la variation de la distance et de la vitesse.

GNSS/Odomèter/Gyroscope Intégration des mesures pour la prédiction des PRs

Le filtre d'intégration de navigation à l'estime utilise un seul odomètre pour mesurer le déplacement et un gyroscope pour mesurer la direction (i.e. le cap) du véhicule. La figure 5.7 montre le filtre de navigation mis en œuvre dans cette recherche qui a une configuration d'une fusion lâche du GPS, gyroscope et odomètre. Nous utilisons une approche standard de navigation à l'estime pour prédire la position 2D du véhicule sur la base des mesures obtenues à partir de l'odomètre et du gyroscope. En même temps, l'EKF du GNSS fournit des corrections à la sortie du navigateur à l'estime et également à l'entrée de lacet du gyroscope. Par conséquence, lorsque les signaux satellites sont bons, ils vont corriger la sortie de navigateur à l'estime. Le positionnement hybride dans ce travail est réalisé par la formulation suivante:

$$\hat{x}_{user}(k) = \hat{x}_{user}(k-1) + V_{odo}.\cos\theta.dt + \Delta x \quad (21)$$

$$\hat{y}_{user}(k) = \hat{y}_{user}(k-1) + V_{odo}.\sin\theta.dt + \Delta y \quad (22)$$

$$\theta(k) = \theta(k-1) + gyro.dt - b_{gyro}.dt \quad (23)$$

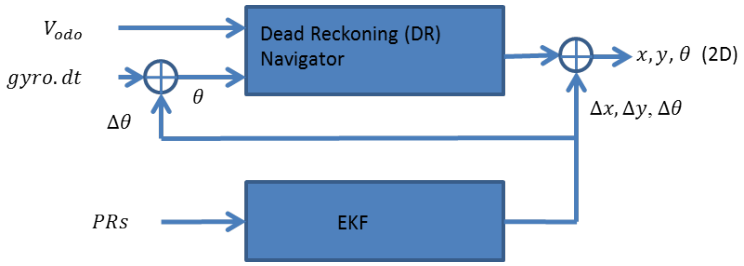

FIGURE 7: Le schéma de principe du filtre de navigation hybride

où:

- $\hat{x}_{user}(k)$ est la position de l'utilisateur dans les coordonnées x
- $\hat{y}_{user}(k)$ est la position de l'utilisateur dans les coordonnées y
- V_{odo} est la vitesse linéaire mesurée par l'odomètre
- $\theta(k)$ est l'angle du cap
- $gyro$ est la vitesse angulaire du cap fournie par la gyroscope
- b_{gyro} est le biais estimé de la vitesse angulaire du cap de la gyroscope
- Δx est la correction de la position estimée de coordonnée x
- Δy est la correction de la position estimée de coordonnée y

Le vecteur d'état d'erreur mis en œuvre pour le filtre EKF dans ce travail est défini par:

$$\mathbf{x} = \begin{bmatrix} \delta x \\ \delta y \\ \delta\theta \\ b_{gyro} \\ b_c \\ d_c \end{bmatrix} \tag{24}$$

où

- δx : erreur de position sur l'axe des x
- δy : erreur de position sue l'axe des y

- $\delta\theta$: erreur du cap
- b_{gyro} : biais du gyroscope
- b_c : biais d'horloge récepteur GNSS
- d_c : dérive de l'horloge récepteur GNSS

La matrice de transition d'état, $\mathbf{F}$, est donnée par:

$$\mathbf{F} = \begin{bmatrix} 1 & 0 & V_{odo}.\cos(\theta)dt & 0 & 0 & 0 \\ 0 & 1 & -V_{odo}.\sin(\theta)dt & 0 & 0 & 0 \\ 0 & 0 & 1 & -dt & 0 & 0 \\ 0 & 0 & 0 & 1 & 0 & 0 \\ 0 & 0 & 0 & 0 & 1 & dt \\ 0 & 0 & 0 & 0 & 0 & 1 \end{bmatrix} \tag{25}$$

L'odomètre utilisé dans les expériences de ce travail est le capteur iMWS-V2 de iMAR, qui est un capteur de roue montée sur le véhicule de l'ISAE sur une bande magnétique. Pour obtenir l'angle du cap, la gyroscope iMAR de la centrale inertielle IMU-FSAS a été utilisée. Les signaux GPS sont mesurés à l'aide d'un récepteur u-blox LEA-4T. Les données de référence, le long de la trajectoire, sont fournies par un système NovAtel SPAN.

Le résultat de la figure 5.11 montre que la vitesse mesurée par l'odomètre a une ressemblance très proche de la vitesse de référence avec un coefficient de corrélation de 0,987. Cette très forte corrélation indique que l'odomètre peut être un bon capteur de référence. Cependant, il existe certaines zones mortes pour la sortie de l'odomètre, soit lorsque la vitesse du véhicule est faible, l'odomètre ne délivre pas une information de vitesse valide.

Métriques de fiabilité

Dans ce travail, trois types de résidus ont été étudiés, qui sont les résidus de PR, de vitesse et de taux de la distance. Ici, nous analysons leur capacité de contrôler la fiabilité des mesures qui sont utilisées pour calculer la solution PVT.

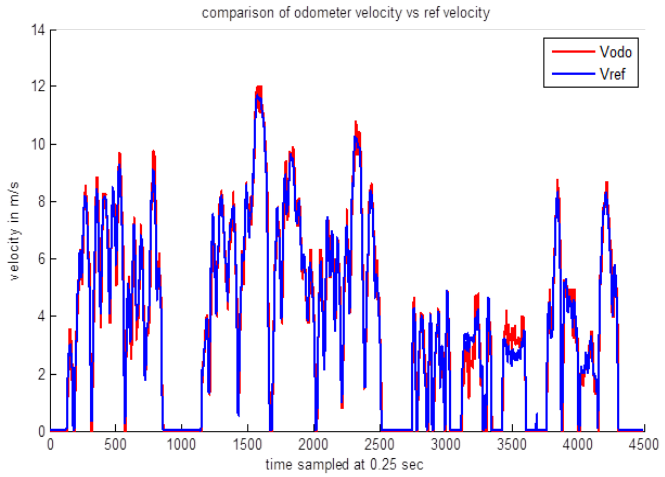

FIGURE 8: Comparaison de la vitesse odomètre avec une vitesse de référence

a. Test de fiabilité par le résidu de pseudodistance. Dans cette approche, le résidu de PR est calculé comme la différence absolue entre une pseudodistance mesurée et la pseudodistance prédite. À chaque instant k et pour chaque satellite i, le résidu de PR est:

$$r^i(k) = PR^i_{measured}(k) - PR^i_{predict}(k) \tag{26}$$

Les PR prédites sont calculées à partir des positions des satellites, $\mathbf{X}_{sat}$ et les positions estimées de l'utilisateur, $\hat{\mathbf{X}}_{user}$

$$PR^i_{predict}(k) = |\mathbf{X}_{sat} - \hat{\mathbf{X}}_{user}| \tag{27}$$

Pour calculer le $PR^i_{predict}(k)$, les valeurs de $\hat{\mathbf{X}}_{user}$ sont calculées en utilisant des mesures hybrides à partir d'un odomètre, un gyroscope, et toutes les PR qui sont disponibles à l'instant k (sauf de la $PR^i_{measured}(k)$ que est on veut tester). Ainsi, le $PR^i_{predict}(k)$ est prédite sans l'influence de $PR^i_{measured}(k)$. Si aucun des signaux satellites sont disponibles, la PR est estimée à par des capteurs de navigation à l'estime seulement.

La formulation globale du résidu de PR est donc donnée par,

$$r^i(k) = |y^i(k) - (\sqrt{[(X^i_{sat}(k) - \hat{X}_{user}(k))^2 + (Y^i_{sat}(k) - \hat{Y}_{user}(k))^2 + (Z^i_{sat}(k) - \hat{Z}_{user}(k))^2]})| \tag{28}$$

où:

- $y^i(k)$ est la pseudodistance mesurée à partir de satellite i à l'instant k

- $\hat{X}_{user}(k), \hat{Y}_{user}(k), \hat{Z}_{user}(k)$ sont des positions d'utilisateur dans le cadre de ECEF à chaque période de temps

Afin d'identifier les pseudodistances défectueuses, une statistique de test T, est comparée à une valeur de seuil pour rejeter ou accepter la $PR^i_{measured}(k)$. Pour calculer la statistique de test pour chaque PR, une métrique de chi-deux pondérée est utilisée:

$$T = r^t.Z^{-1}.r \tag{29}$$

où r est le résidu de la PR caracterisé par sa variance:

$$Z = cov(r) = var(PR^i_{measured}) + var(PR^i_{predict}) \tag{30}$$

La variance de $PR^i_{measured}$ peut être déterminée à partir du modèle de variance qui est principalement liée à son C/No ou l'angle d'élévation [14]. Ici, le modèle SIGMA-ε [11] est utilisé.

D'autre part, la variance de la $PR^i_{predict}$ peut être obtenue à partir de la norme euclidienne du vecteur de ligne de vue et de la loi de propagation de l'erreur [15]:

$$var(PR^i_{predict}(k)) = e_{sat,user}(k).P_{user}(k).e^t_{sat,user}(k) \tag{31}$$

où:

$$e_{sat,user}(k) = \frac{x^i_{sat}(k) - \hat{x}_{user}(k)}{\|x^i_{sat}(k) - \hat{x}_{user}(k)\|} \tag{32}$$

$$P_{user}(k) = \begin{bmatrix} \sigma_x^2 & \sigma_{xy} & \sigma_{xz} \\ \sigma_{yx} & \sigma_y^2 & \sigma_{yz} \\ \sigma_{zx} & \sigma_{zy} & \sigma_z^2 \end{bmatrix} \tag{33}$$

Pour la matrice de covariance de la position de l'utilisateur $P_{user}(k)$, en supposant la non-corrélation entre x, y et z, seulement les éléments de la diagonale sont considérées ici. En outre, puisque le positionnement est en 2D, σ_z^2 peut être mis à zéro. La matrice $P_{user}(k)$ n'est pas accessible directement à partir du navigateur hybride utilisé dans ce projet.

Cependant, les variances σ_x^2 et σ_y^2 peuvent être calculées en utilisant la règle de combinaison de la variance et de la loi de propagation de la variance. Une fois que σ_x^2 et σ_y^2

sont calculées, la $cov(r)$ peut être déterminée par la mise en œuvre des équations 5.72, 5.73, 5.74 et 5.75. Le seuil est fixé par le niveau de confiance appliqué à la distribution de chi-deux avec 1 degré de liberté, $r^t.Z^{-1}.r \sim \chi_1^2$.

Figures 5.12 et 5.13 montrent les courbes qui comparent les résidus des PR calculées (tracées en rouge) contre les erreurs réelles de distance des satellites (tracées en bleu). La performance du résidu de PR varie pour différents satellites en fonction de la précision de la position estimée par rapport à la position du récepteur réel. La figure 5.14 indique le nombre de satellites visibles (bleu) contre le nombre de satellites 'non-défectueux' (rouges) après la mise en œuvre du procédé de détection de défaut et d'identification. Dans cette expérience, le seuil est fixé à 2,706 (99% de niveau de confiance). Le résultat montre que dans une partie de la trajectoire, les satellites non-défectueux ont été réduits à 4 ou même moins. Dans ce cas, l'algorithme RAIM traditionnelle ne peut être mise en œuvre car il a besoin d'au moins 5 satellites visibles. Ensuite, la figure 5.15(a) montre l'erreur de position 2D avant (vert) et après (rouge) l'exclusion des mesures défectueuses en utilisant un filtre hybride GPS/odomètre/gyroscope tandis que la figure 5.15(b) est le résultat de l'utilisation de seulement GPS pour le positionnement. Le résultat montre que le filtre hybride GPS/odomètre/gyroscope améliore le positionnement. En outre, la détection de défaut et l'exclusion (FDE) pour véhicule terrestre en milieu urbain peuvent être effectuées mieux quand l'odomètre et gyroscope est hybridé avec le GPS par rapport au cas du GPS seul. Figure 5.16(a) montre le résultat de la détection d'erreur de PR, l'identification et l'adaptation (DIA) qui a été mis en œuvre sur le navigateur hybride à l'aide du contrôle de l'intégrité de la mesure (la technique proposée dans cette thèse). L' adaptation a été réalisée en remplaçant les PR défectueuses identifiées avec leurs PR prédites. En d'autres termes, les PR défectueuses ont été corrigées. D'autre part, la figure 5.16(b) montre que cette approche de la correction d'erreur de PR ne pourrait être atteint que lorsque le signal GPS a été utilisé dans le positionnement sans l'intégration de l'odomètre et du gyroscope.

b. Test de fiabilité par le résidu de la vitesse. Lorsque la vitesse du satellite est connue, la vitesse de l'utilisateur peut être déterminée à partir des mesures Doppler selon l'équation suivante,

$$D = -\frac{L1}{c}[e_{sat,user}.(V_{user} - V_{sat}) + d_t] + \varepsilon \tag{34}$$

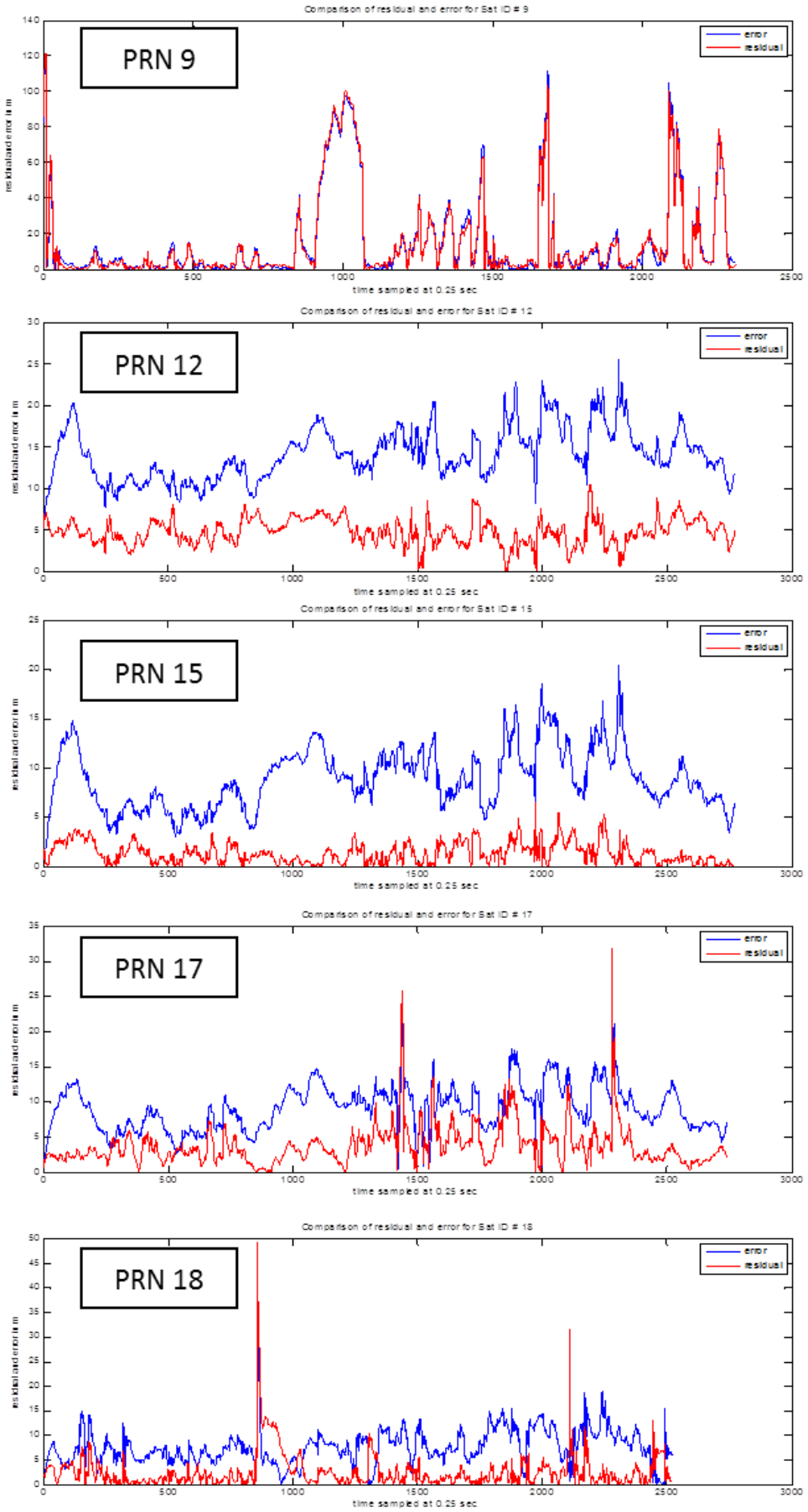

FIGURE 9: Comparaison des résidus de PR contre l'erreurs de pseudo-distance par satellite (predites en utilisant la référence)

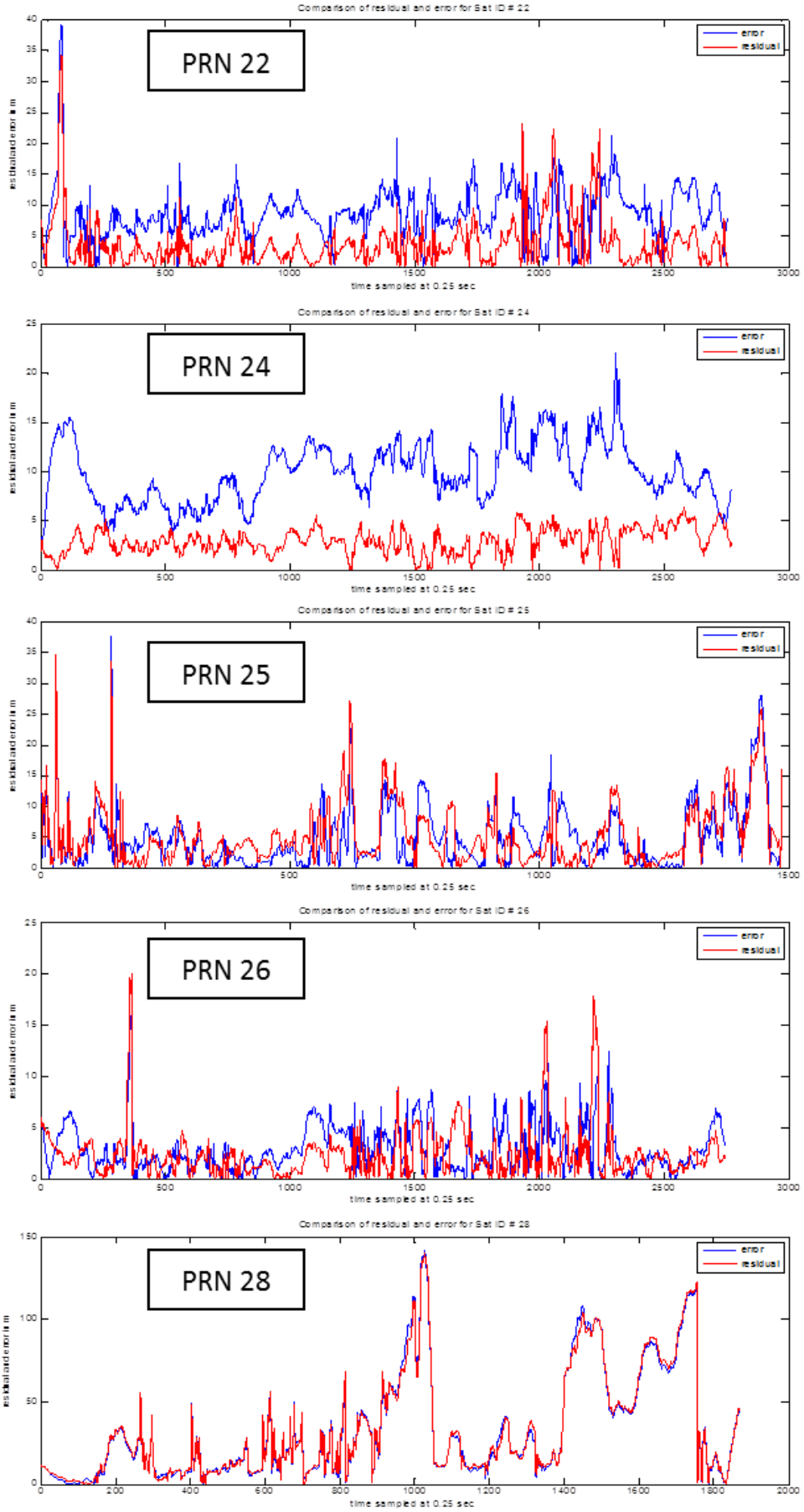

FIGURE 10: Comparaison des résidus de PR contre l'erreurs de pseudo-distance par satellite (predites en utilisant la référence)

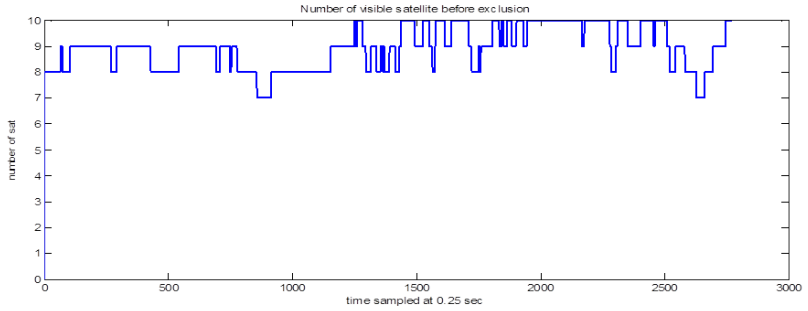

(a)

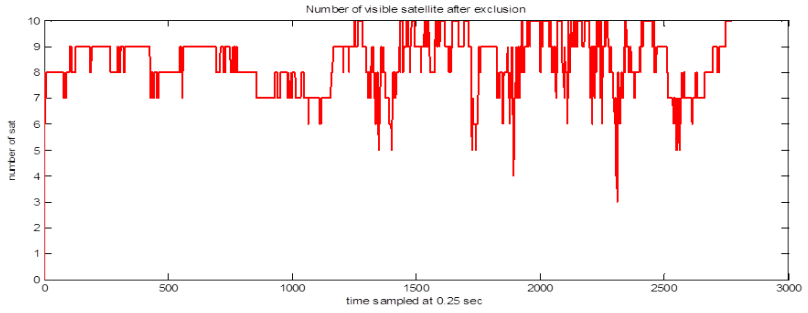

(b)

FIGURE 11: Comparaison du nombre de satellites visibles par rapport au nombre de satellites non-défectueux

où:

- D est la mesure de l'effet Doppler en Hz
- $L1$ est la fréquence de la porteuse
- c est la vitesse de la lumière
- $e_{sat,user}$ est la vecteur unité de la ligne de vue entre le satellite et le récepteur
- V_{user} est le vecteur de vitesse de l'utilisateur
- V_{sat} est le vecteur de vitesse du satellite
- d_t est la dérive d'horloge du récepteur
- ε est le bruit de mesure

On peut envisager de tester la position estimée en générant un résidu, r_V en utilisant la différence entre la vitesse de l'utilisateur et la vitesse prédite.

$$r_V = |V_{user} - V_{predict}| \tag{35}$$

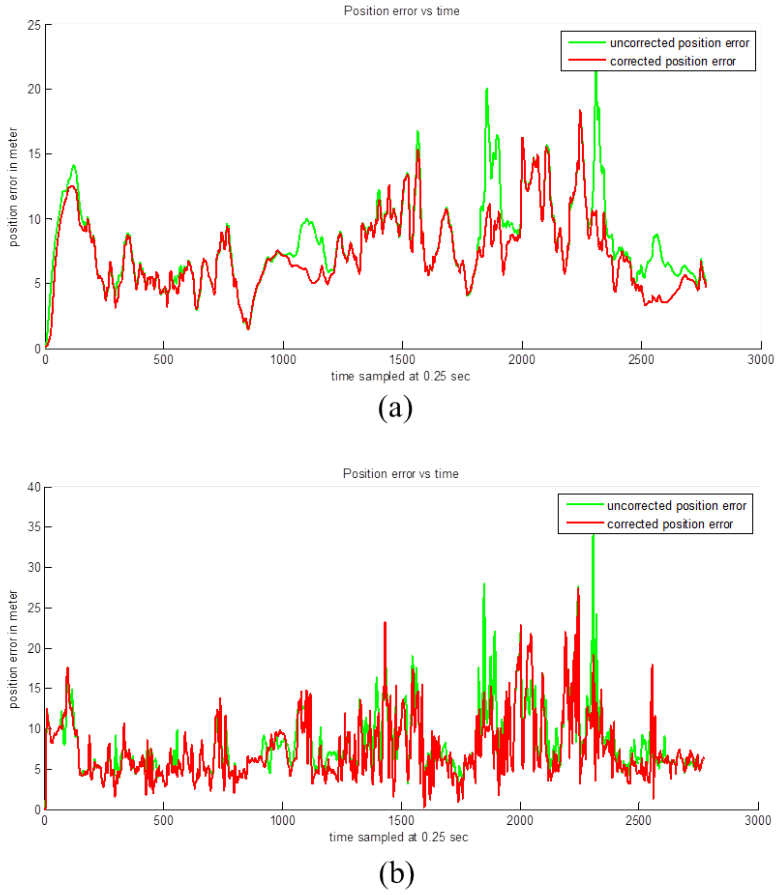

FIGURE 12: Comparaison d'erreur de position après l'exclusion de défaut (a)filtre hybride avec exclusion (b)GPS seulement

Dans cette thèse, nous proposons de calculer la vitesse prédite à partir de V_{odo}. La vitesse de l'utilisateur, V_{user} est déterminée à partir des données GPS. Par conséquent, ici, V_{odo} est totalement un capteur de référence externe et ne contribue pas à la solution de positionnement. Par conséquent, le résidu de vitesse est défini par,

$$r_V = |V_{GPS} - V_{odo}| \tag{36}$$

La figure 5.17 montre la performance du test du résidu de vitesse. Comme on peut le voir dans la courbe, il est difficile d'établir un lien direct entre le résidu de vitesse (bleu) et l'erreur de position (rouge). Autres recherches et analyses sont nécessaires afin de l'utiliser pour le contrôle d'intégrité.

c. Test de fiabilité en utilisant le taux de la distance.

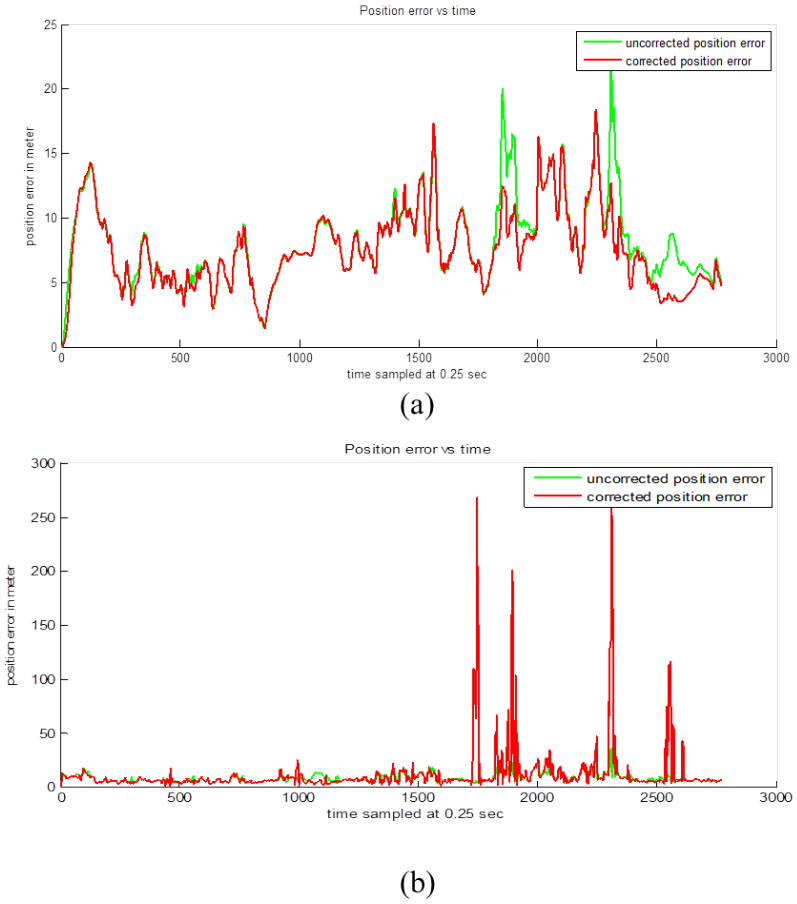

FIGURE 13: Comparaison d'erreur de position après correction de défaut (a)filtre hybride avec correction (b)GPS seulement

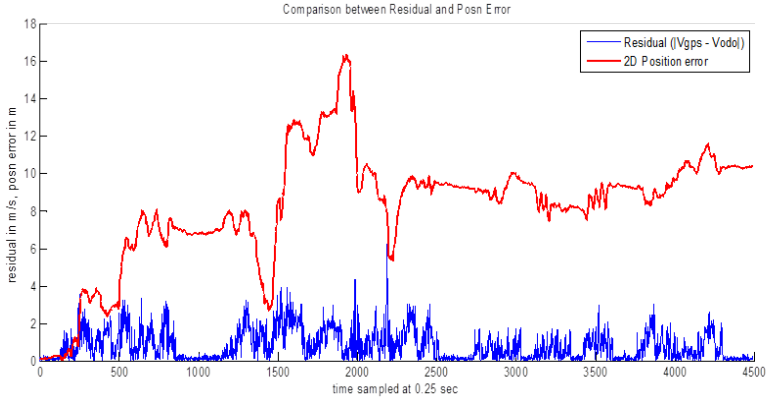

FIGURE 14: Comparaison du résidu de vitesse (bleu) contre l'erreur de position 2D (rouge)

L'équation du taux de la distance est donnée par

$$\begin{aligned} \dot{\rho} &= -\frac{c}{L1}D = e_{sat,user}.(V_{user} - V_{sat}) + d_t + \varepsilon \\ &= \dot{r} + d_t + \varepsilon \end{aligned} \tag{37}$$

où:

- $\dot{\rho}$ est le taux de variation de la pseudodistance
- $\dot{r}$ est le taux de la distance géométrique entre le récepteur et le satellite

Le résidu p, est calculé en utilisant les valeurs prédites et mesurées de $\dot{\rho}$,

$$p = |\dot{\rho}_{measured} - \dot{\rho}_{predict}| \tag{38}$$

où:

$$\dot{\rho}_{measured} = \frac{PR(k) - PR(k-1)}{dt} \tag{39}$$

et

$$\dot{\rho}_{predict} = e_{sat,user}.V_{user}(k) - e_{sat,user}.V_{sat}(k) + d_t \tag{40}$$

où la $V_{sat}(k)$ est calculée à partir des données d'éphémérides et $V_{user}(k)$ est obtenue à partir du filtre de Kalman en fonction du V_{odo} et de l'angle du cap θ. La statistique de test, $T = p^t.Z^{-1}.p$ est utilisée pour ce résidu. Ici, la covariance, Z, est déterminée *a priori* à partir des données observées.

La figure 5.18 montre le résultat de la mise en œuvre l'un FDE fondée sur des résidus du taux de distance. Comme le résidu de la PR , l'erreur de positionnement peut également être améliorée en utilisant la FDE basée sur les résidus du taux de distance.

Les résultats de ces différents modes pour la réalisation de test des résidus suggèrent que le résidu de PR a l'avantage d'effectuer le contrôle d'intégrité dans le domaine de distance même si quand il y a moins de 5 satellites disponibles. Cependant, pour les applications de l'utilisateur qui nécessitent la surveillance de la vitesse, le résidu de vitesse semble être plus approprié. Bien sûr, il y a une possibilité de les combiner comme multi-indicateurs pour surveiller la fiabilité du récepteur. Toutefois, d'autres études sont nécessaires pour déterminer la performance de chaque test des résidus dans les environnements environnants et les comportements dynamiques de l'utilisateur. Cette connaissance est cruciale

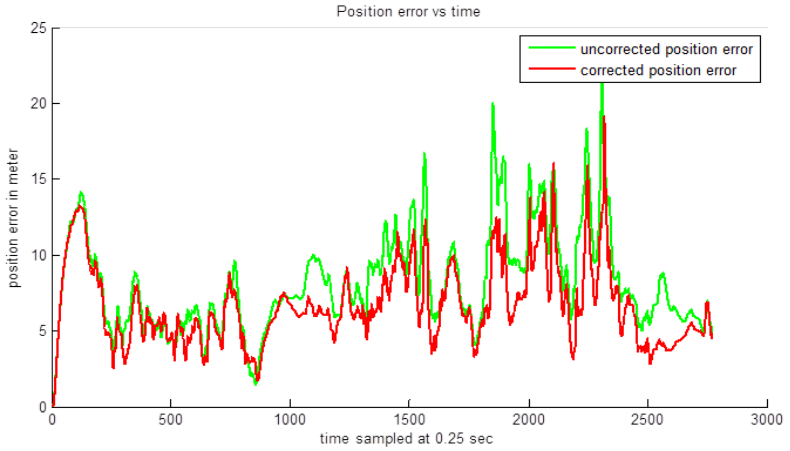

FIGURE 15: Erreur de position après correction de défaut en utilisant le résidu de taux de la distance

pour le développement d'un algorithme approprié pour le récepteur de décider à partir de plusieurs indicateurs, en particulier chaque fois qu'il y a une contradiction entre eux.

La confiance du positionnement GNSS dans des environnements urbains en utilisant la majoration de la CDF des HPE

Enfin, nous avons développé une nouvelle approche expérimentale de surveillance de l'intgrité pour le positionnement en milieu urbain. En travaillant directement dans le domaine de la position, des erreurs de position horizontale (HPE) sont caractérisées en utilisant la distribution de Pareto généralisée. Puis, une statistique de test est dérivée basée sur les résidus de position (plutôt que des résidus de pseudodistance) où sa CDF est estimée et adaptée à la CDF qui borne la distribution d'erreur de position. En surveillant de la statistique de test contre un seuil spécifique, l'intégrité et la continuité de positionnement sont évoluées à un certain niveau de confiance. En outre, le calcul du niveau de protection horizontale (HPL) en utilisant une approche composite a également été proposée.

La caractérisation de l'erreur de position

Dans ce travail, la caractérisation de l'erreur de position du récepteur en utilisant la distribution d'HPE est obtenue à partir de l'erreur de position sur les composantes nord et est. Les erreurs sont calculées sur la base de la différence entre les positions mesurées

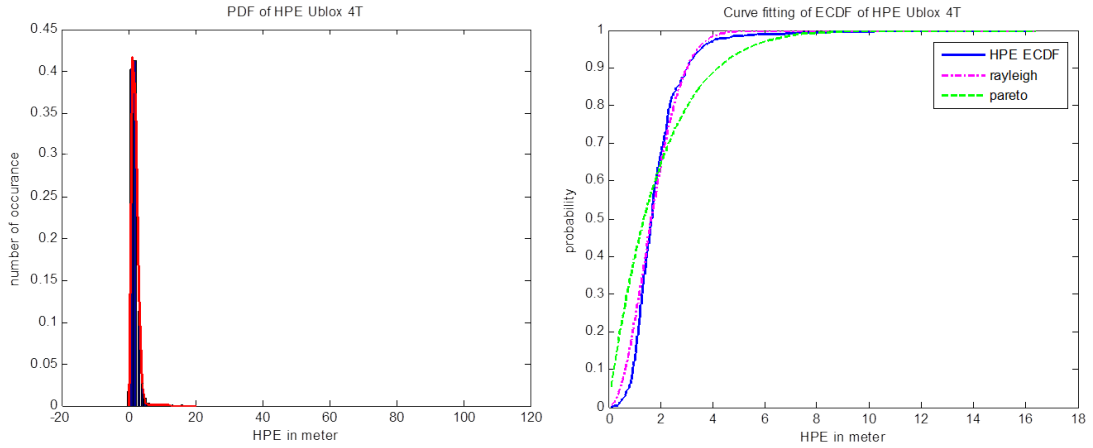

FIGURE 16: PDF et CDF d'HPE dans la zone degagée

et les positions référencées. Puisque l'erreur horizontale 2D a deux composantes nord et est, la HPE peut être représentée comme une erreur radiale, définie par:

$$HPE = \sqrt{E_{east}^2 + E_{north}^2} \tag{41}$$

Dans les environnements degagés, en général, les erreurs de pseudodistance mesurées ont tendance à être distribués selon une loi normale. Dans l'estimation de la position du récepteur en utilisant les PR mesurées, ces erreurs gaussiennes de PR sont combinées et propagées au domaine de la position par l'intermédiaire qui est la matrice d'estimation linéaire pour former des erreurs avec une distribution gaussienne ègalement. Autrement dit l'E_{est} et l'E_{nord} ont tendance à avoir une distribution gaussienne aussi. Théoriquement, en supposant des conditions idéales où les distributions de E_{est} et E_{nord} sont également indépendantes et ont moyennes nulles, la distribution de leur norme, qui est l'HPE, aurait une distribution de Rayleigh. Selon cette hypothèse, la PDF et la CDF de l'HPE sont calculées en utilisant les données empiriques et tracées dans la figure 6.1. Les résultats de ces expériences indiquent que la distribution d'HPE dans des environnements degagés peut être représentée par une distribution de Rayleigh.

Dans le cas de milieux urbains, il a été montré que les distributions des erreurs de PR peuvent être non gaussienne en raison des biais multi-trajets et signal NLOS. Pour cette raison, l'ajustement de courbe pour l'HPE en milieu urbain est réalisé en utilisant la distribution de Pareto. En général, cette distribution est adaptée pour les distributions à queue lourde, comme c'est le cas de l'erreur de positionnement en milieu urbain où on

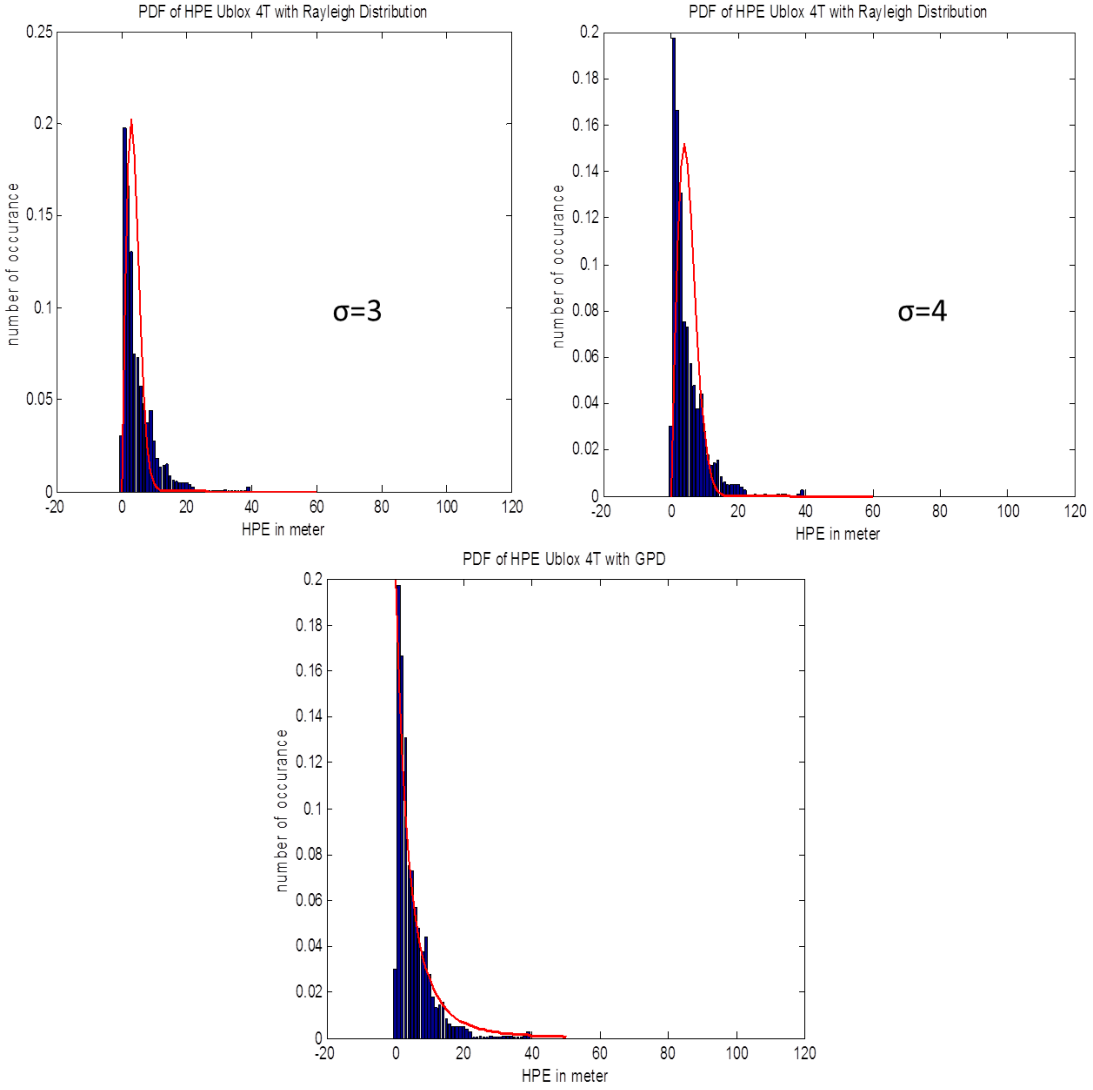

FIGURE 17: Comparaison des PDF en milieu urbain

trouve des large valeurs d'erreurs avec une faible probabilité. La CDF de la distribution de Pareto généralisée est égale à:

$$F(x) = \begin{cases} 1 - (1 + \frac{\xi(x-\mu)}{\sigma})^{\frac{-1}{\xi}} & \text{pour } \xi \neq 0 \\ 1 - exp(-\frac{x-\mu}{\sigma}) & \text{pour } \xi = 0 \end{cases} \tag{42}$$

La figure 6.3 montre la PDF de l'HPE d'un récepteur uBlox-4T dans un environnement urbain. En comparant la PDF de l'HPE contre la courbe de distribution de Rayleigh (les 2 premiers figures), on peut voir que la distribution d'HPE est significativement différent de celui des tracés de Rayleigh avec $\sigma = 3$ (figure en haut à gauche) et $\sigma = 4$ (figure en haut à droite). D'autre part, la comparaison avec le traçage Pareto génralisée (figure du bas) montre un meilleur ajustement de la queue lourde de l'HPE PDF. Dans la figure

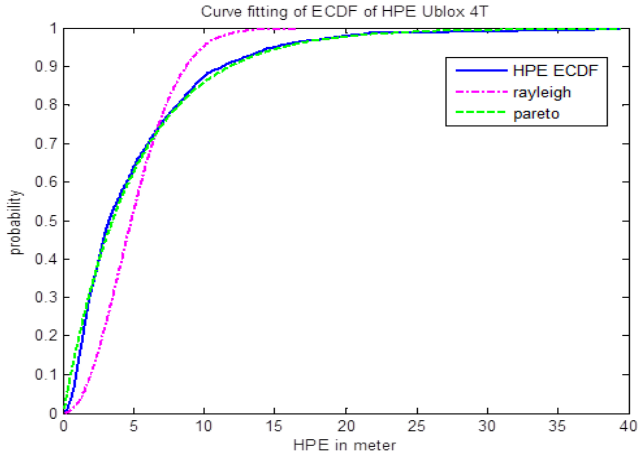

FIGURE 18: CDF en milieu urbain

6.4, le tracé de CDF montre également que la GPD correspond mieux que la Rayleigh à la CDF d'HPE. Dans ce travail, les résultats analysées à partir des données des trois récepteurs différents (uBlox-4T, Novatel, et uBlox-6T) indiquent que la distribution de Pareto généralisée est mieux adaptée pour modéliser les distributions d'HPE en milieu urbain.

La majoration de CDF d'HPE par Pareto généralisée dans le domaine de la position

La CDF d'une GPD a la forme suivante:

$$CDF_{GPD} = 1 - [1 + \xi(\frac{x-\mu}{\sigma})]^{\frac{-1}{\xi}} \ for\ x \geqslant \mu \tag{43}$$

où le paramètre d'échelle σ agit sur la taille et la pente de la distribution, le paramètre de forme ξ affecte la forme de la queue de la distribution et le paramètre de la tendance centrale μ est associé à la valeur de x lorsque la CDF $= 0$.

Une fois que la CDF Pareto généralisée borne la CDF de l'HPE, le niveau de protection horizontale (HPL) peut être calculé à partir de son inverse, de la manière suivante:

$$CDF_{GPD} = 1 - [1 + \xi(\frac{x-\mu}{\sigma})]^{\frac{-1}{\xi}} = Prob(erreur\ de\ position \leqslant x) \tag{44}$$

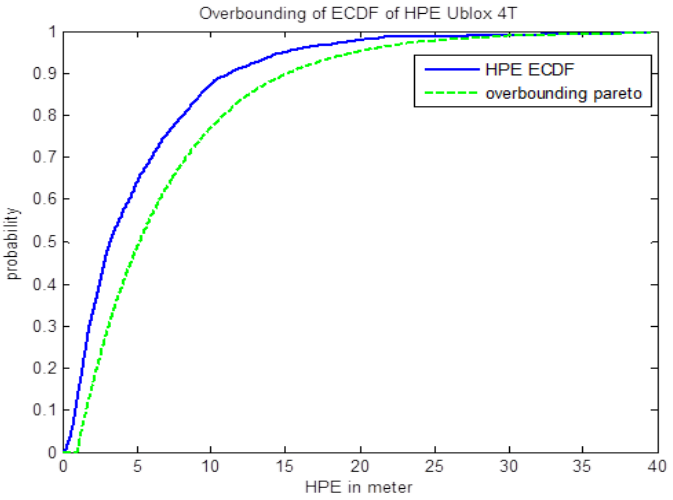

FIGURE 19: La majoration de l'HPE par GPD

Soit R_p la PL d'erreur sur la position. Nous mettons la CDF égale à la probabilité de l'intgrité P_B,

$$1 - [1 + \xi(\frac{R_p - \mu}{\sigma})]^{\frac{-1}{\xi}} = (1 - P_{HMI}) = P_B \tag{45}$$

Pour obtenir l'HPL, nous résolvons R_p,

$$\begin{aligned}
[1 + \xi(\frac{R_p - \mu}{\sigma})]^{\frac{-1}{\xi}} &= 1 - P_B \\
\frac{-1}{\xi} ln[1 + \xi(\frac{R_p - \mu}{\sigma})] &= ln(1 - P_B) \\
ln[1 + \xi(\frac{R_p - \mu}{\sigma})] &= -\xi ln(1 - P_B) \\
[1 + \xi(\frac{R_p - \mu}{\sigma})] &= (1 - P_B)^{-\xi} \\
\xi(\frac{R_p - \mu}{\sigma}) &= (1 - P_B)^{-\xi} - 1
\end{aligned}$$

Ainsi,

$$HPL = R_p = \frac{\sigma}{\xi}[(1 - P_B)^{-\xi} - 1] + \mu \tag{46}$$

La figure 6.13 montre la majoration de l'HPE par la CDF de Pareto généralisée dans le cas du récepteur uBlox 4T. Dans ce cas, l'HPL de l'intégrité à 90 % est de 15 mètres (HPE à 12 mètres) et l'intgrité à 95 % est de 20 mètres (HPE à 15 mètres).

Contrôle d'intégrité du positionement en milieu urbain

La vraie valeur de l'erreur sur la position n'est pas connue en temps réel. Par conséquent, pour le contrôle de l'intégrité de position, un test statistique est utilisé et ce test doit être calculé en utilisant des mesures observables. Dans ce travail, l'intégrité des positions estimées dans les milieux urbains est surveillée en fonction du résidu de la position horizontale. Le résidu de la position horizontale observé est calculé en utilisant une estimation des moindres carrés (LS), puis adapté à la borne d'HPE qui est caractérisée à priori par la GPD CDF. De cette façon, la statistique du test est en mesure de représenter la limite de l'HPE. L'appariement de l'espace de résidu de position avec l'espace de délimitation d'erreur de position peut être décrite par le principe de transformation des variables aléatoires.

a. Calcul du résidu de la position horizontale. Le vecteur des résidus de la position, $\delta\hat{x}$ est calculé en utilisant l'estimation des moindres carrés. Nous considérons le modèle de pseudodistance linéaire suivant:

$$\Delta Y = H.\Delta X + E \tag{47}$$

Pour l'estimation des moindres carrés,

$$\Delta\widehat{X} = G.\Delta Y \tag{48}$$

où

- $G = (H^T H)^{-1} H^T$
- $\Delta\widehat{X}$ est la position estimée
- ΔY est le vecteur des PR mesurées

Le résidu de la PR est exprimé par:

$$\delta\rho = \Delta Y - H\Delta\widehat{X} \tag{49}$$

Par conséquent, le rèsidu de la position est donné par:

$$\delta\hat{x} = G.\delta\rho \tag{50}$$

Ensuite, le résidu de position horizontale, $\text{HPE}_{\delta\hat{x}}$ est obtenu en caculant la norme de la $\delta\hat{x}$ dans les directions nord et est:

$$HPE_{\delta\hat{x}} = \sqrt{\delta\hat{x}_{east}^2 + \delta\hat{x}_{north}^2} \tag{51}$$

b. Calcul des paramètres adaptés. En égalant la CDF d'$HPE_{\delta\hat{x}}$, qui est désigné comme HPE_R, à la distribution de Pareto généralisée, nous avons les équations,

$$HPE_R = \frac{\sigma}{\xi}[(1 - P_B)^{-\xi} - 1] + \mu \tag{52}$$

$$HPE_R = \frac{\sigma}{\xi}[(P_{HMI})^{-\xi} - 1] + \mu \tag{53}$$

Les paramètres de HPE_R: σ, ξ et μ sont déterminés à partir de l'ajustement de courbe des données expérimentales de la même trajectoire que l'HPE ont été calculés.

Afin de calculer les paramètres adaptés, les paramètres du résidu de CDF de la position horizontale, HPE_R, sont liés aux paramètres de CDF prédéterminés qui délimitent l'HPE qui ont été calculées hors ligne.

La GPD CDF qui borne l'erreur de position horizontale caractérisé qui est utilisé pour le calcul de l'HPL est,

$$HPL = \frac{\sigma_o}{\xi_o}[(P_{HMI})^{-\xi_o} - 1] + \mu_o \tag{54}$$

Ensuite, ce que l'on souhaite: $Matched\ HPE_R = HPL$

Alors nous laissons,

$$A\sigma = \sigma_o,\ B\xi = \xi_o,\ \mu + C = \mu_o$$

En conséquence,

$$Matched\ HPE_R = \frac{\sigma.A}{\xi.B}[(P_{HMI})^{-\xi.B} - 1] + \mu + C \tag{55}$$

et les paramètres adaptés sont:

$$A = \frac{\sigma_o}{\sigma},\ B = \frac{\xi_o}{\xi},\ C = \mu_o - \mu \tag{56}$$

c. Dérivation du test statistique. Pour le contrôle de l'intégrité de la position, le test statistique est calculé en fonction de l'$HPE_{\delta\hat{x}}$:

$$Matched\ HPE_R = \frac{\sigma.A}{\xi.B}[P_{HMI})^{-\xi.B} - 1] + \mu + C \tag{57}$$

En réorganisant et en substituant l'équation, on obtient:

$$\begin{aligned}
Matched\ HPE_R - (\mu + C) &= \frac{\sigma.A}{\xi.B}[(P_{HMI})^{-\xi.B} - 1] \\
Matched\ HPE_R - (\mu + C) &= \frac{\sigma}{\xi}[(1 - P_B)^{-\xi} - 1]\frac{A}{B}[\frac{(P_{HMI})^{-\xi.B} - 1}{(P_{HMI})^{-\xi} - 1}] \\
Matched\ HPE_R - (\mu + C) &= (HPE_R - \mu)\frac{A}{B}[\frac{(P_{HMI})^{-\xi.B} - 1}{(P_{HMI})^{-\xi} - 1}] \\
Matched\ HPE_R &= (HPE_R - \mu)\frac{A}{B}[\frac{(P_{HMI})^{-\xi.B} - 1}{(P_{HMI})^{-\xi} - 1}] + \mu + C
\end{aligned} \tag{58}$$

Par conséquent

$$Test\ Statistique = (HPE_{\delta\hat{x}} - \mu)\frac{A}{B}[\frac{(P_{HMI})^{-\xi.B} - 1}{(P_{HMI})^{-\xi} - 1}] + \mu + C \tag{59}$$

$$Test\ Statistique = Matched\ HPE_{\delta\hat{x}}$$

Une fois que les paramètres adaptés A, B et C sont déterminés, l'intégrité de positionnement peut être surveillée en calculant le test statistique et en le comparant contre le seuil. La figure 20 montre les étapes du procédé de surveillance de l'intégrité proposées dans cette thèse. Dans cette approche, la distribution observée est adaptée à la borne d'HPL. En conséquence, contrairement à la RAIM traditionnelle, la distribution des statistiques du test est ajustée pour assurer que l'HPE a la même majoration comme l'HPL.

Chaque figure 6.17, 6.18, 6.19 et 6.20 montre les courbes de la CDF d'HPE (rouge solide), la CDF de sa délimitation (pointillé rouge), la CDF du résidu de la position (bleu solide) et la CDF du résidu adapté de la position (en pointillés bleu) pour chaque trajectoire 1, 2, 3 et 4. En général, on peut voir sur chaque figure que la CDF du résidu adapté est en mesure de borner la CDF d'HPE. Cependant, en terme de correspondance avec la délimitation de CDF du GPD, les trajectoires 1 et 2 ont performé mieux que les trajectoires 3 et 4.

Le tableau 6.2 montre la P_{FA} et la P_{MD} calculées lorsque la statistique de test a été

Etape 1	**Calculer l'HPE et les résidus de la position horizontale sur le même trajectoires référencés.**
Etape 2	**Déterminer la CDF de l'HPE puis majorée par la CDF de la distribution de Pareto généralisée (GPD). Cette borne est désigné comme HPL.**
Etape 3	**Modéliser la CDF du résidu la position horizontale (HPER) en utilisant la GPD également.**
Etape 4	**Adapter l'HPER à l'HPL en ajustant les paramètres de HPER.**
Etape 5	**Une fois que les paramètres adaptés sont obtenus, les résidus de la position horizontale adaptés sont utilisés comme des statistiques de test pour surveiller l'intégrité de positionnement.**

FIGURE 20: Les étapes du procédé de surveillance de l'intégrité

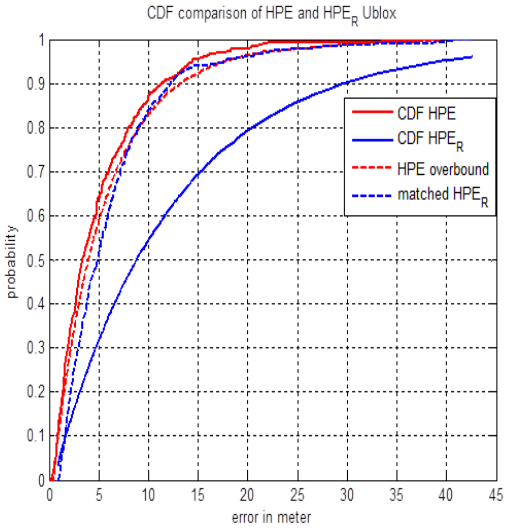

FIGURE 21: Résultat de la correspondance du résidu de la position à la CDF majorée (Trajectoire 1)

utilisé pour surveiller l'intégrité de positionnement le long des quarte trajectoires. Aux fins de la comparaison, les probabilités d'erreur ont été calculées également en utilisant le résidu de la position (sans ajustement), $HPE_{\delta\hat{x}}$ comme la statistique de test. La P_{HMI} a été fixé à 0,05.

Ces résultats montrent que l'exigence d'intégrité est respectée et la statistique de test proposée est en mesure d'équilibrer entre la P_{FA} et la P_{MD} et donc d'optimiser la surveillance de l'intégrité et la continuité de positionnement en milieux urbains. La technique proposée est capable de surveiller l'intégrité du positionnement. Cependant,

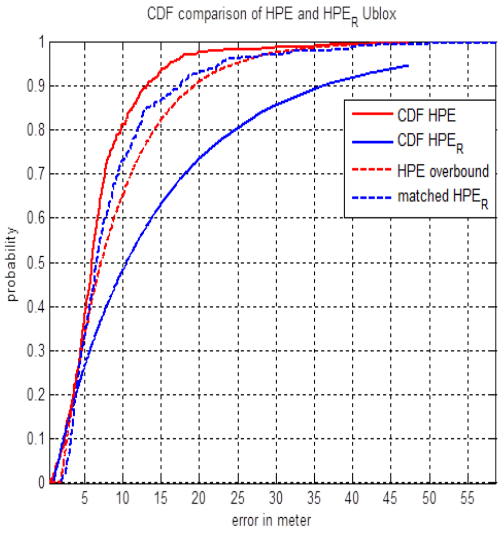

FIGURE 22: Résultat de la correspondance du résidu de la position à la CDF majorée (Trajectoire 2)

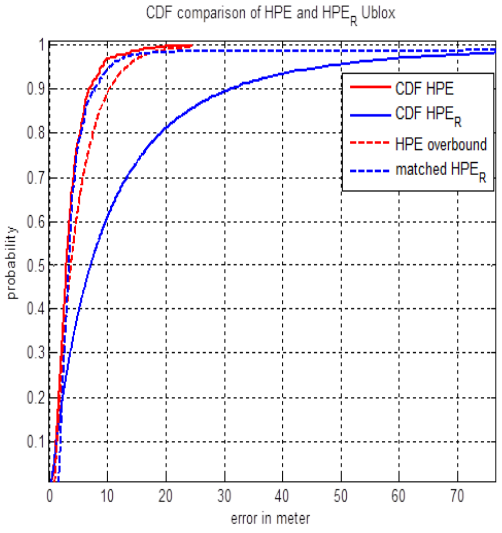

FIGURE 23: Résultat de la correspondance du résidu de la position à la CDF majorée (Trajectoire 3)

	Threshold (m)	***Inflated*** $HPE_{\delta\hat{x}}$		$HPE_{\delta\hat{x}}$	
		P_{FA} (%)	P_{MD} (%)	P_{FA} (%)	P_{MD} (%)
Trajectory 1	18.08	4.23	2.33	20.72	1.69
Trajectory 2	24.35	3.84	1.64	15.07	1.37
Trajectory 3	13.64	2.65	1.94	21.16	0.01
Trajectory 4	15.83	4.07	1.85	23.89	0.18

TABLE 3: Performances de surveillance de l'intégrité de positionnement

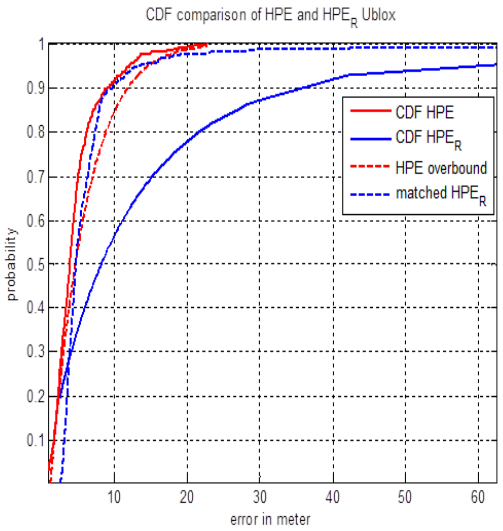

FIGURE 24: Résultat de la correspondance du résidu de la position à la CDF majorée (Trajectoire 4)

puisque ce régime a adopté l'approche directe dans le domaine de la position, il ne peut pas identifier les mesures erronées pour les isoler. D'autre part, cette approche est capable de surveiller l'intégrité de tout type de récepteur sans la nécessité de connaître les algorithmes d'estimation de positionnement tant que nous avons l'erreur de position caractérisé du rècepteur.

L'approche composite pour la surveillance de l'intégrité

Dans l'approche composite, la PL peut être formulée comme une somme de composante de bruit, PL_n, plus une composante de biais, PL_b [16–19]:

$$PL = PL_n + PL_b \tag{60}$$

Dans le domaine d'aviation civile, les sources et les effets du biais spécifiques ont été considérés et bien modélisés. Par contre, dans les milieux urbains, les biais sont principalement à cause de NLOS et multi-trajets réceptions qui sont difficiles à modéliser, donc il est très difficile d'arriver à une expression pour le PL_b.

Afin de mettre en œuvre l'approche composite pour surveillance de l'intégrité de la position en milieu urbain, l'HPE a besoin d'être décomposé en deux composantes celle du biais et une autre du bruit gaussien. Ensuite nous avons caractérisé ces deux composantes séparément. À cet effet, dans ce travail, nous choisissons le modèle autorégressif

(AR) pour estimer la série chronologique de l'HPE, car il est convenable et assez simple pour décomposer les erreurs dans les composantes du bruit et du biais.

$$HPE = AR(p) + \epsilon \tag{61}$$

Le 1^{er} ordre $AR(1)$ peut être écrite comme:

$$x_t = \phi x_{t-1} + \epsilon_t \tag{62}$$

où ϵ_t $N(0, \sigma^2)$

Pour l'ordre p, le $AR(p)$ est donné par:

$$x_t = \phi_1 x_{t-1} + \phi_2 x_{t-2} + \cdots + \phi_p x_{t-p} + \epsilon_t \tag{63}$$

En réarrangeant l'équation,

$$\epsilon_t = x_t - \phi_1 x_{t-1} - \phi_2 x_{t-2} - \cdots - \phi_p x_{t-p} \tag{64}$$

Par conséquent, on peut voir que ce modèle décompose l'erreur en une composante de bruit gaussien ϵ_t et d'autres composantes régressives qui peuvent être le représentant du biais. Dans ce travail, un modèle AR du 4ème ordre est utilisé et la méthode de Burg est choisie parce qu'elle produit toujours des modèles causaux et elle fournit une probabilité gaussienne plus souvent que la méthode de Yule-Walker [20].

Dans la prochaine étape, le bruit est séparé du biais de sorte qu'ils peuvent être caractérisés séparément. Cela peut être fait par filtration de la série chronologique. La fonction de transfert du filtre dans la transformée en z est donnée par:

$$Y(z) = (1 - \phi_1 z^{-1} - \cdots - \phi_p z^{-p}) X(z) \tag{65}$$

où $Y(z)$ est la transformée en z de ϵ_t. Etant donné que ϵ_t est supposé être un bruit gaussien de moyenne nulle, il peut être caractérisé par sa variance, σ_ϵ^2.

Une fois que le ϵ_t est obtenu, le $bias_t$ est calculé par:

$$bias_t = HPE_t - \epsilon_t \tag{66}$$

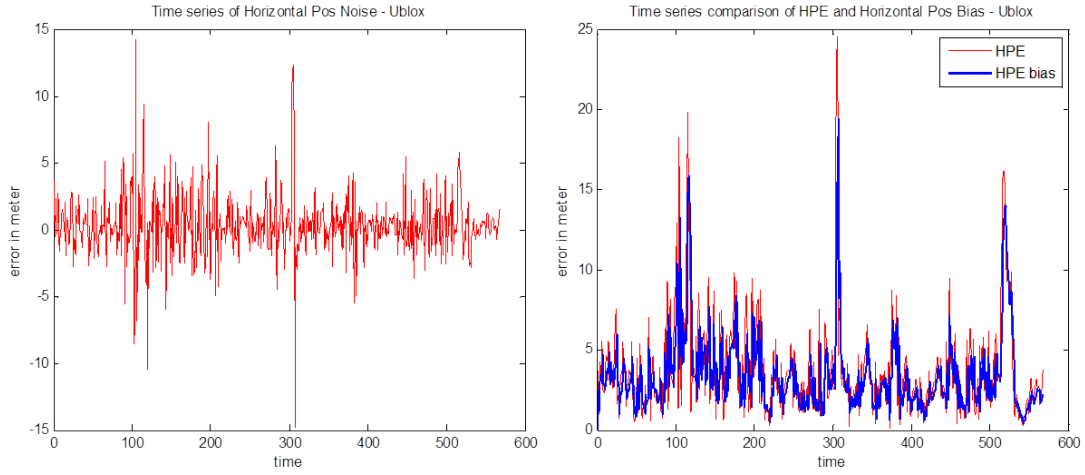

FIGURE 25: Le bruit et le biais décomposés de l'HPE du récepteur uBlox

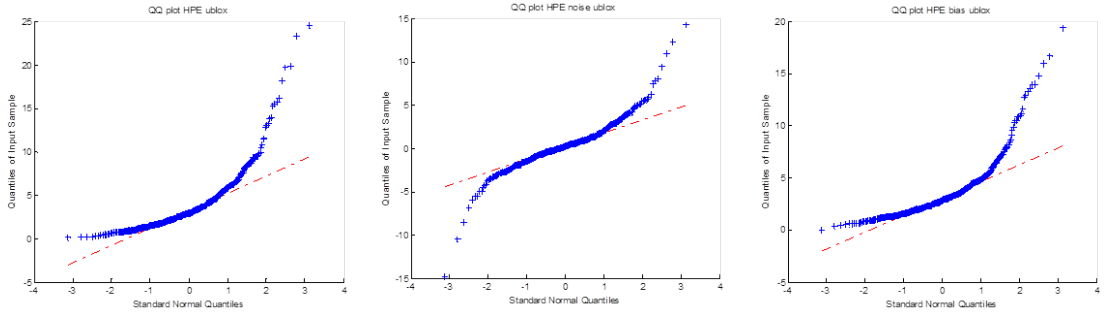

FIGURE 26: Diagramme Q-Q de l'HPE de récepteur uBlox, le bruit et le biais décomposés

Les résultats de la décomposition de l'HPE dans les composantes du bruit et du biais sont tracés dans les figures 6.21 et 6.22 pour le récepteur uBlox, les figures 6.23 et 6.24 pour le récepteur Novatel et les figures 6.25 et 6.26 pour le récepteur Septentrio. Comme indiqué dans les diagrammes Q-Q, le bruit extrait semble avoir une distribution gaussienne au centre mais avec des queues lourdes. Le quantile dans laquelle la queue commencent à devenir lourdes diffère entre les récepteurs. Ces situations indiquent que l'approche de modèle AR utilisée dans ce travail pour extraire le bruit gaussien d'HPE n'est pas très efficace pour supprimer totalement la queue lourde et extraire uniquement un bruit blanc gaussien de l'HPE. Cependant, même si il y a certains éléments de queues lourdes, l'utilité de cette technique dépend de l'AL, du seuil et de la P_{HMI} qui sont requis pour les applications visées.

Contrairement à les environnements degagés, un biais dans les environnements urbains sont principalement dues à les réceptions multi-trajets et NLOS qui font leur modélisation déterministe d'être très complexe. Ainsi, dans ce travail, la délimitation

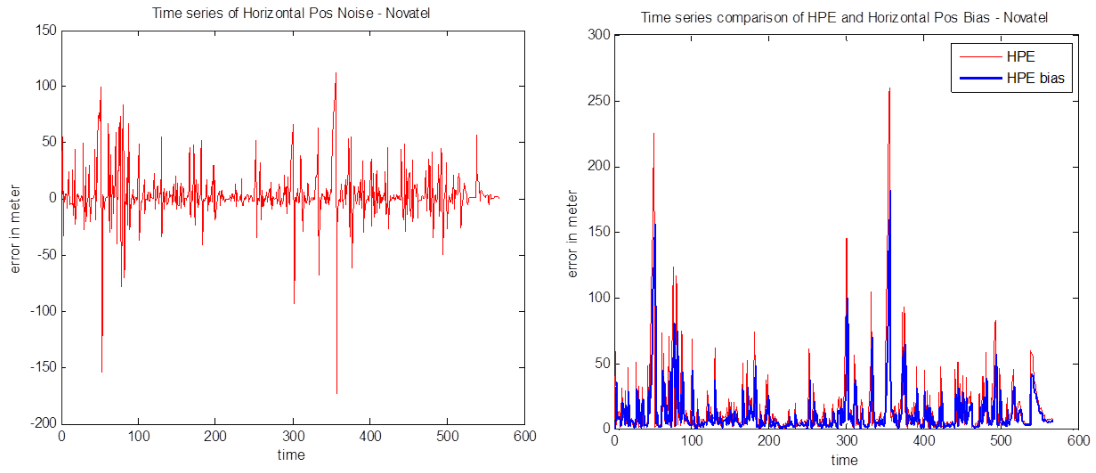

FIGURE 27: Le bruit et le biais décomposés de l'HPE du récepteur Novatel

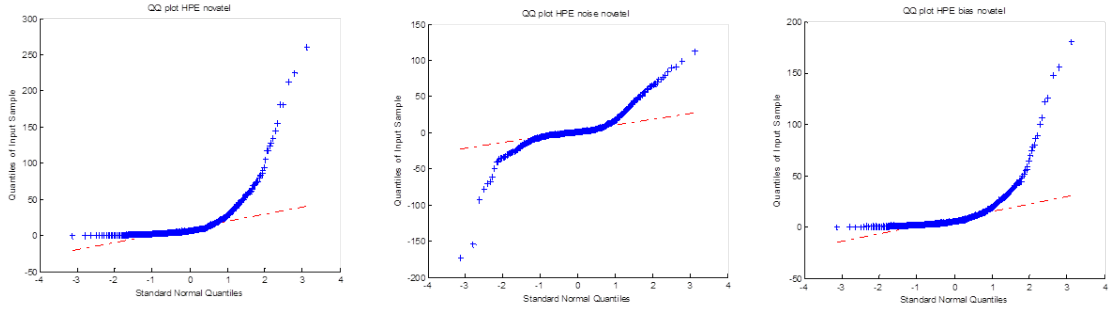

FIGURE 28: Diagramme Q-Q de l'HPE de récepteur Novatel, le bruit et le biais décomposés

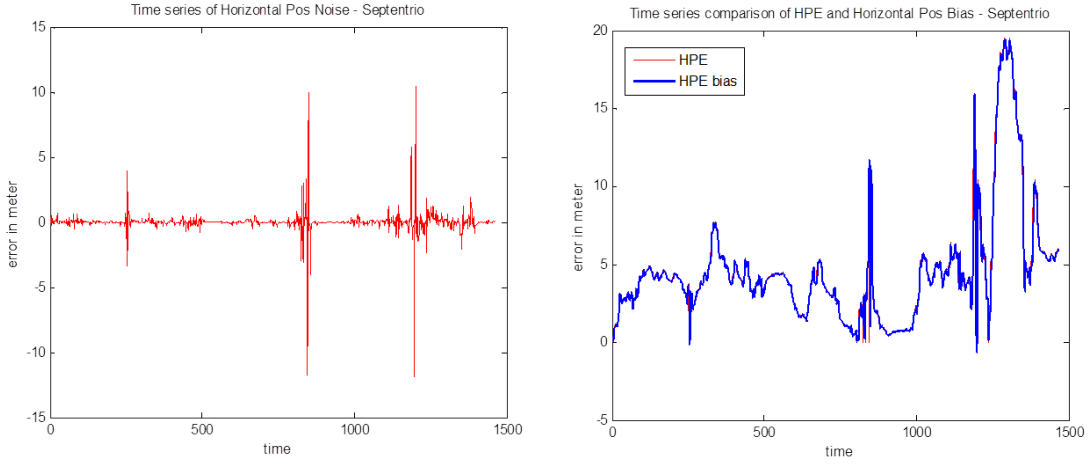

FIGURE 29: Le bruit et le biais décomposés de l'HPE du récepteur Septentrio

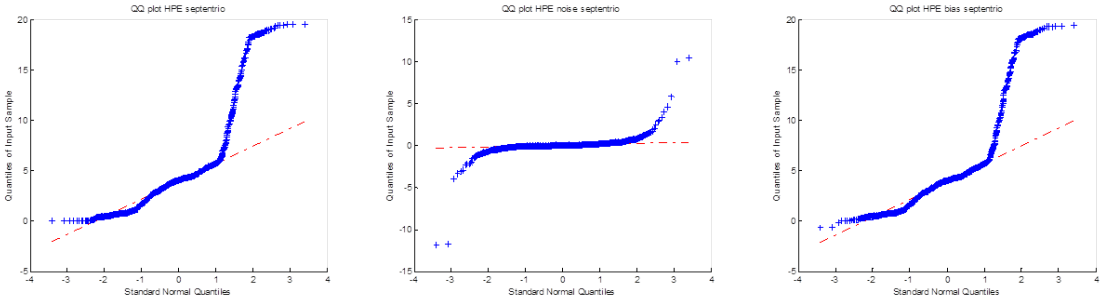

FIGURE 30: Diagramme Q-Q de l'HPE de récepteur Septentrio, le bruit et le biais décomposés

de la biais a été fait en utilisant l'approche statistique où la distribution de biais est délimitée par une distribution gaussienne. En tant que tel, la distribution de délimitation de biais peut être caractérisée comme [19]:

$$HPE_{bias} = \mu_b + \sigma_b \sqrt{2} erf^{-1}(2P_b - 1) \tag{67}$$

où P_b est la probabilité d'intégrité. En une notation simplifiée,

$$HPE_{bias} = \mu_b + \sigma_b K_H \tag{68}$$

Les valeurs de μ_b et σ_b sont obtenus *a priori* en ajustant la courbe de la borne de CDF empirique (ECDF) du biais d'HPE.

Comme cela a été établi, il est l'HPL qui est utilisé pour surveiller l'intégrité de positionnement. Pour l'approche composite, l'HPL doit être calculé pour les deux termes: la composante du biais et la composante du bruit.

a. HPL pour la composante de bruit. Contrairement aux systèmes d'augmentation tels que SBAS et GBAS, positionnement de véhicule terrestre en milieu urbain n'a pas de références. Ainsi la variance du bruit qui est utilisée pour le calcul de l'HPL est obtenue à partir du modèle de la variance de PR. Dans ce travail, le modèle de la variance du CNo-élévation de PR [21] est adopté:

$$\sigma_i^2 = k \times \frac{10^{(-0.1 \times CNo_{measured})}}{\sin^2(\theta_i)} \tag{69}$$

où k égale 1 pour le signal LOS et il change pour le signal NLOS.

Dans la mise en œuvre, il existe certains éléments d'incertitude car l'estimation de la distribution du bruit de l'HPE n'est pas parfait et σ_p est obtenu à partir d'un modèle de variance de PR qui est différente de la σ_ϵ du bruit d'HPE estimé. Par conséquent, le sigma doit être gonflé pour compenser ces incertitudes et de veiller à ce que le bruit d'HPL délimite le bruit d'HPE.

Dans ce travail, l'inflation du bruit HPL est mis en œuvre dans le domaine de position avec un facteur d'inflation A tel que:

$$HPLnoise_{inflated} = A.K_H\sigma_p \tag{70}$$

Pour estimer l'A, nous égalons l'$HPLnoise_{inflated}$ à la distribution de délimitation de ϵ_t de sorte que:

$$A.K_H\sigma_p = K_H\sigma_\epsilon \tag{71}$$

et donc

$$A = \frac{\sigma_\epsilon}{\sigma_p} \tag{72}$$

où σ_ϵ est l'écart-type du bruit de HPE et σ_p est l'écart-type de l'erreur de la position prédite basé sur le modèle de la variance de PR.

b. HPL pour la composante du biais. L'HPL de biais est basé sur le résidu de la position (qui est observable en temps réel) et ensuite gonflé/adapté statistiquement afin de borner l'ECDF de biais d'HPE. L'adaptation de CDF est fait en utilisant des paramètres de transformation de CDF similaire à l'approche de l'inflation sigma dans le délimitation de CDF. La CDF du résidu de la position est:

$$HPE_r = \mu_r + K_H\sigma_r \tag{73}$$

En adaptant l'HPE_r:

$$HPLbias_{inflated} = \mu_r + B + C.K_H\sigma_r \tag{74}$$

En réorganisant et en substituant 6.44 en 6.45,

$$HPLbias_{inflated} = HPE_r - K_H\sigma_r + B + C.K_H\sigma_r \tag{75}$$

$$HPLbias_{inflated} = HPE_r + B + (C-1).K_H\sigma_r \tag{76}$$

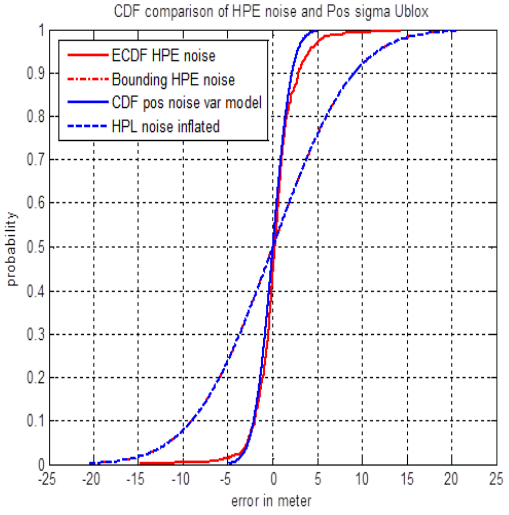

FIGURE 31: Délimitation gonflée de la CDF du bruit (Ublox)

Pour estimer les paramètres B et C, nous laissons

$$\mu_r + B = \mu_b$$

et

$$C.K_H\sigma_r = \sigma_b K_H$$

où μ_b et σ_b sont des paramètres de 6.37. De ce fait,

$$B = \mu_b - \mu_r \tag{77}$$

ce qui signifie que, la moyenne de $HPLbias_{inflated}$ est réglée pour correspondre à la moyenne de $HPEbias$, et

$$C = \frac{\sigma_b}{\sigma_r} \tag{78}$$

ce qui signifie que, le sigma de $HPLbias_{inflated}$ est gonflé pour correspondre au sigma de $HPEbias$.

Les figures 6.27, 6.28 et 6.29 tracent l'HPL gonflé délimitant les CDF des bruits pour les récepteurs uBlox, Novatel et Septentrio, respectivement. Dans ces courbes, l'HPL gonflé est représenté par une ligne pointillée bleue. La CDF initiale observée à partir du modèle de la variance est représentée par la ligne bleue. La CDF de la distribution de bruit est représentée en rouge solide alors que sa limite est tracée par une ligne rouge

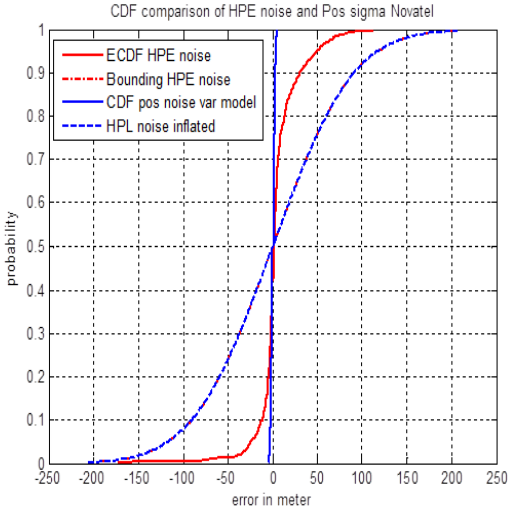

FIGURE 32: Délimitation gonflée de la CDF du bruit (Novatel)

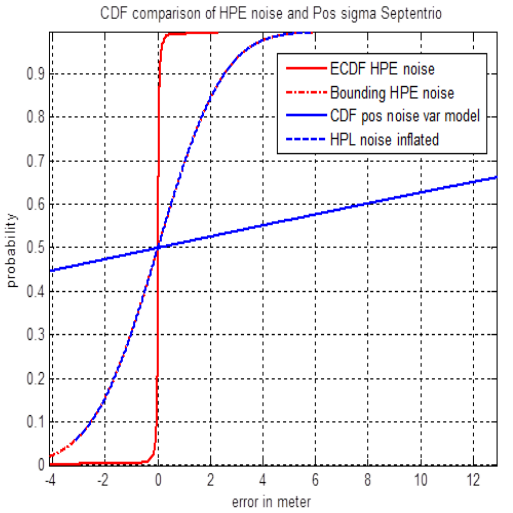

FIGURE 33: Délimitation gonflée de la CDF du bruit (Septentrio)

pointillée. Dans tous les trois figures, on constate que l'HPL gonflé est en mesure de borner la CDF de la distribution du bruit.

La délimitation des CDF des biais par l'HPL gonflé dans le cas des récepteurs uBlox, Novatel et Septentrio sont présentées dans les figures 6.30, 6.31 et 6.32 respectivement. Parce que l'HPE est défini comme une norme des erreurs 2D, les biais de l'HPE restent en valeur positive. Par conséquent, la délimitation du biais ne concerne que le côté positif de la CDF. Dans les figures 6.30, 6.31 et 6.32, après l'inflation, les distributions du biais sont respectivement limitées par leur HPL gonflées. Il est intéressant de noter que tandis que le récepteur multi-constellation Septentrio a une meilleure précision dans des environnements urbains, sa performance d'intgrité en raison du biais n'est pas très

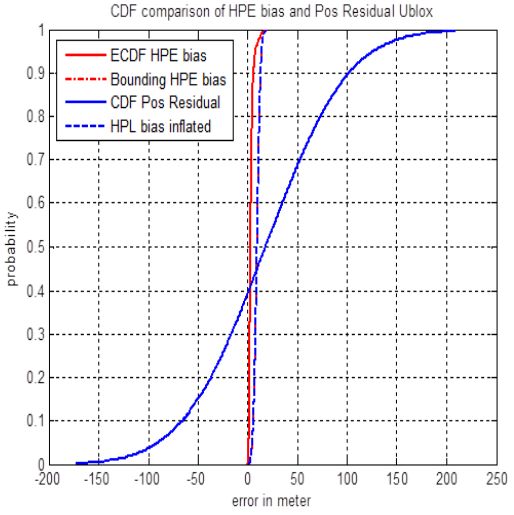

FIGURE 34: Délimitation gonflée de la CDF du biais (Ublox)

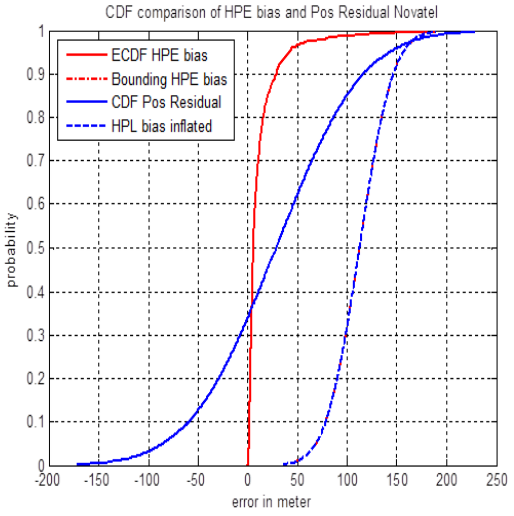

FIGURE 35: Délimitation gonflée de la CDF du biais (Novatel)

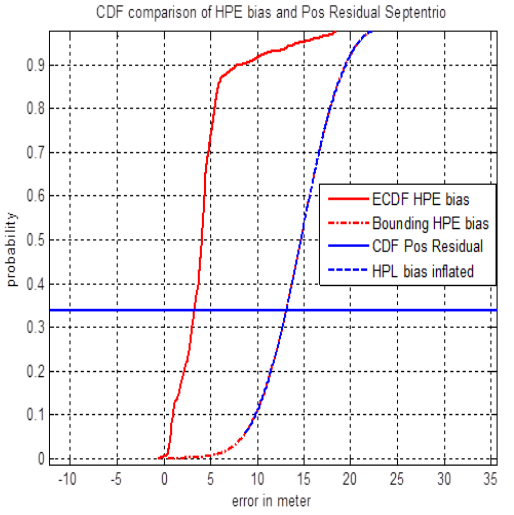

FIGURE 36: Délimitation gonflée de la CDF du biais (Septentrio)

différent que celui du récepteur uBlox. Pour 90% de confiance, l'HPL gonflée pour Septentrio est d'environ 19 mètres alors que pour le uBlox est d'environ 13 mètres. Par conséquent, il montre que l'effet du biais dépend de l'environnement plutôt que de la précision du récepteur.

En obtenant la majoration de CDF d'HPE, l'approche directe du domaine de la position est en mesure de contourner les difficultés et la complexité de la modélisation des erreurs de PR dans les milieux urbains que la majoration dans le domaine de la distance doit affronter. Cependant, la limitation de cette approche directe du domaine de la position est que chaque canal de satellite n'est pas surveillé individuellement.

D'autre part, si les biais multiples de la PR mesurée combinés avec la géométrie dans une telle manière que les résidus de la PR restent faibles, mais les erreurs de position devient grande, l'approche du domaine de la position pourrait détecter l'erreur et pas le contrôle dans le domaine des mesures. En tant que tel, une combinaison de ces deux domaines des pseudo distance et de position peut être mise en œuvre en tant que concept de surveillance d'intégrité multicouche.

Des systèmes parallèles peuvent aussi être mises en œuvre où plusieurs estimations de position sont calculées en même temps avec chacun ayant une PR exclue. De cette façon, il est également possible d'identifier la PR erronée causant un biais inacceptable de positionnement.

Une des questions pertinentes de majoration d'erreur dans le secteur de l'aviation est la rareté des données observantes de la queue de la distribution d'erreur. Par conséquence, les techniques d'extrapolation tels que la théorie des valeurs extrêmes a été mis en œuvre pour faire face à le problème. Toutefois, cette question pourrait être détendit un peu dans les applications terrestres considérant que toutes les applications ne nécessiteraient une telle petite valeur de P_{HMI}. Par exemple, un P_{HMI} de 10^{-2} peut déjà être acceptable pour certaines des applications terrestres.

En outre, cet exercice de caractériser les erreurs de position des récepteurs différents en milieu urbain peut également bénéficier de l'effort de catégoriser et de certifier les récepteurs. En ayant les caractéristiques de HPE des récepteurs, les récepteurs peuvent être classés en différentes qualités de performance et cela doit permettre une sélection correcte d'un récepteur approprié pour un certain type d'applications terrestres.

Conclusions et Perspectives

Cette thèse porte sur les défis en matière de contrôle de la fiabilité de la navigation par satellites GNSS pour les applications des véhicules terrestres dans les milieux urbains. L'objectif principal de cette recherche est de développer des méthodes de positionnement avec confiance en utilisant des mesures GNSS et d'autre mesures exterieurs pour les utilisateurs dans des environnements urbains contraintes. Essentiellement, la confiance de positionnement est identifiée avec la capacité de faire confiance à la position estimée.

Dans la première partie de nos travaux de recherche, les erreurs NLOS dans les milieux urbains sont caractérisés à l'aide d'un modèle 3D de l'entourage urbain. Dans un environnement avec un nombre limité de satellites visibles, l'exclusion des signaux dégradés pourrait aboutir à ne pas avoir assez de mesures acceptables pour obtenir une solution de position ou de nuire à la géométrie des satellites. Par conséquent, si le signal dégradé peut être identifié, et si son biais peut être estimé, le signal peut être corrigé et efficacement utilisé pour le positionnement. A cet effet, un simulateur de GNSS est utilisé conjointement avec le modèle 3D afin d'identifier les signaux NLOS et de prédire leurs biais. De cette prédiction, les signaux NLOS sont corrigés et utilisés pour améliorer la précision et l'intégrité des positions estimées. La capacité du modèle 3D à prédire l'état de réception du signal soit dans LOS ou NLOS a été jugée acceptable et encourageante. Néanmoins, en raison des limites du modèle 3D en termes de la grande variabilité des facteurs géométriques, sa capacité de prédire le biais NLOS instantané a été jugé modeste et pas concluante pour les données traitées. De même, quand les biais prédits ont été utilisées pour les corrections de PR dans le filtre de Kalman d'estimation de la position, les résultats ont montré que les erreurs de positionnement sont généralement presque similaires à celles calculées en utilisant le biais calculé à partir de la trajectoire de référence. Cela signifie que cette information est très utile.

Dans cette thèse, nous avons proposé dans la deuxième partie du travail une technique de surveillance de la fiabilité du GNSS en environnement urbain à l'aide d'un capteur de vitesse de confiance. L'approche prend une prédiction de pseudodistance déduite en utilisant l'hybridation avec d'autres capteurs pour maintenir la continuité du positionnement, même dans la situation de la réduction du nombre des satellites visibles. Un odomètre et un gyroscope sont utilisés comme des capteurs de DR qui sont couplés avec le récepteur GNSS pour obtenir une position de référence pour le contrôle de la fiabilité

de la pseudodistance GNSS. En utilisant l'approche hybride, des résidus sont générés pour formuler un test statistique testé contre un seuil. Quelques formes de résidus ont été obtenues sur la base de plusieurs observables, à savoir les PR, le taux de la distance et de la vitesse. Pour le résidu de vitesse, l'odomètre a été capteur de référence. Le résultat considéré comme un de la représentation du résidu de la PR sur les erreurs varie d'un satellite à un autre. Le résidu a une bonne représentation pour les satellites avec erreurs de grandes valeurs. Puisque dans un tel cas, les résidus de PR ont été en mesure de détecter les erreurs de mesure avant qu'ils ne soient acceptés comme mesures valides pour le positionnement. En ce sens, le résidu de PR peut être utilisé comme la première couche dans les couches multiples comme métrique de surveillance de la fiabilité. Un potentiel similaire a également été mise en évidence par la technique FDE qui est basé sur le résidu du taux de la pseudo-distance. Cependant, son inconvénient dans ce travail par rapport à l'approche basée sur le résidu des PR est qu'il ne peut pas être mis en œuvre pour corriger ou remplacer la mesure défectueuse. D'autre part, nous avons constaté qu'il est très difficile de lier le résidu de vitesse à l'erreur de positionnement. Au contraire, il serait utile pour la détection d'erreur de vitesse. Nous avons examiné le modèle 3D et d'autres capteurs parce que nous sommes convaincus que dans des environnements difficiles, la surveillance de l'intgrité a besoin d'informations supplémentaires autres que du GNSS.

La recherche dans cette thèse a également conduit au développement d'une nouvelle méthodologie expérimentale de surveillance d'intégrité pour le positionnement dans les environnements urbains. Travailler directement dans le domaine de position, les distributions d'erreurs de position horizontale (HPE) sont caractérisées par la distribution de Pareto généralisée. Puis, une statistique de test est dérivée basée sur les résidus de position (plutôt que des résidus de pseudodistance) qui CDF sont adaptés ou gonflés pour correspondre à la majoration de la CDF d'erreur de position caractérisée. En surveillant la statistique de test contre un seuil spécifique, l'intgrité et la continuité de positionnement sont remplies à un certain niveau de confiance. Les résultats à l'aide de données recueillies dans les zones du centre-ville de Toulouse montrent que la technique est assez prometteuse.

La méthode est ensuite étendue à calculer de manière autonome le niveau de protection horizontale (HPL) en milieu urbain à l'aide d'une approche composite. La décomposition des distributions HPE dans ses composantes de bruit et de biais a été mis en œuvre

avec un filtre AR. En ciblant la simplicité et la mise en œuvre directe, la distribution gaussienne est utilisée comme une distribution limite via sa CDF tant pour le bruit que pour et les distributions des biais. Alors que la question des queues lourdes a été confrontée dans cette approche, son application est potentiellement plus élevée pour les récepteurs multi-constellation, comme indiqué dans les résultats.

Plusieurs perspectives sont notables résultant des travaux de cette thèse, en particulier, les points suivants présentent un intérêt particulier:

- Utilisation des échantillons de mesure obtenus dans de diverses villes pour l'analyse des performances. Avec ces données, une évaluation plus approfondie sur la robustesse de la distribution de surdélimitation de Pareto généralisée comme l'approche de l'intégrité de positionnement de surveillance en milieu urbain peut être effectuée. Autres types de distributions qui peuvent prendre en compte la queue lourde des erreurs peuvent être étudiées pour caractériser les biais GNSS.
- Chercher une technique plus efficace pour extraire le bruit gaussien aléatoire de la distribution HPE. Cela contribuera à une délimitation plus efficace du bruit dans l'approche composite de calcul du HPL pour les environnements urbains.
- Identifier et développer des techniques qui peuvent combiner de manière optimale les méthodes heuristiques, des approches du domaine des mesures et du domaine de la position dans une procédure de surveillance de l'intégrité. Ils pourraient être en couches multiples, à exécuter de manière séquentielle ou en parallèle, ou de manière sélective en fonction des situations particulières.
- Pour étudier plus en avant l'efficacité de la technique résiduelle de vitesse pour le suivi d'applications liées à la vitesse. Il pourrait être également intéressant de rechercher des méthodes permettant de relier la vitesse résiduelle à la position de sorte qu'elle peut être utilisée pour le contrôle du positionnement.
- Étudier l'utilisation des approches statistiques non-paramétriques pour modéliser les erreurs soit dans le domaine de pseudo-distance ou dans le domaine de la position.

Chapter 1

Introduction

Free accessibility and suitable accuracy of the Global Navigation Satellite System (GNSS) signals for location and timing, along with the availability of affordable receiver chipsets, had promoted the GNSS as the preferred solution for a very wide and growing range of applications. Nowadays, the GNSS encompass operational systems such as GPS, GLONASS and the under development systems mainly like the Chinese BEIDOU and the European GALILEO. Satellite navigation and timing are used all over the world in a plethora of fields such as transportation, agriculture, fisheries, law enforcement, search and rescue, and many others. Expectations of their evolution in the coming years, especially with the development of the European Galileo system and other regional systems, forecast on a large increase of these products and of new services. According to the European GNSS Agency, location-based-service (LBS) and road applications such as in Intelligent Transport System (ITS) will be the market sectors with the highest revenue generation for the GNSS related industry [22].

In view of such progress, there have been many initiatives to further develop GNSS based applications. For example, in the case of road applications, the GSA had commissioned a research initiative known as GIROADS (GNSS Introduction in Road Sector) which aimed at aggregating the road community's proposals to facilitate the technical and commercial introduction of Europe's satellite navigation programme to the road transport sector [23]. As an illustration, road user charging (RUC) is one of the road applications (where GPS is used as the primary technology) that has been successfully implemented

in Germany [24] and Slovakia [25]. In October 2014, Singapore had announced the decision to replace its existing congestion pricing system (called ERP - Electronic Road Pricing) by 2020, with a GNSS-based system that will allow more dynamic and variable pricing by individual road and time of day [26]. In France, a project called EcoTax has been developed but its implementation is facing social and political objection. Indeed, many sectors are using more and more GNSS based applications such as in the agriculture, robotics, machine-based services and so forth. Nevertheless, these exciting and promising potentials for the progress of GNSS applications in land navigation are not without major hurdles in their course of development. It is acknowledged that reliable performance is difficult to achieve in restraint environments such as in urban settings or roads under heavy foliage canopy. Performance reliability of satellite navigation is especially critical for applications which potentially have impacts on financial, legal or even safety-of-life aspects.

In open sky environments, the performance of the GNSS positioning have been improved over the time. The accuracy of a single point positioning already lies in meter level. Further performance improvements have been achieved by using carrier-phase measurements and by implementing differential technique. However, there is no concluding study exist in improving the performance of GNSS positioning in urban environments.

This introduction begins with the research motivation and followed by a short overview of the existing and future planned GNSS systems and some brief descriptions of the basic working principle of satellite navigation and the concept of integrity developed originally in augmentation systems for civil aviation. Then, different concepts and performance measures for reliability in positioning are briefly described. After that, the thesis objectives and contributions are highlighted before delineating the thesis structure.

1.1 Motivation

The GNSS positioning services for land applications have grown in popularity and usefulness that they are poised to be receiving more demands from users. These existing terrestrial applications together with many more potential services cover a broad range of applications such as location based charging, pay-as-you-drive (PAYD) road charging, specific car tracking (racing, insurance, criminals, etc.) and geo-localization reporting

[27]. In addition, the applications for Advance Driver Assistance System (ADAS) such as lane keeping, collision avoidance and so forth also make use of the GNSS positioning system [28]. Since many of the services involve financial, legal and potentially safety-of-life repercussions, these applications would need compliance with safety and reliability requirements. In order to foster innovation and further expedite the development for the land navigation applications, a lot of effort is needed to achieve the technical and regulation requirements.

More often than not, in these land-based applications, the GNSS receiver is a sub-system for providing positioning, velocity and time (PVT) information that would be used as subsequent inputs by the next module in the application system as a whole. In fact, the GNSS is not the only technology involved in the positioning module when hybrid solution is implemented. In such case, the GNSS technology is complemented by other sensors, for instance inertial or odometric, in order to improve the performance of the PVT solution. Because of these arrangements, there is a need to choose a suitable receiver type and to know its minimum performances so that the final applications requirement at the user level will be met [29, 30]. For this purpose, the characterization of positioning error is needed to provide the final user with the level of confidence needed by his application which uses the technical requirements of the GNSS solution.

Many factors affect the final performance of a GNSS receiver. Some of them are related to the inherent quality of the receiver and its antenna (sensitivity, quality of signal processing, resilience to interference and jamming, etc.), while some are related to the atmospheric layers which the signals pass through and finally some are related to the receiver environment of reception. The interference sources in local reception environment (masks, multipath, diffraction, etc.) including the dynamics of mobile objects has crucial effects on the performance. Indeed, along with the appearance and innovation of new land applications, many of the demands and challenges on their performances come from urban environments where the processing needs of the received signals are extensively more complex than in open sky environments.

Reliable GNSS positioning is difficult to be achieved in dense urban areas because in these environments the satellites signals are often obscured or reflected by buildings and receiver-surrounding objects, which distort measurements and bias the calculated position. Diffracted and reflected signals received together with the direct signal can

result in ten-meter-order positioning errors, and hundreds of meters of positioning error can be present in non-line-of-sight (NLOS) signals situations. As these issues hinder or slow down the adoption of GNSS in applications which require high service availability or a good level of confidence in PVT information for usage in urban environments, effective and timely solutions are very much sought after. For all these reasons, we choose to work on monitoring the reliability of GNSS aided positioning for land vehicle applications in urban environments.

1.2 GNSS Systems Overview

A GNSS system is usually separated into 3 main segments namely, the Space Segment, the Ground Control Segment and the User Segment. The Space Segment consists of satellite constellation where the satellites orbit around the earth while transmitting radio signals to users. The Ground Control Segment has a network of monitoring stations on earth. In general, this segment controls, monitors and maintains the operations of the satellites such as generating the NAV message. Finally, the User Segment is simply the GNSS receivers, which function is to receive and process the GNSS signals to obtain the PVT solution.

As of today, there are several GNSS systems in existence and under development. Among the established systems are the United States' NAVSTAR-GPS (commonly referred to as GPS - Global Positioning System) and the Russian's GLONASS. Europe has already put in space four satellites and two are planned to be launched this month to form its own GNSS constellation known as Galileo and the Chinese BeiDou is already global now. Apart from these, there are also regional systems which are the Japanese Quasi-Zenith Satellite System (QZSS), and the Indian Regional Navigational Satellite System (IRNSS). Some brief descriptions of these GNSS systems are as follows:

a. Global Positioning System (GPS) GPS is the oldest and the most widely used GNSS system today. It was developed in 1973 by the United States Department of Defence (U. S. DoD) and became fully operational in 1995. As for the current number, the constellation consists of 30 Medium Earth Orbit (MEO) satellites operating on six orbital planes with 55 degrees inclination at an altitude of 20,200 km. This configuration allows a good coverage of the globe except for the polar regions.

Originally, GPS satellites transmit two BPSK signals with carrier frequency L1 (1575.42 MHz) and L2 (1227.60 MHz). Two pseudo-random (PRN) codes are applied to the L1 signal via modulation by phase quadrature: the C/A code (Coarse Acquisition) and the P-code (Precise) which can be encrypted and called P(Y) code which is reserved for military applications. The L2 signal is modulated by the P code only. The two signals are also modulated by the navigation message which has a bit rate of 50 bits/sec and carries the satellite ephemeris data.

However, technological advancements that coupled with new demands on the existing GPS have led to the system modernization effort since the year 2000. Two new civil signals are being transmitted by GPS satellites in each the L2 and L5 bands. The third new signal shall be implemented in the next generation of GPS satellites. Further information on GPS may be obtained, for instance, in [3, 31–33]

b. GLObal NAvigation Satellite System (GLONASS) The Russian GNSS system, GLONASS was developed by the ex-Soviet Union around the same time as the GPS development. GLONASS constellation of 24 satellites reached its initial full operation capability in 1995. Soon after, due to the lack of funding by the Russian government, the system fell into a state of decay where at its lowest, only six satellites were operational in 2001.

However, later on the government made the restoration of the system as one of its top priority with substantial increase of funding. By October 2011, the operation of 24 satellites was finally restored. The GLONASS satellites are placed in three orbital planes at an altitude of about 19.100 km (MEO) in such a way that they cover the whole Russia. As a result, GLONASS constellation also covers the polar regions which are not the case for GPS.

In its original design, GLONASS uses Frequency Division Multiple Access (FDMA) approach to distinguish its various satellites unlike GPS which use Code Division Multiple Access (CDMA) technique. However, during the restoration effort, the GLONASS satellites have been upgraded where the new satellites will transmit in the L3/L5 band apart from the original broadcast in the L1 (standard and high accuracy signals) and L2 (high accuracy signal) bands by the legacy satellites . In the planning, both Frequency Division Multiple Access (FDMA) and Code Division Multiple Access (CDMA) will be used

for the signals to be transmitted in those bands. Additional information on GLONASS may be obtained in [31, 34, 35].

c. Galileo Realizing the impact of GNSS applications in the present and future European economy, the European Union (EU) has embarked to develop Galileo with the objective to have an alternative GNSS independently from the US GPS and Russian GLONASS systems. The system is designed to have a constellation of 30 satellites (27 operational and 3 active spares), which occupy three orbital planes at 56^o inclination at altitude of 23,222 km (MEO).

Fully administered and controlled by civilian body, Galileo will provide four main services.The Galileo Open Service (OS) is provided without charge and accessible by everyone. It can be used either in single or dual frequency mode at L1/E1 and E5 (1191.795 MHz) bands.

The Public Regulate Service (PRS) is specially allocated to government-authorized users and is guaranteed of continuous availability even if other services are disabled in time of crisis. The bands allotted for this service are the E1 and E6 (1278.75 MHz).

With a charged fee, the Commercial Service (CS) offers higher performance than the OS and provides added services such as guaranty of service, integrity and continuity of signal. CS broadcast on the same bands as OS but complemented by two signals at the E6 band (1278.75 MHz)

Galileo's Support to Search and Rescue Service (SAR) represents Europes's contribution to the international cooperative effort on search and rescue activities under COSPAS-SARSAT organisation. Apart from improvement in terms of the satellite visibility to detect distress signal, SAR/Galileo also introduces a return link from the SAR operator to the distress emitting beacon.

d. BeiDou Navigation Satellite System (BDS) Started as a demonstration system when two navigation experiment satellites were launched in 2000, BDS is now already in the third step of its development which is designed and aimed to provide global coverage around the year 2020. The system will have two types of service modes; an open service and an authorized service. In order to achieve this capability, China planned to have a constellation of 5 GEO satellites, 27 MEO satellites and 3 IGSO satellites.

Apart from the mixed composition of satellite orbits, BDS is also different from the other global GNSS systems in that it uses its GEO satellites to transmit augmentation signals for error correction.The B1I and B2I are the two civil signals described in the documents published by the China Satellite Navigation Office which respectively use the E2 and the E5B frequency bands.

Since December 2012, BDS has been declared fully operational over China and the surrounding areas with 14 operational satellites in orbit, including 5 GEO satellites, 5 IGSO satellites, and 4 MEO satellites [36–38].

e. Indian Regional Navigational Satellite System (IRNSS) The IRNSS is an independent regional navigation satellite system that is being developed by Indian Space Research Operation (ISRO). The complete system will have seven satellites in the constellation (three satellites in geostationary orbit (GEO), and four satellites in inclined geosynchronous orbit (IGSO)). For the time being, two geosynchronous and one geostationary satellite had been launched making three of the IRNSS satellites are already in the orbit. Full constellation is expected to be accomplished by 2015.

The IRNSS will provide two types of service which are the Standard Positioning Service for common civilian users and the encrypted Restricted Service for special authorized users. Two signals in the L5 and S bands will be used in this system[39, 40].

f. Quasi-Zenith Satellite System (QZSS) The QZSS is being developed by Japan with the target of having four satellites in orbit (three satellites with an IGSO and one with GEO) by the year 2018. Further on, it is intended for the system to have a total of seven satellites in its constellation.

The main concept for QZSS is to have a compatible system with the GPS so that it complements the availability of GPS satellites, hence increase the total number of available satellites over Japan and the Asia-Pacific region. With this intention, the QZSS is designed to provide signals similar to GPSs L1 C/A, L1C, L2C, and L5. In addition, QZSS will also transmit augmentation signals for error corrections which are the Sub-meter Level Augmentation (SLAS) in the L1S band and the Centimeter Level Augmentation Signal (CLAS) in the L6 band [41, 42].

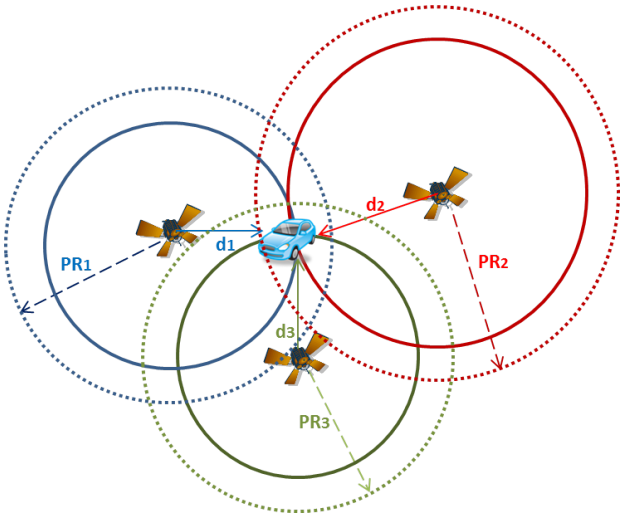

FIGURE 1.1: GNSS positioning and trilateration concept

1.3 GNSS General Working Principle

1.3.1 Pseudorange measurement and positioning

Positioning by GNSS can be explained by a trilateration process, which is a method of determining point locations based on measurement of distances in a defined geometric space. By having distance measurements from three or more known points of location in the same space, such as the known locations of GNSS satellites, circles can be formed around those points (satellite positions) and where they overlap identifies the user position (Figure: 1.1). However, GNSS receiver does not actually measure the distance but rather a pseudo-distance or a pseudorange (PR) thus, not applying the strict concept of trilateration.

A GNSS receiver computes its pseudo-distance from a satellite based on the estimation of the propagation time of the satellite signal multiplied by the speed of light. The travel time of the signal can be estimated given the synchronization of the receiver with the pseudorandom code of the signal and when the starting time of transmission by the satellite is known [43].

$$d = c(t_{rcv} - t_{xmit}) \tag{1.1}$$

where d is the distance between receiver and satellite, t_{rcv} is the time at which a specific, identifiable part of the signal is received, t_{xmit} is the time at which that same part of the signal is transmitted, and c is the speed of light.

However, in practice, GNSS receivers are not synchronized to GNSS time. Therefore, the effect of this receiver clock error can be included in the range estimation. This estimate is called *pseudorange* (PR) *measurement*. It is based on the transition duration of the signal and the time difference between the clock of the receiver and that of the satellite.

The actual PR measurements are also affected by various propagation and system specific errors. Accounting for the noises and errors in the measurement, PR can be represented by the equation[3],

$$\rho_i = d_i + c.dt_r - c.dt_s + I_i + T_i + \epsilon_i \tag{1.2}$$

where

- d_i is the straight line distance between the receiver and the satellite
- $c.dt_i$ is the satellite clock offset
- $c.dt_r$ is the receiver clock offset
- I_i is ionospheric delay
- T_i is tropospheric delay
- ϵ_i represents the receiver noise, multipath and NLOS

The size and statistical characteristic of these errors contribute to the quality of the PVT solution. When the errors are smaller and more uncorrelated, the quality of the solution tends to be better. Hence, PR measurements are commonly preprocessed to reduce the effect of the errors. Among these error terms, the clock receiver bias, dt_r, is dependent on the receiver and has the same effect to all the PR measurements. As for the rest of the errors, they can be different for each satellite at any given time. Although can never be completely eliminated, the error terms can be minimized to some extent using various techniques.

The clock receiver bias, dt_r, is determined as one of the unknowns in the navigation equation. The satellite clock bias, dt_s, can be compensated for based on the information transmitted in the satellite signal. As the atomic satellite clocks are very stable, a second order polynomial model is used to predict the satellite clock bias. The Tropospheric, T, and Ionospheric, I , errors can be estimated using the transmitted data along with

certain atmospheric models. Assuming that the satellite clock, ionosphere, and troposphere corrections are applied to the PR, ϵ will include residuals from these corrections and all other errors, e.g. multipath, NLOS and the receiver thermal noise. A more comprehensive overview of the PR measurement errors can be obtained in [3, 31, 32]. In the urban settings however, the error in ϵ_i is dominated by multipath and NLOS which is known to be local environment dependent, non-Gaussian, non-stationary and can be time correlated. Therefore, the multipath and NLOS biases are very difficult to be estimated and indeed become one of the focused subjects in this thesis. Their further elaborations will be provided in the following sections.

Once the PRs are measured, ones have a set of nonlinear equations with four unknowns, called the navigation equation. In a Cartesian coordinate system,

$$\begin{aligned} \rho_1 &= \sqrt{(x_1 - x)^2 + (y_1 - y)^2 + (z_1 - z)^2} + c.dt_r \\ \rho_2 &= \sqrt{(x_2 - x)^2 + (y_2 - y)^2 + (z_2 - z)^2} + c.dt_r \\ &\vdots \\ \rho_i &= \sqrt{(x_i - x)^2 + (y_i - y)^2 + (z_i - z)^2} + c.dt_r \end{aligned} \tag{1.3}$$

for simplification,

$$\rho_i = d_i + c.dt_r \tag{1.4}$$

where

$$d_i = \sqrt{(x_i - x)^2 + (y_i - y)^2 + (z_i - z)^2} \tag{1.5}$$

where x, y, z represent the position of the receiver; x_i,y_i,z_i, represent the position of the i^{th} satellite at the time of the transmission of the signal, c is the speed of light and dt_r is the clock offset of receiver. From the equations above, it is deduced that at least four pseudorange measurements are needed to estimate the 4 unknowns (x, y, z and dt_r). The satellite positions are computed by using the demodulated Kepler parameters obtained from satellite navigation message. The position is calculated and then transformed to a system of coordinates in longitude, latitude and ellipsoidal height. The most commonly used coordinate system is WGS84 (World Geodetic System 1984)[4].

Using the PR measurements, several different algorithms can be used to calculate various solutions for example; position, clock bias, velocity, time and acceleration. The most commonly utilized navigation algorithms are the Weighted Least-Square and the Kalman

filter. Apart from the PR measurements, navigation solution can also exploit other GNSS measurements such as the *Doppler* (DP) *measurement* or *Carrier-Phase* (CP) *measurement* to smooth the solution in measurements or position domain. Existing smoothing methods use CP and DP to take advantage of the high precision characteristic of CP and DP, in order to improve the accuracy of the PVT.

1.3.2 Doppler Measurement and its relation to range rate and carrier phase

Due to the movement of satellites relative to the receiver, the received signal frequency is offset from the carrier frequency, a condition known as the Doppler effects. GNSS receivers can provide this offset observable, called Doppler measurement, which unit is the Hertz (Hz)[31].

$$\triangle f_D = f_{Ri} - f_{Ti} = -f_{Ti}\frac{(v - \dot{u})a}{c} \tag{1.6}$$

where

- $\triangle f_D$ is the Doppler offset
- f_{Ri} is the unbiased received frequency from *i-th* satellite
- f_{Ti} is the theoretical transmitted satellite frequency from *i-th* satellite
- v is the velocity of the *i-th* satellite
- $\dot{u}$ is the velocity of the user
- a is the unit vector pointing along the line of sight from the user to the *i-th* satellite
- c is the speed of light

Doppler measurements are usually estimated in two different ways. One option is the use of raw Doppler measurements from the direct output of the Phase Lock Loop (PLL) filter. Another method uses time-differenced GNSS carrier phase measurements [44].

Unlike carrier-phase, Doppler measurement does not suffer from cycle slips and it is more precise than the PR measurements. Therefore, Doppler measurements can be benefitted when used for PR smoothing and velocity estimation. One way to smooth the navigation

solution is by using both PRs and Doppler measurements as the inputs to a filter that estimate position and velocity solutions.

For velocity estimation using Doppler measurement, first we can relate Doppler measurement to a range rate, which is the time derivative of the PR.

$$\mathbf{v}.\mathbf{e}_{los} = \mathbf{v}_{los} \rightarrow \dot{\rho} = -\lambda D = \frac{-cD}{f} \tag{1.7}$$

where λ is the wavelength of satellite signal carrier, c is the speed of light, D is the Doppler frequency and f is satellite signal carrier frequency.

Since Pseudorange rate is the time derivative of the PR, the same approach for position determination using equation 1.4 may be used to calculate velocity using the PR rate.

$$\dot{\rho} = \dot{d}_i + c.ddt_r \tag{1.8}$$

With at least 4 measurements, one can then estimate the velocity of the receiver in three dimensions. For measurements on the L1 frequency, the set of equations are:

$$\begin{aligned}
-D_1.\frac{c}{L_1} &= (v_{x1} - v_x)\gamma_{x1} + (v_{y1} - v_y)\gamma_{y1} - (v_{z1} - v_z)\gamma_{z1} + c.ddt_r \\
-D_2.\frac{c}{L_1} &= (v_{x2} - v_x)\gamma_{x2} + (v_{y2} - v_y)\gamma_{y2} - (v_{z2} - v_z)\gamma_{z2} + c.ddt_r \\
&\vdots \\
-D_i.\frac{c}{L_1} &= (v_{xi} - v_x)\gamma_{xi} + (v_{yi} - v_y)\gamma_{yi} - (v_{zi} - v_z)\gamma_{zi} + c.ddt_r
\end{aligned} \tag{1.9}$$

where v_x, v_y, v_z represent the velocity of the receiver,v_{xi}, v_{yi}, v_{zi} are the velocity of the ith satellite, ddt_r is the clock drift of the receiver clock, and coefficients γ are the receiver-to-satellite line-of-sight unit vectors which equal to:

$$\begin{aligned}
\gamma_{xi} &= \frac{x_i - x}{\|x_i - x\|} \\
\gamma_{yi} &= \frac{y_i - y}{\|y_i - y\|} \\
\gamma_{zi} &= \frac{z_i - z}{\|z_i - z\|}
\end{aligned}$$

1.3.3 Dilution of Precision (DOP) - Impact of Satellite-User Geometry on positioning

Apart from measurement accuracy, the satellite-user geometry also has a significant effect on the accuracy of the PVT estimates obtained from GNSS [45]. The metric that is commonly used for comparing this effect is known as dilution of precision (DOP). The geometry can be said to dilute the range domain accuracy by the DOP factor.

DOP expresses how ranging accuracy is scaled by a geometry effect to yield position accuracy. The more favorable is the geometry, the lower the DOP value. For example, the optimal geometry (i.e. the lowest DOP value) for four satellites is achieved when three satellites are equally spaced on the horizon, at minimum elevation angle, and one satellite is directly overhead [1].

The DOP is identified when expressing the variance of the position error. From the PR equation:

$$\rho_i = d_i + c.dt_r \tag{1.10}$$

To linearize Equation 1.10, the method of Taylor series expansion is applied and truncated after the first-order partial derivatives in order to eliminate nonlinear terms (detail description can be found in [31, 43] . The resulting linearized equation is,

$$\triangle\rho_i = a_{xi}\triangle x_r + a_{yi}\triangle y_r + a_{zi}\triangle z_r - c\triangle t_r \tag{1.11}$$

or in matrix form,

$$\mathbf{\Delta\rho} = \mathbf{H\Delta x} \tag{1.12}$$

where **H** is known as geometry matrix. Then, the DOP matrix, **G** is computed from **H** as follows:

$$\mathbf{G} = (\mathbf{H}^T\mathbf{H})^{-1} = \begin{bmatrix} G_{11} & - & - & - \\ - & G_{22} & - & - \\ - & - & G_{33} & - \\ - & - & - & G_{44} \end{bmatrix} \tag{1.13}$$

The most general DOP parameter is *Geometric Dilution of Precision* (GDOP) which is defined as:

$$GDOP = \sqrt{G_{11} + G_{22} + G_{33} + G_{44}} \tag{1.14}$$

Other types of DOPs are:

$$\begin{aligned} PDOP &= \sqrt{G_{11} + G_{22} + G_{33}} \\ HDOP &= \sqrt{G_{11} + G_{22}} \\ VDOP &= \sqrt{G_{33}} \\ TDOP &= \sqrt{G_{44}} \end{aligned}$$

1.4 Navigation solution reliability performance in civil aviation

In civil aviation, the reliability of the navigation solutions are quantified by the following parameters [1, 46]:

- **Accuracy**: The accuracy of a navigation system is a measurement of the degree of conformance between estimated and true positions, i.e. the position error. Accuracy requirements are given as the maximum allowable 95% percentile of the position error. If the position error is modelled with a zero-mean normal distribution, the accuracy is approximately twice the maximum allowable standard deviation.

- **Availability**: The availability of a navigation system is the ability of the system to provide usable service within the specified coverage area, i.e. the ability to provide the required function and performance at the initiation of the intended operation. Signal availability is the percentage of time that navigational signals transmitted from external sources are available for use. Availability is a function of both the physical characteristics of the environment and the technical capabilities of the transmitter facilities.

- **Continuity**: The continuity of a system is the ability of the total system (comprising all elements necessary to maintain aircraft position within the defined airspace) to perform its function without interruption during the intended operation. More specifically, continuity is the probability that the specified system performance will be maintained for the duration of a phase of operation, presuming that the system

was available at the beginning of that phase of operation and was predicted to operate (to exist) throughout the operation.

- **Integrity**: The integrity is a measure of the trust that can be placed in the correctness of the information supplied by the total system. Integrity includes the ability of a system to provide timely and valid warnings to the user (alerts). The following terms are related to integrity requirements:

  - **Integrity Risk** : The integrity risk is the probability of providing a position that is out of tolerance without warning the user within the time-to-alert.

  - **Protection Level (PL)**: There are Horizontal Protection Level (HPL) and Vertical Protection Level (VPL). The HPL, is the radius of a circle in the horizontal plane ... with its centre being at the true position, ... for which the missed alert and false alert requirements are met for the chosen set of satellites when autonomous fault detection is used. It is a function of the satellite and user geometry and the expected error characteristics: it is not affected by actual measurement. Therefore, this value is predictable.

    The VPL, is half the length of a segment in the vertical axis ... with its centre being at the true position, ... for which the missed alert and false alert requirements are met for the chosen set of satellites when autonomous fault detection is used. It is a function of the satellite and user geometry and the expected error characteristics: it is not affected by actual measurement. Therefore, this value is predictable.

  - **Alert Limit (AL)**: There are Horizontal Alert Limit (HAL) and Vertical Alert Limit (VAL). The HAL is the radius of a circle in the horizontal plane (the local plane tangent to the WGS-84 ellipsoid), with its center being at the true position, that describes the region that is required to contain the indicated horizontal position with the required probability for a particular navigation mode ....

    The VAL is half the length of a segment on the vertical axis (perpendicular to the horizontal plane of WGS-84 ellipsoid), with its center being at the true position, that describes the region that is required to contain the indicated vertical position with a probability of per approach, for a particular navigation mode ....

– **Time to Alert (TTA)**: The TTA is the maximum allowable elapsed time from the onset of a positioning failure until the equipment annunciates the alert.

1.5 GNSS Augmentation System

Originally, in order to use the GPS in civil aviation operations, different augmentation systems have been implemented to enhance the GPS performance so that to meet the stringent ICAO standards. These augmentation systems can be categorized as [45, 47]:

- **Ground Based Augmentation System (GBAS)**. As officially defined in [1], GBAS consists of ground and aircraft elements. A GBAS ground subsystem typically includes a single active VHF data broadcast (VDB) transmitter and broadcast antenna, referred to as a broadcast station, and multiple reference receivers. A GBAS ground subsystem may include multiple VDB transmitters and antennas that share a single common GBAS identification (GBAS ID)and frequency as well as broadcast identical data. The GBAS ground subsystem can support all the aircraft subsystems within its coverage providing the aircraft with approach data, corrections and integrity information for GNSS satellites in view. All international aircraft supporting APV should maintain approach data within a database on board the aircraft. The Type 4 message must be broadcast when the ground subsystem supports Category I precision approaches. The Type 4 message must also be broadcast when the ground subsystem supports APV approaches if the approach data is not required by the State to be maintained in the on-board database. GBAS ground subsystems provide two services: the approach service and the GBAS positioning service. The approach service provides deviation guidance for FASs in Category I precision approach, APV, and NPA within the operational coverage area. The GBAS positioning service provides horizontal position information to support RNAV operations within the service area. The two services are also distinguished by different performance requirements associated with the particular operations supported including different integrity requirements. A primary distinguishing feature for GBAS ground subsystem configurations is whether additional ephemeris error position bound parameters are broadcast. This feature is required

for the positioning service, but is optional for approach services. If the additional ephemeris error position bound parameters are not broadcast, the ground subsystem is responsible for assuring the integrity of ranging source ephemeris data without reliance on the aircraft calculating and applying the ephemeris bound.

- **Satellite Based Augmentation System (SBAS)**. Also officially defined in [1], an SBAS is made up of three distinct elements: the ground infrastructure, the SBAS satellites, and the SBAS airborne receiver. The ground infrastructure includes the monitoring and processing stations that receive the data from the navigation satellites and compute integrity, corrections and ranging data which form the SBAS signal-in-space. The SBAS satellites relay the data relayed from the ground infrastructure to the SBAS airborne receivers that determine position and time information using core satellite constellation(s) and SBAS satellites. The SBAS airborne receivers acquire the ranging and correction data and apply these data to determine the integrity and improve the accuracy of the derived position. The SBAS ground network measures the pseudo-range between the ranging source and an SBAS receiver at the known locations and provides separate corrections for ranging source ephemeris errors, clock errors and ionospheric errors. The user applies a tropospheric delay model. The ranging source ephemeris error and slow moving clock error are the primary bases for the long-term correction. The ranging source clock error is adjusted for the long-term correction and tropospheric error and is the primary basis for the fast correction. The ionospheric errors among many ranging sources are combined into vertical ionospheric errors at predetermined ionospheric grid points. These errors are the primary bases for ionospheric corrections.

- **Aircraft Based Augmentation System (ABAS)**. ABAS augment and/or integrate GNSS information with information available on-board the aircraft to enhance the performance of the core satellite constellations. The most common ABAS technique is called receiver autonomous integrity monitoring (RAIM). RAIM requires redundant satellite range measurements to detect faulty signals and alert the pilot. The requirement for redundant signals means that navigation guidance with integrity provided by RAIM may not be available 100 per cent of the time. RAIM availability depends on the type of operation; it is lower for non-precision approach than for terminal, and lower for terminal than for en-route. It is

for this reason that GPS/RAIM approvals usually have operational restrictions[47]. Another ABAS technique, aircraft autonomous integrity monitoring (AAIM), uses information from additional on-board sensors (e.g. barometric altimeter, clock and inertial navigation system (INS))[1].

The following terms are relevant to the RAIM and FDE process as defined in [46]:

- A **positioning failure** occurs whenever the difference between the true position and the estimated position exceeds the applicable alert limit. If the equipment is not aware of the alert limit, a positioning failure is defined to occur whenever the difference between the true position and the estimated position exceeds the applicable protection level (HPL, VPL).
- A **false detection** is defined as the detection of a positioning failure when a positioning failure has not occurred.
- A **missed detection** occurs whenever a positioning failure is not detected.
- A **failed exclusion** occurs whenever a true position failure is detected and the detection condition is not eliminated within the time-to-alert (from the onset of the positioning failure). A failed exclusion would cause a navigation alert.
- A **wrong exclusion** is defined to occur when a detection occurs, and a positioning failure exists but is undetected after exclusion.
- A **missed alert** is a positioning failure that is not annunciated as an alert within the time-to-alert are defined to. Both missed detection and wrong exclusion can cause missed alerts after the time-to-alert expires.
- A **false alert** is defined as the indication of a positioning failure when a positioning failure has not occurred (a result of false detection). A false alert would cause a navigation alert.

1.6 Integrity of GNSS Positioning

Positioning confidence is essentially identified with the ability to trust the estimated position. With respect to the confidence of GNSS-based positioning, there are generally

two fields of profession that had invested tremendous efforts in this issue. They are the geodesy/surveying community and air transport navigation community.

The concept of outlier detection in parameter estimation of positioning variables was introduced in the surveying community where reliability is defined as a statistical measure of the confidence that in performing a positioning survey no blunders were made and no undetected outliers are present [48, 49]. There are two types of reliability as applied to the geodetic field; *internal* and *external reliability*. Internal reliability refers to the ability to detect outliers and quantified by the minimum detectable bias (MDB), i.e. the smallest measurement error that can be detected using the appropriate test statistics. As described in [50], the test statistic T has a Chi-squared distribution, which is central under H_0 and non-central under H_a. The non-centrality parameter λ_0 is a measure of the distance between H_0 and H_a. This non-centrality parameter can be computed once reference values are chosen for the level of significance (the probability of rejecting H_0 when it is true) and the detection power (the probability of rejecting H_0 when H_a is true). Once the parameter is known, the corresponding size of the bias that can just be detected (i.e. the MDB) can be calculated. On the other hand, the external reliability describes the impact of the MDB on the position estimate. In order to avoid surveying error, outlier is detected based on the procedure known as Detection, Identification and Adaptation (DIA) [49, 51].

For some applications, such as horizontal navigation, and against some specific threats, e.g. Major Service Failure, the air transport community employed comparatively the same techniques for detecting faulty GPS measurements, which rely on having redundant measurements in order to employ a consistency check [52, 53]. However, the adopted terminologies are different. In the aviation sector, the quality or the reliability of position estimates can be demonstrated by their accuracy, integrity, continuity and availability. While initially developed for air transport navigation, these metrics have been considered as a methodology of inspiration and are being investigated for land vehicle navigation such as the work in [54]. The aviation industry's approaches to integrity measurement mainly rely on Fault Detection and Exclusion (FDE) algorithms to reject outliers from measured data and the computation of Protection Level (PL) associated to an integrity risk [55]. Also known as Receiver Autonomous Integrity Monitoring (RAIM), the techniques are accomplished either in the position domain or in the range domain.

Existing RAIM techniques are suited to aerospace applications where high redundancy of data exists, mature standards provides the needed performance to be achieved for each phase of navigation and only a single fault is expected. Many efforts were made to adapt these techniques for land vehicle applications [56], and to deal with multiple faults [57–60]. However, the problem is still quite challenging especially since the requirements are not clear yet for each land application or service, and the metrics of performance is not defined and highly variable. However, it is worth noting that several working groups around the world are making serious efforts to propose standard for other than civil aviation applications. Such an example is the initiative in the frame of the European Telecommunications Standards Institute (ETSI) led by the group Satellite Communication and Navigation (SCN) of the Technical Committee Satellite Earth Station and Systems (TC SES) [27].

Algorithms for positioning integrity and reliability monitoring are usually based on statistical inference and hypothesis testing. Since actual position error cannot be known or measured in real time, RAIM calculates a measurable scalar parameter that provides information about pseudorange measurement errors (which can be linked to the position error). This measurable parameter is called test statistic. It is a random variable with known distribution. For example, in Least Square RAIM, the test statistic is calculated from PR residuals, which are the difference between the measured PR and the PR derived from the estimated navigation solution.

In RAIM, failure detection is achieved by comparing a test statistic, T, against a detection threshold, Th:

$$P(|\delta Position| \geqslant \varepsilon) = T \leqslant Th \Leftrightarrow \text{no failure detection}$$
$$T > Th \Leftrightarrow \text{failure detection}$$

For implementation in urban settings, T has to be formulated to detect errors in the measurements like outliers coming from NLOS and MP effects. The challenge is to be able to characterize T in this kind of non-Gaussian environments. The decision threshold, Th is also computed using the standard distribution of T.

RAIM is developed to detect a positioning failure with required missed detection probability P_{MD} and false alarm probability P_{FA} (non-faulty positioning that are considered

Typical operation	Accuracy horizontal 95%	Accuracy vertical 95%	Integrity	Time-to-alert	Continuity	Availability
En-route	3.7 km (2.0 NM)	N/A	$1-1\times10^{-7}$/h	5 min	$1-1\times10^{-4}$/h to $1-1\times10^{-8}$/h	0.99 to 0.99999
En-route, Terminal	0.74 km (0.4 NM)	N/A	$1-1\times10^{-7}$/h	15 s	$1-1\times10^{-4}$/h to $1-1\times10^{-8}$/h	0.99 to 0.99999
Initial approach, Intermediate approach, Non-precision approach (NPA), Departure	220 m (720 ft)	N/A	$1-1\times10^{-7}$/h	10 s	$1-1\times10^{-4}$/h to $1-1\times10^{-8}$/h	0.99 to 0.99999
Approach operations with vertical guidance (APV-I)	16.0 m (52 ft)	20 m (66 ft)	$1-2\times10^{-7}$ in any approach	10 s	$1-8\times10^{-6}$ per 15 s	0.99 to 0.99999
Approach operations with vertical guidance (APV-II)	16.0 m (52 ft)	8.0 m (26 ft)	$1-2\times10^{-7}$ in any approach	6 s	$1-8\times10^{-6}$ per 15 s	0.99 to 0.99999
Category I precision approach	16.0 m (52 ft)	6.0 m to 4.0 m (20 ft to 13 ft)	$1-2\times10^{-7}$ in any approach	6 s	$1-8\times10^{-6}$ per 15 s	0.99 to 0.99999

TABLE 1.1: GNSS SIS Performance Requirements from ICAO-ISRP, 2006 [1]

as faulty)[61]. The detection threshold value is stipulated for achieving the specified P_{FA} as a constant false detection rate in fault free conditions. In civil aviation, a constant false alarm rate is chosen to meet the specific performance requirements depending the phase of flight (see Table 1.1). However, in modern applications the position is not always the final used information; sometimes travelled distance or passing a checkpoint, etc. Thus, the integrity problem could be formulated differently.

1.7 Thesis objectives

This thesis addresses the challenges in reliability monitoring of GNSS aided navigation for land vehicle applications in harsh environments. Considering that GNSS integrity requirements and monitoring techniques have been originally defined and well established in the civil aviation framework, their research and developments provide the bedrock for in-depth understanding and serve as a launch pad for aspiration, adaptation and further development to satisfy the particular needs of the land applications. Due to the unique circumstances posed by the urban settings, the developed approaches for open sky environments are not effective in ensuring reliability in restricted environments. The main challenge in these harsh urban environments is the difficulty to have a reliable model of the received measurements, from which most of performance and integrity metrics are usually formulated as in the case of civil aviation applications.

The main objective of this research is to develop methods of trusted positioning using GNSS measurements and confidence measures for the user in constrained urban environments. In pursuance of the objective, the following goals are set in this research:

- Testing on the performance of a 3D model of an urban setting to predict NLOS signals and the resulting biases in order to reduce or negate the NLOS effect on positioning.
- Experimenting on GNSS observables augmented by trusted sensor (odometer and gyro) for predicting PR error in order to improve positioning accuracy hence reliability in urban environment.
- Characterizing the horizontal position error (HPE) in the position domain using generalized Pareto distribution to account for the heavy tail characteristic of the HPE in urban scenario. This approach permits us to consider the GNSS receiver as a black box mixing all errors together and modeling the global positioning error without caring about the modeling of error in range domain.
- Develop new statistical tests to check the integrity of the position estimate in urban environments.

It is worth mentioning here that until now, there is no standardized performance requirements yet for land applications, therefore the work in this thesis cannot be based on any specific integrity requirements. In addition, the main focus for the source of GNSS measurements in these works is on the PR rather than the carrier phase or Doppler measurements.

1.8 Thesis contributions

The contributions of this thesis are:

NLOS characterization using 3D model. In this part of the research, 3D model of the receiver's environment is used jointly with a GNSS simulator to identify NLOS signals and predict their biases. The NLOS signals can still be used rather than discarded in order to improve the positioning accuracy and integrity in environments with reduced

satellites visibility. SE-NAV environment simulator software from OKTAL-SE is used to generate the 3D model.

Reliability checking based on trusted velocity sensor. Here, the work proposes a reliability monitoring technique in the range domain for urban environment using a trusted velocity sensor. In this work, a single mechanical odometer is used and complemented by a gyroscope as reference sensor for integrity checking of the measured PRs through a hybridized navigation filter.

Characterization of Horizontal Position Error in Urban Environment. This part of the research directly characterizes the horizontal position error (HPE) in urban environments (rather than the PR error) using generalized Pareto distribution (GPD) to bypass the complexity of PR error modelling. Usually, the position error is assumed to be Gaussian distributed, which is not true in urban environments due to the correlated errors from NLOS and multipath.

Novel scheme for position integrity monitoring in urban environments. Based on the characterized horizontal position error (HPE), the inflated version of the fitted Pareto model is used to overbound the CDF of the HPE, i.e., for bounding the radial position errors. By matching the distribution of position residuals to this overbounding CDF, a novel test statistic is derived to monitor the integrity of the position estimation for each specific type of receiver.

1.9 Thesis Structure

This PhD thesis is organized into seven chapters as follows:

Chapter 1 presents the motivation and objective of the thesis, as well as the contributions and the structure of the thesis report.

Chapter 2 introduces the principles of GNSS navigation and its implementations for land navigation applications. The challenges faced for GNSS navigation in urban environments are also highlighted along with the state of the art approaches to meet these challenges.

Chapter 3 focuses on describing the current techniques for reliability and integrity monitoring in GNSS positioning. It draws attention to some of the advantages and

constraints of the existing approaches, which are largely developed based on the civil aviation experiences and requirements.

Chapter 4 describes the characterization of NLOS errors in urban settings by means of a 3D model of the urban surrounding. In an environment with limited number of visible satellites, excluding degraded signals could result in not having enough number of acceptable measurements for a position fix or adversely affect the satellites geometry. Using a GNSS simulator together with the 3D model, NLOS signals are identified and their biases are predicted. From this prediction, NLOS signals are corrected and used to improve the accuracy and integrity of the estimated positions. The results are analyzed and presented.

Chapter 5 elaborates the work on pseudorange (PR) prediction using hybridization with other sensors. Single odometer and gyro are used to obtain a reference position for reliability checking in the range domain. By using the hybrid approach, residuals are generated and test statistic are calculated, and tested against a threshold. Few forms of residuals were derived based on several observables, namely the PR, the range rate and the velocity. Their performances in reducing positioning errors are then analyzed and discussed.

Chapter 6 presents a novel experimental scheme in integrity monitoring for positioning in urban environment. Working directly in the position domain, position errors are characterized using generalized Pareto Distribution. Then, a test statistic is derived based on position residuals (rather than pseudorange residuals) and mapped or inflated to match the characterized overbounding position error CDF. By monitoring the test statistic against a specific threshold, the positioning integrity and continuity are met at a certain level of confidence. In addition, a composite approach for HPL computation is also investigated for autonomous implementation in urban environments.

Chapter 7 summarizes the main results and concludes this thesis by offering some perspectives on the directions for further continuation of the present work.

1.10 List of Publications

International Conference:

- Khairol Amali bin Ahmad, Mohamed Sahmoudi, Christophe Macabiau, Aude Bourdeau and Grégory Moura, Reliable GNSS *Positioning in Mixed LOS/NLOS Environments Using a 3D Model*, Proceedings of The European Navigation Conference, ENC 2013, 23-25 April 2013, Vienna, Austria.

- Bin Ahmad, K. A., Sahmoudi, M. and Macabiau, C., *Reliability of GNSS Measurements via Pseudorange Prediction Using an Odometer for Robust Land-Vehicle Navigation*, Proceedings of the 26th International Technical Meeting of the Satellite Division of the Institute of Navigation (ION GNSS+ 2013), Nashville, TN, 16-20 September 2013, pp. 1299-1307.

- Bin Ahmad, K. A., Sahmoudi, M. and Macabiau, C., *Characterization of GNSS Receiver Position Errors for User Integrity Monitoring in Urban Environments*,Proceedings of The European Navigation Conference, ENC-GNSS 2014, 15-17 April 2014, Rotterdam, The Netherlands.

- Bin Ahmad, K. A., Sahmoudi, M. and Macabiau, C., *Trusted Overbounding Position Errors for GNSS Positioning in Urban Environments*, Proceedings of the 27th International Technical Meeting of the Satellite Division of the Institute of Navigation (ION GNSS+ 2014), Tampa, Florida, 8-12 September 2014, pp. 3618-3628.

- Bin Ahmad, K. A., Sahmoudi, M. and Macabiau, C., *A Composite Approach for HPL Computation of GNSS Positioning Confidence in Urban Environments*, The European Navigation Conference, ENC 2015, 7-10 April 2015, Bordeaux, France.

Chapter 2

GNSS-based Navigation in Urban Environments: state-of-the-art

Positioning may be achieved in a *relative* or *absolute* sense. Dead-reckoning is based on sensors that provide an estimate of the incremental movement of an object between two points of time. If the initial position and heading of the object are known, it is possible to estimate the new position based on its movement. Such measures can have a good accuracy for short distances, but the accumulation of errors in the estimation of each movement causes significant drift over long distances. Whereas in absolute positioning, the position is estimated and referenced to a certain coordinate. Hence, the advantage of absolute positioning in navigation as opposed to dead-reckoning is that it does not suffer from drift or accumulation of error.

Currently, the GNSSs are the best systems for absolute positioning in a global navigation cue, like the surface of the earth. However, the structure of the GNSS system introduced some limitations to its smooth operation. First of all, there must be no obstacle to obstruct the receiver from receiving the transmitted signal from the satellites. In reality, this signal can be blocked for example, by buildings, hills or dense foliage. Hence, for the receiver to have the best of reception, it requires maximum visibility of the sky, i.e. to have as many direct line-of-sights visibility to the satellites as possible. In addition, the quality of the measured signals can become degraded such that the accuracy of the calculated position can be affected. For instance, the propagated signal can be contaminated by noise or other perturbations that exists external to the GNSS system

or even by the replicas of the reflected satellite signals from the surfaces surrounding the receiver. These problems of satellite signal obstruction and degradation are much more prominent in urban settings as oppose to open sky environments.

In this chapter, the problems of achieving reliable positioning in urban environments will be described in detail. For this purpose, the chapter starts with the elaboration of the positioning and navigation challenges in urban environments. Then, it highlights the use of GNSS and applications for land vehicle navigations which require positioning reliability and continues afterwards by the state of the arts approaches to meet those challenges.

2.1 Positioning challenges in urban environments

The presence of several error sources such as multipath, NLOS, signal masking, poor constellation geometry, and etc. are significantly more prominent in urban scenarios as compared to the open-sky environments. Because of these errors, the usual approaches and techniques used for navigation in open-sky environments are not effective or reliable for positioning in urban environments. In addition, due to their strong environmental dependency, urban navigation errors cannot be easily modeled as it is the case for errors in the open sky scenarios. Figure 2.1 shows the effect of urban environment on satellite signals reception.

2.1.1 Obstruction of satellite visibility

One of the main problems encountered in urban areas is the masking of the satellite signals. Buildings, foliage and other structures tend to obstruct the GNSS signals propagation from satellites to receiver hence effect the signal reception. For example, tall buildings block the visibility of the low or even medium elevation satellites while tunnels disrupt the GNSS navigation completely.

Due to these circumstances, the continuity of position estimation by the GNSS cannot be guaranteed if only less than 4 signals are received. In fact, multiple GNSS constellations are needed in order to achieve high positioning-solution availability for many urban locations [62]. Even if when the position fix is possible, the visible constellation geometry

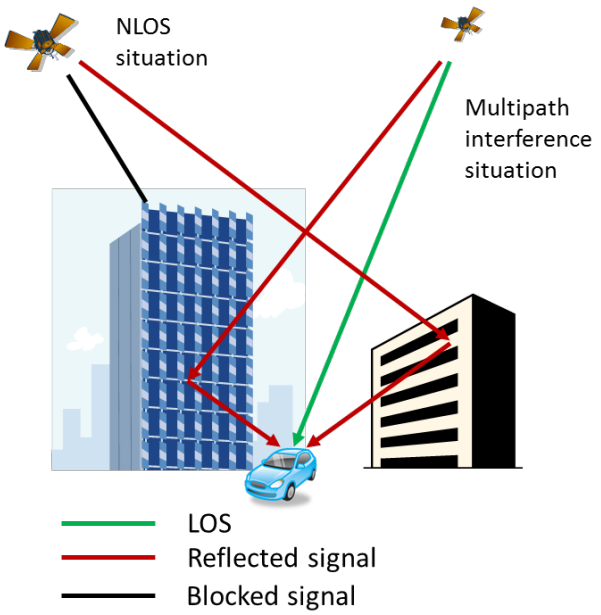

FIGURE 2.1: Effects on GNSS signals propagation in urban environment

may affect the DOP unfavorably that could reduce the positioning quality. Since many buildings are located along the streets, they block most of the signals from across the street but leave the along-street signals available to the receiver. Consequently, the DOP along the street is better than the DOP across the street when positioning is possible [62]. The satellite signal could also be only partially blocked which will attenuate the signals strength, hence reduce the signal-to-noise ratio (SNR) at the receiver which degrade the quality of the navigation performance.

2.1.2 Multipath

Another major issue for GNSS measurements in urban environments is the multipath phenomena. In urban environments, it is very common that the transmitted satellite signals are reflected or diffracted, causing the creation of the signal replicas which follow different paths than the original direct or line-of-sight (LOS) signal before arriving to the receiver. Therefore, the eventual received signal is the sum of different and attenuated delayed replicas. Although multipath signals are always delayed, because they take extra distances than the direct LOS satellite signals, the resulting measured range can be larger or smaller in comparison to the true range, depending on the phase of the reflected signal.

Theoretically, the magnitudes of multipath error can reach about 0.5 of a code chip depending on the receiver correlation technology [32]. However, it is very complex and difficult to analyze the multipath bias since it depends on the power, phase and delay of each reflected signals. Furthermore, notably for non-static applications, the changing magnitudes of the multipath errors make it difficult to anticipate and challenging to model mathematically [10].

2.1.3 NLOS signal

Non line-of-sight reception is the situation when the receiver receives the reflected replicas of the signal but not its LOS component at all. This condition can occur in urban canyons when the LOS signals are completely blocked or they are too weak vis-a-vis the strength of their multipath components. The receiver tracks the reflected signal only and therefore highly biased measurement can be obtained. In this case, the induced error will no longer be limited to half a chip code, since only the multipath signal is being tracked. NLOS signal is always positive and potentially unlimited in range. The use of high-sensitivity receivers can significantly increase the received number of NLOS signals since the receiver can acquire much weaker signal [63].

2.2 Reliability needs of GNSS navigation for land applications

With the growing usage and benefits of GNSS as the system for land navigation, many more applications are conceived and envisaged in the near future. Nevertheless, some of these promising applications require a certain level of acceptance and trust on their performance since the service could have some repercussion on the financial, legal or safety aspects. Therefore, positioning accuracy is no longer sufficient as a performance criterion. More and more, there is a pressing need for measurable confidence or reliability especially on the safety and liability critical applications.

Safety-critical and liability-critical GNSS applications are those applications in the category where large and undetected positioning errors may have negative safety, legal or economic implications. For this reason, the location must provide sufficient guarantees

	End User	System Operator	System Operator & End user
Safety of life	- Advance driver assistance	-Emergency services management	
Liability critical	-Pay per use insurance pricing -Taxi service pricing -Car rental pricing -Recovery after theft	-Speed limit enforcement -On street parking pricing -Accident reconstruction	-Road user charging (RUC) -Livestock tracking -Tracking of special vehicles
Non-Safety of life/ Non Liability critical	-Navigation services -Information for vulnerable road users -Fleet management -Passenger transport management	-Traffic management -Road lighting management -Infrastructure management -Road research	-Traffic information -Transport on demand

FIGURE 2.2: Broad classification of land vehicle application

of an acceptable level of risk for its utilization. The first required information is a quantification of the maximum error of position made by the system. The second piece of information needed is a quantification of the risk of exceeding the error bounds. An integrity mechanism must be put in place to ensure that the position meets these criteria and therefore to assure the system reliability and credibility [64–66].

Figure 2.2 shows the identified land applications based on a broad classification according to the signal integrity requirements by the European Union Road Federation (ERF)[23]. Here, it can be seen that quite a number of applications have been categorized as safety critical and liability critical.

The National Aeronautics and Space Administration(NASA) defines safety critical applications as those that possess the potential of directly or indirectly causing harm to humans, destruction of the system, damage to property external to the system, or damage to the environment[67]. On the other hand, the liability critical applications are those in which the computed PVT solutions are used as the basis for legal decisions or economic transactions. As such, an error in those magnitudes above certain threshold can provoke a wrong legal decision or the computation of a wrong charge. Note that economic liabilities are also associated to the legal aspects due to the repercussion of potential claims [64].

The liability critical applications have a major added value in the road sector. As an example, traffic law enforcement related to speed control have obvious legal implications and, therefore, if a GNSS unit is to be used as the basis for speed monitoring, it is essential that the probability of incorrectly fining some driver for speeding is extremely low and this have direct impact not only in the errors associated to velocity estimation but also in the position (for instance when a highway is running in parallel to a normal road which have very different speed limit). Pay as you drive insurance is another good example of liability critical application. However the most relevant example today in terms of potential number of users is GNSS based Electronic Toll Collection [64, 68].

Facing with the issues of generated pollution, traffic congestion and high number of accidents, the automotive industry is also keen to find solutions that would solve or at least reduce these constraints for further development in land transportation. These potential solutions include driving aids systems (Advanced Driving Assistance Systems, ADAS), and inter- vehicles communication systems with their infrastructure (Intelligent Transportation Systems, ITS). Other relevant applications are automatic toll, fleet management and collision avoidance. Efforts in the ADAS and ITS are notably driven by the European Union, in which three major projects with a total budget of one hundred million euros were launched in 2006: CVIS (Cooperative Vehicle Infrastructure Systems), SAFESPOT (Cooperative Systems for Road Safety) and COOPERS (Co-operative systems for intelligent Road Safety) [69]. Their implementations require vehicle localization function and whenever safety critical applications are considered, there is a need for a reliable localization [70]. Among other projects initiated by GSA in relation to GNSS usage for road applications are:

- **GNSS For Innovative Road Applications (GINA)** - the project proposes to address the existing obstacles that prevent a large-scale take-off of road pricing and other value-added services based on the use of EGNOS/Galileo [71].
- **Simple GNSS Assisted And Trusted Receiver (SIGNATURE)** - demonstrates that a robust positioning solution offering high availability and integrity, even in demanding urban environments, can be based upon low-cost GNSS components by using EGNOS Data Access Service (EDAS)[72].
- **Galileo/EGNOS Enhanced Driver Assistance (GENEVA)** - the general objective of the GENEVA project is to develop an innovative application within

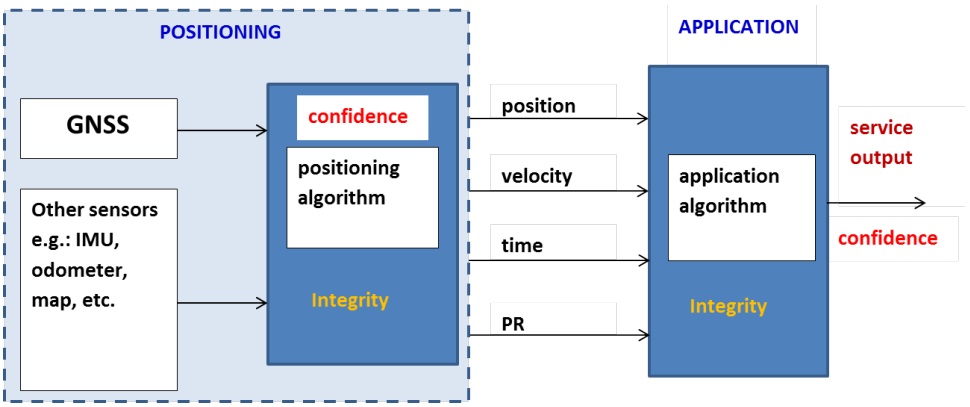

FIGURE 2.3: Generic structure for land application system

the context of advanced driver assistance for high precision, reliable and certifiable use. GENEVA focuses on high-precision road telematics applications. The project concentrates on applications with a social and public dimension, and with a high level of innovation i.e. highly Advanced Driver Assistance Systems (ADAS)[73].

- **Trusted Multi Application Receiver for Trucks (TACOT)** - will develop an innovative function which will deliver trusted GNSS-based position, velocity and time data to ITS applications [74].

2.2.1 Impact of positioning integrity on the reliability of land application

In the design of land based applications (such as RUC, ITS, ADAS) , most of the time, the GNSS receiver is used as the positioning sub-system which provides the PVT solution as required by the next module or next processing step in order to process the output for the application system as a whole. Figure 2.3 shows a generic structure of the concept. It is also possible that the GNSS is not the only technology utilized in the positioning module. When hybrid approach is adopted, the GNSS technology is complemented by other information or external sensors, such as inertial or odometric, with the intention to obtain the required PVT solution. Due to this configuration, the positioning module has a crucial role in achieving reliable required performance of the final output of the application. In other words, only the positioning with confidence and integrity can produce the application outputs with confidence and integrity.

2.3 Performance measures for land applications

The concept of positioning integrity is particularly mature and well developed in the aviation sector, where it has well defined specifications. In the field of land vehicles applications, this problem is still in its infancy. Several studies have been initiated since the late 90s, but no methodological principle dominates to this day [66]. Among the more recent efforts are the researches conducted in [64, 66, 75–82].

Unlike the aviation applications which has specific Required Navigation Performance (RNP)[1], until today, there is really no international standard of user performance requirements for the land vehicle applications. There are some localized or non-global efforts in pursuant of this matter. An example of the effort on specific type of land application is the production of GMAR Performance Assessment Framework (GPAF) by the GNSS Metering Association for Road user charging (GMAR) [83]. Since there is no standard performance requirement, it means that there are also no standard performance measures for the land-based GNSS applications.

Nevertheless, several projects on land based navigation have adopted the performance measures based on the experience from the civil aviation, where the quality of positioning are generally indicated in terms of accuracy, availability, continuity and integrity [1, 46]. These performance parameters are related to one another and some trade-off are involved among them. In urban environments, the quality of received signals varies rapidly especially for the case of moving receiver. Buildings and other objects could partially or totally hinder satellite signals propagation, resulting in poor geometric constellation of visible satellites hence degrading the position estimates accuracy. In worse conditions, position fixes could not even be calculated if available satellites are less than four which in this situation interrupt the continuity of the navigation. Therefore, due to poor and changing signal availability, quality, and geometry in urban environments, the application is often unable to cater continuous navigation accuracy and integrity throughout the operation. Solutions could be developed using redundant navigation sources of information (multi-GNSS, multi-sensors) jointly with smart mathematical modeling and filtering.

2.4 Previous works on improving GNSS positioning Quality in Urban Environments

Many researches had been conducted to develop methods and technics to overcome the challenges and improve the quality of positioning in urban environments. The works can be largely grouped into those focusing on mitigating the unwanted effects of urban environments on the GNSS signals and those that hybridize other sensors or information sources with the GNSS received signals.

2.4.1 GNSS Errors Mitigation

In order to improve or achieve required accuracy in GNSS navigation, the main practiced approaches are to characterize and mitigate the measurement errors. For open sky operation as in the civil aviation applications, the sources of errors in the GNSS measurements have been identified mainly as satellite clock error, ephemeris error, relativistic effects, atmospheric effects (ionospheric effect and tropospheric delay), receiver noise and hardware bias and multipath. These errors are usually assumed to be independent, zero mean and Gaussian distributed. Table 2.1 shows the typical standard deviation of the errors [2]. These errors are extracted from the the User Equivalent Range Error (UERE) budget in the GPS Standard Positioning Service (SPS) Performance Standard. The progress in GNSS augmentations and modernization result in the reduction of many of the sources of errors. A more comprehensive overview can be found for example in [31, 84]. However, in urban environments, the challenge to mitigate multipath and especially NLOS still prevail. For a receiver with narrow correlators, the multipath is typically less than 2 meter. For NLOS case, error of tens of meters may occur [81].

2.4.1.1 In receiver methods

a. In-receiver MP mitigation methods. One of the approaches for MP mitigation is by the in-receiver signal processing methods. For examples, the techniques include the narrow correlator [85], strobe correlator [86], the Multipath Estimating Delay Lock Loop

Segment	Error Source	UERE Contribution (95%) (meters)
Space	Clock stability	8.9
	Group delay stability	3.1
	Sat acceleration uncertainty	2.0
	Other space segment errors	1.0
Control	Clock/Ephemeris estimation	2.0
	Clock/Ephemeris prediction	6.7
	Clock/Ephemeris curve fit	0.8
	Ionospheric delay model terms	9.8-19.6
	Group delay time correction	4.5
	Other control segment errors	1.0
User (for illustration only, actual receiver performance varies significantly)	Tropospheric delay compensation	3.9
	Receiver noise and resolution	2.9
	Multipath	2.4
	Other user segment errors	1.0
95% System UERE (SPS)		17.0-24.1

TABLE 2.1: Std Dev of Errors in the Range Measurements [2]

(MEDLL) [87], Multipath Elimination Technology (MET) [88], the Multipath Mitigation Technology (MMT) [89], the Vision Correlator [90] and Fast Iterative Maximum-Likelihood Algorithm (FIMLA) [91]. A comprehensive review on these techniques may be obtained in [92].

The performance of the more advanced methods such as the Vision Correlator, are approaching the theoretical performance limits. However, their implementations are complex and expensive due to the use of multiple correlators and complex algorithms. Furthermore, these in-receiver techniques do not bring the best improvement in the case of NLOS situations due to the absent of LOS signal.

b. High sensitivity (HS) receiver. The idea with high sensitivity receiver is to be able to acquire and track as many satellite signal possible even when the received signal is very weak [93]. With higher redundancy, better position estimation can be obtained. Usually high sensitivity receivers make longer integration time [94], or use more correlators [93] in order to extract the correlation peak. On the other hand, HS

receiver will receive low powered signals that increase the chance to accumulate more degraded signals (MP and NLOS) as well.

c. Assisted GNSS (A-GNSS). A-GNSS uses separate communication channel, such as a mobile phone network, to provide information to a GNSS receiver that would otherwise be received by the receiver directly from the satellite themselves [93, 95, 96]. This approach allows the receiver to achieve position fix quicker in degraded satellite signals situations. Consequently, it helps to increase the receiver's sensitivity. However, this approach has several drawbacks to include the cost of the additional communication channel and the A-GNSS capable device and also the assistance source cannot be expected to be always available [97].

2.4.1.2 Hardware-based approaches

In mitigating the effects of multipaths by means of hardware/antenna, the concept is to eliminate the MP signals or attenuate them before the signals being processed in the signal processing stage. This is achieved in several ways:

a. Antenna design. One of the antenna-based multipath mitigation techniques is to improve the antenna gain pattern to overcome multipath [98]. Among the most common practices is to use a choke ring antenna and to select the antenna site with less reflections as possible [88]. The original choke ring design is intended to attenuate the reception the reflected signals from the Earth surface [99]. However, these solutions are not always practical, especially in mobile situations [100]. As such, choke ring design is typically implemented for high accuracy static applications.

Direct LOS satellite signals have right-handed circular polarization (RHCP) and the reflected signals mostly have left-handed circular polarization (LHCP). Therefore, the LHCP signals can be attenuated since almost all GNSS antennas are tuned for RHCP [101]. The work in [102] makes use of dual-polarization antenna to reject the LHCP as a technique to reject NLOS signals. However, the method was proven to detect most but not all of the NLOS. Polarization-based techniques are difficult in practice because without specific antenna like in reflectometry, it is difficult to predict the polarization of the received signal ray.

b. Multiple antenna. Using the concept of interferometric attitude determination, antenna array can be used to measure the angle of arrival (AOA) of GNSS signals [103]. With known orientation of the antenna, NLOS may be identified from direct-LOS signals by comparing azimuth of the received signal (measured) to the lines of sight to the satellite position using ephemeris data (predicted). However, if the orientation of the antenna is not known, the work proposes to compare the AOA measurements across satellites with the predictions. Both signals may be assumed to be LOS only if they match. Else, either signal or both could be NLOS.

c. Sky-pointing camera. An image of the field of view above the receivers masking angle can be captured by a panaromic lens camera or an array of cameras pointing towards the sky. By superimposing the satellite positions on the image, the blocked and unblocked line of sights can be known. Comparing these with the received signals, the NLOS can be identified when the signal is still received even when the satellite has a blocked line of sight [104, 105]. Apart from requiring additional physical equipment, this approach also needs additional processing for the image. Another limitation is the visibility requirement for the camera itself.

With the hardware/antenna based techniques discussed above, their main limitations are usually related to cost, size, weights and power consumption. In addition, the dual-polarization and antenna-array methods also require additional front ends and correlation channels in the GNSS user equipment [63].

2.4.1.3 MP and NLOS modelling

Classical positioning algorithms in GNSS assume that the observation noise is white-Gaussian distributed. This assumption is not correct when the signals include MP and NLOS. This wrong noise modelling leads to a decrease of positioning accuracy and continuity. Position estimates are mainly based on the PR measurements and the satellites geometry. Wrongly modelled noise or error can caused erroneous PR measurements which can lessen the accuracy of the position estimates. It follows that the less accurate position estimates are more prone to exceed the set threshold or the Alert Limit value. Hence, the continuity of the service would be interrupted whenever the positioning estimates are rejected. Therefore, in optimizing the use of all received

satellite signals, a few works propose a new PR error modeling in association with an adapted filtering process for estimating PVT solution.

Mixing the bias with the additive noise, the resulting term is considered as random error and may be modeled by a Gaussian mixture [9] since the NLOS measurements noise has been observed to be non-Gaussian, or by adapting the measurements variance [11]. In addition, authors in [10] shows that the measurement errors distributions depend on the observation window size. Over a short observation period, PR errors can be modeled by a Gaussian distribution, with time-varying mean and variance.

In order to adopt such measurements error-model based processing, a reliable decision on the reception state of the received signal (i.e. LOS or NLOS status) is needed. In [9], authors use the Jump Markov System as probabilistic model with received signal-to-noise-ratio (SNR) as indicator of the LOS/NLOS reception state. However, although it has the potential to be used independently of any heavy environment assumptions, SNR estimation is a critical issue in harsh environments, thus the decision based on contaminated information will affect the result. Furthermore, SNR values which are obtained from PRs collected in one area will not be representative any more for another area since the transition between LOS and NLOS depends greatly on the geometrical structure of the location.

Viandier [106] further proposed the use of Dirichlet Process Mixture (DPM) to track the observation noise density on-line. This density modelling is used together with the Rao-Blackwellised Particle Filter. While using DPM provide better result than the Gaussian mixture model, the computation using particle filter is more complex.

From the perspective of a non-static GNSS receiver, in dense urban setting, the quality of the received signal varies in time and can be generally categorized either as blocked, multipath-LOS or NLOS signals. In order to characterize the measurement errors, the reception states need to be identified for a particular epoch and then suitable error model need to be used depending on the reception states. The adoption of a measurement model is also related to processing technique. Some model can only be used with a certain type of solution estimation filter. For example, position estimation using Kalman filter is suitable for measurements with white Gaussian noise but will give non-optimal solution if the noise is non-Gaussian [10, 79, 82].

2.4.1.4 NLOS detection

a. RAIM/consistency checking. In post-receiver techniques (i.e., prior to the position calculation), one way to solve the NLOS situation problem is to identify and exclude the associated measurements in the navigation algorithm by using techniques such as consistency-checking. This is the concept used in RAIM, but RAIM consistency checking was designed to detect and exclude faulty satellite signals. However, this approach is not well adapted to positioning in harsh environments, when only degraded measurements may be available [56].

Consistency checking functions on the basis that NLOS measurements and multipath measurements produce a less consistent navigation solution than the direct-LOS measurements. Researchers in University College London (UCL) [56] has implemented a basic recursive-elimination consistency-checking algorithm to investigate its performance in urban environment. The applied method calculates a conventional single-epoch least squares position solution and then a chi-square test statistic based on the residuals [107]. The results show that position errors are reduced under moderate multipath conditions, but the performance is unreliable in dense urban environments with large numbers of reflected signals. However, performance was significantly improved by using consistency checking on the weighted least-squares position solutions, where the weighing is according to the signal C/No [56].

The UCL group has also explored the consistency checking performance in a bottom up or position-domain approach [108]. In this work, multiple position solutions are estimated using different combinations of measurements and then scored based on their consistency with the remaining measurements. This technique is inspired from RANdom SAmple Consensus (RANSAC) and the scoring scheme does not have to assume a Gaussian error distribution. While accuracy was generally improved by the scheme compared to the conventional technique, occasional degradation of performance can occur when there is an insufficient number of clean signals received or the algorithm simply converges to the wrong subset of signals [108].

b. Outlier detection from signal elevation angle. The higher is the elevation angle, the less likely the signal is to be blocked or reflected by a building. Considering this characteristic, the signal elevation can be used as an indicator of the quality of the

received signals. Conceptually, MP and NLOS signals may be mitigated by choosing the signals with high elevation.

However, the configuration of the surrounding buildings may cause drastic exceptions to this notion. For example, if there is a tall building nearby, high elevation signals may still be reflected or become NLOS signals. On the other hand, low elevation signals could be LOS signals since not all directions are hindered by buildings in urban areas. Another consequence of selecting only high elevation signals is the unfavorable effect on the satellite geometry. The results of the work in [109] suggest that elevation-based weighting on received signals has little impact on positioning performance.

c. C/No-based NLOS detection. Another possible indicator of NLOS reception is the signal-to-noise ratio (SNR) or C/No. In general, reflected signals are attenuated. Nevertheless, other phenomena also reduce the SNR. For example, due to propagation through foliage, masking or a null in the antenna gain pattern. On the contrary, smooth reflecting surfaces such as glass or wet surface could produce reflected signals that are almost as strong as direct signals. Furthermore, constructive multipath increases C/No. All these make it is very difficult to make decision of LOS or NLOS using only C/No. In addition, there are other uncertainties related to C/No such as how it is computed, which threshold or which PDF of the SNR to be used.

Therefore, due to those various effects, rejecting or down weighting low C/No measurements may lessen but will not totally nullify the impact of the NLOS and MP receptions. From the results in [109], weighting the measurement based on C/No give more accurate position estimate than weighting based on satellite elevation angle.

d. 3D Model. Some works also make use of 3D model to detect NLOS signals. In [110], the authors used 3D digital map in order to detect and mitigate multipath in real-time where a ray tracing algorithm is used to check if satellite signals are reflected or blocked. The suspicious PRs are simply excluded from the observation set. 3D model along with camera image were used in [111] to filter out the PR measurements which are considered to be NLOS based on the comparison of the actual satellite elevation angle with the critical elevation angle calculated using the 3D model.

Since the estimated user position is generally erroneous in urban areas, the work in [63] proposed elaborate approaches to resolve the position solution and at the same time

differentiate between the NLOS and LOS signals by using the 3D city model. First, one needs to calculate the GNSS signal shadowing by the buildings at multiple locations in real time [62]. Then, the concept is to search for position and signal selections that are mutually consistent. This is because, whether a signal is LOS or NLOS varies with the reception positions and the variation can be predicted by means of the 3D model. In [63], two approaches are outlined: searching by signal combination and searching by position.

Using the *urban trench* model, the work in [81] demonstrated that it is able to identify the LOS and NLOS signals with a vehicle moving along the narrow streets of European cities. Once identified, the NLOS are either discarded or corrected for position estimation. The trench model is a geometrical street model approximated by a trench with constant width and height. However, this model is suitable for the narrow type roads with buildings that are regular and symmetric enough along both sides of the streets. The authors acknowledged that the model is not quite suitable for some urban areas such as squares, crossroads or streets where the building heights are very different between the two sides of the streets. The work also does not specify any required accuracy of the 3D model. However, the dimensions of the trench model (width and height) have been implemented with a meter level accuracy.

2.4.1.5 Constructive use of NLOS/MP

Under the poor conditions of satellites visibility, the positioning algorithms have to take into account the fact that the received signal may reach the antenna from a non-direct path with an additional distance. For this purpose, few works exist in the literature on constructive use of NLOS signals.

The work of [112] demonstrated that, multipath delays may be modeled based on geometric representations rather than based on its statistics. When the positioning accuracy is sufficiently high, the model estimate a maximum of three unknown MP parameters per path, assuming a series of specular reflections off planar surface. Whenever some of the direct paths became undetectable afterwards, it is still possible to maintain the positioning accuracy using the indirect path measurements under certain conditions.

In [113], a method to identify MP is developed based on the difference in Doppler shift. In identifying the MP reflections, the proposed method exploits an open-loop batch-processing GPS receiver, together with laser scanner and inertial navigation system (INS). Multipath frequencies are predicted based on laser scanner and inertial measurements. Then, the predicted frequencies are compared to the frequencies of local energy maxima in the receiver. A multipath reflection is identified if there is a match and once identified the multipath reflections can be used constructively for navigation.

In this work [114], the authors predict the geometric paths of NLOS signals using a high realistic 3D model of the environment. The predicted paths are then used constructively in order to have enough information to compute users position. For this purpose, they proposed a new version of the extended Kalman filter augmented by the information provided by the 3D model for GNSS navigation in NLOS context.

In [115], the work proposed a technique termed a Signal Delay Matching (SDM) algorithm. The authors use the NLOS signals constructively with the help of a 3D city model to incorporate the information related to nearby reflectors. The positioning technique is then based on matching the NLOS signal delays predicted using a 3D city model with those observed from correlator outputs.

2.4.2 Hybridizations

In open sky situation, availability of GNSS signal for positioning is generally not a major issue except in the case of satellite outages (scheduled or unscheduled) or faulty signal which is very rare or in stringent operations such as precision landing. In urban setting, signal availability is affected by blockage. When too many signals are blocked or degraded to the extent of losing required accuracy, the service is no longer available and its continuity is disrupted. Even when four or more satellites are available, strong multipath effect might cause a positioning error of more than 100 m [116].

Therefore, in order to counter the degradation of the navigation solutions resulting from the unfavorable conditions of satellite signal reception in urban environments, vehicle navigation systems usually use complementary navigation methods known as Dead Reckoning (DR) which relies on information from vehicle motion sensors such as

accelerometers, gyroscopes, odometers and magnetometers. Apart from the motion sensors, complementary information may also be obtained from other RF signals (such as wireless communication systems), vision sensors or lidar, map or other feature matching, or vehicle models and motions constraints [116–118]. By integrating these additional information from different sources, their complimentary properties may be exploited.

In fusing these complementary data with GNSS system, commonly used filters are the Extended Kalman Filter(EKF) [43, 119, 120], Unscented Kalman Filter(UKF) [121, 122] and Particle Filter(PF) [123]. The hybridization may be implemented at different levels of information integration known as loosely coupled, tightly coupled, ultra-tightly coupled, or deeply integrated. Detailed description of these various architectures are found for instance in [31, 117, 124].

2.4.2.1 GNSS/DR Fusion

Essentially, DR is a relative navigation process which calculates one's position, velocity and potentially attitude based on the changes from the previous position, velocity and potentially attitude over a time interval. Conceptually, DR makes use of two or more sensors in order to measure the displacement and heading of the vehicle. Most of the time, obtaining these parameter changes requires transforming the measurements provided by the onboard vehicle sensors. With most of the DR sensors, the measurement transformations are integrative in nature. Therefore, the initial state of the vehicle is needed and the measurement errors will accumulate with time or travelled distance; a condition known as drift.

DR is commonly hybridized with GNSS system to overcome the drawbacks in degraded signal conditions. Unlike the GNSS signal, these sensors are not affected by space propagation phenomena or radio-frequency (RF) impairments such as blockage, multipath and NLOS, and they are accurate in the short term [125]. The aim is to bridge the gap when GNSS signal is unavailable or severely attenuated. This information may improve both the availability and accuracy of the navigation system [126]. However, the DR will drift during long GNSS outages.

Varied sensor configurations can be utilized in the DR system. Among the most popular and common sensors used for this purpose are the inertial sensors (accelerometers and

gyroscopes), odometers, wheels speed sensors, magnetic compass, etc. When using only the inertial sensors, the term Inertial Navigation System (INS) is regularly used. Reviews of these sensors are available in [31, 117, 127].

In GNSS/INS integration using a Kalman Filter, the errors dynamic model of the INS is linearized and used to predict INS errors. With the GNSS measurements available, the KF update step will estimate the INS errors and correct the INS output; hence the GNSS calibrate the INS. When the GNSS is not available, the KF only rely on the linearized dynamic model to predict the INS errors. Since the linearized model is not accurate, positioning solution degrades tremendously even for a short period of GNSS signals unavailability [128]. There are also two options exist for this kind of integration: open loop hybridization or closed loop hybridization. Performances of GNSS/INS in various environments and different type of integrations are studied in [129].

Reduced Inertial Sensor System (RISS) has been introduced in order to reduce the cost of INS [130]. To achieve low cost applications for vehicle, reduced Micro Electro-Mechanical Systems (MEMS) inertial measurement unit (IMU) with two accelerometers and one gyroscope, or three accelerometers and one gyroscope have been utilized. An example of a reduced IMU algorithm and ultra-tight GNSS/DR system are described by Li et al. [126]. However, low-cost MEMS-based INS with high levels of nonlinearity can further deteriorate the navigation performance that can result in significant position drifts even during short durations of GPS outages. One way to tackle this issue is to integrate more sensors such as wheel speed, steering encoder and etc. as described in [131, 132] or engage in higher level of fusion among the sensors such as by ultra-tight integration [126].

Integration of GNSS with DR may also be achieved without the INS. For example, the work in [133] compares the navigation performance of GPS/wheelspeed sensors hybrid system and GPS/wheelspeed sensor/gyroscope hybrid system. When compared between differential wheelspeed based dead reckoning system to a gyro based system for land navigation, results show that both heading schemes perform equally well when modeling assumptions hold, such as when traversing smooth road surfaces. However, when navigating speed bumps and uneven road surfaces, the position errors of the wheelspeed-heading estimator grow about twice as fast as those of the gyro based system [134].

2.4.2.2 Map matching

The purpose of a map-matching (MM) algorithm is to merge positioning data with a spatial road network data. For this purpose, it identifies the correct road segment on which a vehicle is travelling and determines the vehicle position on that segment [135, 136]. Other than merely from GNSS, the positioning data may also be obtained from a hybridized system (e.g., GNSS/DR). In map-matching, it is commonly assumed that the vehicle is constrained to a finite road network. While, such assumption is generally valid, there are some exceptions. For example, in situations that involves off-road driving, such an assumption could cause problem to the MM process.

Various MM techniques have been developed. In general, the approach for MM algorithms can be grouped into a few categories, namely: geometric, topological, probabilistic, and advanced. Detailed descriptions of these approaches may be obtained for example in [135] and [137]. Ochieng et al. [138] highlights that MM can also improve positioning accuracy provided that good spatial road network data are available.

Since MM is related to positioning, it becomes necessary to consider the errors pertaining to a spatial map and a MM process when monitoring the positioning integrity of vehicle in land-based applications. MM techniques have their own constraints and limitations in the performance. Sometimes, MM fails to identify the correct road segment, in particular at roundabouts, level-crossings, and Y junctions. Problems also persist in dense urban network and on parallel roads [135, 139].

Few works on land-based navigation incorporate MM in the integrity monitoring. For example, the work in [77] provides positioning integrity at the lane level for combined positioning and map-matching. The approach uses particle filter to process measurements from GNSS receiver, a gyroscope, the odometry of the vehicle and the road data stored in an Emap. This way, the road information is also processed as the filter observation. However, to achieve high integrity, GNSS outliers and multipath effects need to be removed effectively.

The work in [140] considers integrity of raw positioning data obtained from GPS together with the integrity of the MM process and digital map errors. Then it proposes a sequential map-aided integrity-monitoring method for land vehicle navigation. The process sequentially checks faults in the raw positioning fixes by using a WLS RAIM method,

then it ascertains the operational environment, and finally examines the integrity of the MM process. To determine the overall integrity, an integrity scale is derived using fuzzy inference system (FIS). The integrity scale is compared to a threshold to decide on the integrity level of the whole navigation system. In this work, the threshold value is based on an empirical analysis rather than on any specific distribution.

2.4.2.3 GNSS/2D or 3D GIS Fusion

In [141], the authors uses 2D map to aid a hybrid GNSS systems. GNSS, DR and road cache data are fused by an Extended Kalman Filter to estimate navigation solutions. Conceptually, after the DR measurements update, the map heading is determined from a road selection process of the MM. Then, the estimated state is corrected by the map heading. This form of a map-aiding odometry compensates vehicle heading error due to the DR drift and also even during satellites outage. Nevertheless, the altitude estimation is poor under challenging situations.

Cappelle et al.[80] propose the integration of 3D model with GNSS measurements, odometers, a gyrometer and a video camera for vehicle positioning. Using the Unscented Kalman Filter (UKF), the satellite measurements are hybridized with odometers and gyrometer measurements. In order to compensate the drift of odometers and gyrometer during long GNSS unavailability, another observation is used. This observation is obtained by matching between the current image from the onboard camera and the 3D model. A major advantage of using 3D model is that there is no addition of external systems. Only the data base is needed. However, camera is required and the model tend to represent the environment as structured and regular and the data base need to be updated often and its quality need to be addressed.

In the researches, several models have been developed and utilized. For example, in the method proposed in [141], a map of the road networks provided by NavTeQ or TeleAtlas is used to obtain information of the carriageways' center-lines in a 2D representation. In the work of Bourdeau [114], a 3D model developed by Oktal-SE called SE-NAV, is used to provide the synthetic environment for the calculation of GNSS line of sight signals and multipath signals. BATI 3D model is used inside an embedded Geographical Information System (GIS) developed by BeNomad is used in the frame of the French CityVIP project [142]. BATI 3D has been built by the French National Geographical

Institute (IGN) from high resolution aerial pictures (10 cm). Another virtual 3D model is produced by Tecnomade company which has been used in [80]. For all these models and maps, it is quite difficult to quantify their quality. Information on their accuracy or other specifications are difficult to obtain. In term of road networks, the common practice is to display only at the road width representation rather than down to the lane-level.

2.5 Conclusion

By having constellation of satellites orbiting around the earth, GNSS systems are envisaged to perform positioning everywhere around the globe. While it is being used regularly by millions of users today, there are still situations in which the GNSS receivers find it difficult to provide PVT solutions that are reliable enough. This is why researches to improve the performance of satellite positioning in constrained environment are still actively ongoing. Particularly, the increasing reliance on these systems by the general public provide strong motivation to industries and researchers alike in solving the navigation problems pertaining to urban environments.

The chapter has presented the challenges of achieving reliable positioning in urban settings. Blocking of satellite signals by buildings and other objects, multipath signals propagation and NLOS are the typical phenomena in urban environments which degrade the performance of navigation solutions. In the meantime, the users are expecting more and more GNSS based applications that can be used in urban areas to include applications that potentially have safety or liability repercussions. For this reason, apart from mitigating the impacts of contaminated GNSS signals on positioning, the aspect of confidence in the navigation solutions has also become crucial.

In the development of performance measures for the land applications, the experience and knowledge from the civil aviation proved to be invaluable especially in the concept of integrity monitoring. Even though direct adaptations of the methods and performance metrics are not possible due to the specific challenges posed by the urban environments as opposed to the open sky environment, those methods provide strong foundations from which further research may be pursued for the land application case. This chapter has

reviewed extensively many of the previous techniques and approaches to improve positioning reliability in urban environments. These approaches mainly focus on mitigating the errors in the GNSS measurements and also fusing the GNSS with other sensors or information, i.e. using the hybridization approach to take advantage of the other sensors while reducing the disadvantage of the GNSS.

In reducing the GNSS error, the in-receiver signal processing methods are effective against multipath errors. However, their implementations are complex and they do not produce the best improvement against NLOS. With high sensitivity receivers, more signals can be received thus increase redundancy. Unfortunately, it also increases the chance of receiving degraded signals. Some error mitigation techniques make use of additional hardware such as ring, polarized and multiple antennas and antenna arrays in order to reject degraded signals. Sky-pointing camera had also been proposed for identifying NLOS. Nevertheless, the issues with extra hardware are their additional cost, weight, size and power consumption that are usually not convenient for mobile applications.

Some efforts were targeted on better modelling the MP and NLOS to replace the commonly assumed Gaussian distribution so that they can be used effectively in the PVT algorithms. While a few models had been proposed, their usage or implementation is related to the more complex and heavy computation of PVT estimation algorithms, such as particle filter. Many researches had also been done to detect the NLOS so that it can be excluded from the good signals. One of the approaches adopted the concept of RAIM by checking the consistency among the received signals. But RAIM was originally designed for single fault detection. Its direct adoption for detecting multiple biases due to NLOS and MPs did not give the same good result. Detection of NLOS based on the measurements C/No and satellite elevation angles had been studied as well. However, it is difficult to decide on LOS/NLOS just based on the C/No and satellite elevation as indicators because there are many aspects of the received signals other then the LOS/NLOS conditions that affect the C/No or satellite elevation angles. As 3D models are becoming more and more advance, attempts to use them for identifying LOS/NLOS reception has been proposed. However, the 3D models' representation of the receiver surrounding environments is merely an approximation. Hence, there is a need to ensure the quality of the 3D model to be suitable with the purpose of it's usage. Some early

works have also been propose to use the NLOS/MPs constructively for positioning since LOS signals may be too scarce in urban environments.

To counteract the disadvantages of GNSS signals in urban canyons, hybridized concept have been proposed to complement the GNSS. Among the common approaches is to fuse the GNSS with dead reckoning sensors, map matching or GIS. However, with more sensors, the algorithms tend to be moderately more complex and errors related to the other sensors need to be considered as well.

Unlike in the civil aviation, the approach for ensuring reliable positioning for land applications in urban environments is highly dependent on the type of the application itself. Hence, an approach that is suitable for an application may not be suitable to another application. Therefore, several levels or combination of approaches has to be taken into consideration in monitoring the reliability of positioning in urban environments. For example, monitoring need to be done both at the range domain and at the position domain. Degraded measurement may be excluded or amended and used in the PVT estimation, depending on the situation.

Chapter 3

Existing Works on Reliability and Integrity Monitoring of GNSS Positioning

As has been introduced in previous chapters, reliability in navigation has been defined in several ways. For example, in geodetic measurement network, reliability means the capability of the estimation to detect blunder in the measurement. Whereas in the case of the civil aviation community, a set of performance metrics to represent the reliability of the navigation solution has been developed, which are the accuracy, availability, continuity and integrity. In this chapter, the focus is more on the aspect of positioning confidence which is closely related to the integrity monitoring topic in the civil aviation.

Here, descriptions on existing techniques and approaches related to integrity monitoring are presented. Starting with the classical RAIM techniques, further elaborations include the benefits of multi-constellation and the issues of handling simultaneous multiple faults (which is highly relevant and a crucial issue in urban environments). Then, the narration on using positioning error overbound to provide conservative confidence measure is also delineated. Deliberation on these works is intended to provide better insights in dealing with the integrity issue for land navigation in urban settings.

3.1 RAIM and Fault Detection

RAIM is an integrity monitoring method which has been categorized by ICAO as ABAS. It is a technique that uses an over-determined solution (i.e., having more data than is required to form a navigation solution) to perform a consistency check on the satellite measurements [31, 45, 124]. As defined in [46], RAIM is the fault detection part of the Fault Detection and Exclusion (FDE), which is a receiver processing scheme that autonomously provides integrity monitoring for the position solution, using redundant range measurements. The objective of RAIM is to detect the presence of an unexpectedly large position error for a given mode of flight. Upon detection, fault exclusion follows and excludes the source of the unacceptably large position error, thereby allowing navigation to return to normal performance without interruption in service.

Conceptually, RAIM assures to detect a positioning failure with a probability of missed detection P_{MD} and probability of false alarm P_{FA}, given that the HPL does not exceeds the HAL. To achieve this, the detection threshold value is set in order to achieve the required P_{FA} as a constant false detection rate under fault free conditions. The P_{MD} requirement is ensured by checking the availability of RAIM, i.e., by comparing the HPL to the HLA.

In general, there are four approaches or methods which can be considered as the traditional or basic RAIM. They are the range comparison method [53], the least-squares residual (LSR) method [107], the parity method [143], and the solution-separation method [52]. The first three methods, which operate in the range domain, were shown to be similar in concept and their obtained results [61]. Unlike the other three methods, the solution-separation method operates in the position domain. Here, only the LSR RAIM and the concept of solution separation RAIM approaches are presented.

3.2 LSR RAIM

In LSR RAIM, integrity monitoring is applied to the position solution by using the Least Square (LS) estimate on the linearized PR measurement equation:

$$\mathbf{\Delta y} = \mathbf{H\Delta x} + \mathbf{E} \tag{3.1}$$

$$\begin{pmatrix} \Delta y_1 \\ \Delta y_2 \\ \vdots \\ \Delta y_n \end{pmatrix} = \mathbf{H}. \begin{pmatrix} \Delta x \\ \Delta y \\ \Delta z \\ \Delta b_c \end{pmatrix} + \begin{pmatrix} E_1 \\ E_2 \\ \vdots \\ E_n \end{pmatrix}$$

where

- $\mathbf{\Delta y}$ is a $n \times 1$ measurement vector that consist of the difference between the actual measured PR and the predicted ranges based on nominal user position (i.e the linearization point).
- $\mathbf{H}$ is a $n \times m$ observation matrix which describe the linear connection between $\mathbf{\Delta y}$ and $\mathbf{\Delta x}$.
- $\mathbf{\Delta x}$ is a $m \times 1$ vector that consist incremental deviation from the nominal state about which the linearization took place.
- $\mathbf{E}$ is the measurement error vector, which consist of the combination of all ranging errors. The PR errors are usually separated into nominal errors (noise) and fault (bias):

$$\mathbf{E} = \boldsymbol{\varepsilon} + \mathbf{b} \tag{3.2}$$

where

  - nominal errors are assumed to be independent and zero mean Gaussian distributed:

$$\boldsymbol{\varepsilon} \sim \mathcal{N}(0, \Sigma) \tag{3.3}$$

$$\mathbf{\Sigma} = \begin{bmatrix} \sigma_1^2 & 0 & \cdots & 0 \\ 0 & \sigma_2^2 & & \vdots \\ \vdots & & \ddots & 0 \\ 0 & \cdots & 0 & \sigma_n^2 \end{bmatrix}$$

where σ_i is the standard deviation of the nominal error for the i^{th} measurement.

– In classical RAIM, it is assumed that only one bias is possible in each epoch:

$$\mathbf{b} = [0, \cdots, 0, b_i, 0, \cdots, 0]^T \tag{3.4}$$

The LS estimate of Equation 3.1 is given by:

$$\boldsymbol{\Delta}\widehat{\mathbf{x}} = (\mathbf{H}^T\mathbf{H})^{-1}\mathbf{H}^T\boldsymbol{\Delta}\mathbf{y} \tag{3.5}$$

From the LS solution of Equation 3.5, a predicted measurement vector, $\boldsymbol{\Delta}\widehat{\mathbf{y}}$, can be calculated by:

$$\boldsymbol{\Delta}\widehat{\mathbf{y}} = \mathbf{H}\boldsymbol{\Delta}\widehat{\mathbf{x}} \tag{3.6}$$

For Weighted Least-Square (WLS) method, the estimate is given by:

$$\boldsymbol{\Delta}\widehat{\mathbf{x}} = (\mathbf{H}^T\mathbf{W}\mathbf{H})^{-1}\mathbf{H}^T\mathbf{W}\boldsymbol{\Delta}\mathbf{y} \tag{3.7}$$

where $\mathbf{W}$ is the inverse of the covariance matrix, $Cov(\mathbf{E})$.

3.2.1 Test Statistic

The LSR RAIM calculates PR residual as a measurable scalar parameter to infer about PR measurement errors which are not directly measurable. From this residual, a test statistic is computed in order to detect, within a certain level of confidence, whether the position error exceeds an acceptable threshold.

A $n \times 1$ residual vector $\mathbf{w}$ can be obtained by taking the difference between the measured and the predicted PR vectors [31],

$$\begin{aligned}
\mathbf{w} &= \boldsymbol{\Delta}\mathbf{y} - \boldsymbol{\Delta}\widehat{\mathbf{y}} = \boldsymbol{\Delta}\mathbf{y} - \mathbf{H}(\mathbf{H}^T\mathbf{H})^{-1}\mathbf{H}^T\boldsymbol{\Delta}\mathbf{y} = [\mathbf{I} - \mathbf{H}(\mathbf{H}^T\mathbf{H})^{-1}\mathbf{H}^T]\boldsymbol{\Delta}\mathbf{y} \\
&= [\mathbf{I} - \mathbf{H}(\mathbf{H}^T\mathbf{H})^{-1}\mathbf{H}^T](\mathbf{H}\boldsymbol{\Delta}\mathbf{x} + \mathbf{E}) \\
&= [\mathbf{I} - \mathbf{H}(\mathbf{H}^T\mathbf{H})^{-1}\mathbf{H}^T](\mathbf{H}\boldsymbol{\Delta}\mathbf{x}) + [\mathbf{I} - \mathbf{H}(\mathbf{H}^T\mathbf{H})^{-1}\mathbf{H}^T](\mathbf{E}) \\
&= (\mathbf{H}\boldsymbol{\Delta}\mathbf{x} - \mathbf{H}\boldsymbol{\Delta}\mathbf{x}) + [\mathbf{I} - \mathbf{H}(\mathbf{H}^T\mathbf{H})^{-1}\mathbf{H}^T](\mathbf{E}) \\
&= [\mathbf{I} - \mathbf{H}(\mathbf{H}^T\mathbf{H})^{-1}\mathbf{H}^T](\mathbf{E})
\end{aligned} \tag{3.8}$$

To simplify the notations, let $\mathbf{S} = [\mathbf{I} - \mathbf{H}(\mathbf{H}^T\mathbf{H})^{-1}\mathbf{H}^T]$,

Therefore

$$\mathbf{w} = \mathbf{S}\boldsymbol{\Delta}\mathbf{y} = \mathbf{S}\mathbf{E} \tag{3.9}$$

where the observable residuals $\mathbf{w}$ are related to non-observable errors $\mathbf{E}$. Essentially, this derivation is a linear transformation that also relates range measurement vector $\boldsymbol{\Delta}\mathbf{y}$ with the residual vector $\mathbf{w}$.

In this LSR RAIM method, the sum of the squares of the residuals is the basic observable for forming the test statistic. It is called the sum of the squared error (SSE) and defined as:

$$SSE = \mathbf{w}^T\mathbf{w} \tag{3.10}$$

Assuming that each nominal PR errors is independent, normally distributed and has a unit variance, SSE has a chi-square distribution with $(n-4)$ degrees of freedom in the fault free case. Whenever the element of $\mathbf{E}$ is biased, the SSE has a non-central chi-square distribution with $(n-4)$ degrees of freedom,

$$SSE = \mathbf{w}^T\mathbf{w} = \|\mathrm{w}\|^2 \sim \begin{cases} \chi^2_k & \text{if } \mathbf{E} \sim N(0, I) \\ \chi^2_{k,\lambda} & \text{if } \mathbf{E} \sim N(b, I) \end{cases} \tag{3.11}$$

where k is the degrees of freedom and λ is the non-centrality parameter of the chi-squared distribution. Further description of λ and its relation to P_{MD} is explained in section 3.2.3.

For the case of RAIM, the number of degrees of freedom of the chi-squared distribution is the number of redundant PR measurement. To satisfy the characteristics of a chi squared distribution, the PR nominal error of the SSE must have equal variance. This is achieved when the residual is normalized. As defined in [107], the LSR RAIM test statistic is,

$$T = \sqrt{\frac{SSE}{n-4}} \tag{3.12}$$

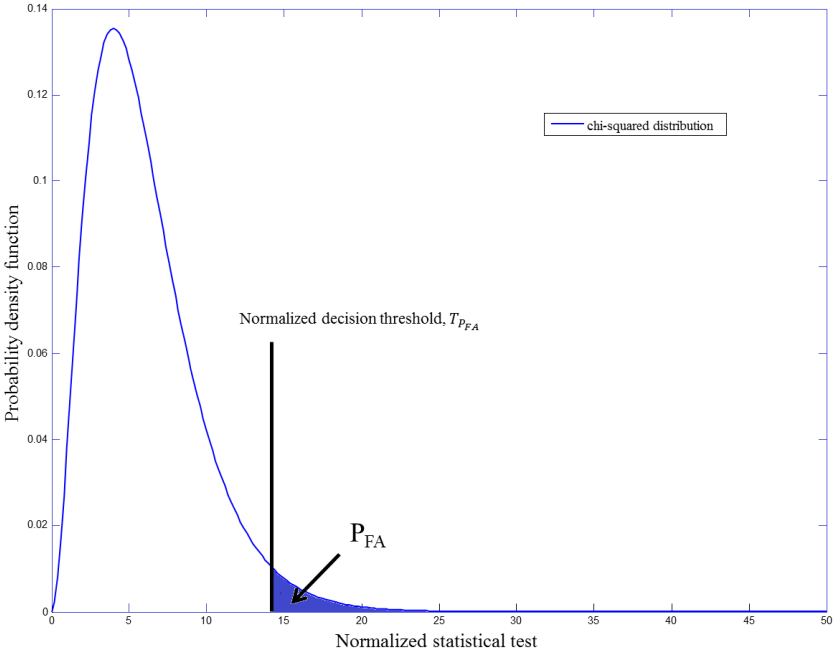

FIGURE 3.1: Derivation of Detection Threshold

3.2.2 Detection Threshold

In RAIM, failure detection is achieved by comparing a test statistic T, against a detection threshold, Th.

$$\begin{aligned} T \leqslant Th &\Leftrightarrow \text{no failure detection} \\ T > Th &\Leftrightarrow \text{failure detection} \end{aligned} \tag{3.13}$$

RAIM is set to provide a constant false alert rate equal to the required P_{FA}, and a non-fixed probability that the undetected positioning failures equal to or lower than P_{MD} [61]. To relate the detection threshold to the required P_{FA}, the test statistic distribution is considered in the fault free case. Specifically, the detection threshold is determined by integrating the pdf from the detection threshold to infinity so that the area under the curve is equal to the P_{FA}.

$$P_{FA} = P\{detection|faultfree\} = P\{T > Th|T \sim \chi^2_k\} = 1 - CDF_{\chi^2_k}\{Th\}, \tag{3.14}$$

where CDF is the empirical Cumulative Distribution Function.

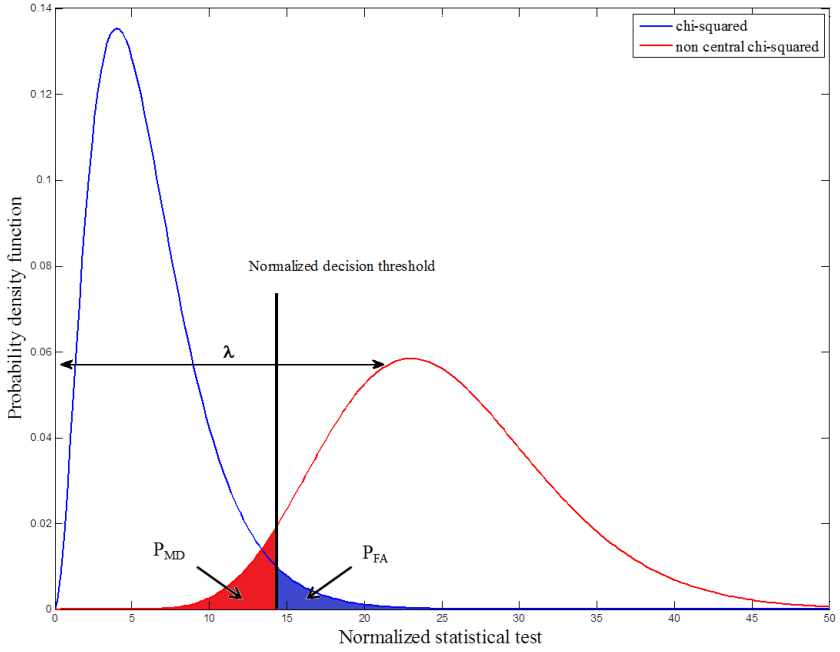

FIGURE 3.2: Fault free and faulty LSR statistical test distrbution

Figure 3.1 demonstrates the normalized detection threshold is set to achieve a detection rate equal to P_{FA} under fault free conditions. It follows that the detection threshold,

$$Th = \sqrt{\frac{T_{P_{FA}}\sigma^2}{n-4}} \tag{3.15}$$

Where $T_{P_{FA}}$ is the normalized decision threshold while σ^2 is the variance used for the normalization.

3.2.3 Relation between test statistic and position error

In order to describe the relationship between the test statistic to the position error, several other relations have to be addressed first. The HPL is derived from the smallest bias that the LSR RAIM is able to detect while satisfying the P_{FA} and the P_{MD} requirements. In the faulty case, the measurement error $\mathbf{E}$, contain noise and a bias, b and the *SSE* takes the non-central chi-square distribution. The P_{MD} is related to HPL from this χ^2 PDF, by integrating from 0 to the detection threshold, to determine λ, which is the non-centrality parameter that satisfy the P_{MD} (Figure 3.2). This obtained λ is the smallest one that can be detected by the test and it does not depend on any PR.

Next, the relationship between position error vector, $\mathbf{e}$ and measurement error, $\mathbf{E}$ is shown as follows:

$$\begin{aligned} \mathbf{e} &= \boldsymbol{\Delta}\widehat{\mathbf{x}} - \boldsymbol{\Delta}\mathbf{x} = (\mathbf{H}^T\mathbf{H})^{-1}\mathbf{H}^T\boldsymbol{\Delta}\mathbf{y} - \boldsymbol{\Delta}\mathbf{x} \\ &= (\mathbf{H}^T\mathbf{H})^{-1}\mathbf{H}^T(\mathbf{H}\boldsymbol{\Delta}\mathbf{x} + \mathbf{E}) - \boldsymbol{\Delta}\mathbf{x} \\ &= (\mathbf{H}^T\mathbf{H})^{-1}\mathbf{H}^T\mathbf{E} = \mathbf{A}\boldsymbol{\varepsilon} + \mathbf{A}\mathbf{b} \end{aligned} \tag{3.16}$$

Therefore, the effect of a bias b_i in the i^{th} satellite to the position error can be written as,

$$\mathbf{e}_H = \mathbf{A}\begin{bmatrix} 0 \\ \vdots \\ b_i \\ \vdots \\ 0 \end{bmatrix} = \mathbf{A}b_i e_i \; ; \; \|\mathbf{e}_i\| = 1 \tag{3.17}$$

$$|e_H| = |b_i|.\|\mathbf{A}\| = |b_i|\sqrt{A_N^2 + A_E^2} \tag{3.18}$$

where $\mathbf{A} = (\mathbf{H}^T\mathbf{H})^{-1}\mathbf{H}^T$.

Since the PR errors, $\mathbf{E}$ has a statistic component (i.e. the nominal error) and a deterministic component (i.e. the bias of faulty measurement, b), the test statistic and the horizontal position error, $|e_H|$ also have a deterministic and stochastic or random components considering that they are essentially derived from the PR errors. Therefore, the impact of the bias b in the position domain is the projection of b on to the horizontal position error $|e_H|$. Designating this deterministic horizontal position error as $|b_H|$, we have:

$$|b_H| = \sqrt{b_N^2 + b_E^2} = \sqrt{A_N^2 + A_E^2}.|b_i| \tag{3.19}$$

The simplified relation of the smallest detectable PR bias and the test statistic is given by [84, 144]:

$$\sigma^2\lambda = b^T S_{ii} b = S_{ii} b^2 \tag{3.20}$$

$$\lambda = \frac{S_{ii}}{\sigma_i^2} b_i^2 \tag{3.21}$$

Hence, the smallest detectable measurement bias b_i is related to the non-centrality parameter λ by:

$$b_i = \sigma_i \sqrt{\frac{\lambda}{S_{ii}}} \tag{3.22}$$

Finally, it follows that, the deterministic component of the horizontal position error is related to the test statistic by,

$$|b_H| = \sqrt{A_N^2 + A_E^2}.b_i = \sqrt{A_N^2 + A_E^2}\sigma\sqrt{\frac{\lambda}{S_{ii}}} \tag{3.23}$$

For the random noise component however, it has been proven by [145] that there is no correlation between the test statistic and the positioning error due to the orthogonality principle [84].

a. HPL Calculation

Aside from the FDE function, a typical RAIM system usually provides the HPL. An integrity algorithm aims to provide a position estimate within HPL. If the position integrity cannot be assured to be within the HPL with the required probabilities, an alarm must be raised to the user. In other words, the purposes of HPL are to bound the horizontal position error and to screen out bad satellite from the constellation geometry.

The HPL is calculated as [31]:

$$HPL = Slope_{max} \times pbias \tag{3.24}$$

where

$$slope_i = \frac{\sqrt{A_{N,i}^2 + A_{E,i}^2}}{\sqrt{S_{ii}}} \tag{3.25}$$

$$Slope_{max} = \max_i(slope_i) \tag{3.26}$$

$$pbias = \sigma_i \times \sqrt{\lambda} \tag{3.27}$$

Accordingly, the estimated position sensitivity to measurement errors depend on the particular geometry of the satellites. Therefore, some satellites affect the position error more than others. Similarly, different satellite measurement errors contribute differently to the fault detection statistic. Hence, the slope represents the relationship between the test statistic and the horizontal position error due to bias on a particular measurement (assuming all other measurements are perfectly without error). Depending on the satellite geometry, the bias of the satellite with the highest slope ($Slope_{max}$) is the most difficult to detect.

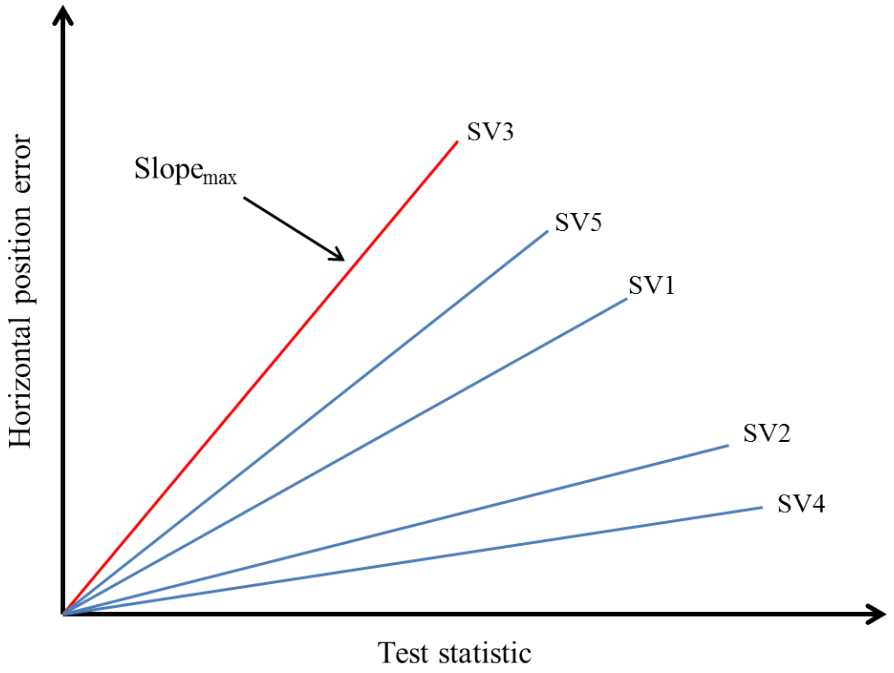

FIGURE 3.3: Characteristic slopes for five visible satellites

3.2.4 Weighted LSR RAIM

LSR RAIM was developed assuming the PR nominal errors are independent Gaussian distributed with equal variance. This assumption was acceptable when the selective availability (SA) was the dominant error in the PRs. Once the SA was switched off, the error variance of each of the PR is significantly different from each other and usually depends on the satellite elevation angle. In adapting to this situation, the Weighted Least Squares Residual (WLSR) RAIM was proposed [55]. For WSLR RAIM, the following adjustment to the relevent formulas are adopted:

$\mathbf{A} = (\mathbf{H}^T\mathbf{\Sigma}^{-1}\mathbf{H})^{-1}\mathbf{H}^T\mathbf{\Sigma}^{-1}$
$\mathbf{S} = [\mathbf{I} - \mathbf{H}(\mathbf{H}^T\mathbf{\Sigma}^{-1}\mathbf{H})^{-1}\mathbf{H}^T\mathbf{\Sigma}^{-1}]$

$$\mathbf{\Sigma} = \begin{bmatrix} \sigma_1^2 & 0 & \cdots & 0 \\ 0 & \sigma_2^2 & & \vdots \\ \vdots & & \ddots & 0 \\ 0 & \cdots & 0 & \sigma_n^2 \end{bmatrix}$$

$$HPL = Slope_{max} \times \sqrt{\lambda} \tag{3.28}$$

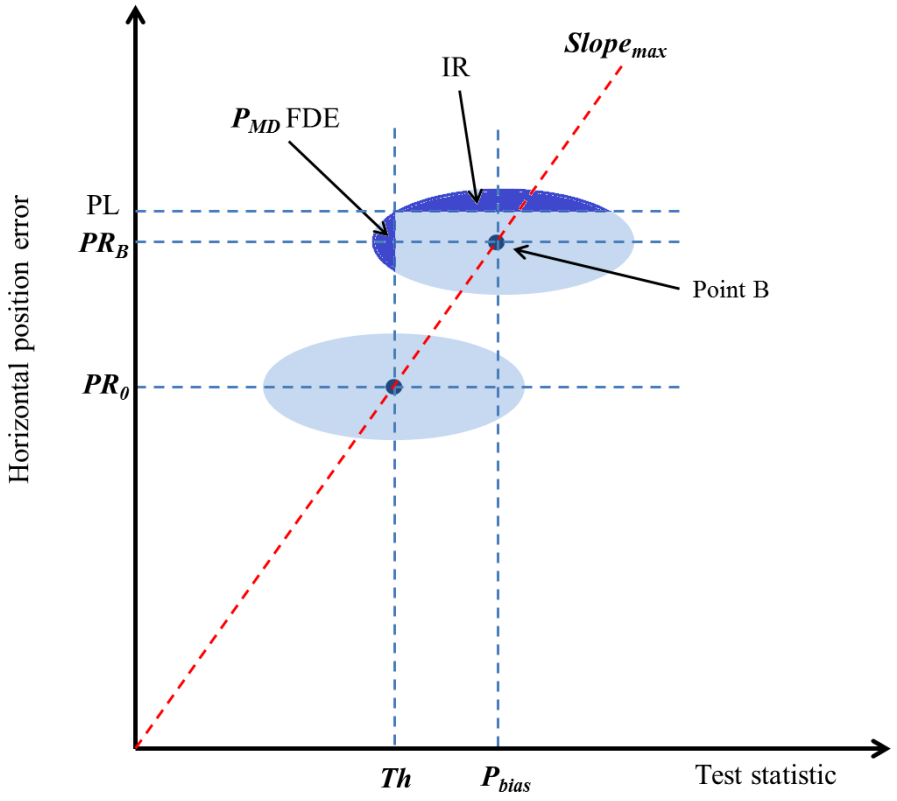

FIGURE 3.4: Protection level computation in classic RAIM

where

$$slope_i = \sigma_i . \frac{\sqrt{A_{N,i}^2 + A_{E,i}^2}}{\sqrt{S_{ii}}} \quad (3.29)$$

$$Slope_{max} = \max_i (slope_i) \quad (3.30)$$

3.2.5 Slope based HPL

Previously, the HPL calculation only considers the effect of bias and satellite geometry that produce the $Slope_{max}$. In this subsection, the HPL derivation will also take into account the nominal error statistic [55, 146]. If we only consider a deterministic bias, the HPL would be set at PR_0 (Figure 3.4) since it corresponds with the position error related by the maximum slope to the test statistic at the threshold. However, if we also consider the nominal error which construes the statistic component of the measurement errors, even when the test statistic is below the threshold, there can be positions errors that exceed the protection limit, PR_0. In classic RAIM, the distribution of the nominal error is assumed to be zero mean Gaussian (represented by the ellipse in the Figure 3.4).

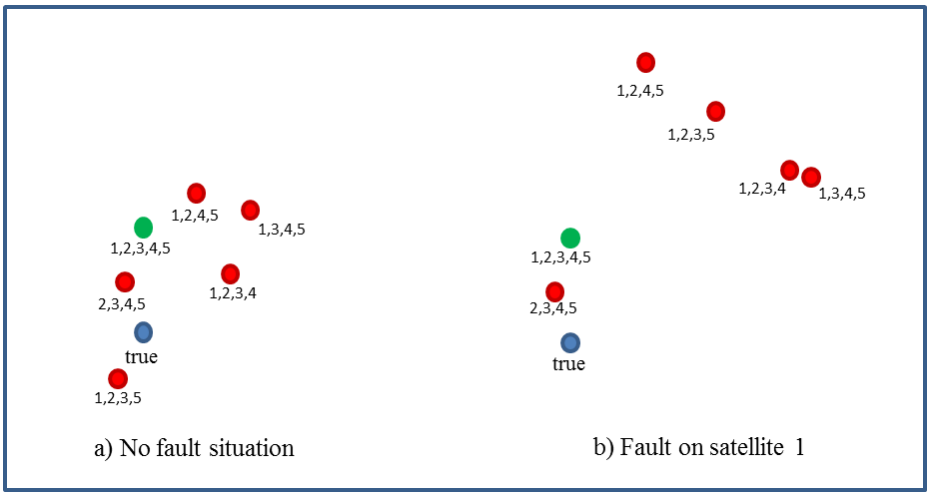

FIGURE 3.5: Fault Detection Concept of Maximum Solution Separation RAIM

The left half of the ellipse represents the FDE misdetection probability (P_{MD} FDE). This P_{MD} usually need to be further reduced to meet operational requirement. To do so, the ellipse is moved along the maximum slope line until reaching a point B where the probability mass on the left of Th meet the P_{MD} FDE requirement (represented by the upper ellipse in the Figure 3.4). The corresponding shift in the horizontal axis that is needed to reach point B is called P_{bias}.

At point B, if PR_B is used as the protection level, the upper half of the new ellipse still represent the position errors that exceed the protection level. Therefore, the protection level can be adjusted upward to a value PL, depending on the variance of the nominal error distribution and in accordance with a targeted integrity risk (IR) to meet the integrity requirement for a specific operation.

3.3 Maximum Solution of Separation (MSS) RAIM

Maximum solution of separation (MSS) RAIM was introduced by Brown et al. [52]. In this method, the difference between position solution obtained using all n satellites in view and the solution using $(n-1)$ satellite is used as the test statistic (Figure 3.5). When compared against a threshold, the test statistics that exceed the threshold indicate a fault in the PR that was omitted in the calculation of the test statistic.

In this approach, the observable test statistic is derived directly in the position domain rather than in the range domain such as the approach used in LSR RAIM. In the LSR

based methods, the PR residuals are used to characterize the integrity in the position domain. Therefore, the relationship model of the residuals to the position errors has to be precise in order to qualify as a test statistic. On the other hand, the protection level computation in the MSS RAIM is more complicated than the LSR based methods where statistical bounds have to be used in order to check requirements compliance as described in [144].

3.3.1 Test Statistic

The test statistic used in MSS RAIM to compare against the threshold is the discriminators, d:

$$\mathbf{d}_i = \boldsymbol{\Delta}\widehat{\mathbf{x}}_0 - \boldsymbol{\Delta}\widehat{\mathbf{x}}_i = (\mathbf{A}_0 - \mathbf{A}_i)\mathbf{E} \tag{3.31}$$

where

- $\boldsymbol{\Delta}\widehat{\mathbf{x}}_0$ is estimated position using all visible satellite.
- $\boldsymbol{\Delta}\widehat{\mathbf{x}}_i$ is estimated position using all but the i^{th} visible satellite.
- $\mathbf{A}$ is the matrix that relates estimated position error to the measurement errors. The subscript 0 indicates the matrix is obtained using all visible satellites, while the subscript i indicates the matrix is obtained without the i^{th} visible satellite.
- $\mathbf{E}$ is the measurement errors vector.

The covariance matrix of the discriminator is given by:

$$dP_i = (A_i - A_0)\Sigma(A_i - A_0)^T \tag{3.32}$$

3.3.2 Detection Threshold

The detection test for horizontal positioning is based on:

$$\begin{aligned} |d_{i,H}| \leqslant D_i \quad &\Leftrightarrow \quad \text{no failure detection} \\ |d_{i,H}| > D_i \quad &\Leftrightarrow \quad \text{failure detection} \end{aligned} \tag{3.33}$$

where D_i is the threshold.

The detection threshold need to satisfy the false alert rate. As given in [147], the detection threshold is,

$$D_i = \sqrt{\lambda_i} Q^{-1}(\frac{P_{FA}}{2n}) \tag{3.34}$$

where

$Q(x) = \frac{1}{\sqrt{2\pi}} \int_x^\infty e^{\frac{-t^2}{2}} dt$

λ_i is the largest eigenvalue of the covariance matrix $dP_{i,H}$

3.3.3 HPL computation

Even in the position domain, the actual position error remains unknown for the user. Therefore, statistical bounds have to be used in checking requirements compliance. One of the methods to calculate HPL for MSS RAIM is by finding a bound of the horizontal position error that is consistent with the required probability of missed detection and the required probability of false alarm as described below.

Given position error as $\mathbf{\Delta x} - \mathbf{\Delta \hat{x}_0}$,

$$P(\|\Delta x - \Delta \hat{x}_0\|_H \leqslant \text{HPL } / \exists \text{ a non detected bias on PR}) = P_{MD} \tag{3.35}$$

The position error can be decomposed as:

$$\mathbf{\Delta x} - \mathbf{\Delta \hat{x}_0} = \mathbf{\Delta x} - \mathbf{\Delta \hat{x}_i} + \mathbf{\Delta \hat{x}_i} - \mathbf{\Delta \hat{x}_0} \tag{3.36}$$

Therefore, to bound the horizontal position error,

$$\|\Delta x - \Delta \hat{x}_0\|_H \leqslant \|\Delta x - \Delta \hat{x}_i\|_H + \|\Delta \hat{x}_i - \Delta \hat{x}_0\|_H \tag{3.37}$$

$$\|\Delta x - \Delta \hat{x}_0\|_H \leqslant \delta_i + D_i \tag{3.38}$$

where

D_i is from equation 3.34

$\delta_i = \sqrt{\mu_{1,i}} \sqrt{-2ln(P_{MD})}$

$\mu_{1,i}$ is the largest eigenvalue of the covariance matrix $C_{i,H}$; where $(\Delta x - \Delta \hat{x}_i)_H \sim \mathcal{N}\left(\begin{bmatrix} 0 \\ 0 \end{bmatrix}, C_{i,H} \right)$

A more detailed elaboration for the HPL of MSS RAIM is available for example in [144]. It is worthwhile to note that the HPE for land applications in urban environments are affected by NLOS and MPs which can be considered as multiple biases. Therefore, to adopt the largest eigenvalue of the covariance matrix as being done in the formulation above with a single bias assumption would not be valid calculating the bound for HPE in urban environments.

3.4 Benefits and Opportunity from Multi-constellation and multi-frequencies

Following the GPS modernization with multiple frequencies and with the addition of other GNSS constellations such as Galileo, it is foreseen that the accuracy of GNSS position solution will improve significantly. This is because, the use of multiple frequencies allow better reduction of errors and the availability of greater number of satellites at a given location due to the increased number of satellite constellation provides better satellites geometry for position estimation. Integrity is also potentially improved by better satellite availability because increased redundancy will also improve RAIM performance and better accuracy will also allow tighter protection limits. Continuity will also improve since it is directly related to satellite availability.

For example, the research results in [148] show evidence of improvements from the GPS/GLONASS configurations with respect to stand-alone GPS in terms of solution availability and accuracy in urban scenarios. Least squares and Kalman Filter estimators are used to process GNSS data in single point positioning and GLONASS inclusion yields evident benefits in both methods of estimation. However, despite all these potential improvements, the challenges of positioning in urban environment will not be negated just by multi-constellation as demonstrated in [62].

3.5 Multiple Faults

In its inception, RAIM was intended for monitoring the integrity of aircraft positioning where under the open sky environment, the received signals are generally in the LOS condition. Also, there are well defined integrity requirements depending on the flight

modes. The purpose of the monitoring has been to detect and exclude unacceptably large measurements errors such as satellite clock or ephemeris errors. Since this type of satellite errors are very rare (no more than 3 major service failure per year) [149], it was assumed in the conventional RAIM that only one fault or blunder need to be detected in a measurement epoch. And once a fault is detected, a few approaches may be adopted to identify the faulty measurement. As an example, with the LSR based RAIM, the residual larger than the threshold is associated to the faulty measurement. In the case of MSS RAIM, the greatest separation is obtained with the solution that omits the faulty measurement.

However, with the increased number of the GNSS constellations, despite the potential benefits that come with it, the probability of having multiple faults simultaneously in one epoch of measurement will also increase [150]. Also, the RAIM concept needs to include multiple failures consideration due to multipaths if it is to be adapted for the urban scenarios.

Using traditional RAIM against multiple faults is ineffective for several reasons. For example (except in MSS RAIM) if the test statistic exceeds the threshold, it is not possible to identify if the failure is due to a single or multiple failures. It is also possible to have a masking effect or unobservable multiple fault condition [64]. This is a situation where due to the satellite geometry and interactions among the multiple biases, the resulting test statistic remains lower than the threshold while if tested individually or in different geometry, there exist a bias or more that would exceed the threshold.

In some cases, especially with many outliers (for example three large biases), the solution can shift that when residuals are calculated, the good measurements can appear as outliers (i.e. exceed the threshold). In this situation, even after the good measurements are removed, the solution appears to remain statistically sound. Hence the solution is accepted while it is actually in error [151]. This effect is significantly reduced with greater redundancy and geometric strength of the measurements.

In [152], variation of RAIM availability with the number of faults is studied for the case of combined GALILEO/GPS case. The results indicate that, when the faults number increases to four, RAIM ability would be greatly reduced. The effect of multiple failures on the LSR RAIM test statistic is also discussed in [59]. It is analytically shown that an error vector always affects the detection criterion when N-4, or less, pseudorange

measurements are erroneous (N being the number of visible satellite). On the contrary, it always exists errors that do not affect the detection criterion when more than N-4 pseudorange measurements are affected by errors.

3.5.1 Iterative approach of multi-faults detection

While the interest on multiple faults in the aviation community is invigorated by the expectation of the increasing number of satellite constellations, the surveying/geodesy community has considered the issue of multiple blunders using what is known as data snooping approach [48]. It is necessary to identify outliers in surveying of large networks to avoid surveying errors during the post processing phase. The general concept is to detect multiple blunders by iterative detection and exclusion of the largest residual one at a time until no more outliers is identified. The method is developed further and structured under a procedure called Detection, Identification and Adaptation (DIA)[51, 153]. Usually, the model adaptation is performed by rejecting measurements or by inflating their variance.

In order to identify m potential outliers, a redundancy of at least $m + 1$ is required. However, as has been described earlier on the issue of using traditional single fault consistency checking approach on simultaneous multiple faults, erroneous rejection of a good measurement is probable particularly when involving larger and multiple biases.

Moreover, in degraded signal-environments, the redundancy is usually poor hence it is desirable to retain as many measurements as possible for achieving an efficient estimate. Due to this reason, when more than one observation is being excluded, the iterated fault detection and exclusion process should include a reconsideration of observations rejected earlier. This concept is implemented in the work of Kuusniemi [12] where three techniques were proposed in order to cope with such situation. The techniques are Observation Subset Testing, Forward-Backward FDE, and Iterative Reweighted Estimation –The Danish Method. In these FDE approaches, two types of basic test are employed; the Global Test (GT) and Local Test (LT). GT is similar to the test statistic of the LS RAIM and its purpose is to detect a blunder in a positioning solution. Once a blunder is detected, LT is conducted to identify the faulty measurement by analyzing each standardized residual. The variations of the techniques are as follows:

a. Subset testing. This technique uses only GT. Whenever a complete measurements set is above the threshold, all the possible combinations of measurements are checked, to find a subset from which the supposed blunders are excluded. Only the subset that passes the GT and is declared consistent is used to compute the navigation solution; if more subsets pass the GT, priority of choice is given to the set with the minimum statistic variable and the largest number of measurements.

b. Forward-Backward. This technique uses of both GT and LT and consists of two different steps; Forward and Backward. In the first step (Forward), the GT is performed and if the GT declares the set inconsistent, the LT is performed to identify and exclude the faulty measurement. Forward process is performed recursively until no more faulty measurements are detected. Due to the mutual influence of the observations, it is possible to reject a good observation. After the Forward process, if the solution is declared reliable and m measurements are excluded (with $m > 1$), the Backward scheme is then performed to reintroduce observations that were wrongly excluded. The rejected measurements are iteratively implemented backward and the GT is conducted; the observation set which passes the GT this time is used selected for position estimation.

c. Danish Method. The Danish method is an iteratively re-weighted least squares algorithm. By modifying the a priori weights of the measurements, this technique aims to achieve consistency among them. In the implementation, the GT is performed to verify the consistency of the measurements, and the LT, to identify and de-weight (rather than reject) the outliers.

3.5.2 Other approaches to deal with multiple faults

Apart from the geodesy community, the navigation community also uses the RAIM method. However, since it is notably developed for civil aviation services, the algorithms are required to be implemented onboard of aircrafts and to detect real time failures. In addition, the integrity algorithm is also expected to provide information about the protection level.

One proposed method to handle multiple faults is called group separation (GS) method [58]. Rather than assuming failures are independent, this approach is based on the concept that most of multiple failures are caused by a common fault that affects a group

of satellites. With this consideration, failure detection and exclusion are carried out by adapting the solution separation approach in which a group of measurements (rather than a single one) is excluded in turn. Potentially, this technique would decrease the number of sub filters to be checked for failure. However, it also may cause the depletion of measurement redundancy and unfavorable satellite geometry if used in restricted environments.

In [154], the authors presented an approach to detect multiple failure situations by employing an error reconstruction strategy from the LS residual based test statistic. However, the technique is limited to special cases of high magnitude failures (e.g 5 km) and the results are provided only for static receiver case.

Using the error characterization approach (ECA), the work by Vassileva [155] proposes a user-based computation of PL. As oppose to the measurement rejection approach (MRA) which operates on the principle of rejecting faulty measurements, ECA characterize measurements errors and compute a protection level without identifying and removing degraded measurements [156]. Vassilevas proposed technique works directly in position domain and uses high accuracy velocity measurements. Adopting the premise that position error is a combination of noise and bias [16, 17], the bound of the position error can also be achieved by adding the bound of the noise and the bound of the bias:

$$HPL = HPL_{noise} + HPL_{bias} \tag{3.39}$$

While only the HPL is described here, the work is also applicable to VPL.

First, the zero mean position error (i.e. the noise component) is extracted by filtering the measured user position and velocity in each east and north component using an ARMA filter. This estimation is used to form the HPE due to noise. For this error estimation purpose, the input velocity must be highly accurate (std dev less than 0.01 m/sec). Once the HPE is obtained, then the HPL_{noise} is calculated by a modified Cell Averaging Constant False Alarm Rate (CA CFAR) algorithm. This radar processing CA CFAR assumes zero mean Gaussian distributed noise of unknown power level [157]. As for the calculation of HPL_{bias}, the formulation follows the basis of the given maximum possible range bias, number of used satellites, and DOP value [17].

Several approaches on integrity monitoring for land applications have been proposed in the literature. Some of them is an adaption from the works in aviation sector but some are new. Adapting the concept of PL, the work in [158] developed the Horizontal Trust Level (HTL) as a novel integrity process for land vehicle navigation application. This technique was further enhanced and called Horizontal Integrity Threshold (HIT) [159]. However, this approach had a disadvantage that since the HIT value depends on the sensor variances and the covariance of the state, if corrupted data are included in the filter calculation, the integrity parameter may provide aberrant information.

The concept of Isotropy Based Protection Level (IBPL) was introduced in [64] where the vector of least squares estimation residuals are used as a characterization of the position error. It does not implement measurement rejection techniques. Instead, it computes a protection level based on the all-in-view least squares solution. In this approach, there is no requirement for the errors to be represented in any specific distribution.

To adapt RAIM for land vehicle navigation, [160] proposed a localization integrity approach that combines both vehicle sensors and GNSS data, by storing them within a short term memory (called data horizon). This is to avoid the impact of the past measurement bias in the filter so that the RAIM approach FDE algorithm and PL can be calculated. The main drawback of this formulation is that it is not possible to separate input sensor failures from evolution model failures.

In [66], the authors implemented a Robust Set Inversion via Interval Analysis method in a bounded error framework for positioning confidence. The technique is used to compute three-dimensional location zones in real time, at a given confidence level. This confidence measurement approach is significantly different from the Gaussian error model concept. Here, the satellite positions and the PR measurements are represented by intervals comprising the actual value with a certain level of confidence, i.e. bounds are set on the measurements with error and risk taken into account. These bounded-error measurements translate into constraints in the location domain. Then, the constraint satisfaction problem can be solved using interval analysis. If data redundancy is sufficient, inconsistent measurements can be detected and rejected.

In [161], the authors modified the WLS RAIM in order to adapt the integrity monitoring specifically to the Electronic Toll Collection (ETC) application. The aim of the modification is to improve the availability rate in the reduced satellite visibility environment

without increasing the missed detection rate. Conceptualy, unlike in the civil aviation, ETC system does not require continuity; therefore its RAIM algorithm does not need to assure maximum allowed P_{FA}. Hence, by fixing the P_{MD} and $slope_{max}$, the HPL can be reduced by increasing P_{FA}.

The work in [162, 163] initiate a new methodologies to provide Position, Navigation and Time (PNT) trust level for land applications. The proposed position confident level is made of a 5-state high level indicator which characterizes the signal processing events, and a protection level computed differently from the traditional approach. In accordance with the types of error faced by land application navigation, the 5-state feedbacks are:

- No detected fault
- Multipath detected on SV used in PVT
- Interference detected
- Doppler or Delay incoherence detected on SV used in PVT
- Anomaly detected in PVT

In order to monitor these states, several Key Performance Indicators (KPI) are employed. Specifically, they are Interference indicator, Multipath indicator, Doppler coherency indicator, delay coherency indicator and SV fault detection/exclusion. These indicators are implemented by means of several methods and techniques. For example, the Interference is monitored by setting 5 dB above the mean spectrum as a threshold. Multipath detection relies on code minus carrier and multicorrelator. Doppler coherency, delay coherency and SV fault are detected using LS RAIM. All these indicators help to reject or weight the measurements in optimal fashion so that the most accurate PVT solution is obtained with the lowest Protection Level and not to introduce any missed integrities. The computation for the protection level is:

$$HPL = K_H \times d_{major} + \sqrt{|\mathbf{K}_{1,:}|^2 + |\mathbf{K}_{2,:}|^2} \times \beta \tag{3.40}$$

Where:

- HPL is the horizontal protection level

- K_H is the protection coefficient dependent on the missed detection probability
- d_{major} is the square root of the maximum eigenvalue of the horizontal components of the position covariance matrix
- **K** is the projection matrix from the measurements domain to the position domain
- β is a vector of measurement bias

The work proposed in [164] is dedicated to the development of the integrity concept for land applications based on simulation approach. Under the European Space Agency (ESA) activity Signal Processing Techniques for the Integrity of Navigation for Land Users (INLU), a simulation tool is being developed in order to establish the integrity concept for land applications. For this purpose, the simulator is designed to be versatile and comprehensive with the following components:

- Scenario generator
- Software-Defined Receiver
- GNSS/IMU Sensor Integration
- Fault Detection at Signal Processing Level
- Fault Detection at PVT Level
- Protection Level Calculation
- Integrity Analysis Tool

Having such simulator is highly beneficial for integrity concept development because analysis based on experimental collected data alone is a monumental task.

3.5.3 Slope-based HPL in multi-faults case

In addition to the objective of multiple failures detection, identification and adaptation (DIA) by the geodesy community, in RAIM, protection level calculations are also needed by the users in Aviation.

As has been alluded in subsection 3.2.5, slope-based HPL is generally calculated as [55, 146]:

$$HPL = bias_H + k_H \sigma_{noise} \tag{3.41}$$

where the first term is intended to bound the effect of biases in the range measurements and the second term is intended to bound the effect of noise in the range measurements. In the single fault case, the HPL can be computed using the $Slope_{max}$ consept.

In the context of multiple failures, the slope max concept is extended to calculate the HPL for multiple faults RAIM. Generally, instead of using a single maximum slope, the approach is to search for suitable techniques for combining the faulty satellites to yield a combined maximum slope. Some of the proposed techniques are discussed in [165–168]. However, the works tend to assume only 2 simultaneous faults since considering open sky environments. For land applications in urban environments, larger number of biases are common due to NLOS and MPs. To calculate the 'combined' maximum slope in this case is very complex.

3.5.4 NIORAIM: HPL Optimisation

The HPL computation based on the slope-max concept has a limitation that even if the faulty satellite is not the one with the maximum slope, the maximum slope is still used for the protection level calculations. This caused the HPL to be higher than necessary and can result in reduced availability (Walsh et al. 2005). The Novel Integrity-Optimized RAIM (NIORAIM) which is initially presented by [169] is able to increase the integrity availability of the conventional single fault RAIM algorithm. In [170], the authors present an analysis under a dual satellite fault hypothesis where multi-constellation satellites of GPS+GLONASS are used. The results show a dramatic improvement of the integrity availability offered by the NIORAIM algorithm if compared to that achieved by such algorithm when applied to a single GPS constellation under the assumption of one satellite fault at a time.

In NIORAIM, the approach is to use a non-uniform weighted least square and adjust them until the integrity limits (or slopes) of the satellites become nearly equal. However, by adjusting the weights of the LS solution, the position accuracy decreases. Another

effect of the weight adjustment is that the covariance of position error and parity vector (test statistic) no longer remains zero. This affects the independent distribution assumption for chi-squared distribution of the position errors.

3.5.5 Multiple Hypothesis Solution Separation (MHSS) RAIM

Ene's work [171] on MHSS seeks to eliminate the possibilities of fault misidentification by guaranteeing integrity for the computed error bound in all possible cases of fault. As such it includes multiple faults case. Then, the calculated VPL determines whether continuity and availability requirements are also met.

The MHSS RAIM provides the basis for the Advance RAIM (ARAIM) implementation. The MHSS RAIM algorithm requires to calculate the P_{HMI} by including the contribution of each possible fault mode weighted by its prior probability.

$$P(HMI) = \sum_{i=0}^{m} P(HMI|H_i)P_{prior}(H_i) \tag{3.42}$$

where the overall $P(HMI)$ is the probability that the true user position lies outside the error bound determined by the integrity algorithm. The hypothesis set is denoted as $\mathbf{H} = \{H_0, H_1, H_2, \ldots, H_i, \ldots\}$, where H_0 always denotes the fault-free state of the system. The index i represent the number of the current fault mode, ranging from 0 and the maximum possible number of faults ($m = 2^n$).

With each hypothesis there will be an associated prior probability for that particular fault mode to occur, denoted as $P_{prior}(H_i)$ and under each hypothesis there will exist a separate probability for an integrity fault to occur, denoted as $P(HMI|H_i)$. While obtaining these prior probabilities is possible in the aviation application, it is not practically probable for multipath or NLOS occurrences in urban environment.

3.6 Error Overbounding

In integrity monitoring, the aim is to detect horizontal positioning failure, i.e, when $|e_H| >$ HAL. However, actual position errors are not observable without knowing the actual position. Hence, some types of observable measurements are used to represent the

position errors. In the LSR RAIM, it has been shown that the HPL is used to represent the horizontal position error. For this reason, whenever HPL exceeds HAL, RAIM is declared unavailable (i.e. integrity cannot be guaranteed). As has been described in the calculation of the slope based HPL in RAIM (section 3.2.5), the HPL has to bound the horizontal position error with a certain acceptable integrity risk (IR). In fact, the observables used in the LSR RAIM are the range residuals that are transformed into a test statistic that further related to the position errors. By setting a threshold on the test statistic based on the P_{FA} and P_{MD}, any violation of the threshold is interpreted as the position error exceeding the HPL within the required P_{FA} and P_{MD}.

All of these relations are derived based on the assumption that the residual and the actual measurement errors are independent, zero mean Gaussian distributed. Most of the time however, the actual distributions of the errors are biased, correlated and non-Gaussian [45]. Considering these non-ideal navigation error distributions, a concept of overbounding is used in GNSS navigation. Ideally, error modelling and characterization must include all possible sources of error in order to obtain the true distribution. However, in practice, it is not possible to absolutely validate the error models because it is realistically impossible to collect data that consists of all possible errors. Additionally, some of the physical processes behind the error sources (such as multipath) are too complex to be described or modelled and the error sources are also rarely stationary. These factors, contribute to the uncertainty of the modelled error distribution [172]. Therefore, the navigation community has explored the provision of integrity by the method of overbounding. This way, positioning integrity is quantitatively appraised using the position bounds that assure an acceptable level of integrity risk.

In short, overbounding refers to the process of replacing the actual error distribution by a simplified conservative model, generally a gaussian distribution to make use of all the interesting mathematical properties from the gaussian distribution, with the objective of having enough margins to take into account the risk of non-modelled errors [173]. What is interesting with overbound is that it can substitute the actual error distribution in obtaining a confidence interval such as the PL. However, the contention issue is the overbounding optimization, i.e. to overbound by how much. An overbound that inflate the PL too much will reduce the system availability but a 'too tight' overbound may risk not having enough margin.

In the civil aviation, works on using overbounding for establishing conservative confidence level in GNSS positioning integrity are mainly applied to the SBAS and GBAS systems. In the slope RAIM approach, the proof of safety is based on certain approximation without the prove of being conservative [174].

3.6.1 Range Domain Overbound

In [16], DeCleene had demonstrated a method based on the CDF for bounding individual ranging source errors in order to construct a conservative bound for the vertical positioning. He observed that a conservative PL could be computed from a set of range-domain overbounds when the integrated probability in the tails of each overbounding model was greater than the one in the tails of the corresponding actual distribution. According to the theorem, a position domain bound can be established from the convolution of the range domain bounds. However, DeCleenes overbounding formulation is only applicable to actual distributions which are independent, symmetric, and unimodal. A series of works in [175–177] further introduced other overbounding methods to address the limitations of the original concept, which include techniques for bounding arbitrary-shaped, independent distributions while a work in [178] described bounding for symmetric, correlated distributions.

In the concept of CDF overbounding, the overbounding CDF must cover larger errors than the actual data for a given level of probability or conversely, the overbounding CDF has lower probability than the actual CDF for the same error value [179].

$$\begin{aligned} G_o(x) &\geqslant G_a(x), \forall x \leqslant 0 \\ G_o(x) &\leqslant G_a(x), \forall x \geqslant 0 \end{aligned} \tag{3.43}$$

where $G_o(x)$ is the overbounding CDF and $G_a(x)$ is the actual CDF. Figure 3.6 shows the CDF overbounding concept.

In the range domain approach, the range error measurement data are used to compute overbounding (conservative) error models that are then mapped into the position domain to produce the PLs. To illustrate this approach, the calculation for the case of zero mean Gaussian PL is as follows:

$$PL_o = A_o \sigma_p \tag{3.44}$$

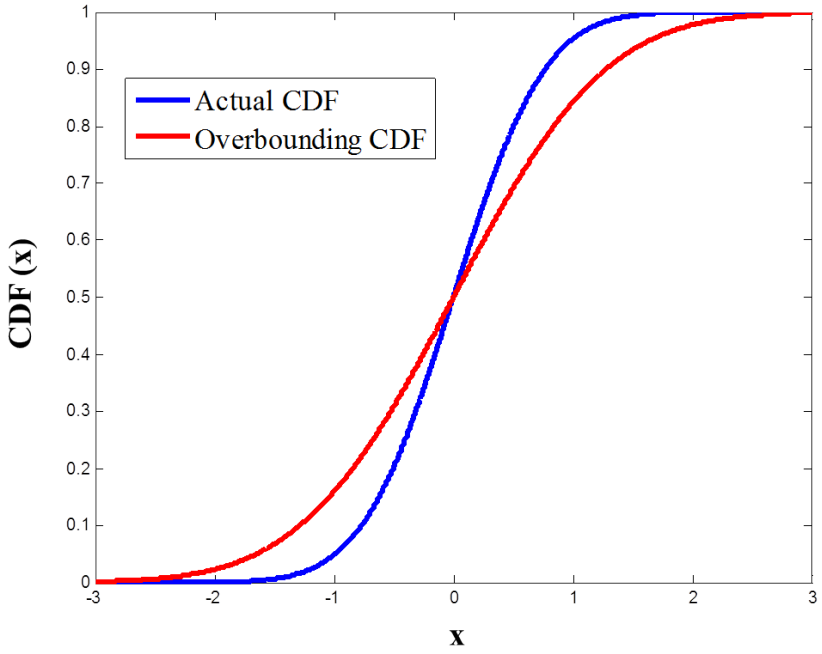

FIGURE 3.6: CDF Overbound concept

$$\text{with } \sigma_p = \sqrt{\sum_{i=1}^{N} S_i^2 \sigma_i^N} \text{ and } A_o = \sqrt{2} erfc^{-1}(P_{HMI})$$

σ_p is the root of the sum squares of the weighted range-domain sigmas for each of the total N observed satellites, and A_o describes the inverse cumulative distribution that associate the sigma with the integrity probability [175, 180].

In presence of bias, the PL can be formulated as a sum of nominal component plus a bias component:

$$PL = PL_o + PL_b \tag{3.45}$$

$$PL = A_o \sigma_p + PL_b \tag{3.46}$$

Let μ_i be the bias of each PR, PL_b is the total bias expressed as:

$$PL_b = \sum_{i=1}^{N} S_i \mu_i \tag{3.47}$$

In civil aviation, specific sources and effects of the bias have been considered and modelled [19]. However, in urban environments, the biases are mainly due to NLOS and

multipath receptions which are difficult to model, hence it is very difficult to come up with an expression of PL_b.

3.6.2 Position Domain Overbound

In the range domain approach, overbound is applied to each pseudorange measurement error distribution individually. Alternatively, bounding can also be implemented directly in the position domain. The concept of the position domain overbound has been elaborated in the works of [19, 181–183]. Osechas [183] highlighted the main difference of direct position domain overbounding as compared to the conventional indirect position domain overbounding approach is that in the direct approach, the overbounds are calculated by inspecting error data directly, without transforming the errors from the range domain to the position domain.

The position domain method is able to produce tighter PL and therefore increase availability because the conservatism assumptions were applied only to the position-domain error distribution model and not to each individual range-domain error distribution model [182]. The method also reduces the conservatism intended to protect against the pseudorange error distribution mismodeling [184].

The transformation process of the measurement errors to position error is commonly assumed to be linear while in reality, the processing is non-linear [185, 186]. Overbounding nonlinear processing is rather problematic in that they introduce excessive margin, which leads to poor system availability. Hence, the position domain overbound may be perceived as a method that bypasses the nonlinear transformation issue.

3.6.3 Parameter Inflation

The common method for generating the PL assumes an independent, zero-mean Gaussian error model. However, the actual error distribution is not necessarily zero-mean Gaussian. In order to ensure that the Gaussian model overbounds the true error, its variance is usually inflated to cover other kind of errors (bias from satellite, multipath, etc.)

For example, in the GBAS application, sigma inflation is performed to take into account the uncertainty of the true error distributions that are caused by the estimation error of the mean and sigma during site installation, and non-stationarity error distributions caused by environmental changes which affect multipath. The work of [182] had studied a comprehensive sigma inflation factor that accounts for all of these uncertainty sources, specifically due to finite sample size, process mixing, and the limitation of sigma monitors.

3.6.4 Heavy Tail Overbounding

Gaussian distribution is attractive as an overbound for several reasons [187]. Among them, it has a property that the convolution of two Gaussian functions is another Gaussian function. In a bandwidth limited system, information about the distribution is efficient since it only requires two parameters (mean and standard deviation). Also, functions that compute probability and cumulative densities are easily available. Nevertheless, most additional errors either from satellite, environment or the processing algorithm have large amplitude with low probabilities which yield to a heavier tail of the actual error distribution than the Gaussian one. In such situation, a simple Gaussian sigma inflation will not likely be able to overbound the distribution [175]. When dealing with the non-Gaussian tail or heavy tail error distribution, Shively [188] derived the sigma inflation factors by using a model of Gaussian core and Laplacian tails. Rife et. al [176] had proposed Gaussian core and Gaussian sidelobes to mitigate over-conservatism when bounding heavy tails.

In dealing with the issue of limited number of samples to ensure overbounding at the tail ends of the actual error distributions, works in [189, 190] have applied the extreme value theory to extrapolate the samples at the far tails of the distributions.

3.7 Conclusion

From the presented approaches used in monitoring integrity, several limitations and challenges are readily observed for their implementation in urban environments:

- Generally, the monitoring techniques are not designed to handle many simultaneous faults. Even the proposed techniques to deal with multiple faults only envisage a few simultaneous faults and some of them have not considered mobile user. Applying those techniques can result in non-effective performance due to the reasons described above.

- The algorithms are based on consistency checking which require a certain level of measurement redundancy. This redundancy are scarce in urban canyons, hence lead to ineffective performance of the algorithms.

- The distribution of errors are assumed to be independent and zero mean Gaussian. This assumption is invalid in the urban scenarios. Therefore, wrong modelling of the error distribution will cause ineffective performance of the integrity monitoring schemes.

Therefore, in developing a suitable techniques or approach for confidence measure of positioning in urban environments, those main issues have to be taken into considerations. Many relevant previous works in tackling some of the issues in integrity monitoring are presented in this chapter. With the development of multi-constellation GNSS, improvement in positioning performance is expected. However, the challenges in urban environment cannot be totally met only with the multi-constellation and additional source of positioning information is needed. In view of such need, external information on the geometric structure of an environment affecting GNSS signals propagation provided by a city model shall be exploited in the work of the next chapter. Subsequently, additional navigation sensors will be used in chapter 5.

Chapter 4

NLOS Characterization in Urban Environments Using a 3D Model

4.1 Introduction

To achieve reliable GNSS positioning in harsh urban environment is a very challenging task. The main source of error in the measurements is due to NLOS reception and multipath phenomena. The effect of assuming a direct path in a NLOS propagation environment leads to serious degradation in accuracy. Hence, degraded PR measurements are often excluded from the position solution calculation. However, in urban settings, simply rejecting PR measurements may have negative impact on the satellite geometry and may also reduce the available number of PR for trilateration process. Therefore, instead of discarding all measurements which are found to be in NLOS conditions, this work proposes to properly use these observations to improve the positioning accuracy and integrity in harsh environments.

For that purpose, this work combines the sigma-ε variance model with a mean jump (i.e. NLOS bias) to model the PR errors. First, a 3D model of the environment is used to detect the NLOS state of reception and to predict the NLOS bias related to the excess delay phenomenon. For reliable positioning, a C/No-based variance adjustment for the LOS PRs is implemented. Also, the bias is subtracted from the NLOS PRs during the trilateration step of position computation. The NLOS biases were obtained *a priori* for each satellite by measuring the difference between the measured PRs and the

referenced PRs when the state of reception is determined to be NLOS by the 3D model. The performance of the proposed scheme is assessed using real data and compared to a standard Kalman filter without the assisting information from the 3D simulator.

4.2 Predicting GNSS signal propagation conditions via 3D model

As 3D city models becoming more accurate and widely available, there are growing interests in their application to predict satellite reception availability. The works of [62, 191] used 3D city model to predict GNSS availability considering LOS, diffracted and re-radiated signals. In [110], the authors used 3D digital map in order to detect and mitigate multipath in real-time where a ray tracing algorithm is used to check if satellite signals are reflected or blocked. Then, the suspicious PRs are simply excluded from the observation set. 3D model along with camera image were used in [192] to filter out the PR measurements which are considered to be NLOS based on the comparison of the actual satellite elevation angle with the critical elevation angle calculated using the 3D model. Whereas in [80], the image captured by an on-board camera is matched with the 3D model as an additional observation to counteract against DR drift in the absent of enough satellite signals for positioning in urban environments. The comparison between the camera image and the 3D model is also applied for obstacle detection since it only appears in the image but not in the 3D model. In [114], the authors use a 3D model to predict the geometric paths of NLOS signals so that they may be used constructively in order to obtain enough information to compute the users position in harsh urban environment.

An interesting approach has been developed at UCL by the team of Professor Groves consisting of 3D model. To tackle the problem of degraded positioning due to multipaths and NLOS in urban environments, first, the team proposed to calculate the GNSS signal shadowing by the buildings at multiple locations. This provides building boundaries with different azimuth and elevation resolutions for a grid of candidate positions [62]. Then, to select the most likely correct position out of the candidate positions, three possible approaches had been described. First, the shadow matching technique [193] may be used to reduce the number of candidate positions. In simple term, shadow matching

affirms the receiver's general position by considering the satellite signals that are not visible to the receiver due to blockage. However, it has limited reliability because shadow matching is susceptible to NLOS being mistaken as LOS. Hence, they proposed another approach which is to combine the 3D model with consistency checking. The limitation of this combined approach is that the performance of consistency checking, which is similar to RAIM, is also not very effective in urban environments [109]. The third proposal is to determine the correct position solution by searching among the candidate positions for the one with signal conditions that are mutually consistent. The signal conditions are predicted using the 3D model for the candidate positions [63]. Of course, this approach requires that the 3D model provides reliable predictions. Another work that proposed similar approach of candidate position searching is provided in [194]. However, the algorithm for the search and the decision criteria for position selection is different from the one proposed by the UCL group.

By means of a specific 3D model called the *urban trench* model, the work of [81] demonstrates an approach to identify between LOS and NLOS signals. The urban trench model is implemented for vehicles moving along narrow streets which are predominantly the streets of European cities. Nevertheless, the urban trench model is mostly suitable for narrow roads with building along both sides of the road. In some other types of urban areas, the technique is not quite suitable.

In this work, SE-NAV software [7] is used to predict the signal reception of GNSS systems such as GPS into 3D virtual scenes of known urban areas. The propagation of signals is based on a ray-tracing algorithm that computes the shadowing and multipath effects. SE-NAV uses geometric optics to calculate the reflected, diffracted and transmitted rays. Based on these multiple rays that reach the receiver, the LOS or NLOS reception state of a satellite is provided. In order to characterize the biases *a priori*, the position of the satellites and the receiver must be known. The satellite positions are calculated based on the ephemeris data whereas the positions along the trajectory are obtained from the receiver.

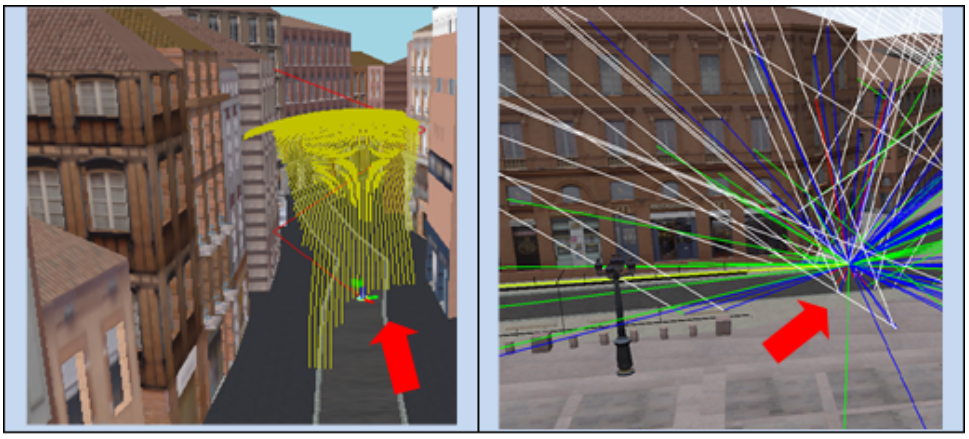

FIGURE 4.1: Left: Mask sphere showing the masking impact. Right: Example of multipaths reception in an urban area - Red arrows point to the location of the receiver

4.2.1 SE-NAV deterministic simulator of GNSS reception in urban environment

SE-NAV simulates the propagation of GNSS signals in urban environment. Examples of the simulated environments are shown in Figure 4.1. This software, developed by the company OKTAL Synthetic Environment, embeds a graphic processing unit (GPU) raytracing kernel to compute the masks and the multipath (reflections, transmission and diffractions) generated by the objects/buildings near the receiver. Next, the details of SE-NAV simulator is presented.

a. Raytracing and BVH optimization. A Raytracing algorithm consists in finding the intersections between a ray and a defined geometry as fast as possible. SE-NAV uses geometries made of a large number of triangles. For high frequency asymptotic electromagnetic (EM) simulation, a large number of such intersections has to be computed. A very naive approach would require N*M ray-triangle intersections, N being the number of triangles and M the number of rays. Except for very simple situations, this cost is prohibitive, hence the need for acceleration methods. Among these methods, the Bounding Volume Hierarchy (BVH), an object-based subdivision structure is chosen (Figure 4.2). The principle is to build a tree-structure of a set of triangles. Each triangle is stored in a leaf of the tree. Each internal node stores for each of its children the bounding volume of the descendant triangles. A bounding-volume hierarchy is built according to the location of each triangle of the database, trying to minimize the extent and the number of nodes.

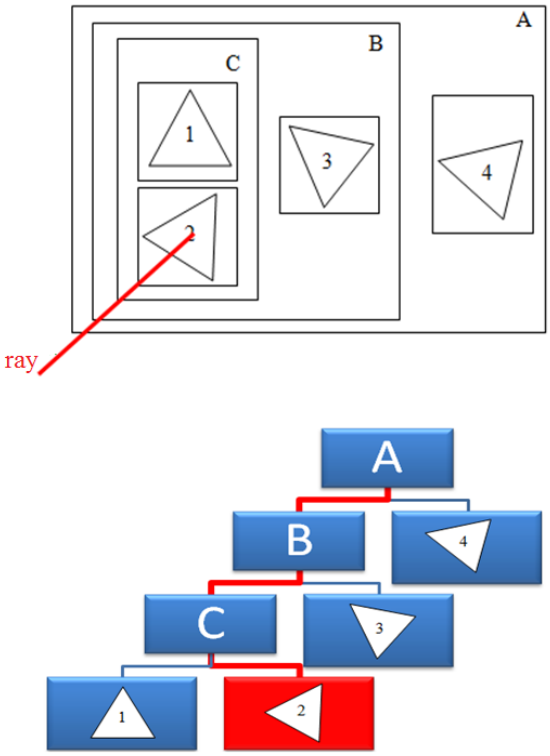

FIGURE 4.2: Top: Triangle sorting. Bottom: Bounding volumes hierarchy

Once the structure is built, the intersection between a ray and the scene is done by traversing the tree recursively from the root. A child is processed only if the ray intersects its bounding volume. If the two children are traversed, the process is repeated first on the children closest to the ray origin. If the child is a leaf, the ray is intersected with all triangles contained in the leaf, potentially updating the intersection data. Traversal is stopped as soon as no intersection closer than the current one can be found. This method decreases drastically the ray-scene intersection computation time, computing only O(log(N)*M) intersections instead of N*M for N triangles and M rays.

b. GPU Resources. The Raytracing kernel has been developed in CUDA 4.0 language and uses the GPU resources in order to compute masks and multipath in record times (1000 times quicker in optimal configurations). SE-NAV uses GPU to find rays and CPU to filtrate them according to Geometrical Optics rules.

SE-NAV runs on NVIDIA Graphics board series 8 or later. The video memory shall be greater than 512 Mo and the compute capability rate greater than 1.1 (atomic operations shall be allowed).

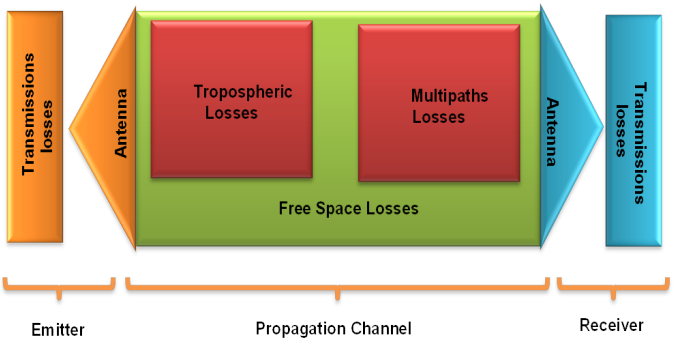

FIGURE 4.3: Link budget

c. Model Outputs. SE-NAV uses Geometrical Optics (GO) to model reflections and transmissions and Uniform Theory of Diffraction (UTD) to detect signal's diffractions on the edges of the objects. As SE-NAV uses a deterministic method, the software can calculate and display the geometry of each ray reaching the receiver and then computes the total link budget and errors needed to forecast the local pseudorange. Thanks to the different DOPs provided as an output and also the visibility of the constellation (LOS, NLOS, and hidden satellite), the user can assess the availability of the navigation system and its performance within a given area.

SE-NAV computes a link budget and provides in output the received power per multipath and per channel. To do so, SE-NAV assesses the main source of attenuations during the propagation of the signal in the environment (Figure 4.3).

SE-NAV takes into account cabling losses, antenna gain (satellite and receiver), free space losses, tropospheric losses and multipath losses. However, with the version used in this work, the receiver specific parameters such as the cabling loss and antenna are not accessible for users to change. SE-NAV computes the complete field (modulus and phase) and therefore models interferences and fading effects. SE-NAV also provides Signal-To-Noise Ratio and composite power (i.e. integrated power for a given channel).

4.2.2 Reliability of 3D model for reception state prediction and NLOS bias prediction

The reliability of the computed position depends on the reliability of the PR measurements model. In this work, a 3D model is also included in the position estimation process.

Therefore, the distribution of errors on the final navigation solution does not only depend on the errors affecting the PR measurements (such as the clock bias, ephemeris, ionospheric delay, tropospheric delay and etc.) but also on the errors affecting the quality of the 3D model and its decision of the NLOS/LOS situation of the received signals. Hence, it is crucial to determine the quality of the SE-NAV LOS/NLOS identification as well as the impact of this decision on the error modeling. Among the factors affecting the quality of a 3D model include the accuracy of geometrical representation (shape, orientation, location and etc.) of the model vis-a-vis the actual environment and the detail features of the modelled objects to represent the effects on the propagating signals such reflection and diffraction. It follows that this quality of the 3D model characteristics also affects its decision of LOS/NLOS receptions of the GNSS signals.

While there have been several works such as in [62, 191] where prediction of satellite availability based on 3D model were used, there has not been many works studying the LOS/NLOS state of reception based on 3D model. One of the approaches in categorising the LOS/NLOS state of reception is to base on the received C/No [9]. Hence, this work compares the similarity or the conformity of state reception prediction provided by the 3D model with that one obtained using the C/No value, i.e. to check whether the prediction of the 3D model is consistent with the C/No prediction. An example of conformity is when SE-NAV predicts a received signal as a NLOS and the C/No of that signal is below the set threshold (a value between 40 and 30 dB-Hz).

It is acknowledged that a 3D model can only approximate rather than simulate a perfect reconstruction of the real received signals. First of all, there is an unquantified variability of the real-life surrounding environment of the receiver as compared to the static virtual representation of the reception environment. For example, there are non-permanent objects such as vehicles and people that can affect signal propagation but are not included in the 3D model. Over the time, even the foliage of the vegetation changes and so does the building surface attributes. In fact, to acquire modelling accuracy of the building structures and materials in terms of their effects on the GNSS signals is itself a challenging feat.

The complexity of the electromagnetic signal propagation yet pose another constraint on the 3D model. Deterministic models based on Geometrical Optics (GO) and Uniform Theory of Diffraction (UTD) require detailed geometrical and morphological information

on the propagation environment. In urban scenarios, ray propagation is affected by multiple interactions with scatterers. Whenever a ray is modelled with a reflection or diffraction, there is some error associated with the model's prediction due to inaccurate representation of material properties or dimensions of objects in the environment. For rays that are modelled by multiple reflections, these errors tend to accumulate, making the model's predictions even less accurate. Furthermore, the effect of the actual antenna and receiver on the received signal, more often than not, is unavailable to be included within the 3D model. All of these introduce errors in the PR prediction by the a 3D model.

For the reasons above, in the work of [8], the authors investigated the validity of using a 3D GNSS simulation model, particularly SE-NAV, to predict the PR measurements biases. From the comparison between the biases of the measured PR using referenced position and the predicted biases using the SE-NAV 3D model, the work concludes that the simulated PR errors are quite consistent with the real errors. In addition, the work also considered the effect of positioning estimation errors on the robustness of the SE-NAV simulations by adding some noise with uniform distribution $[-8m; +8m]$ to the reference trajectory. Their results indicates that the simulated PR errors are still consistent with the real ones at almost 60% of the time.

In this chapter, apart from predicting the reception state, the 3D model is also utilized to predict the NLOS bias statistic, which is to be used for the PR corrections. In this case, how close the predicted bias value is to the measured NLOS bias will affect the quality of the final computed position. The measured NLOS bias is calculated from the difference between the measured PR and the referenced PR when the state of reception is determined to be in NLOS by SE-NAV. Whereas, the predicted NLOS bias is obtained from the signal path delay calculated by SE-NAV using the position estimates computed by the receiver when the state of reception is determined to be in NLOS by SE-NAV.

Whenever there are many reflected components of a signal, SE-NAV provides the path delays for all of the components. For the case of a LOS signal, the delay value for the direct signal component is provided as 0. In the case of a NLOS reception, all the received signal components would have path delays since there is no direct signal component. In this work, when there are more than one reflected signal components exist in the NLOS case, an optimistic perspective is chosen when deciding on the predicted bias value in the

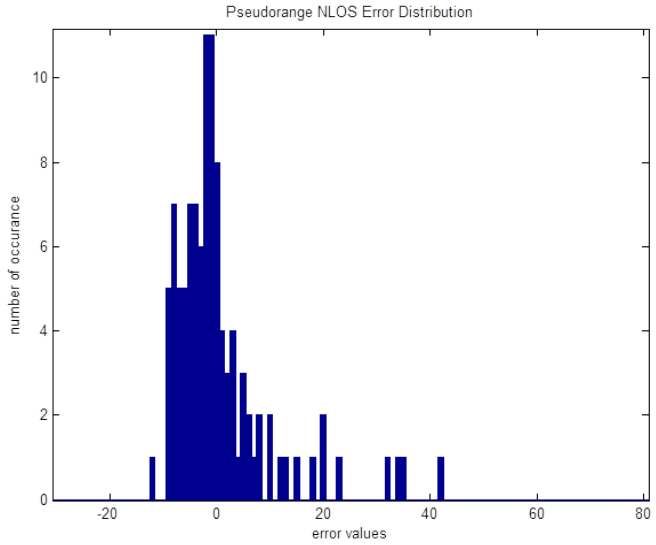

FIGURE 4.4: PR error distribution in the presence of NLOS in urban environment (the Capitole, Toulouse)

NLOS reception. It is assumed that the receiver will acquire the non-direct component with the shortest delay since it is likely that the shortest delay component will have the highest power, i.e. the least attenuated when it arrives at the receiver.

4.3 Proposed approach for positioning with NLOS signals

4.3.1 LOS/NLOS pseudoranges measurements model

Over a relatively long observation window, the NLOS measurements error has been observed to have a non-Gaussian distribution and may be approximated by a mixture of Gaussian distributions [9]. As illustrated in Figure 4.4, this NLOS error distribution is obtained based on referenced positions trajectory in the Capitole, downtown Toulouse and consist of 107 samples. The data is collected using a ublox 4T receiver mounted on a vehicle. The mean and variance of each Gaussian component may be computed iteratively inside the estimation algorithm.

However, for a short observation window, the most common approach consists of modeling the pseudorange error as Gaussian distribution with a time-varying mean and variance [10] as illustrated in Figure 4.5. Here, the error distributions of the same satellite are shown within different 40 seconds windows where it can be seen their change in the mean and variance.

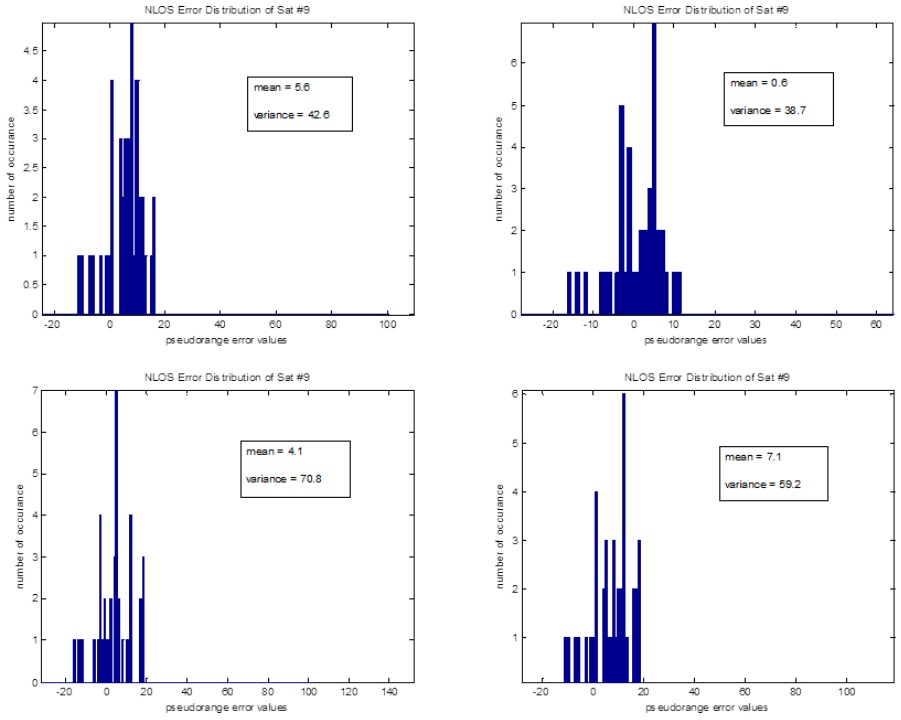

FIGURE 4.5: PR error distributions in urban environment (the Capitole, Toulouse) obtained from a same satellite in various observations periods of 40 seconds

In the NLOS case, the presence of only reflected signals introduce a jump on the mean value as a result of the extra distance. In the case of degraded LOS path, an additional variance is introduced as an increase of the uncertainty on the direct path. Accordingly, these effects of the degraded LOS noise and NLOS bias on the PR measurements error are modelled separately.

For the case of multipath degraded LOS reception, implementing the signal-to-noise ratio based variance model, i.e. the SIGMA-ε model, would improve the positioning accuracy in the urban environment [11, 12]. The covariance matrix of the observation can be constructed as $\mathbf{R} = diag(\sigma_1^2, \sigma_2^2, \ldots, \sigma_k^2)$ where

$$\sigma_k^2 = a + b.10^{\frac{-C/No}{10}} \tag{4.1}$$

and σ_k^2 is the variance of the k^{th} observation. The constants a and b are determined depending on the environment and user equipment, which may be computed a priori off line using PR measurement errors and their C/No values over a certain epoch. In [12], the confidence level of 3σ or 99.7% was used for the estimation of the constants with measurement data collected within 12 hours of observation.

The PR measurement model is commonly expressed as the true distance d between the receiver and satellite, plus with several other types of errors. For each satellite at k^{th} point in time, the pseudorange ρ can be written as,

$$\rho_k = d_k + c.dt_k^{sat} + c.dt_k^{rcv} + atmo_k + m_k + \epsilon_k \tag{4.2}$$

with $c.dt$ represents clock offset (satellite or receiver), $atmo$ represents both the ionospheric and tropospheric delays. m is the multipath delay and ϵ is the receiver noise. In harsh urban environment, m is the major contributor of error and could consist of the mixed LOS/NLOS conditions. Once the ionospheric, tropospheric and clock errors are compensated, the model is reduced to the following expression,

$$\rho_k = d_k + m_k + \epsilon_k \tag{4.3}$$

To further illustrate the LOS/NLOS conditions in the multipath, we may rewrite the equation as [13]

$$\rho_k = d_k + m_k + b_k w_k \tag{4.4}$$

where

$$m_k = \begin{cases} 0, \text{ if LOS condition} \\ m_{NLOS}, \text{ if NLOS condition} \end{cases} \tag{4.5}$$

$$b_k = \begin{cases} \sigma, \text{ if LOS condition} \\ \sqrt{\sigma^2 + \sigma_{NLOS}^2}, \text{ if NLOS condition} \end{cases} \tag{4.6}$$

and w_k is the centralized zero mean white Gaussian noise $\mathcal{N}(0, 1)$. In other words, the NLOS is characterized by its mean, m_{NLOS} and it's variance, σ_{NLOS}^2. Thus, in the case of NLOS, the affected measurement becomes

$$\rho_k' = \rho_k - m_{NLOS} = d_k + b_k w_k \tag{4.7}$$

and

$$b_k = \sqrt{\sigma^2 + \sigma_{NLOS}^2} \tag{4.8}$$

4.3.2 Integration of the 3D-based bias estimation in the PVT Kalman Filter

In this work, the well-established Extended Kalman Filter (EKF) is chosen as the positioning estimator for post-processing the measured PRs. Based on the measurement model in equation 4.4, the state equation can be provided by:

$$\mathbf{X_{k+1}} = \mathbf{F}\mathbf{X_k} + \mathbf{v_k} \tag{4.9}$$

where $\mathbf{X}$ is the state vector, $\mathbf{F}$ is the state transition matrix and $\mathbf{v}$ is the process noise with zero mean Gaussian distribution.

For the purpose of this work, a nearly constant velocity is assumed for the kinematic model since there is no significant acceleration in the vehicle movement in urban environments. Hence, from the discretized nearly constant velocity model [25,26], the state vector is:

$$\mathbf{X_k} = [p_k, \dot{p}_k, ct_k, \dot{ct}_k]^T \tag{4.10}$$

where p_k is the x_k, y_k, z_k position coordinates, $\dot{p}_k$ are the velocities, ct_k is the clock bias and $\dot{ct}_k$ is the clock drift.

Based on a constant velocity assumption, the state transition matrix is given as:

$$\mathbf{F} = \begin{bmatrix} \mathbf{I} & T_s\mathbf{I} & 0 & 0 \\ 0 & \mathbf{I} & 0 & 0 \\ 0 & 0 & 1 & T_s \\ 0 & 0 & 0 & 1 \end{bmatrix} \tag{4.11}$$

where $\mathbf{I}$ is the identity matrix and T_s is the sampling period.

The discrete-time process noise is given as:

$$\mathbf{v_k} \sim \mathcal{N}(0, diag(\mathbf{Q_1}, \mathbf{Q_2})) \tag{4.12}$$

where

$$\mathbf{Q_1} = \begin{bmatrix} \frac{T_s^3}{3}\sigma_a^2\mathbf{I} & \frac{T_s^2}{2}\sigma_a^2\mathbf{I} \\ \frac{T_s^2}{2}\sigma_a^2\mathbf{I} & T_s\mathbf{I} \end{bmatrix} \tag{4.13}$$

and

$$\mathbf{Q_2} = \begin{bmatrix} \sigma_b^2 T_s + \frac{T_s^3}{3}\sigma_d^2 & \frac{T_s^2}{2}\sigma_d^2 \\ \frac{T_s^2}{2}\sigma_d^2 & T_s\sigma_d^2 \end{bmatrix} \tag{4.14}$$

The clock bias variance σ_b^2 and clock drift variance σ_d^2 depend on the quality of the receiver, while the acceleration variance σ_a^2 depends on the motion of the receiver.

Based on the prediction from the 3D model of the LOS/NLOS reception condition of each satellite, the PR measurement and its variance are treated accordingly. If the measured PR is predicted as a LOS signal, its covariance is adapted to the value using equation 4.1. However, if the measurement is predicted as a NLOS reception, the NLOS bias m_{NLOS} is predicted from SE-NAV where it provides the delayed distance of the NLOS ray tracing as compared to the straight line ray tracing distance from satellite to receiver. Then, the bias is subtracted from PR measurement and the NLOS variance σ_{NLOS}^2 is included in the covariance as described by equations 4.4 and 4.7. Therefore, the observation equation can be formulated as,

$$\mathbf{z_k} = \mathbf{h}(\mathbf{X_k}) + \mathbf{m_k} + \mathbf{b_k w_k} \tag{4.15}$$

where $\mathbf{h}$ describes the non-linear dependence of the observations on the state. The observation covariance is,

$$\mathbf{b_k w_k} \sim \mathcal{N}(0, \mathbf{R}) \tag{4.16}$$

where $\mathbf{R}$ depends on the LOS/NLOS condition of the reception state.

Usually, the values for the bias and variances of NLOS errors are obtained based on the PR error distributions. In this study, the PR error values are initially calculated based on the difference between the measured PRs vis-à-vis the reference PRs which are acquired by computing the distance from the satellite positions and the reference positions. However, such approach would be limited for positioning applications with a fixed and predetermined route.

In an attempt to make the application to be less restrictive, this work further considers the PR errors values generated from the predictions of the 3D-model. The delays of the PR ray-tracings from the 3D-model are treated as the errors of the PR measurements.

FIGURE 4.6: Reference trajectory in Toulouse, France.

4.3.3 Data collection, equipment and software

In this work, the measurements were obtained from a trajectory around Toulouse, France (Figure 4.6). The area represents a deep urban environment with narrow streets and buildings alongside the streets. The GPS receiver used for the PR measurements is the u-blox LEA-4T receiver while the NovAtel SPAN system is used for the reference trajectory. The measurement was sampled at 1 Hz. All data processing was accomplished using Matlab and SE-NAV.

4.4 Results and analysis

4.4.1 Estimation of Variance (C/No) Model Parameters

In order to implement the SIGMA-ε variance model as in equation 4.1, the values for parameters a and b have to be determined. This is achieved by fitting the *Standard Deviation*$= \sigma_k = \sqrt{a + b.10^{\frac{-C/No}{10}}}$ to the plot of absolute pseudorange errors vs. C/No. The standard deviation is simply the square root of the variance in equation 4.1 and the absolute pseudorange errors are the magnitude of the pseudorange errors. In this equation, when b is positive, the value of sigma improves as C/No increases. The magnitude of b represent the rate of change (slope) in the relation between sigma and

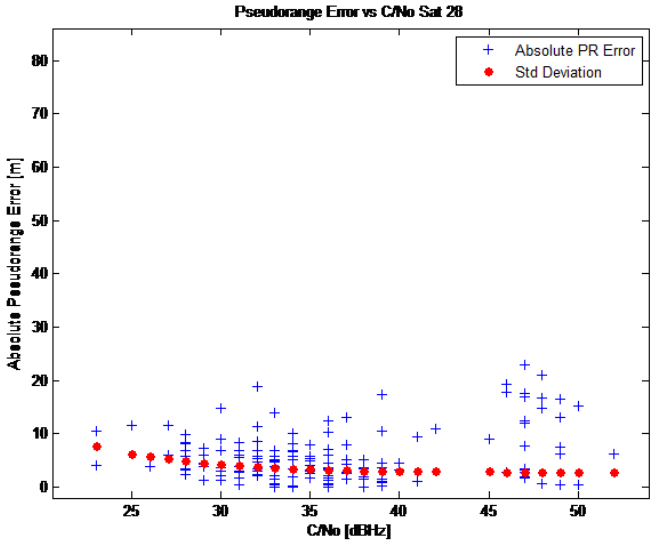

FIGURE 4.7: C/No variance model

C/No. Figure 4.7 shows an example of the plot and Table 4.1 lists all the determined a and b values per visible satellite during data collection. It is noted that during this early stage of research, the number of sampled measurements is rather small. Nevertheless, they are sufficient for the purpose of this part of the works. It is observed that for several satellites, there are negative values of the constant b which reflects a degradation of sigma for higher C/No. This situation affirms the issue of the difficulty of using only C/No as a measurement quality indicator in urban environments especially with this short data. As has been highlighted in Chapter 2, signal receptions in urban environments are degraded by multipath and NLOS that it is possible for erroneous signal to have high C/No. Based on these results, it is observed that the model can be applicable for the range of C/No between 25 to 40. However, a more exhaustive measurements and longer data are needed to verify this observation.

4.4.2 NLOS/LOS prediction by SE-NAV

To differentiate between LOS/NLOS reception is indeed a challenging task. In this work, the LOS/NLOS prediction by SE-NAV is compared to the received C/No values of the PR measurements. Threshold values of 40, 38 and 30 dB-Hz are used for these comparisons. Percentages of agreement or conformity between SE-NAV prediction and C/No values are listed in Table 4.2. It can be seen that the threshold < 40 dB-Hz has the highest conformity between SE-NAV prediction and C/No.

Sat #	Number of samples	*a*	*b*
5	164	164	-1 x 10^4
8	127	115	1 x 10^4
9	152	127	3336
10	132	171	2 x 10^4
15	165	136	-1 x 10^4
17	24	325	1339
18	114	48	2 x 10^4
24	18	982	- 4649
26	161	55	-1 x 10^4
27	155	29	-7603
28	162	8	1 x 10^4

TABLE 4.1: List of parameters for variance (C/No) model obtained by curve fitting with the absolute PR errors

Sat PRN, Elevation	Threshold < 40 dB-Hz	Threshold < 38 dB-Hz	Threshold < 30 dB-Hz
5, 35°	61 %	45 %	2 %
8, 26°	98 %	95 %	48 %
9, 26°	89 %	87 %	54 %
10, 12°	86 %	82 %	75 %
15, 65°	64 %	47 %	5 %
17, 9°	100 %	100 %	62 %
18, 17°	100 %	100 %	72 %
24, 4°	100 %	100 %	100 %
26, 43°	91 %	80 %	14 %
27, 40°	94 %	93 %	38 %
28, 48°	93 %	83 %	15 %
Total	**89 %**	**83 %**	**44 %**

TABLE 4.2: Conformity between SE-NAV LOS/NLOS prediction and the C/No values

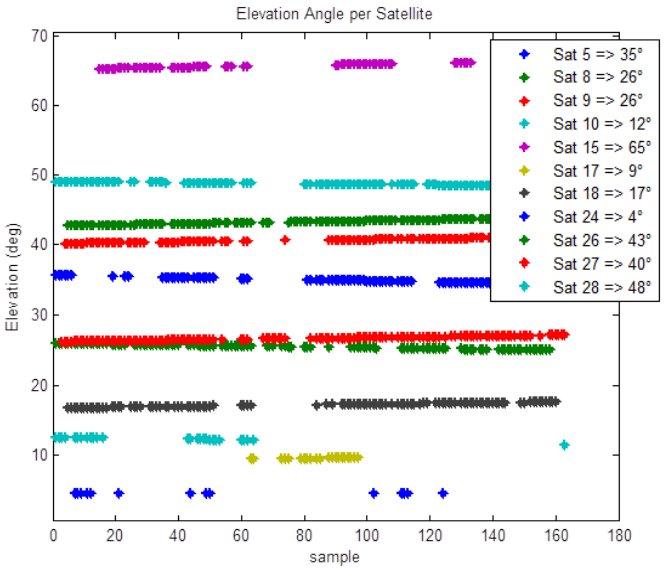

FIGURE 4.8: Elevation angle per satellite

These C/No values may also be cross referenced with the elevation angle of the satellites (Figure 4.8) since the signals of the lower elevation satellites are more likely to be received as NLOS in the urban environment as compared to those of the higher elevation ones. In Table 4.2, satellites with lower than 26^o elevation tend to be the satellites with higher agreement with the SE-NAV LOS/NLOS prediction. In other words, the prediction of LOS/NLOS reception by the 3D model is more similar to the prediction based on C/No when the satellites elevation is low as opposed to when the satellite elevation is high.

4.4.3 Results of the estimated position

As a base of comparison, the error sequence of position estimation with NLOS bias correction is plotted against the error sequence of position estimation using the variance (C/No) only (i.e., without considering LOS/NLOS reception). Figure 4.9 shows the comparison of a 3D position estimation errors while Figure 4.10 and 4.11 are their respective position error plots in ENU format.

From Figure 4.9, it can be seen that the estimation with NLOS bias correction was generally better than the performance of the position estimation using only the variance (C/No) model. After about the 100th sample it can be said that both estimators seemed to converge on more or less of equal performance at the end.

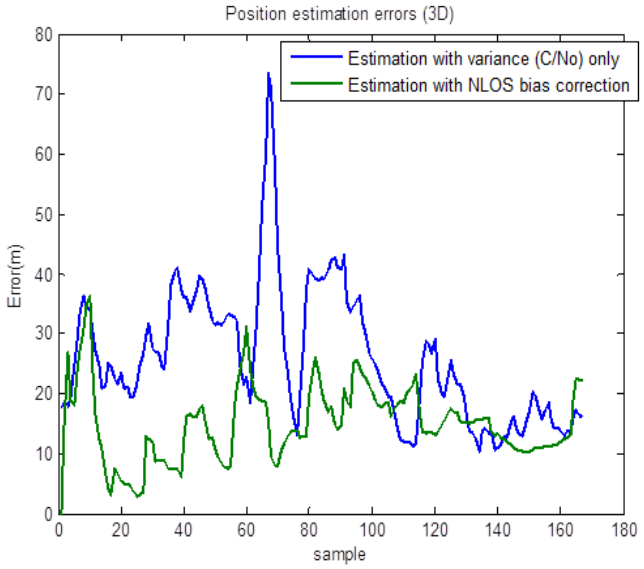

FIGURE 4.9: Error of position estimates in 3D

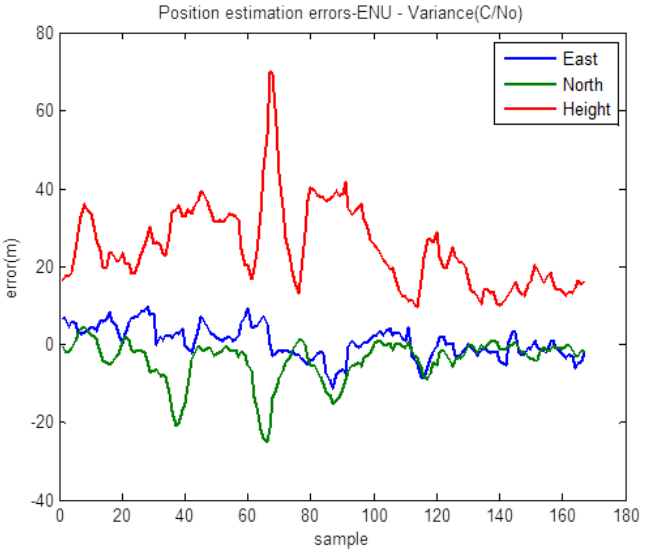

FIGURE 4.10: Error of position estimates using variance model

When comparing their performance in the ENU format, it is obvious that both of the error patterns of the two position estimation approaches are strongly influenced by their error estimation in the height direction. If the height error is discounted, their performance can be compared in the X-Y plane (Figure 4.12) where their performances are much better. The estimation with bias correction was able to reduce several large error values that exist in the estimation with variance (C/No) around the 37th, 66th and 87th samples.

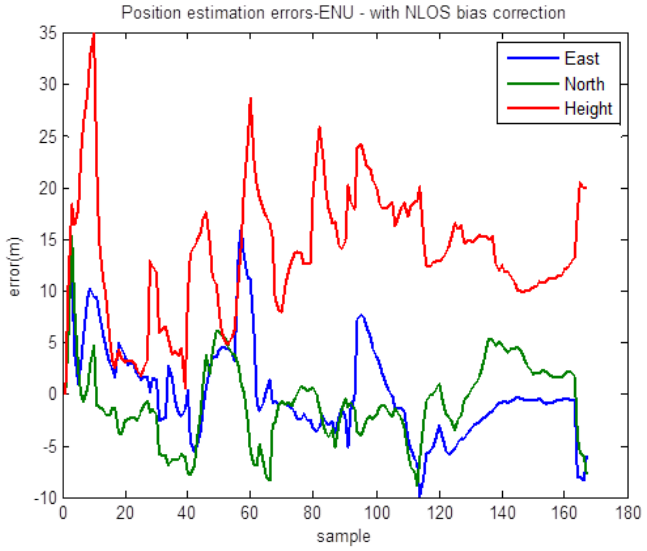

FIGURE 4.11: Error of position estimates with NLOS bias correction

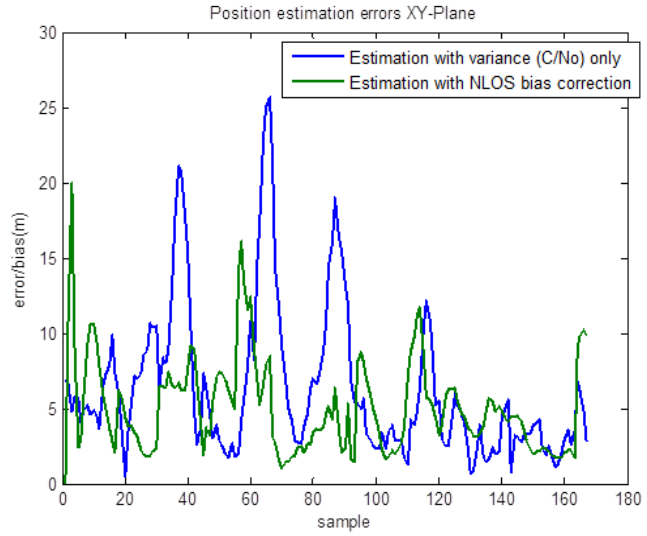

FIGURE 4.12: Error of position estimates in X-Y plane

4.4.4 Bias prediction by SE-NAV

Apart from predicting the LOS/NLOS reception, this study also attempts to use the 3D model to predict the NLOS bias. The predicted NLOS bias is calculated by SE-NAV from the ray tracing path delay based on the receiver estimated position when the state of reception is predicted by SE-NAV to be in NLOS. Whenever there are several reflected components of the ray tracings, the shortest delay is chosen under the assumption that it has the highest power when reaching the receiver. Figure 4.13 shows the comparison of the measured bias versus the predicted bias for satellite 5, 8 and 28. The difference

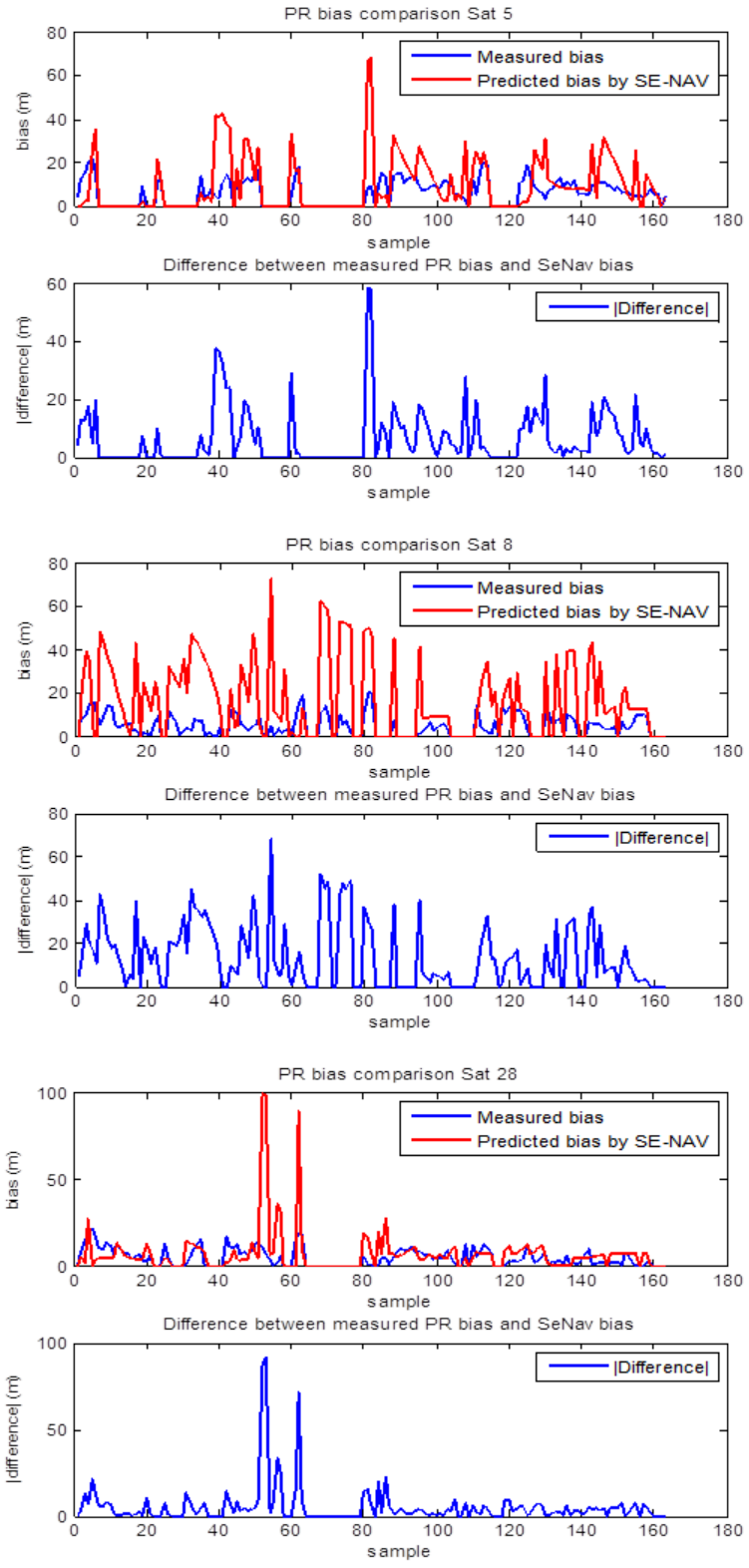

FIGURE 4.13: Comparison of measured NLOS bias vs. predicted bias

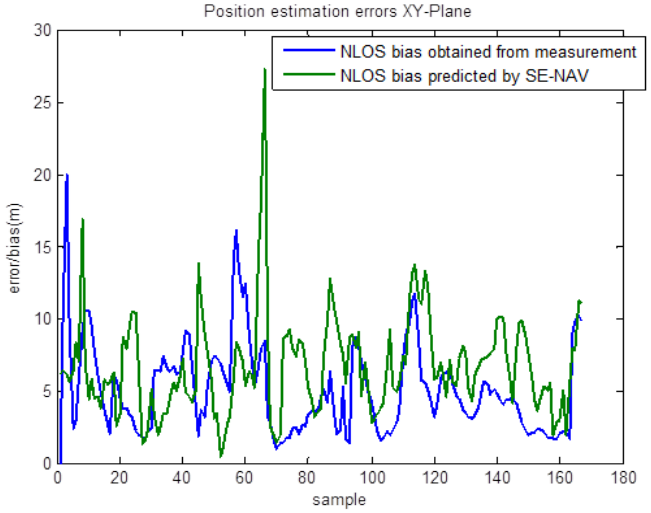

FIGURE 4.14: Position errors - measured NLOS bias against SE-NAV predicted NLOS bias

between them are also plotted for the three satellites. The measured bias is computed using the reference trajectory of the positions. The comparison shows that while there is some similarity in the patterns, the values of the bias are quite different between them. Further research could be pursued in order to improve NLOS bias prediction by the 3D model.

Figure 4.14 is the position error comparison between the positions estimate using measured bias for PR correction against the positions estimate using bias predicted by SE-NAV for the PR correction. The plot is in the XY plane to discount the effect of the estimation error in the height direction. Despite the difference between their bias values as indicated in Figure 4.13 before, their positioning performances in XY plane are quite similar in general. This effect is due to the projection of range biases onto the position domain which is also influenced by the satellites constellation geometry. The difference of the predicted measurement biases may also be contributed to other real objects in the surrounding of the receiver which are not taken into account in the 3D model.

4.5 Conclusion

This work proposed the utilization of 3D model in predicting the LOS/NLOS reception state. In addition, the 3D model is also used to predict the NLOS bias of the measurements. These simulated information is used for the correction of the PR error

according to the LOS or NLOS case and then processed in the PVT computation algorithm. The ability of the 3D model to predict LOS/NLOS was found to be encouraging when compared with other indicators such as C/No and satellite angle of elevation.

On the other hand, when comparing the bias predicted by the 3D model with the biases computed using the reference trajectory, the ability of the 3D model to predict the NLOS bias was deemed modest and not concluding for the short processed data. Further research and analysis are required to validate the quality of the predictions by 3D model. Because the bias prediction depends on the changing environment and other factors such as inaccurate geometrical and morphological modelling and the complexity of electromagnetic signal propagation modelling which are described in section 4.2.2, the predicted bias did not necessarily match the actual bias. Furthermore, since the predicted bias values are calculated based on inaccurate or even erroneous position estimates, the ray tracing path would not be truly representative of the actual signal propagation path. Hence, the ray tracing delay would also be unrepresentative of the actual signal propagation path delay. Even so, when the predicted biases were utilized for PR corrections in position estimation, the result showed that the positioning errors are generally almost similar to those calculated using the measured bias computed from the reference trajectory.

Therefore, in term of the bias prediction, other technics of exploiting better the 3D information need to be developed. In general, the awareness of significant environment change need to be detected and relevant actions should be taken. For example, in a situation where the signal is being blocked a big vehicle, the 3D model will not function correctly and therefore should not be employed. It should be highlighted also that OKTAL-SE is actively pursuing to improve the reliability of the 3D model such as by gathering more data and collaborating in various researches with others.

Chapter 5

Measurement Reliability via Pseudorange Prediction Using a Hybrid Approach

5.1 Introduction

For geolocalization-based applications and services in urban environments, achieving reliable positioning is difficult. Hence, quality monitoring at several levels and in both range and position domains are highly recommended [45, 124]. Since reliable GNSS positioning depends on reliable measurements and good satellite geometry, this chapter investigates an approach of checking the measurement reliability by predicting the PR using a hybrid approach.

Range errors are not directly observable without a reference position, therefore PR residuals have been used instead to represent the range errors. The residual is obtained by taking the difference between measured and predicted PRs. The predicted PRs are usually calculated based on the estimated position. However, in multiple bias situations such as in urban environments, residual becomes less representative of the actual PR error as opposed to in the situations of a single PR fault [59, 151]. Therefore, hybridization with other trusted sensors is investigated to ascertain whether the residual can perform better in multiple bias situation with hybridized estimator. Many works on combining GNSS with other sensors have been done such as in [129, 195–200]

For land vehicle navigation, dead-reckoning (DR) sensors are usually used together with the GNSS measurements[75, 117, 201]. In this work, the combination of odometer/gyro-1D is chosen as a lower-cost alternative to a good inertial measurement unit (IMU) for assisting a GNSS receiver in severe conditions. The advantage of this navigation system is the simplicity of the integrated navigation algorithm. A mechanical odometer, which is very precise, is used and then provides a reference for the vehicle speed. Coupled with a simple yaw-sensor, a navigator is built and able to predict the GNSS PR measurements.

Then, a PR residual is calculated based on the difference of the measured PR and the predicted counterpart. From these computed residuals, test statistics can be used to detect and identify faulty PRs. To improve positioning accuracy, the identified faulty PRs can be excluded when enough satellites are still available for position fix. If the number of available satellites with reliable observable is no longer sufficient, the faulty PR may be replaced by the predicted one.

As an additional investigation, alternatives to the PR residual are also considered. These residuals are generated from the difference between the measured and predicted user velocity and also from the successive range rates. Overall, this work evaluates the benefit of using odometer and studies its capability for reliability checking.

5.2 GNSS Quality control

In devising techniques for reliability monitoring of GNSS positioning, many factors in real life situations make theoretical analysis difficult and pose constraints on the theoretical models. Therefore, it is recommended that several approaches to be implemented in the monitoring process to include heuristic decision logic in order to deal with faulty measurements [45, 124]. Typically in urban environments, due to the effects of multipaths and NLOS, GNSS signals are often correlated in time, not normally distributed and the effects can grow slowly rather than abruptly. This multipath errors can also correlate among various satellites [45]. Such effects may cause the statistical test approaches (for example, the traditional RAIM) to be not effective as long as its basic assumptions are violated. Hence, additional heuristic tests may prove to be useful in ensuring the reliability of the PVT solutions. Examples of these tests could be a decision based on the SNR, elevation angles of the satellites, number of measurements and their

redundancy or the size of the residuals that can be used as quality indicators of the measurements or the navigation solutions.

An example of using the constellation geometry as a quality indicator of the positioning solution is provided in the work of Sairo et al [202]. They proposed a weighted dilution of precision, called KDOP, as a quality measure in satellite based positioning. KDOP denotes a geometric dilution of precision weighted by user-equivalent range errors (UERE). Of course the premise of this work is that the modelled UERE is assumed to be reliable. Since the lower KDOP value indicates the more favourable geometry, the fault exclusion algorithm choose the subset with the smallest KDOP value:

A satellite sat_i is excluded when KDOP with $sat_i >$ KDOP without sat_i

Contrary to RAIM, there is no need of a threshold value to reject a measurement in this technique. In addition, it was recognized that the positioning accuracy is further improved when KDOP method is combined with another fault detection method which is based on measurement consistency approach [203, 204].

One technique of using residual and the number of available measurements or redundancy to affect the decision on the positioning reliability is demonstrated in the Isotropy-Based Protection Level (IBPL) approach [64]. In the HPL formulation of the IBPL approach which is,

$$HPL = k.|r|.HDOP \tag{5.1}$$

r is the least squares residual vector and k is the proportionality constant which relates the residual size with the state estimation error. The value of k depends on the the number of available measurements with the effect that when measurement redundancy is low, the residuals constitute much less reliable a measure of position errors. As described in [64], the calculated HPL defined here is also a probabilistic bound on the position error taking into account nominal and abnormal measurement errors. However, the IBPL method does not make any hypothesis about the statistical behaviour of the errors of the individual measurements. Instead, it is based on only one hypothesis called isotropy where measurement errors combine in an error vector which can point in any direction (of the measurement space) with the same probability. Nevertheless, it has been recognized by the authors that IBPL needs a good redundancy (i.e. large number of available satellites), thus it is suitable only for open sky applications.

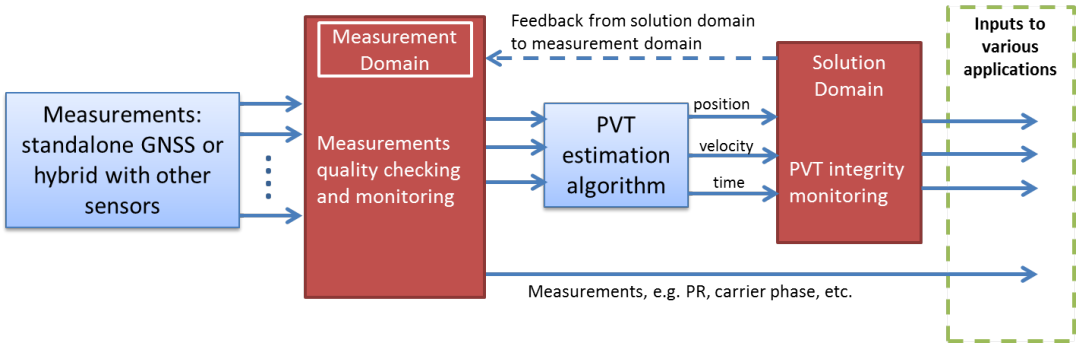

FIGURE 5.1: User level quality checking and monitoring on navigation process

As an overview to visualize where quality checking may be implemented in the navigation process at the user level, figure 5.1 depicts the general flow of the navigation process. It starts from the measurements inputs to the navigation outputs, which then will be used by various applications. The diagram shows that to ensure the reliability of the navigation solutions, quality monitoring may be implemented at the solution domain and also at the measurements domain. The measurement quality checking may also receive a feedback from the integrity status of the navigation solution. Instead of receiving the PVT solutions, some applications may also require the measurements as their inputs to calculate the PVT solution by themselves. In this chapter, with the aid of the DR sensor, the PR and the range rate residuals are used to check the validity of the measurements and the velocity residual is used to monitor the solution.

5.3 Hybrid navigation for vehicle in urban areas

As has been described in Chapter 2, GNSS based positionings for land applications face various challenges especially when operating in urban environments. For example, despite the existence of multi-constellation and high sensitivity receivers, a mobile stand-alone GNSS receiver can never achieve 100% satellite visibility (i.e. able to receive enough number of direct satellite signals to compute PVT solution at all times on all occasions). This is simply because, vehicles traversing in urban areas often pass through tunnels, under bridges and trees or underpasses and uses routes with urban canyon characteristics. Another issue is the weak positioning accuracy due to GNSS signals degradation such as multipath and NLOS. In addition, a GNSS positioning system has low dynamic characteristics in terms of signal frequency and latency. To deal with these issues in land navigation, a multi-sensors solution or multiple sources of information are

utilized. This approach of hybrid positioning essentially aims at benefiting from the complementary characteristics of the different sensors. In general, the purpose of data fusion in hybrid positioning is firstly to fill in the time gaps whenever there is a loss of position estimate and secondly to improve the position estimate by ensemble averaging and exploiting information redundancy (given that the sensors added to the GNSS have better accuracy than the GNSS) [196, 200, 201].

For in-car positioning and navigation technologies , among the common motion sensors used in the complementary systems are inertial sensors or the inertial measurement unit (IMU) (which consist of accelerometer & gyroscope), electronic compass, odometer, velocity encoders and steering encoders [117]. In the vehicles nowadays, there exist a number of modern automotive sensors used for dead reckoning even though originally they were not installed for this purpose. For example, an ABS system uses sensors on each wheel in order to measure the rotational speed by pulse tachometer. The signals produced by these sensors can be integrated by a counter and then used as odometers. A control system of the entire dynamic behavior of a vehicle (ESP) frequently uses a steering wheel angle sensor, a yaw gyro and a transverse accelerometer. Data from these sensors can also be integrated with a localization module [75, 131]. However, the access to these data is not permitted yet by all of the car manufacturers.

The inertial measurement unit (IMU) and odometer (or wheel speed sensor) were the two popular sensors used for dead reckoning [196]. As described in [31, 124, 195, 201], a differential odometry technique is able to calculate the vehicle traveled distance and the heading of the vehicle by integrating the outputs from two odometers, each on the pair of either front or rear wheels of the vehicle. On the other hand, the IMU determines the inertia characterized by the vehicles acceleration and angular velocity in 3 dimensions. Through a process known as INS mechanization, after being rotated into a proper reference frame, the measured acceleration is integrated twice to obtain position information and the integration of the angular rate measurements provides the attitude [205]. Therefore, by using these sensors, the vehicle positioning can be calculated by applying kinematic equations together with an initial position obtained from other source of information. The computations of the travelled distance and the changing of the azimuth allow the determination of a new position from the measurements and the last known positions.

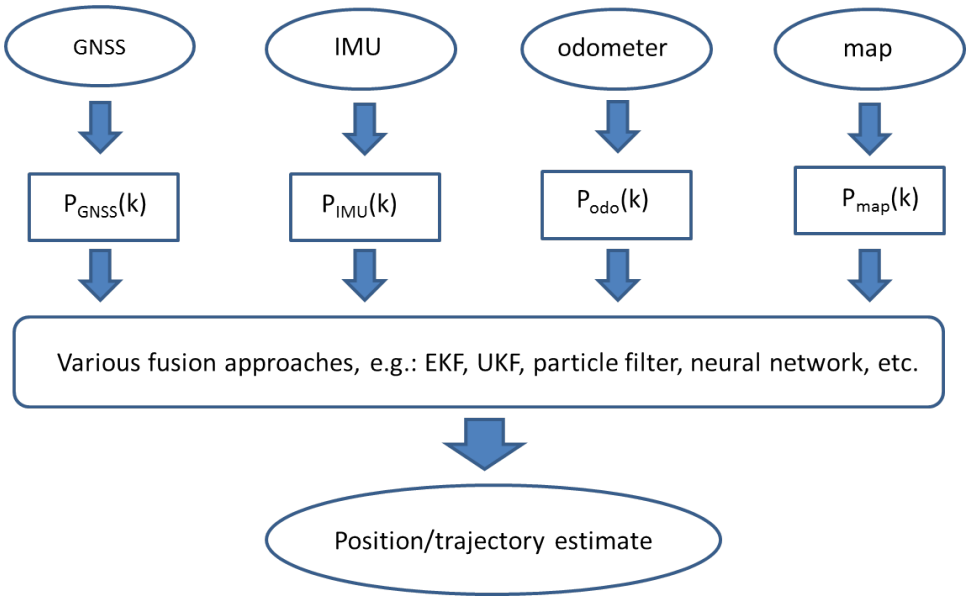

FIGURE 5.2: Overview of multi-sensors fusion approaches for land navigation

For land navigation, most of the time a vehicle travels on a road network. Therefore, the vehicle position must be portrayed on maps. Due to this fact, positioning hybridization also considers the aspect of map-matching. Examples of works that include map-matching in the hybridization are available in [75, 77, 206]. Figure 5.2 shows an overview of the multiple sensors hybrid navigation for land vehicle navigation where $P(k)$ are the position estimates calculated using the relevant sensors.

In implementing the hybrid navigation system for the mass market utilization, cost consideration plays one of the crucial roles. The cost is directly related to sensor configurations and technologies, and the computational complexity. It follows that the final performance of the navigation system is affected directly by vehicle models, sensor configurations and fusion method that is chosen by the designers [207].

5.4 Vehicle models

The choice of vehicle model used in the positioning system has an impact on the system performance. The most popular option is the 2D kinematic model [208]. This model provides the vehicle pose in a two-dimensional reference frame, i.e. two coordinates and yaw angle, in a manner compliant with the non-holonomic constraints. Figure 5.3 refers to the classical 2D kinematic model of a vehicle in a plane. It is assumed in this model that there is no slipping, sliding, skidding or jumping of the road. In the classical 2D

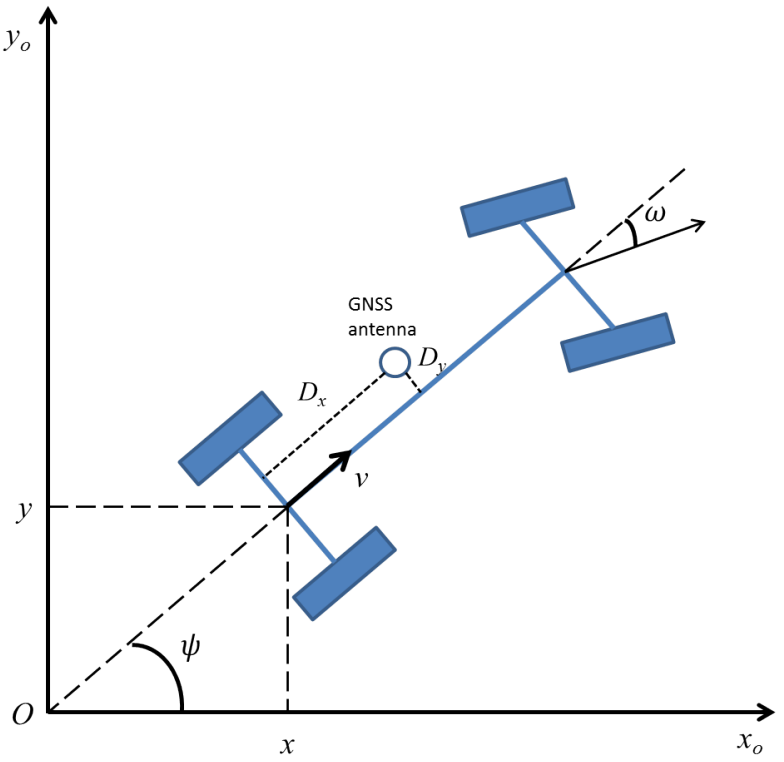

FIGURE 5.3: A vehicle 2D-Kinematics model

model, the trajectory is assumed to be locally linear or circular. The followings are the relevant equations of the kinematic model in discrete time [207]:

$$\begin{aligned} x(k+1) &= x(k) + ds(k)\cos(\psi(k) + \omega(k)T/2) - \omega(k)T(D_x \sin\psi(k) + D_y \cos\psi(k)) \\ y(k+1) &= y(k) + ds(k)\sin(\psi(k) + \omega(k)T/2) + \omega(k)T(D_x \cos\psi(k) - D_y \sin\psi(k)) \\ \psi(k+1) &= \psi(k) + \omega(k)T \end{aligned} \tag{5.2}$$

where:

- $x(k)$ is vehicle position in x coordinate axis
- $y(k)$ is vehicle position in y coordinate axis
- $\psi(k)$ is the yaw or heading angle of the vehicle
- T is the sampling period
- $ds(k)$ is the increment of travelled distance
- $\omega(k)$ is the angular rate

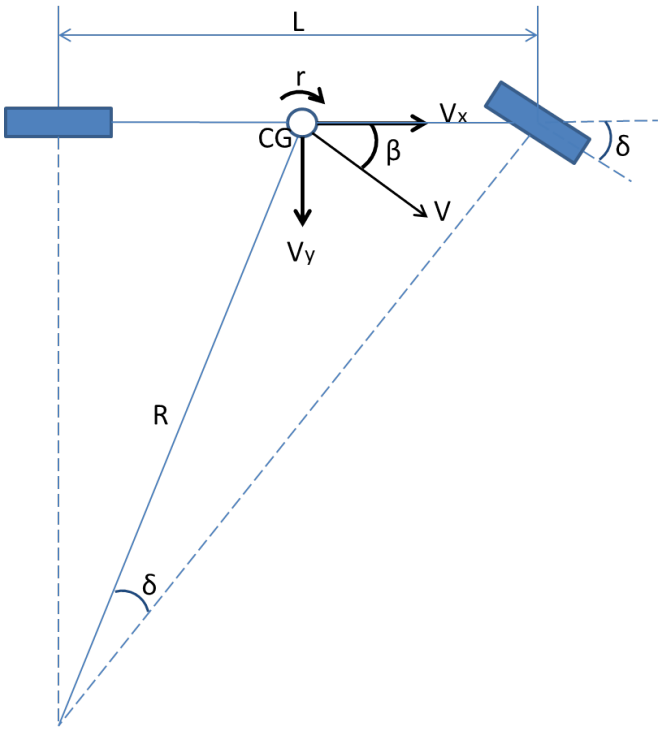

FIGURE 5.4: Kinematic bicycle model

- D_x is the x coordinate of the GNSS antenna in the body frame
- D_y is the y coordinate of the GNSS antenna in the body frame

Another common kinematics model is the bicycle model. In this model, the front is represented by a single front tire and the rear axle is represented by a single rear tire. It assumes that left and right steer angles are the same for front and rear axles. Figure 5.4 shows the kinematic bicycle model. Assuming no slipping, the following equations represent the model kinematics[127]:

$$\delta = \tan^{-1}(\frac{L}{R}) \tag{5.3}$$

$$V = Rr \tag{5.4}$$

$$r = \frac{V}{L}\tan(\delta)\omega \tag{5.5}$$

where:

- CG is the center of gravity of the vehicle
- δ is the steering angle

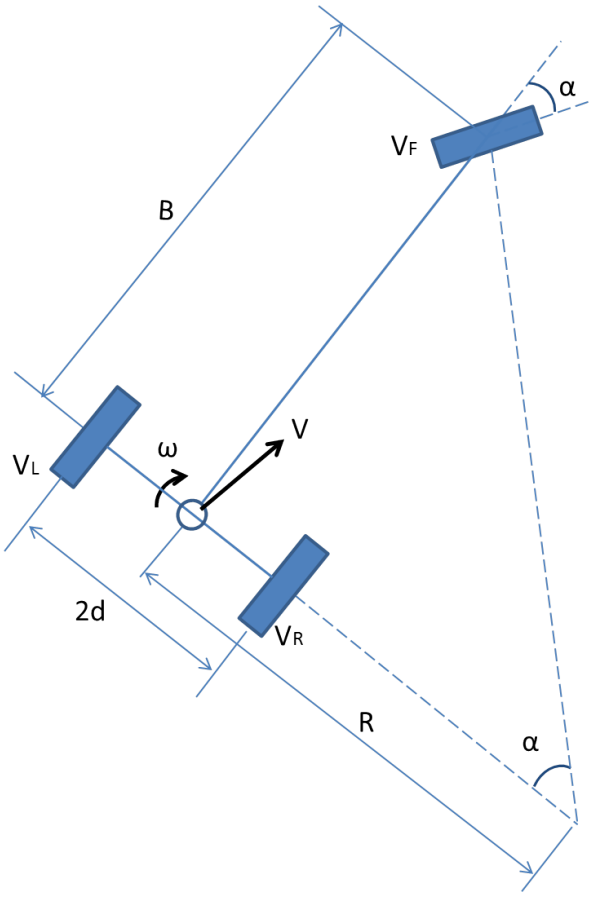

FIGURE 5.5: Kinematic tricycle model

- β is the slip angle
- L is the length between the front and rear tires
- R is radius of turning
- r is the yaw rate
- V is the vehicle velocity
- V_x is the vehicle velocity in x direction
- V_y is the vehicle velocity in y direction

A tricycle model is another frequently used model. Figure 5.5 shows the kinematic tricycle model. Assuming the center of vehicle's reference is at the centre of the rear

axis, the kinematic equations are given as:

$$\omega = \frac{V_F \sin(\alpha)}{B} \tag{5.6}$$

$$R = \frac{B}{\tan(\alpha)} \tag{5.7}$$

$$V = \omega R = V_F \cos(\alpha) \tag{5.8}$$

$$V_L = \omega(R + d) = V + \frac{dV_F \sin(\alpha)}{B} \tag{5.9}$$

$$V_R = \omega(R - d) = V - \frac{dV_F \sin(\alpha)}{B} \tag{5.10}$$

where

- α is the steering angle
- B is the length between the front tire and rear axle
- R is the radius of turning
- ω is the yaw rate
- V_F is the velocity of front tire
- V_L is the velocity of rear left tire
- V_R is the velocity of rear right tire

Other models that can be implemented for the road vehicle are the 3D models which are usually used in aircraft GPS/INS systems [43]. When adopted for land vehicle, the model can be used with the strap-down IMU that provides information on all of the vehicle's degree of freedom. Nevertheless, three-dimensional models require higher computational cost and higher complexity of implementation. Furthermore, the models do not implicitly take into account the vehicle's non-holonomic constraint.

5.5 Sensor configurations

The implementation of hybrid GNSS with full IMU has been described by many books and authors such as in [43, 124, 200, 205]. However, in order to reduce the system cost, hybrid navigation system has been implemented with a reduced inertial sensor system

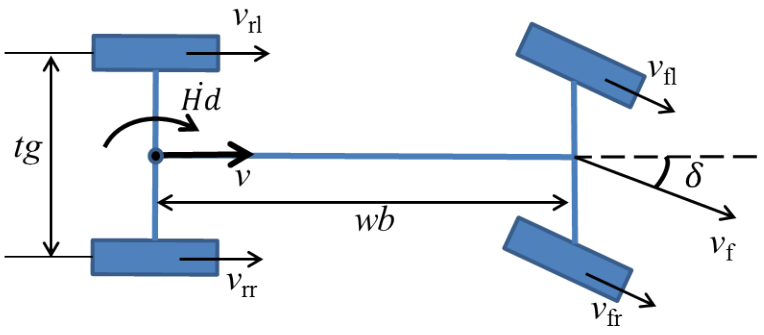

FIGURE 5.6: A vehicle model for odometric dead reckoning

(RISS) [130]. On the other hand, a DR system with odometer offers potentially better benefits as opposed to the totally INS DR system [197]. In implementing a hybridization with odometry, three configurations are possible; differential odometry, odometry with 4 wheels and single odometer with yaw gyro [75]. In principle, DR by odometry is based on the vehicle speed and heading rate. Figure 5.6 and the following equations shows how the vehicle speed and heading rate can be calculated for the cases without a gyro.

The wheel speeds for the rear and front wheels are given as follows [209]:

a) For rear wheels:

$$v_{rl} = v + \frac{tg}{2}\dot{H}d \tag{5.11}$$

$$v_{rr} = v - \frac{tg}{2}\dot{H}d \tag{5.12}$$

b) For front wheels:

$$v_{fl} = (v + \frac{tg}{2}\dot{H}d)\cos(\delta) + \dot{H}d.wb.\sin(\delta) \tag{5.13}$$

$$v_{fr} = (v - \frac{tg}{2}\dot{H}d)\cos(\delta) + \dot{H}d.wb.\sin(\delta) \tag{5.14}$$

where

- v_{fl} : speed of front left wheel
- v_{fr} : speed of front right wheel
- v_{rl} : speed of rear left wheel
- v_{rr} : speed of rear right wheel

- v : vehicle speed (3D speed of centre of rear axis)
- $\dot{H}d$: vehicle heading rate/azimuth rate/yaw rate
- tg : track gauge
- wb : wheelbase
- δ : wheel angle/steering angle

From the speed of the wheels, the vehicle speed and heading rate can be calculated as:

a) Rear wheels:

$$v = \frac{v_{rl} + v_{rr}}{2} \tag{5.15}$$

$$\dot{H}d = \frac{v_{rl} - v_{rr}}{tg} \tag{5.16}$$

b) Front wheels:

$$v = \frac{v_{fl} + v_{fr}}{2\cos(\delta)} - \dot{H}d.wb.\tan(\delta) \tag{5.17}$$

$$\dot{H}d = \frac{v_{fl} - v_{fr}}{tg.\cos(\delta)} \tag{5.18}$$

Those set of equations (equation 5.15 to 5.18) provide the means to implement all the three configurations of odometry based DR. For the 4 wheel configuration, all equations are implemented. However, for the 2 wheelspeed (differential odometry) configuration, only either equations 5.15 and 5.16 or equations 5.17 and 5.18 depending on the implementation of either the rear or the front wheels. Finally, for one odometer implementation with a gyroscope, the wheel velocity is obtained from only one wheel, therefore there is no need of averaging the speeds of left and right wheels. The heading rate measurement is obtained directly from the rate gyroscope (no need to use the formula as in the case of 2 and 4 odometers configurations).

Implementation of differential odometer (2 wheels speed) usually use only the equations for the rear wheels. The 4 wheels configuration use both front and rear wheels equation hence provides redundancy in the measurements. Among them, the configuration with one odometer and a yaw gyro has better precision in the heading as compared to the

hybrid system based on differential odometry [134], and the system with 4 wheels is the most complex one and require the measurement of the steering angle [75]. While the GNSS/odometer/gyro configuration is able to provide reliable positioning most of the time, it performance is lacking for the purpose of high integrity positioning especially when there are plenty of turning movements [207].

5.6 Sensors fusion methods

For the fusion methods of the sensors, system designers usually use Kalman filter or its variation. An example of an implementation using Extended Kalman Filter (EKF) is available in [210] while an implementation using the unscented Kalman Filter (UKF) is given in [211]. More advance filtering techniques are also used for the sensors fusion. They are proposed mainly to improve the weaknesses of the Kalman filter when dealing with a non-linear system or non-Gaussian error distribution. The use of particle filer, which can be considered as a generalization of the Kalman filter when dealing with non-linearities of the sensors or the non-normally distributed signals, are available in [212, 213]. An example of sensors fusion using Gaussian Sum filters is provided in [214]. Alternatively, the sensor data fusion may also be implemented based on the artificial neural networks [215].

The choice of the fusion method affects the computational complexity of the navigation system. In the case of Kalman filter, further choices need to be made, which are whether to use a complete (or total) vehicle model or error state model.

For the implementation with error state model, the integration tend to be done loosely while for the complete vehicle model implementation, the integration tend to be tightly coupled [124]. In general, integration at the PVT solution level is known as loosely coupled and integration at measurement level is considered as tightly coupled. Usually, tight integration produced better performance than the loose integration [124, 129]. However, the tightly integration approach requires accessability to the raw measurements, which may not be available from some low cost receivers.

a. Error state model approach. For the error state model, the state representation of the Kalman filter consists of only error states (i.e. position error, attitude error, etc). The error states dynamics are determined from the linearization of the vehicle

and sensor dynamics around a nominal state. The input observations of the Kalman filter are the differences between the GNSS output and the nominal trajectory, which may be calculated from the measurements of the DR sensors. Then, the error states are used to correct the DR output to improve its positioning accuracy. The following implementation demonstrates the approach using error state model.

Ignoring the antenna distance from body frame centre in the 2D kinematics model, the equations can be simplified as follows [216]:

$$\begin{bmatrix} x(k+1) \\ y(k+1) \\ \psi(k+1) \end{bmatrix} = \begin{bmatrix} x(k) \\ y(k) \\ \psi(k) \end{bmatrix} + T. \begin{bmatrix} \cos(\psi(k) + T\omega(k)/2) & 0 \\ \sin(\psi(k) + T\omega(k)/2) & 0 \\ 0 & 1 \end{bmatrix} . \begin{bmatrix} v(k) \\ \omega(k) \end{bmatrix} \tag{5.19}$$

or in a compact form:

$$\mathbf{x}(k+1) = f[\mathbf{x}(k), \mathbf{u}(k)] + \mu(k) \tag{5.20}$$

where μ is assumed to be a Gaussian white noise.

To implement the approach of error state model, assume that the pose is expressed as the odometric or DR pose plus a small error:

$$\mathbf{x}(k) = \mathbf{x}(k)^{ODO} + \delta\mathbf{x}(k) \tag{5.21}$$

substitute equation 5.21 to equation 5.20:

$$\mathbf{x}(k+1)^{ODO} + \delta\mathbf{x}(k+1) = f[\mathbf{x}(k)^{ODO} + \delta\mathbf{x}(k), \mathbf{u}(k)] + \mu(k) \tag{5.22}$$

Apply first order Taylor linearisation:

$$\mathbf{x}(k+1) \approx f[\mathbf{x}(k)^{ODO}, \mathbf{u}(k)] + |\frac{\partial f}{\partial \mathbf{x}}|_{\mathbf{x}=\mathbf{x}(k)^{ODO}} . \delta\mathbf{x}(k) \tag{5.23}$$

and applying equation 5.20 again:

$$\mathbf{x}(k+1) \approx \mathbf{x}(k+1)^{ODO} + |\frac{\partial f}{\partial \mathbf{x}}|_{\mathbf{x}=\mathbf{x}(k)^{ODO}} . \delta\mathbf{x}(k) \tag{5.24}$$

Therefore, the evolution of the error state is given by:

$$\begin{bmatrix} \delta x(k+1) \\ \delta y(k+1) \\ \delta \psi(k+1) \end{bmatrix} = \begin{bmatrix} 1 & 0 & -v(k)T.\sin(\psi(k)) \\ 0 & 1 & v(k)T.\cos(\psi(k)) \\ 0 & 0 & 1 \end{bmatrix} \begin{bmatrix} \delta x(k) \\ \delta y(k) \\ \delta \psi(k) \end{bmatrix} \tag{5.25}$$

b. Vehicle state estimation-complete vehicle model. On the other hand, the complete vehicle dynamic model may also be used to establish the Kalman state equations. This approach generally results in nonlinear state dynamics. However, this way of modelling the system is considered to be the more robust alternative when dealing with inexact DR measurements [217]. In the work of [199], the implementation of sensor fusion using tightly coupled EKF was performed by means of the complete vehicle model. The integrated sensors are the GNSS and gyroscope plus wheel tick for the DR navigation. The function of the wheel tick is similar to the odometer, i.e. to measure the wheel speed of the vehicle.

From the wheel tick and the gyroscope, the speed v and the heading rate $\dot{H}d$ are derived as follows [199]:

$$v = \frac{T_{raw} 2\pi r}{T_n \delta t} f_T \tag{5.26}$$

$$\dot{H}d = f_\omega(\omega - b_\omega) \tag{5.27}$$

where

- T_{raw} is wheel ticks measured
- r is wheel radius
- T_n is Ticks per wheel turn
- δt is the time period
- ω is the gyroscope reading
- f_T is a wheel tick factor
- f_ω is gyroscope scaling factor
- b_ω is gyroscope bias

The state vector, **x** comprise of the following states:

$$x = \begin{bmatrix} n \\ e \\ d \\ v \\ Hd \\ Pt \\ cb \\ cd \\ f_T \\ b_\omega \\ f_\omega \end{bmatrix} \tag{5.28}$$

where,

- n is vehicle's topocentric North coordinate
- e is vehicle's topocentric East coordinate
- d is vehicle's topocentric Down coordinate
- v is velocity of vehicle
- Hd is heading of vehicle
- Pt is pitch of vehicle
- cb is clock bias of the GNSS receiver
- cd is clock drift of the GNSS receiver
- f_T is wheel tick factor
- b_ω is gyroscope bias
- f_ω is gyroscope scaling factor

Notice that in this approach, the wheel tick factor f_T, gyroscope bias b_ω and the gyroscope scaling factor f_ω are also being estimated by the Kalman filter. The state

prediction of the EKF time update, from epoch $k-1$ to k is given by:

$$\mathbf{x}_k^- = \mathbf{T}\mathbf{x}_{k-1} + \mathbf{B}\mathbf{u} + \mathbf{w} \tag{5.29}$$

where,

- $\mathbf{T}$ is the transition matrix
- $\mathbf{B}$ is the control-input model
- $\mathbf{u}$ is the control-vector (including e.g.wheel ticks)
- $\mathbf{w}$ is the additional process noise (e.g. due to un-modeled dynamics)

Here, the sensor measurements are used within the equations of the EKF time update. The predicted states $\mathbf{x}^-$ then consist of:

$$\begin{aligned}
n_k^- &= n_{k-1} + \bar{v}\cos(\bar{Hd})\cos(Pt_{k-1})\Delta t && (5.30)\\
e_k^- &= e_{k-1} + \bar{v}\sin(\bar{Hd})\cos(Pt_{k-1})\Delta t && (5.31)\\
d_k^- &= d_{k-1} - \bar{v}\sin(Pt_{k-1})\Delta t && (5.32)\\
v_k^- &= v_c && (5.33)\\
Hd_k^- &= Hd_{k-1}^- + \overline{\dot{H}d}\Delta t && (5.34)\\
Pt_k^- &= Pt_{k-1}^- && (5.35)\\
cb_k^- &= cb_{k-1}^- + cd_{k-1}^-\Delta t && (5.36)\\
cd_k^- &= cd_{k-1} && (5.37)\\
f_{T,k}^- &= f_{T,k-1} && (5.38)\\
b_{\omega,k}^- &= b_{\omega,k-1} && (5.39)\\
f_{\omega,k}^- &= f_{\omega,k-1} && (5.40)
\end{aligned}$$

where the mean heading is,

$$\overline{Hd} = Hd_{k-1} + \frac{\overline{\dot{H}d}}{2}\Delta t \tag{5.41}$$

the heading rate is,

$$\overline{\dot{H}d} = f_{\omega,k-1}(\bar{\omega} - b_{\omega,k-1}) \tag{5.42}$$

the current vehicle velocity is,

$$v_c = T f_{T,k-1} \tag{5.43}$$

the mean vehicle velocity is,

$$\bar{v} = \bar{T} f_{T,k-1} \tag{5.44}$$

with,

- T represents the wheel velocity of the current epoch k
- $\bar{T}$ represent mean values of the wheel velocity
- $\bar{\omega}$ represents mean values of gyroscope

Therefore, since both the GNSS and sensor measurements are used in the state vector, a fusion is achieved in a form of a tight-coupling. From the state update equations above, it can be seen that the EKF output the DR solution whenever experiencing GNSS outage. The measurement update matrices are not provided here but may be obtained in [199].

c. Fusing GNSS/DR and map-matching by Particle Filter. On its own, a map-matching is essentially a process of tracking a known or estimated vehicle position in map data with optimal criteria. A comprehensive overview on map-matching may be found for example in [135]. Whenever the map data is fused with other sensors data for determination of the vehicle position, it is called Map Aided Localization. While various research has been done on map aided localization, the work in [77] is described here where it involves the fusion of GNSS, DR and map data by using a particle filter (PF).

The concept of PF is to represent a state by using a set of N samples $\{X_k^i\}_{i=1}^N$ weighted by $\{w_k^i\}_{i=1}^N$. The probability of the state vector $\mathbf{X}_k$ at instant k, given past observation $\mathbf{Y}_{1:k}$ is:

$$p\left(\frac{\mathbf{X}_k}{\mathbf{Y}_{1:k}}\right) \approx \sum_{i=1}^{N} X_k^i . w_k^i$$

In summary, the PF process is as follows:

1. Initialization: Generate N samples or particles for the state vector, X_0^i with equal weight $1/N$.
2. Prediction: Estimate X_{k+1}^i using the model dynamics.

3. Measurement update: Update the weights of particles based on observations Y_k.
4. Normalization of the weights: $w_k^i = w_k^i / \Sigma_{i=1}^N w_k^i$
5. Resampling: To prevent high concentration of probability mass on only a few particles.
6. Cycle end: $k = k + 1$ and repeat step 2.

To fuse GNSS/DR/map data, the state vector is composed of a Cartesian and a Frenet sub-states, $\mathbf{X} = [\mathbf{X}^C, \mathbf{X}^F]$. $X^c = [x, y, \psi]$ where each represents East, North and heading angle at the middle point of the rear wheel axle of the vehicle. $X^F = [l^m, d^m, m]$ respectively represents the values of abscissas and ordinates referred to the lane segment m. Then, a state vector for particle i at instant k is:

$$X_k^i = \left[\begin{array}{ccccccc} x_k^i & y_k^i & \psi_k^i & l_k^{m,i} & d_k^{m,i} & m_k^i \end{array} \right] \tag{5.45}$$

The Cartesian and Frenet representation of a same point are related by:

$$\begin{aligned} x &= x_0^m + \int_0^{l^m} \cos(\tau^m(l^m))dl - d^m \sin(\tau^m(l^m)) \\ y &= y_0^m + \int_0^{l^m} \sin(\tau^m(l^m))dl - d^m \cos(\tau^m(l^m)) \end{aligned} \tag{5.46}$$

where x_0^m and y_0^m are the coordinates of the initial point of the road segment. $\tau^m(l^m)$ is the azimuth angle of the segment at abscissa l^m.

After initialization step, the states are predicted. For the Cartesian sub-states each particle is predicted as follows:

$$\begin{aligned} x_{(k|k-1)}^i &= x_{k-1}^i + \Delta_x^i \\ y_{(k|k-1)}^i &= y_{k-1}^i + \Delta_y^i \\ \psi_{(k|k-1)}^i &= \psi_{k-1}^i + \omega^i \end{aligned} \tag{5.47}$$

where

$$\Delta_x^i = ds^i sinc(\omega^i/2)\cos(\psi^i + \omega^i/2) - \omega^i(D_x \sin(\psi^i) + D_y \cos(\psi^i)) + \delta_x^i \tag{5.48}$$

$$\Delta_y^i = ds^i sinc(\omega^i/2)\sin(\psi^i + \omega^i/2) + \omega^i(D_x \cos(\psi^i) + D_y \sin(\psi^i)) + \delta_y^i \tag{5.49}$$

and

- ω^i : filter input represent angular velocity.
- ds^i : filter input represent traveled distance.
- D_x and D_y : Antenna distance to middle of rear axis in Cartesian coordinates.
- δ_x^i and δ_y^i : errors in the prediction of particles in Cartesian substate.

As for the Frenet variables:

$$\begin{aligned} l_{(k|k-1)}^{m,i} &= l_{k-1}^{m,i} + \cos\left(\tau_{(k|k-1)}^{m,i}\right)\Delta_x^i + \sin\left(\tau_{(k|k-1)}^{m,i}\right)\Delta_y^i \\ d_{(k|k-1)}^{m,i} &= d_{k-1}^{m,i} + \sin\left(\tau_{(k|k-1)}^{m,i}\right)\Delta_x^i - \cos\left(\tau_{(k|k-1)}^{m,i}\right)\Delta_y^i \end{aligned} \tag{5.50}$$

After the prediction step, verification on the particle is performed to ensure it is located in the right road segment. If valid GNSS measurements are available, the GNSS update is also performed. After each update phase, the PF normalization and resample steps are performed. With this approach, vehicle positioning accuracy at the lane level has been demonstrated. Detail descriptions of the technique is available in [77, 218].

d. **GNSS and single odometer fusion by a non-linear Bayesian method**. In [214], the authors proposed the fusion of GNSS measurements with a single odometer by means of a Gaussian Sum Filter (GSF). The objective is to avoid the possible modelling uncertainties which might cause problems with the EKF approach. This fusion approach is also different from the Kalman Filter based approaches in that it does not involve the mechanization process.

Using only GNSS measurements and a single odometer, the vehicle motion model is developed as follows. Consider a vehicle at time t in East-North-Up (ENU) coordinates (x_t, y_t, z_t). Then, its motion in a horizontal plane:

$$x_t = x_{t-1} + \cos(\theta_{t-1})v_{t-1}\Delta T \tag{5.51}$$

$$x_t = y_{t-1} + \sin(\theta_{t-1})v_{t-1}\Delta T \tag{5.52}$$

where θ_t is the vehicle heading, v_t is the vehicle speed and ΔT is the sampling period. Modelling based on random walk,

$$z_t = z_{t-1} + \epsilon_t^z \tag{5.53}$$

$$v_t = v_{t-1} + \epsilon_t^v \tag{5.54}$$

Since there is no sensor to measure heading, the heading variation is modelled by means of jumping process:

$$\theta_t = \theta_{t-1} + \epsilon_t^\theta + \alpha_t^\theta \Delta N_t^\theta \tag{5.55}$$

where α_t^θ is a uniform white noise on $[-\theta_{max}, \theta_{max}]$. ΔN_t^θ is a Poisson jump with frequency β correspond to the frequency of heading change.

The measurements from the odometer pulse n_t, is related to the vehicle speed v_t in a measurement period ΔT as:

$$n_t = \frac{\Delta T}{g_t} v_t + \epsilon_t^n \tag{5.56}$$

with ϵ_t^n being modelled as white Gaussian observation noise. g_t is a possibly unknown scale factor:

$$g_t = g_{t-1} + \epsilon_t^g \tag{5.57}$$

The PR measurement after correction of ionospheric and topospheric delays and satellite clock bias:

$$\rho_t^k = \sqrt{(X_t^k - X_t)^2 + (Y_t^k - Y_t)^2 + (Z_t^k - Z_t)^2} + ch_t + e_t^k \tag{5.58}$$

where

- (X_t^k, Y_t^k, Z_t^k) are the ECEF satellite coordinates
- c is the speed of light
- h_t is the receiver clock bias, $h_t = h_{t-1} + d_{t-1}\Delta T + \Delta T \epsilon_t^h$
- d_t is the clock drift, $d_t = d_{t-1} + \Delta T \epsilon_t^d$
- e_t^k ia a white Gaussian noise with variance $\alpha 10^{-\frac{C/No}{10}}$ where α is a tuning parameter

Then, the state vector is defined as $\mathbf{x}_t = (X_t, Y_t, Z_t, \theta_t, v_t, g_t, d_t, h_t)$. Based on the Poisson jump ΔN_t^θ values, two prediction models are considered with *a priori* probability π_j,

with $j = 1, 2$ and $\pi_1 + \pi_2 = 1$:

$$\mathbf{x}_t = f(\mathbf{x}_{t-1}) + \mathbf{B}\mathbf{w}_t^j \tag{5.59}$$

where

$$f(\mathbf{x}_{t-1}) = \begin{bmatrix} X_{t-1} + g_X(\theta_{t-1})v_{t-1}\Delta T \\ Y_{t-1} + g_Y(\theta_{t-1})v_{t-1}\Delta T \\ Z_{t-1} + g_Z(\theta_{t-1})v_{t-1}\Delta T \\ \theta_{t-1} \\ v_{t-1} \\ g_{t-1} \\ d_{t-1} \\ h_{t-1} + d_{t-1}\Delta T \end{bmatrix}$$

$$\begin{aligned} g_X(\theta_{t-1}) &= -\sin(\lambda)\cos(\theta_{t-1}) - sin(\phi)\cos(\lambda)\sin(\theta_{t-1}) \\ g_Y(\theta_{t-1}) &= \cos(\lambda)\cos(\theta_{t-1}) + sin(\phi)\sin(\lambda)\sin(\theta_{t-1}) \\ g_Z(\theta_{t-1}) &= \cos(\phi)\sin(\theta_{t-1})v_{t-1}\Delta T \end{aligned}$$

$$\mathbf{B} = \begin{bmatrix} \mathbf{b}(\phi,\lambda) & 0 & 0 \\ 0 & \mathbf{I}_3 & 0 \\ 0 & 0 & \mathbf{I}_2\Delta T \end{bmatrix}$$

$$\mathbf{b}(\phi,\lambda) = \begin{bmatrix} \cos(\phi)\cos(\lambda) \\ \cos(\phi)\sin(\lambda) \\ \sin(\phi) \end{bmatrix}$$

$$\mathbf{w}_t^j = \begin{bmatrix} \epsilon_t^z \\ \epsilon_t^{\theta,j} \\ \epsilon_t^v \\ \epsilon_t^g \\ \epsilon_t^d \\ \epsilon_t^h \end{bmatrix}$$

All the noises in $\mathbf{w}_t^j$ are white Gaussian zero mean with respective variances of $(\sigma_z^2, \sigma_\theta^2, \sigma_\theta^2 + \frac{\theta_{max}^2}{3}, \sigma_v^2, \sigma_g^2, \sigma_d^2, \sigma_h^2)$. From equations 5.56 and 5.58, the observation model is given by:

$$\mathbf{y}_t = m(\mathbf{x}_t) + \mathbf{C}_t \mathbf{z}_t \tag{5.60}$$

where

$$\mathbf{y}_t = \begin{bmatrix} n_t \\ \rho_t^1 \\ \rho_t^2 \\ \vdots \\ \rho_t^K \end{bmatrix}$$

and K is the number of satellites.

$$m(\mathbf{x}_t) = \begin{bmatrix} \frac{\Delta T}{g_t} v_t \\ \sqrt{(X_t^1 - X_t)^2 + (Y_t^1 - Y_t)^2 + (Z_t^1 - Z_t)^2} + ch_t \\ \vdots \\ \sqrt{(X_t^K - X_t)^2 + (Y_t^K - Y_t)^2 + (Z_t^K - Z_t)^2} + ch_t \end{bmatrix}$$

$$\mathbf{z}_t = \begin{bmatrix} \epsilon_t^n \\ \epsilon_t^1 \\ \vdots \\ \epsilon_t^K \end{bmatrix}$$

$$\mathbf{C}_t = \begin{bmatrix} 1 & 0 & \cdots & 0 \\ 0 & 10^{-\frac{C/No_t^1}{20}} & 0 & \vdots \\ \vdots & 0 & \ddots & 0 \\ 0 & \cdots & 0 & 10^{-\frac{C/No_t^K}{20}} \end{bmatrix}$$

Further elaboration on implementing the Gaussian Sum filter as sensors fusioning method can be obtained in [214].

The previous methods had been reviewed to present representative contributions from the state of the art. We did not implement these methods and our work is described next.

5.7 GNSS/Odometer/Gyro integration for PR prediction

For the work of this thesis, the DR navigation scheme uses a single odometer to measure the displacement and a gyroscope to measure the heading (yaw) of the vehicle. The choice of the hybrid configuration for this work is aimed for a simple and low cost integration. Of course a more complicated and advance hybrid navigation system will be able to produce better accuracy in the positioning. However, it is worth highlighting that the purpose of the work in this chapter is not specifically on improving positioning accuracy by means of hybridization, rather it is to establish the PR residual from the hybrid positioning system as an indicator of the PRs quality. In fact, it can be said that by using a low cost and simple hybrid position estimator in this work serve as an indicator at the low end of the performance range. With higher quality hybrid position estimator, the end result would be better than the ones obtained by using this simple hybridization configuration.

Some of the advantages of using a single odometer with a single gyroscope over the full INS are described in [219]. In addition to the low cost, the benefit of using fewer inertial sensor is the reduction of the contribution of the inertial sensor errors to the position error. In velocity calculation, the odometer avoids an integration required by an accelerometer of the INS, hence it has relatively less accumulative error than the accelerometer.

In principle, the odometer uses the wheel rotation sensor to measure wheel revolutions. Then, the wheel revolutions are transformed into the traveled distance. Using the time between two consecutive observations, the speed or velocity of the vehicle can also be determined. As described in [210] the accuracy of odometer output are affected by scale factor error, condition of the road and pulse truncation. The most significant error is the scale factor error which is due to calibration error, tire wear and tear, tire pressure vibration and vehicle speed. However, the scale factor error is not significant over a short period of travel.

As for the rate gyroscope, its associated errors are gyro bias drift, gyro scale factor error, installation misalignment, temperature, and vibration and electromechanical properties of the operational environment. The most significant error is the bias drift which depends

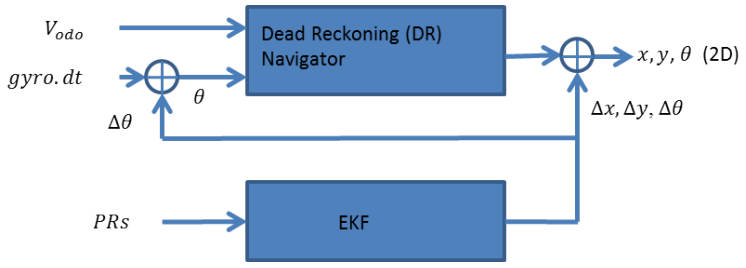

FIGURE 5.7: The block diagram of the hybrid navigation filter

on the quality of the gyroscope. Further information on gyroscope may be obtained for example in [124, 198].

Figure 5.7 shows the navigation filter implemented in this research which has a configuration of a loose fusion of the GPS, gyroscope and odometer. The strategy involves the DR navigator to determine the 2D position of the vehicle based on the measurements obtained from the odometer and the gyroscope. At the same time, the EKF provides corrections to the DR navigator output and also to the yaw input from the gyroscope. Hence, when the satellites signals are good, they will correct the DR navigator output.

In this work, some simplification is applied to the 2D kinematics equations of equation 5.2. First of all, the displacement distance of the GNSS antenna to the center of the rear wheels axis is ignored. Secondly, the following terms are also simplified [207]:

$$\begin{aligned} \sin\left(\psi_k + \frac{\omega T}{2}\right) &\approx \sin\omega_k \\ \cos\left(\psi_k + \frac{\omega T}{2}\right) &\approx \cos\omega_k \end{aligned} \tag{5.61}$$

Then, the gyroscope bias b_{gyro}, is estimated by adding it as a state variable. After these simplifications and addition to the classical 2D kinematics equations (equation 5.2), the hybrid positioning in this work is thus achieved by the following formulation:

$$\hat{x}_{user}(k) = \hat{x}_{user}(k-1) + V_{odo}.\cos\theta.dt + \Delta x \tag{5.62}$$

$$\hat{y}_{user}(k) = \hat{y}_{user}(k-1) + V_{odo}.\sin\theta.dt + \Delta y \tag{5.63}$$

$$\theta(k) = \theta(k-1) + gyro.dt - b_{gyro}.dt \tag{5.64}$$

where:

- $\hat{x}_{user}(k)$ is the user position in the x coordinates

- $\hat{y}_{user}(k)$ is the user position in the y coordinates
- V_{odo} is the velocity measured by the odometer
- $\theta(k)$ is the yaw angle
- $gyro$ is the yaw angle rate provided by the gyro
- b_{gyro} is the estimated bias of the gyro yaw angle rate
- Δx is the estimated position correction in x coordinate
- Δy is the estimated position correction in y coordinate

The error state vector implemented for the EKF in this work is:

$$\mathbf{x} = \begin{bmatrix} \delta x \\ \delta y \\ \delta\theta \\ b_{gyro} \\ b_c \\ d_c \end{bmatrix} \tag{5.65}$$

where

- δx : position error in x coordinate
- δy : position error in y coordinate
- $\delta\theta$: error in yaw
- b_{gyro} : gyro bias
- b_c : clock bias
- d_c : clock drift

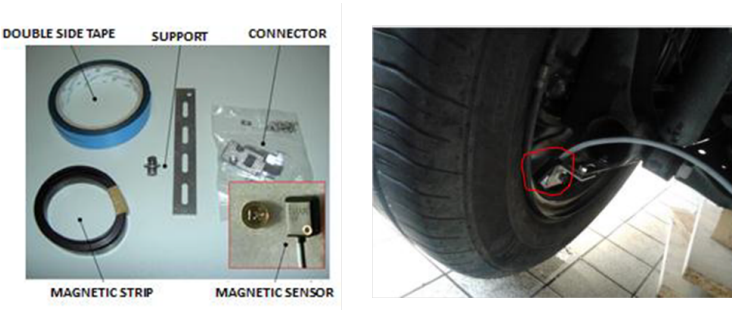

FIGURE 5.8: The iMAR iMWS-V2 magnetic strip based wheel sensor mounted on the wheel of ISAE test vehicle

The state transition matrix, $\mathbf{F}$, is obtained as:

$$\mathbf{F} = \begin{bmatrix} 1 & 0 & V_{odo}.\cos(\theta)dt & 0 & 0 & 0 \\ 0 & 1 & -V_{odo}.\sin(\theta)dt & 0 & 0 & 0 \\ 0 & 0 & 1 & -dt & 0 & 0 \\ 0 & 0 & 0 & 1 & 0 & 0 \\ 0 & 0 & 0 & 0 & 1 & dt \\ 0 & 0 & 0 & 0 & 0 & 1 \end{bmatrix} \tag{5.66}$$

and for the observation equation, the regular approach of the EKF which relates the measurements vector to the state vector $\mathbf{x}$ by means of $\mathbf{h}$ matrix was implemented.

5.7.1 Equipment, Data Collection and Testing

The odometer used in the experiments is the iMAR iMWS-V2, which is a magnetic strip based wheel sensor (Figure 5.8).

The magnetic strip of the odometer was fixed to the inside rim of the left rear wheel of the car which is a non-driving wheel. The magnetic sensor of the odometer detects the number of impulse per seconds as the wheel rotates. This impulse per second output of the odometer, odo_{output} is converted to the rotating speed of the wheel by the scale factor, SC_{odo}.

$$V_{odo} = SC_{odo} \times odo_{output} \tag{5.67}$$

For obtaining the yaw angle, the iMAR IMU-FSAS gyroscope was used. The gyroscope has a rate bias of less than 0.75 degree/hour. As for the GPS signals, they are measured using u-blox LEA-4T receiver.

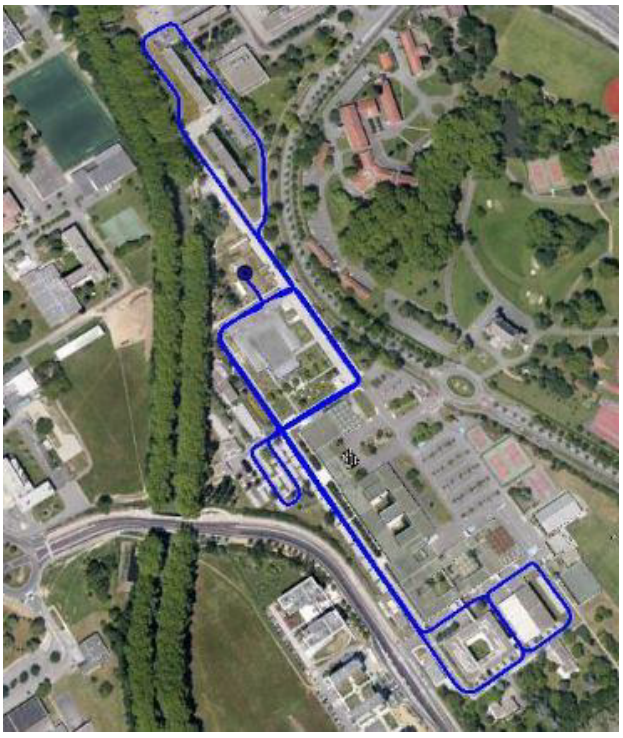

FIGURE 5.9: Trajectory for conducting the experiments

FIGURE 5.10: NovAtel SPAN as the reference system

The data for the experiments were collected along the trajectory at the ISAE campus (Figure 5.9). The route is chosen so that the vehicle traverses under foliage, along and between buildings and also in open sky environment. The vehicle is driven in various speeds, with accelerations and decelerations and also with several abrupt stops. It is also driven over speed bumps and sandy surface. The reference data along the trajectory are provided by the NovAtel SPAN system (Figure 5.10).

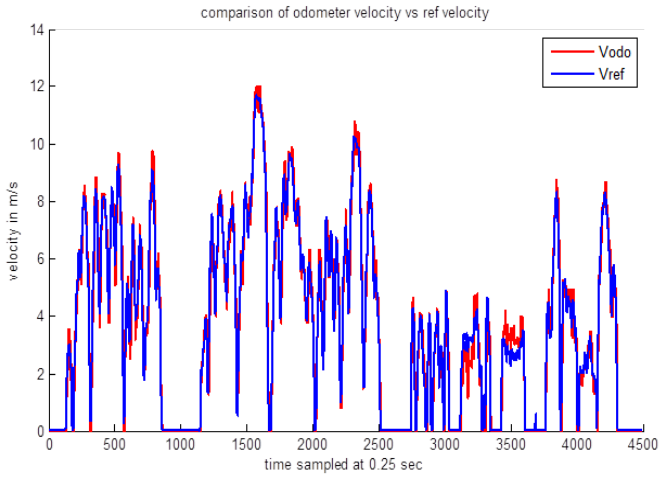

FIGURE 5.11: Comparison of odometer velocity with reference velocity

The purpose of the data collection can be divided into two parts; to analyze the performance of the odometer vis-a-vis the reference velocity, and to measure the GPS signals via the u-blox receiver so that hybrid position estimation and the integrity checking can be performed.

5.7.2 Results on odometer's performance

In analyzing the performance of the odometer, its velocity is compared against a reference velocity (Figure 5.11). The result shows that the velocity measured by the odometer has a very close resemblance to the reference velocity with a correlation coefficient of 0.987. This very high correlation indicates that the odometer can be a good reference sensor. However, there are some dead zones for the odometer output, i.e. when the vehicle velocity is low, the odometer does not output a valid velocity information. Such situation occurred for example around the 318th and the 573rd time sample in figure 5.11). In this experiment, the determined odometer scale factor for calculating its velocity was 0.004. Compared to the reference velocity, the error of the velocity measured by the odometer has a mean of 0.0378 m/s with standard deviation of $\pm$ 0.4642 m/s.

5.8 Reliability Metrics

The work in this chapter studies three forms of residuals in order to analyze their capability in monitoring the reliability of measurements which are used for calculating

the PVT solutions. The residuals being considered are the PR, velocity and range rate residuals. As has been mentioned earlier, the calculations of the residuals in this work involves DR sensors.

5.8.1 Reliability test based on pseudorange

The aim of this approach is to use an aiding sensor in such a way that the relationship from the measurement of the reference sensor to the positioning by GNSS can provide a method for reliability monitoring. The algorithm is based on the pseudorange residuals as difference between the measured and the predicted pseudoranges.

5.8.1.1 Generating pseudorange residual

At each time instant k and for each satellite i, the residual is computed as the absolute difference between a measured pseudorange and its predicted counterpart.

$$r^i(k) = PR^i_{measured}(k) - PR^i_{predict}(k) \tag{5.68}$$

The predicted PRs are computed from the satellite positions, $\mathbf{X}_{sat}$ and the estimated user positions, $\hat{\mathbf{X}}_{user}$

$$PR^i_{predict}(k) = |\mathbf{X}_{sat} - \hat{\mathbf{X}}_{user}| \tag{5.69}$$

In calculating the $PR^i_{predict}(k)$, the $\hat{\mathbf{X}}_{user}$ are computed using hybridized measurements from an odometer, a gyroscope, and all available PRs at the time k (except the $PR^i_{measured}(k)$ that is to be tested). Hence, the $PR^i_{predict}(k)$ is predicted without the influence $PR^i_{measured}(k)$. If none of the satellite signals are available, the PR is predicted based on the DR sensors only.

The overall formulation of the residual is therefore,

$$r^i(k) = |y^i(k) - (\sqrt{[(X^i_{sat}(k) - \hat{X}_{user}(k))^2 + (Y^i_{sat}(k) - \hat{Y}_{user}(k))^2 + (Z^i_{sat}(k) - \hat{Z}_{user}(k))^2]})| \tag{5.70}$$

where:

- $y^i(k)$ is the measured pseudorange from satellite i at instant k

- $\hat{X}_{user}(k), \hat{Y}_{user}(k), \hat{Z}_{user}(k)$ are user positions in the ECEF frame at each time period

5.8.1.2 Test statistic calculation

The received pseudoranges will be tested in order to identify the faulty ones. To do so, a test statistic T, is compared against a threshold value to decide whether to reject or accept the $PR^i_{measured}(k)$. For calculating the test statistic for each PR,

$$T = r^t.Z^{-1}.r \tag{5.71}$$

where r is the residual and,

$$Z = cov(r) = var(PR^i_{measured}) + var(PR^i_{predict}) \tag{5.72}$$

The variance of $PR^i_{measured}$ can be determined from existing variance model which mainly related to its C/No or elevation angle [14]. Here, the SIGMA-ε model [11] is used.

On the other hand, the variance of $PR^i_{predict}$ can be obtained with the Euclidean norm of the line-of-sight vector and the law of error propagation as [15]:

$$var(PR^i_{predict}(k)) = e_{sat,user}(k).P_{user}(k).e^t_{sat,user}(k) \tag{5.73}$$

where:

$$e_{sat,user}(k) = \frac{x^i_{sat}(k) - \hat{x}_{user}(k)}{\|x^i_{sat}(k) - \hat{x}_{user}(k)\|} \tag{5.74}$$

$$P_{user}(k) = \begin{bmatrix} \sigma_x^2 & \sigma_{xy} & \sigma_{xz} \\ \sigma_{yx} & \sigma_y^2 & \sigma_{yz} \\ \sigma_{zx} & \sigma_{zy} & \sigma_z^2 \end{bmatrix} \tag{5.75}$$

For the user position covariance matrix $P_{user}(k)$, assuming non-correlation between x, y and z, only the diagonal elements are of interest. Furthermore, since the positioning is in 2D, σ_z^2 can be set to 0. The $P_{user}(k)$ matrix is not readily available from the hybrid

navigator used in this project. However, the variances σ_x^2 and σ_y^2 can be calculated based on variance combination rule and variance propagation law as follows [220].

Based on the hybrid positioning formulation in equations 5.62, 5.63 and 5.64, the variances σ_x^2 and σ_y^2 of of the estimated user position are formulated as:

1. Variance of $\hat{x}_{user}$ and $\hat{y}_{user}$ are accordingly the user position variance at time $k-1$.

2. To calculate the variance of $V_{odo}.\sin\theta.dt$, since V_{odo} and dt are deterministic variables,

   $var(V_{odo}.\sin\theta.dt) = V_{odo}^2.dt^2.var(\sin\theta)$ and taking the jacobian of $\sin\theta$, we obtain:

   $var(V_{odo}.\sin\theta.dt) = V_{odo}^2.dt^2.\cos^2\theta.\sigma_\theta^2$

   where $var(X)$ denotes the statistical variance of the random variable X. Similarly, the variance of $V_{odo}.\cos\theta.dt$ is given by:

   $var(V_{odo}.\cos\theta.dt) = V_{odo}^2.dt^2.var(\cos\theta) = V_{odo}^2.dt^2\sin^2\theta.\sigma_\theta^2$

3. The variance of Δx and Δy are obtained from the covariance matrix of the EKF.

4. To obtain σ_θ^2, since

   $\theta(k) = \theta(k-1) + gyro.dt - gyro\ bias.dt$

   the variance of $\theta(k)$:

   $\sigma_\theta^2(k) = \sigma_\theta^2(k-1) + (dt)^2\sigma_{gyro}^2(k) + (dt)^2\sigma_{gyro\ bias}^2(k)$

   where σ_{gyro}^2 is obtained from the gyro specification, and $\sigma_{gyro\ bias}^2$ from the covariance matrix of the Kalman filter.

Once σ_x^2 and σ_y^2 are calculated, $cov(r)$ can be determined by implementing equations 5.72, 5.73, 5.74 and 5.75.

The threshold is set by the confidence level applied to the chi-squared distribution with 1 degree of freedom, $r^t.Z^{-1}.r \sim \chi_1^2$. In this work, threshold is set at 2.706 (equivalent to 99% confidence level). To allow us to approximate the test statistic distribution to the χ_1^2 distribution, some pre-processing was done beforehand to exclude obvious outliers in the measured PRs.

5.8.1.3 Results and analysis of residuals based on pseudorange

a. Residual of PR

Figure 5.12 and Figure 5.13 show the plots which compare the calculated PR residuals (plotted in red) against the satellite actual range errors (plotted in blue) for 10 available SVs. It is evident that the residual performance varies for different satellites. In the results, the residual is able to represent the range error very well for satellite 9 and 28, which are the faulty satellites with range errors more than 100 m. For the rest of the satellites (with range errors less than 40 meters), the calculated residuals are generally smaller than the actual range errors.

To elaborate on the results, recall that the residual is the difference between the measured PR and the predicted PR. In the PR prediction process, the user position estimate is calculated without the PR measurement from the satellite which PR is to be predicted. Therefore, in the case of SV 9 and SV 28 in the results, their residuals are very close to the true range errors because the estimated user positions are very close to the referenced user positions that are used to calculate the true range errors. In other words, excluding only one of either the PR of SV 9 or the PR of SV 28 resulted in good accuracy of the user position estimates.

As for the case of other satellites, both PRs of SV 9 and SV 28 were included in the user position estimations during calculating the respective PR predictions of the other satellites. Hence, in this experiments, there exist two 'faulty' PRs that distort the user position estimates when both of them are included. However, if only one of them is included, the impact on use position estimation error is negligible or very minimal. This result provide an example of the complexity to characterize or model the effect of multiple biases or PR faults in GNSS positioning.

Furthermore, since the test statistic is based on the residual, fault identification would be more accurate on satellites with better matched residual to actual error, as oppose to those with the lesser matched. This result gives us an insight that the optimality of the test statistic will vary on different satellites where it will work well to detect the satellites with large faults.

b. Effect on positioning accuracy

Figure 5.14 shows the number of visible satellite (blue) vs. the number of non-faulty

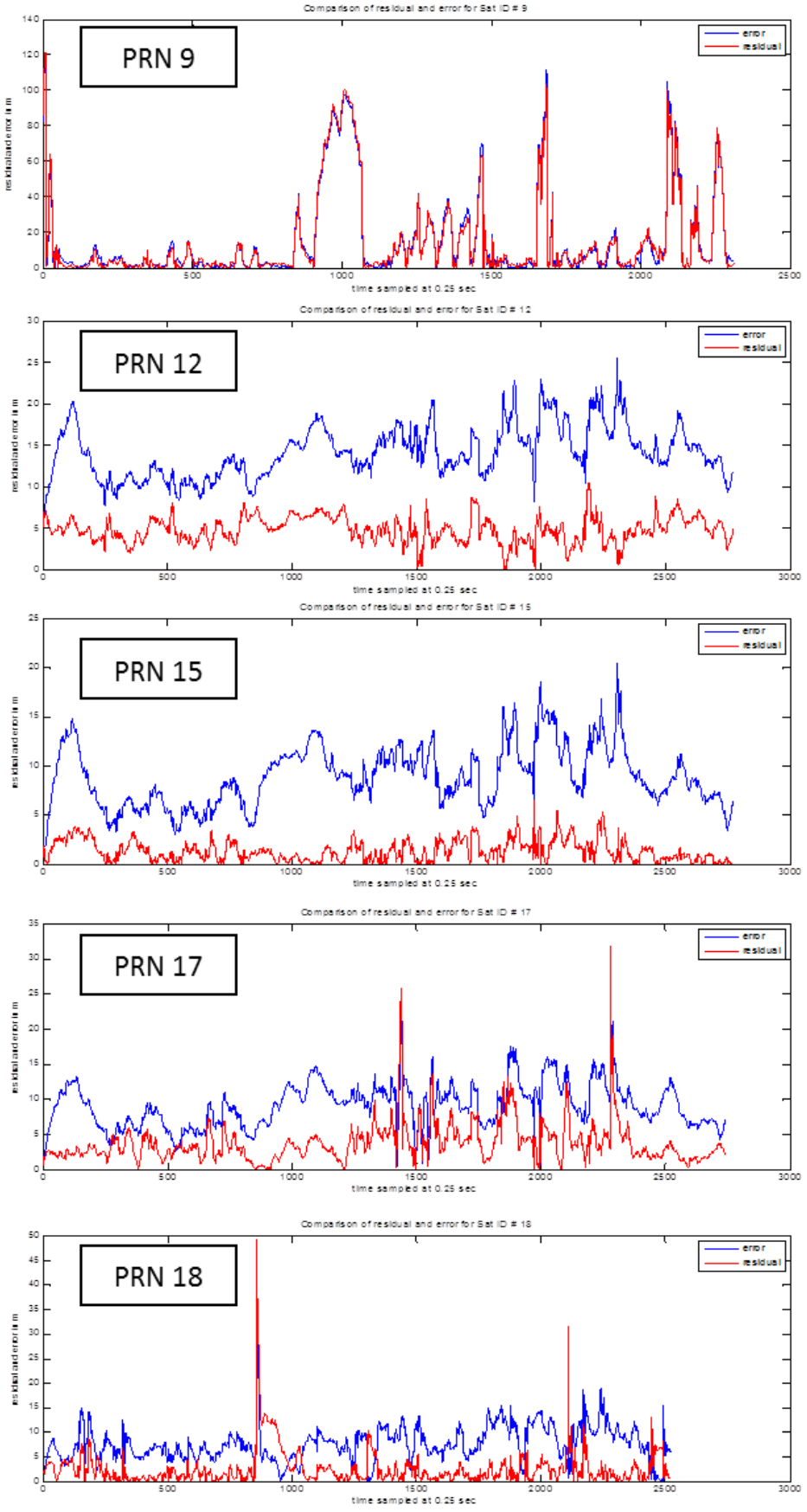

FIGURE 5.12: Comparison of PR residual vs. satellite range error for the available SVs

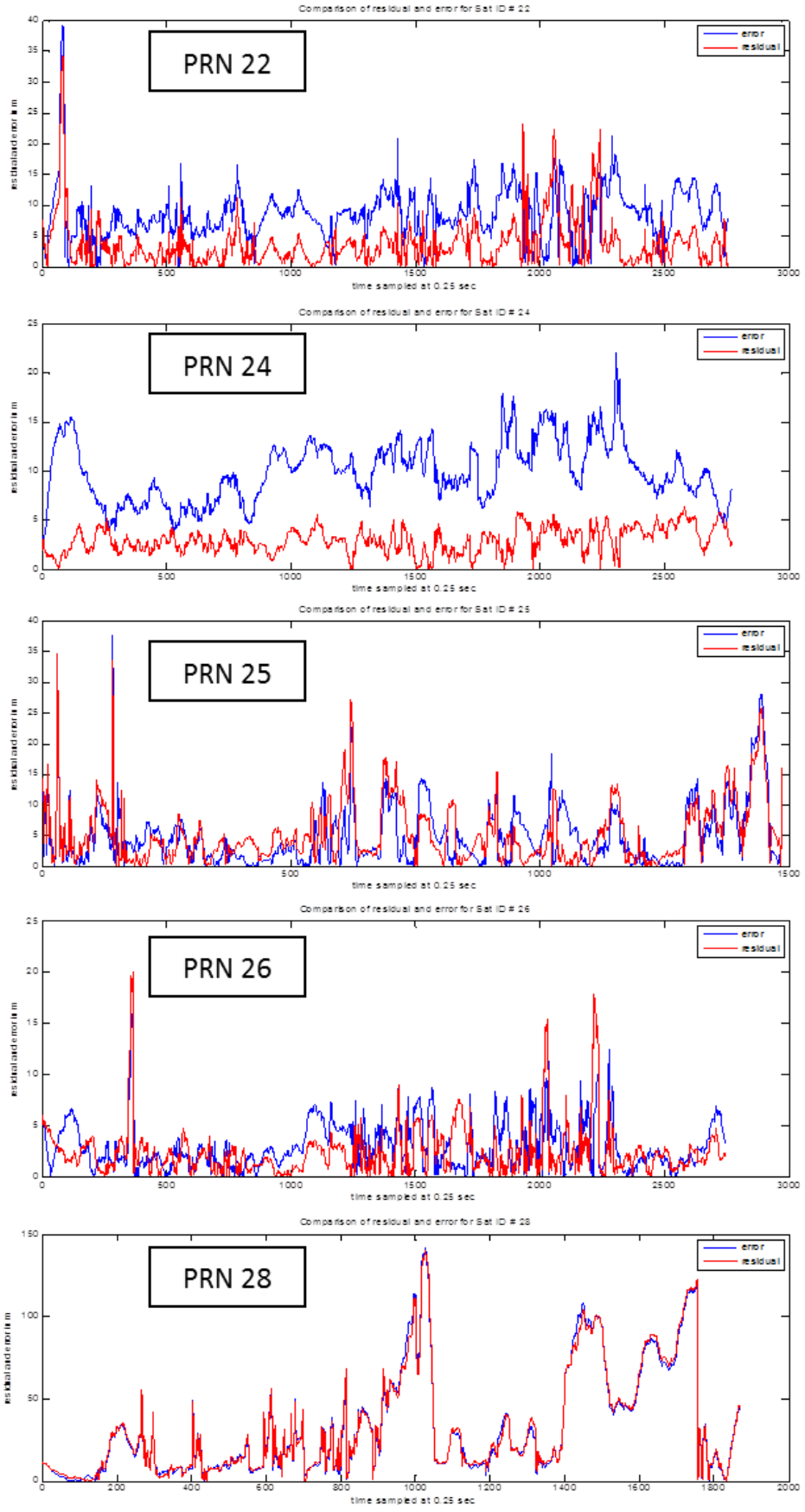

FIGURE 5.13: Comparison of PR residual vs. satellite range error for the available SVs

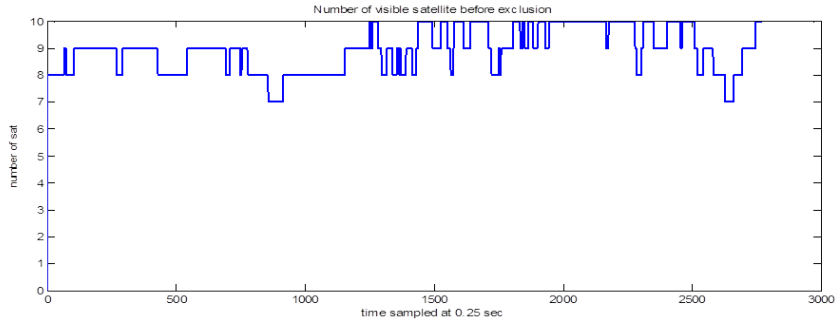

(a)

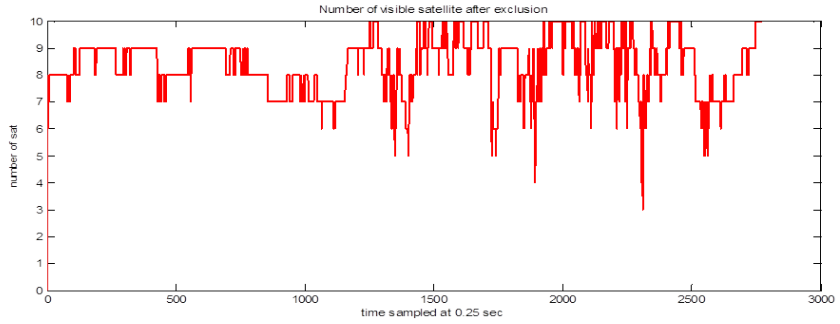

(b)

FIGURE 5.14: Comparison of total number of visible satellites vs. total number of non-faulty satellites

satellites (red) after the implementation of the fault detection and identification. The result conforms that in some part of the trajectory, the remaining non-faulty satellites were reduced to 4 or even less, in which case, the traditional RAIM algorithm cannot be implemented because it needs at least 5 visible satellites.

- **PR fault detection and exclusion**

  Figure 5.15 shows the norms of the 2D position error before (green) and after (red) the faulty satellites exclusion. For the purpose of comparison, Figure 5.15 (a) shows the result of using the hybrid GPS/odometer/gyro navigator while Figure 5.15 (b) is the result from using only GPS for the positioning. Firstly, it can be seen in Figure 5.15 (a) that the positioning is improved after the exclusion of the faulty satellites. This led to imply that the technique had correctly identified and excluded the faulty satellites. Secondly, the positioning improvement is better in Figure 5.15 (a) than that in Figure 5.15 (b). This shows that not only the GPS/odometer/gyro navigator improves navigation but the fault detection and exclusion (FDE) for land vehicle in urban environment can be performed better

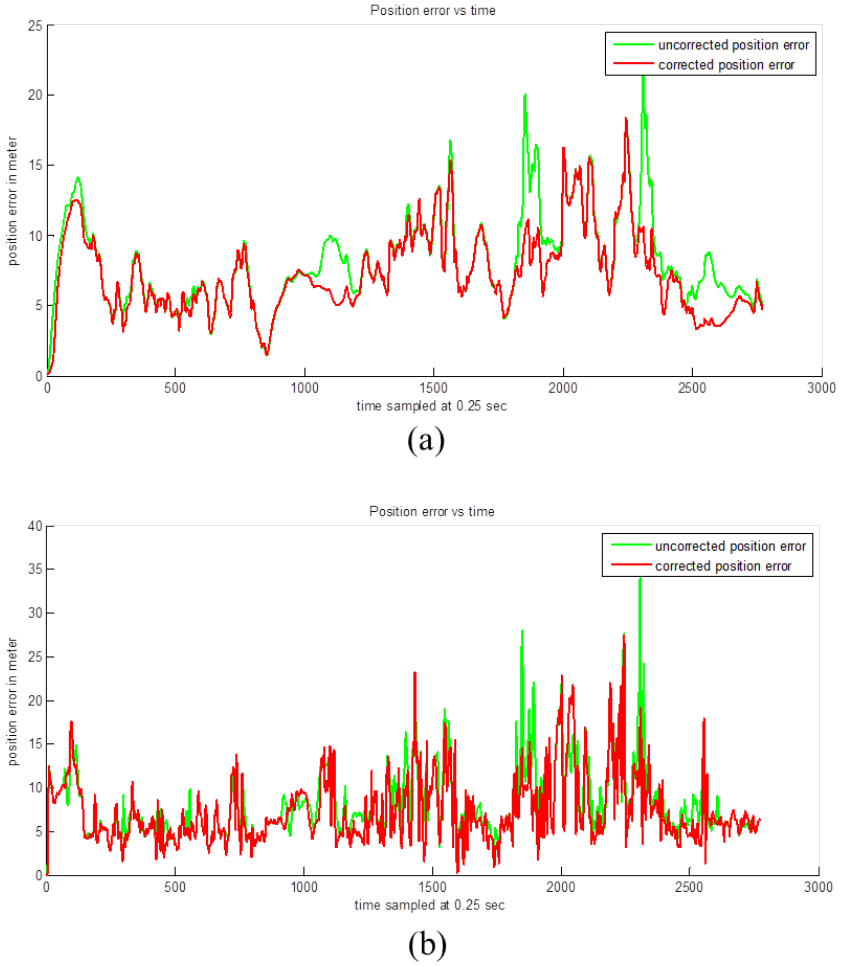

FIGURE 5.15: Position error comparison after fault exclusion

when odometer and gyro is hybridized with the GPS as compared to when only the GPS was utilized.

- **PR fault correction**

  Figure 5.16 (a) shows the result of the PR error detection, identification and adaptation (DIA) that was implemented on the hybrid navigator using the measurement integrity checking technique proposed in this chapter. The adaptation was achieved by replacing the identified faulty measured PRs with their relevant predicted PRs. In other words, the faulty PRs were corrected. This approach is particularly useful in the situation where the remaining number of non-faulty satellites that are visible is less than enough for a position fix. Figure 5.16 (b) serves as a comparison to show that this PR error correction approach could not be achieved without the integration of the odometer and gyro, i.e., when only GPS signal were used in the positioning.

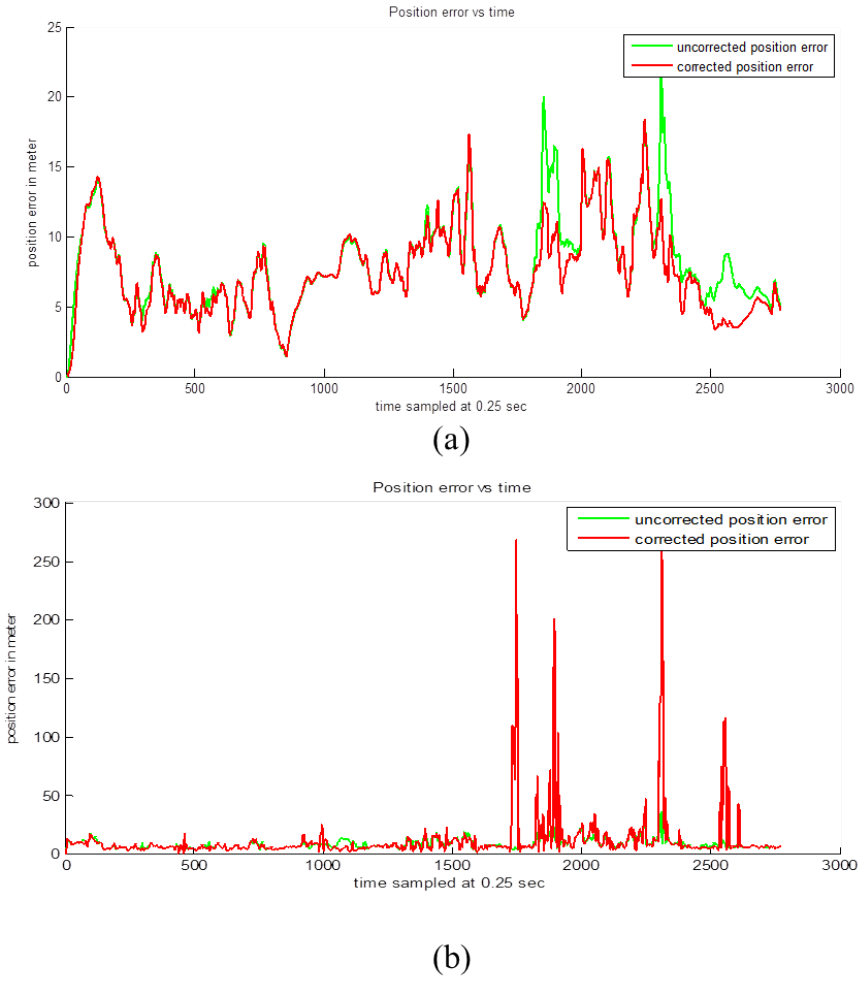

FIGURE 5.16: Position error comparison after fault correction

5.8.2 Reliability test based on user velocity

Other than using the pseudorange, residual may also be derived from user velocity. Knowing the satellite velocity, user velocity can be determined using Doppler measurements according to the following equation,

$$D = -\frac{L1}{c}[e_{sat,user}.(V_{user} - V_{sat}) + d_t] + \varepsilon \tag{5.76}$$

where:

- D is the Doppler measurement in Hz
- $L1$ is the carrier frequency
- c is the speed of light

- $e_{sat,user}$ is the unit line of sight vector between satellite and receiver
- V_{user} is the user velocity vector
- V_{sat} is the satellite velocity vector
- d_t is receiver clock drift
- ε is the measurement noise

For a stand-alone GPS receiver, the position is computed using PRs. If the PVT is computed including the Doppler measurements, the receiver will benefit from the quality of the Doppler measurements to smooth the solution and also skip short outage. Then, if the Doppler is also bad or not available, in the case of degraded or not enough PRs, the stand-alone GPS cannot provide a solution or it will be very unreliable. One may consider to test the estimated position by generating residual, r_V based on the difference between user velocity and predicted velocity.

$$r_V = |V_{user} - V_{predict}| \tag{5.77}$$

This metric will be tested against a practice-designed threshold value.

However, the relation of this residual of velocity to the residual (error) of the position is not easy to establish. Even so, in many applications, users may be interested in reliable velocity information.

In this work, it is proposed to compute the predicted velocity from the V_{odo}. The user velocity, V_{user} is determined from the GPS data; either by using Kalman with PRs or Kalman with Doppler measurements. Therefore, in this scheme, V_{odo} is totally an external reference sensor (just to compare to the user velocity) and do not contribute to the positioning solution at all. Hence, the residual of velocity,

$$r_V = |V_{GPS} - V_{odo}| \tag{5.78}$$

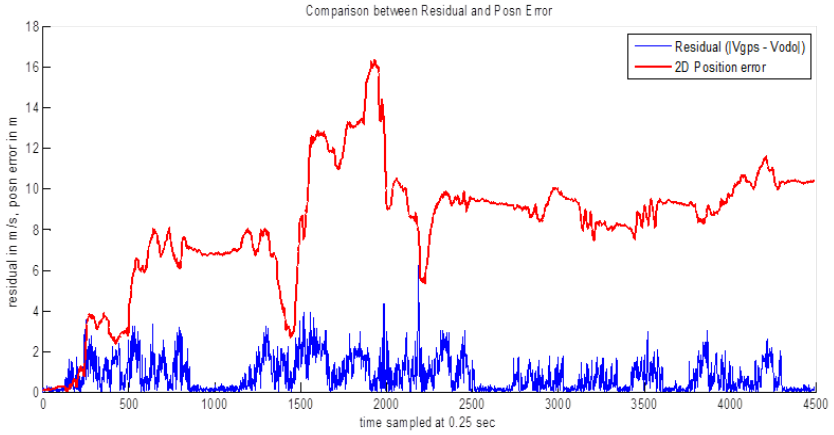

FIGURE 5.17: Comparison of velocity residual (blue) against 2D position error (red)

5.8.2.1 Result of velocity residual vs position error

The plot of Figure 5.17 shows the performance of the velocity residual. The plot was obtained by selecting a combination of good and degraded PRs and Doppler measurements in order to simulate position errors for analyzing the performance of the velocity residual of equation 5.78. As can be seen in the plot, it is difficult to establish a direct relationship between the velocity residual (blue) and the position error (red). However, it appears that the velocity residual is able to detect the 'gradient'of position error instead of the error magnitude. In other words, it seems that the residual can detect if the position error is growing, remain constant, or decreasing. Nevertheless, further research and analysis are needed to truly benefit from this apparent relationship of the velocity residual against the position error in order to use it for integrity checking.

5.8.3 Reliability test based on range rate

The equation of the range rate is related to Doppler, hence to user velocity [221] by,

$$\begin{aligned} \dot{\rho} &= -\frac{c}{L1}D = e_{sat,user}.(V_{user} - V_{sat}) + d_t + \varepsilon \\ &= \dot{r} + d_t + \varepsilon \end{aligned} \tag{5.79}$$

where:

- $\dot{\rho}$ is the pseudorange rate
- $\dot{r}$ is the geometric range rate between receiver and satellite

According to equation 5.79, the range rate is related to the user's line-of-sight velocity. Then, $\dot{\rho}$ can also be used for fault detection. For this technique, the hybrid receiver (odometer/gyro/GPS) is used. The residual p, was calculated based on the predicted and measured $\dot{\rho}$,

$$p = |\dot{\rho}_{measured} - \dot{\rho}_{predict}| \tag{5.80}$$

where:

$$\dot{\rho}_{measured} = \frac{PR(k) - PR(k-1)}{dt} \tag{5.81}$$

and

$$\dot{\rho}_{predict} = e_{sat,user}.V_{user}(k) - e_{sat,user}.V_{sat}(k) + d_t \tag{5.82}$$

where $V_{sat}(k)$ is calculated from the ephemeris data and $V_{user}(k)$ is obtained from the Kalman navigation filter depending on V_{odo} and yaw angle θ.

The test statistic, $T = p^t.Z^{-1}.p$ is used for this residual. Here, the covariance, Z, is determined *a priori* from the observed data.

Even though not implemented in this work, carrier phase observable may also be used to determine user velocity. One way to show this is through its relation with the Doppler measurement,

$$D \approx \frac{\varphi(t + \Delta t) - \varphi(t - \Delta t)}{2\Delta t} \tag{5.83}$$

where:

- φ is the measured carrier phase
- t is the epoch where the velocity is calculated
- Δt is the sample period of measurement

5.8.3.1 Results of range rate residual vs position error

In Figure 5.18, the result of implementing FDE based on residuals derived from the range rate as an alternative to the PR was plotted. Generally, it is observed that the positioning error can be also improved by using the FDE based on the range rate residual.

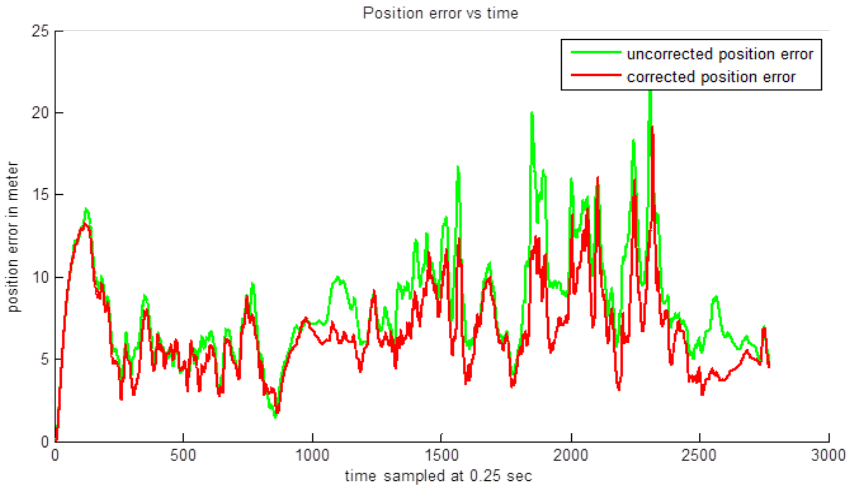

FIGURE 5.18: Position error after fault correction using range rate residual

The results from these various residual implementations suggest that the residual based on PR has the advantage of performing integrity checking in range domain even when the available satellites are less than 5. However, for user applications which require velocity monitoring, velocity based residual appears to be more suitable. Of course there is a possibility of combining them as multi-indicators for reliability monitoring. However, further studies are needed to ascertain each residual performance in both the surrounding environments and the user's dynamic behaviors. This knowledge is crucial for developing an appropriate algorithm for the receiver to decide from several indicators, especially whenever there is contradiction.

5.9 Conclusions

In this chapter, a single odometer and complemented with gyro was implemented as a reference sensor for reliability monitoring of GNSS measurements for land vehicle positioning in urban environment. The result of the analysis conducted on the odometer suggested that it is suitable as a reference sensor. By integrating the odometer, gyro and GPS measurements, various residuals and test statistics were used to check the measurements quality.

With the aiding from the DR sensor, PR can be predicted even when user position fix is not possible if the estimation is only based on satellite measurements. However, when PR residuals are calculated, the quality of the PR residual representation of the actual

range errors varies from satellite to satellite. The residual has good representation for the satellites with large fault value. Firstly, this indicates that hybrid positioning with the implemented configuration may not be accurate enough to have a better effect on the PR residual to represent the smaller values of PRs errors. Secondly, the effect of faulty PRs on positioning accuracy could be severe when combined but individually, the effect could be negligible. This situation could be due to their correlation and/or coupled with the effect of their geometry. Using better hybrid position estimator or adding more sensors in the hybridation, for example with height aiding, may further improve the quality of the residual.

Nevertheless, the positioning error was improved moderately after employing the PR quality checking technique for both fault exclusion and fault correction methods. Since the range errors of SV 9 and SV 28 are much more severe than the other SVs, the PR residual were able to perform its function to detect the faulty measurements before they are accepted as valid measurements for positioning. In this sense, the PR residual can be used as the first layer in the multiple layers of reliability monitoring metrics.

Similar potential has also been demonstrated by the FDE technique based on the range rate residual. However, its drawback in this work when compared to the PR residual based approach is that it cannot be implemented to correct or replace the faulty measurement.

As for the velocity based residual, it was found that it is quite difficult for it to be related to positioning error. Instead, it would be useful for velocity error detection. Further studies are required in order to combine these metrics or with other approach as multiple indicators for reliability monitoring.

Chapter 6

GNSS Positioning Confidence in Urban Environments using Trusted Overbounding Position Errors

6.1 Introduction

Monitoring positioning integrity for land applications in urban environments is very difficult to achieve. In the aviation sector, integrity monitoring is mostly accomplished by Receiver Autonomous Integrity Monitoring (RAIM) techniques which use Fault Detection and Exclusion (FDE) algorithms to reject outliers from measured data and also by augmentation systems like Ground Based Augmentation System (GBAS) and Satellite Based Augmentation System (SBAS). In SBAS, satellites relay integrity information to aircrafts for computing Protection Level (PL) associated to an integrity risk [55]. However these techniques are designed for aeronautics applications where high redundancy of data exists, mature performance standards for each phase of navigation are available, measurement and position errors are assumed to be Gaussian distributed and only a single fault is expected.

As has been established in chapter 2, GNSS positioning in urban environments is difficult due to the degradation of the satellite signals reception. These degradations are the

results of the signal being blocked or due to the multipath and non-line of sight (NLOS) phenomena. In such constrained environments, the distribution of measurement errors is not Gaussian and if only reliable signals are selected, sometimes there is not enough number of non-contaminated GNSS signals that are available for position fix. For these reasons, the standard RAIM or augmentation methods of integrity monitoring coming from the civil aviation community is no longer applicable and new concepts are needed for satellite navigation in urban environments.

Nevertheless, many efforts were made to adapt these techniques for land vehicle applications in harsh environments. For example, researchers in [56] implemented a few types of RAIM algorithms for land vehicle application in urban environments. The findings affirm that RAIM performance is unreliable in urban environments due to the inaccurate modeling of the measurement errors as Gaussian distributed and the existence of many contaminated signals that dominate the positioning estimation. Several other techniques had also been proposed to monitor positioning integrity for land vehicle in urban area. These techniques include the HTL [158], HIT [159], Trajectory Monitoring [160] and the Robust Set Inversion via Interval Analysis [66] which have been described in chapter 3.

However, most of the time, users do not have access to the receivers' positioning algorithms. In fact, for the land navigation applications, the GNSS receiver is more often than not used as a sub-system for the whole system [29, 222]. As such, users are unaware of what sort of filtering or processing that has been done to the pseudoranges (PRs) before they are used for position estimation.

In these land based applications, the GNSS receiver is normally a sub-system for providing positioning, velocity and time (PVT) information that would be used as subsequent inputs by the next module in the application system as a whole. Indeed, the GNSS is not the only technology involves in the positioning module when hybrid solution is implemented. In such case, the GNSS technology is complemented by other sensors, such as inertial or odometric, in order to improve the performance of the PVT solution. Figure 2.3 in chapter 2 shows a generic structure of the concept. Therefore, there is a need to choose a suitable receiver type and to know its minimum performances in order to meet the final application's requirement at the user level [29, 30]. For this purpose, the characterization of positioning error is needed to provide the final user with the level of confidence in the application which uses the level of confidence of the GNSS solution.

In this situation, position integrity monitoring is suitable in the position domain rather than in the range domain. In the position domain approach, protection level may be calculated based on the CDF of the position error distribution [183].

This work focuses on the positioning error characterization because modelling the effect of NLOS on the measurements is quite difficult and does not guarantee the characterization of the final position error [63]. In fact, different PR errors on the PR may combine between them to produce another kind of errors on the position solution. For example, it has been observed in the Satellite-based augmentation system (SBAS) literature that errors terms between different satellites may be correlated and finally challenged the standard protection level (PL) methods based on the non-correlation assumption [223]. Hence, the availability of a statistical characterization of the position error is also very useful for computing integrity indicators. Since there are biases in urban environment due to multipath and NLOS, they need to be taken into account in the position integrity monitoring [19, 224, 225].

In the SBAS approach, the horizontal protection level is defined as "the radius of a circle in the horizontal plane (the plane tangent to the WGS-84 ellipsoid, with its center being at the true position, that describes the region assured to contain the indicated horizontal position. It is the horizontal region where the missed alert requirement can be met. It is based upon the error estimates provided by SBAS."[46] As such, whenever the monitored PL is less than the Alert Limit (AL), the positioning is considered to be within the integrity requirement. However, for land applications especially in urban settings, simple or direct adaptation from the civil aviation approach of integrity monitoring is not possible due to the challenging signal degradation characteristics. In order to adapt the methodology of RAIM or SBAS integrity to GNSS urban navigation, rational modification of existing approaches is required.

In computing the PL, the common approach for overbounding in the aviation sector is to use zero mean Gaussian distribution and then inflate its variance to accommodate additional errors or biases in the actual distribution. While the errors and biases model in the aviation sector is well developed, in urban environments, the NLOS biases are complex and difficult to model.

The purpose of this work is to develop a novice test statistic for monitoring position integrity in urban environments. In real operations, the actual position error (PE)

cannot be assessed. Instead, a statistical measure on the PE, such as the PL, is used to represent the positioning performance. In this work, first we propose to match the CDF of observable position residuals to the referenced position error CDF overbound so that position integrity can be monitored by this transformed position residuals. The CDF overbound used in this part of the work is the Generalized Pareto Distribution (GPD). Before the transformation, the CDF of the position residuals may not or may have already overbound the CDF of the actual position error. Therefore, the transformation aims to optimally match the position residuals CDF to the referenced position error CDF overbound. The CDF matching is done using the CDF parameters transformation similar to the sigma inflation approach in CDF overbounding described in chapter 3.

In the second part of the work, we adopt the composite method of computing the HPL [16–18] because it is a straightforward way to take into account of both the random noise and the bias errors coming from the local environment. The composite approach decomposes the position errors in two components; a zero-mean noise term plus a bias. According to this approach, two bounds corresponding to both the noise and bias errors are added together to obtain composite HPL. The challenge of this methodology is on the capability of separating the noise from the MP/NLOS bias and characterizing the bias on-the-fly in order to compute the related HPL. In [155], the bias is computed by subtracting first a coarse estimation of the position noise, then modelling the remaining bias by an ARMA model and estimating the bias term via its transfer function. In our work, the noise component of the HPL is calculated using the PR variance model based on CNo and elevation angle. As for the additional term which represents the bias, the position residuals obtained from the least-square PVT algorithm are used.

As a chapter organization, it will first review some of the issues of using RAIM for integrity monitoring in urban environment. Then, an explanation on how the position error in urban environment can be characterized and overbound by a Generalized Pareto Distribution CDF (instead of Gaussian) for a specific type of receiver is provided along with the experimental results. Using these characterized position errors which are calculated off line, this chapter will then describe the proposed scheme for positioning integrity monitoring in urban environment that make use of the proposed test statistic. Then, the chapter continues with a brief review of the composite approach in monitoring positioning integrity. The concept to decompose the HPE and characterize the bias and the noise components are described. Using these characterized position bias and noise,

the proposed scheme for positioning integrity monitoring in urban environment that make use of the composite approach is explained. The results of the tests and analysis are presented before the chapter's conclusion.

6.2 RAIM with Gaussian assumption

Unlike GBAS or SBAS, RAIM algorithms do not rely on external information. It monitors integrity inside the receiver at the user level based on statistical consistency checks using redundant measurements. RAIM consists of two tests. The first one is to determine RAIM availability, i.e. if the conditions exist to execute a RAIM calculation. If RAIM is available, a test statistic is used to check if the estimated position is faulty, i.e. if there is any integrity violation.

In the first test, RAIM is available if a protection level (PL) is equal to or lower than the alert limit (AL). Essentially, PL is defined as a circular area centered at the user true position and is assured to contain the estimated position with a probability equal to or higher than 1 minus the probability of missed detection (P_{MD}). AL is the maximum acceptable PL for a specific application. If the PL exceeds the AL, RAIM is not available because it cannot monitor integrity with the required AL.

In RAIM, PL is computed as a projection of the bias in the PR with the maximum slope to the error in position domain. The slope parameter, which varies from one satellite to another, characterizes the linear relationship between PR bias projection in the position error and the test statistic in the faulty case. Since position errors are not directly measurable, the slope provides a link to infer position error based on the measurable scalar test statistic.

RAIM detects positioning failures when the test statistic exceeds certain threshold. For the range domain based RAIM, the baseline algorithms for failure detection mostly employ least-square or parity methods where the threshold is determined by using a probability of false alert (P_{FA}) [226]. Since the threshold is a function of either P_{FA} or P_{MD} which is chosen on the basis of statistical characteristics of the test statistic, it is the key factor that relates the two tests. Hence, it affects the trade-off between integrity risk and continuity risk.

The most common test statistic used in RAIM is the sum of the squared errors (SSE) which is computed from the measurement residuals. These errors are assumed to have a Gaussian distribution, and it follows that the P_{FA} and P_{MD} are assumed to have a chi-squared and non-central chi-squared distribution, respectively [227]. While these assumptions simplify calculations, in reality and notably in urban environments, the residual error distributions are not Gaussian and exhibit heavier tails than represented by the Gaussian model [9, 172]. The insight to the consequences from mis-modelling of the residual distributions on integrity is provided in [186] where the details are described in matrix form to show the effects of covariance uncertainty on the typical chi-squared integrity monitor. Chi-squared monitor assumes the elements of input distribution to be independent, zero mean with unit variance and if there is a bias in the input, the non-central chi-squared distribution is used. When those assumptions are false especially in the urban environment, the conventional RAIM algorithm fails to efficiently compute the decision threshold as both the chi-squared and non-central chi-squared distributions are invalid.

6.3 Position Error Characterization

In principle, GNSS positioning quality depends on the condition of the pseudorange measurements and the satellite geometry. However, for land navigation, characterizing positioning error of a receiver is not a simple matter because the positioning quality depends on the receivers operating environment, the type and characteristic of the receiver (such as its inside signal processing, stand-alone or hybrid), the positioning algorithms and the mitigation techniques being used. Usually, the user does not have access to these receiver design parameters. However, the positioning performance of a stand-alone GNSS receiver would probably be less robust as compared to the hybrid multi-sensor type receiver.

Due to the various affecting factors, a GNSS receiver performance cannot be predicted without knowing under which conditions it will be operated. Therefore, the receiver performance characteristic can only be defined statistically and must also be categorized in relation to the various operational environments which are relevant to the intended applications.

6.3.1 Horizontal Position Error Representation

In this work, the characterization of the receivers position error using the HPE distribution is obtained from the position error in the north and the east components. The errors are computed based on the difference between measured positions and referenced true positions:

$$\mathbf{E}_{pos} = \mathbf{X}_{measured} - \mathbf{X}_{ref} = \begin{bmatrix} E_{east} \\ E_{north} \end{bmatrix} \tag{6.1}$$

Due to the 2D nature of the horizontal error (north and east components), the HPE can be represented as a radial error and defined as:

$$HPE = \sqrt{E_{east}^2 + E_{north}^2} \tag{6.2}$$

6.3.2 HPE distribution in open sky environments

In open sky environments, in general the measured PR errors tend to be normally distributed. In estimating the receiver position using the measured PRs, these Gaussian PR errors are combined and propagated to the position domain via the linear estimation matrix to also form Gaussian distributed errors, i.e. the E_{east} and E_{north} also tend to be Gaussian distributed. Theoretically, assuming ideal conditions where the E_{east} and E_{north} distributions are also zero mean and independent, the distribution of their norm, which is the HPE, would be Rayleigh distributed.

Based on this assumption, the PDF and CDF of the HPE using the empirical data are computed and plotted in figure 6.1. The HPE has been computed using the difference between the measured position of the receiver and reference solution. The HPE distribution is then fitted to a Rayleigh distribution, where the CDF of a Rayleigh distribution is given by [228]:

$$CDF_{Rayleigh} = 1 - e^{-x^2/2\sigma^2} \tag{6.3}$$

and σ is the scale parameter of the distribution.

Figure 6.1 shows the PDF and the CDF of the HPE measured using a Ublox 4T receiver in the open sky environment. The histogram is obtained from the empirical data and the Rayleigh tracing is included to compare its form against the HPE PDF where a close resemblance is observed between them. The PDF shows the deviation of the HPE

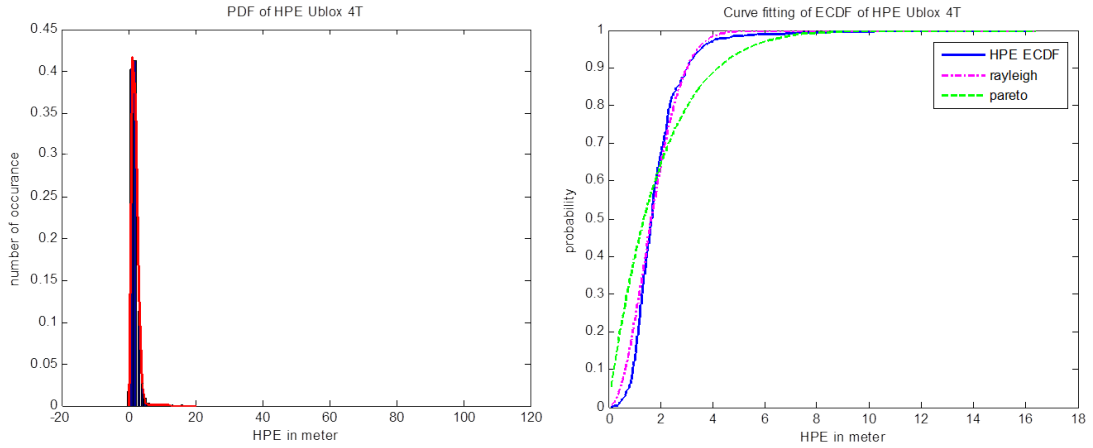

FIGURE 6.1: HPE PDF and CDF in open sky area

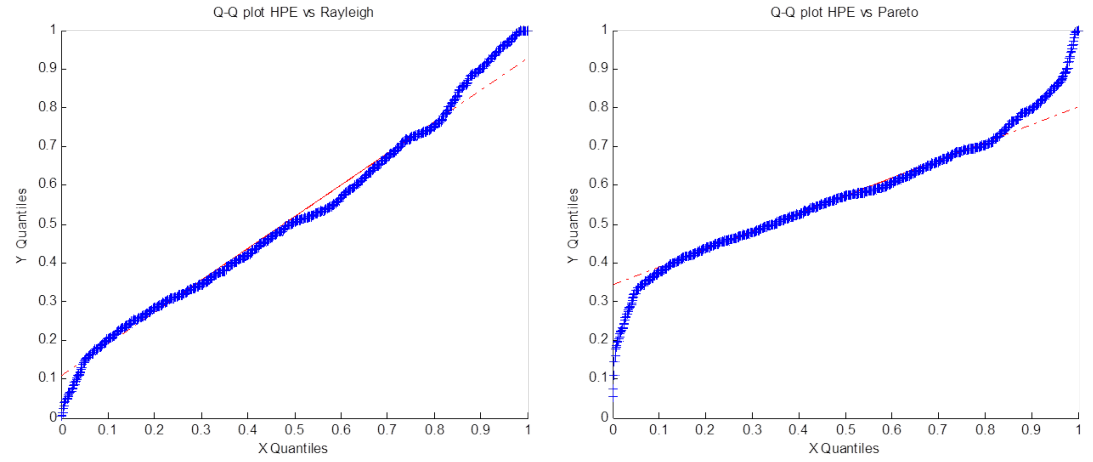

FIGURE 6.2: Q-Q plots comparing HPE vs Rayleigh Distribution (left) and HPE vs Generalized Pareto Distribution (right) in open sky

to be around 16 meters range. From the CDF plot, it can be seen that the HPE has a quite good accuracy of about 3 meters at 90% confidence, 4 meters at 95% confidence and 5 meters at 99% confidence level. When fitting the HPE CDF with Rayleigh and generalized Pareto CDFs, it appears that in the case of open sky, the Rayleigh CDF has a better fitting. This can be related to the fact that Pareto is more suitable for distribution with heavy tail. In the Q-Q plot in Figure 6.2, it can be seen also that the Rayleigh distribution has a better fitting with the HPE CDF when compared to Pareto distribution. Therefore, the results from these experiments indicate that the HPE distribution under open sky environments can be represented by a Rayleigh distribution.

6.3.3 HPE distribution in urban environments

In the case for urban environments, it has been shown that the distributions of the PR errors are likely non-Gaussian due to the biases from the multipaths and NLOS signal propagations. Even though according to the central limit theorem that the non-Gaussian ranging errors would cause the position-domain distribution tends towards a Gaussian distribution as the number of ranging measurements increases, such situation is not probable in the urban environments because the number of visible satellites tend to be limited due to blockage from buildings and other infrastructures. Because of these reasons, the curve fitting for the HPE in the urban environment is performed using the Pareto distribution.

In general, Pareto is suitable for distributions with heavy tail, such as the case of the position error in urban settings where there are plenty of large errors with small probabilities. The classical Pareto distribution (also known as Pareto distribution type I) has a tail function that describes the probability that X, as a random variable, is greater than some number x. This function is given by [229]:

$$\overline{F}(x) = Pr(X > x) = (\frac{x}{\sigma})^{-\alpha} \quad \text{for } x \geqslant \sigma \tag{6.4}$$

where σ is the scale parameter and α is a shape parameter. From this definition, it can be seen that $\overline{F}(x) = 1 - CDF_{Pareto_I}$. Therefore, the algebraically decreasing CDF of Pareto is given by:

$$CDF_{Pareto_I} = 1 - (\frac{x}{\sigma})^{-\alpha} \quad \text{for } x \geqslant \sigma \tag{6.5}$$

The generalized Pareto distribution (GPD) has a CDF expressed as:

$$F(x) = \begin{cases} 1 - (1 + \frac{\xi(x-\mu)}{\sigma})^{\frac{-1}{\xi}} & \text{for } \xi \neq 0 \\ 1 - exp(-\frac{x-\mu}{\sigma}) & \text{for } \xi = 0 \end{cases} \tag{6.6}$$

Figure 6.3 shows the PDF of the HPE of a Ublox 4T receiver in the urban environment. The PDF shows a distribution that has a deviation of about 40 meters, indicating a wider error range than in the open sky area. Comparing the HPE PDF against a Rayleigh distribution tracing (top 2 figures), it can be seen that the HPE distribution is significantly different than the Rayleigh tracings with $\sigma = 3$ (top left figure) and with

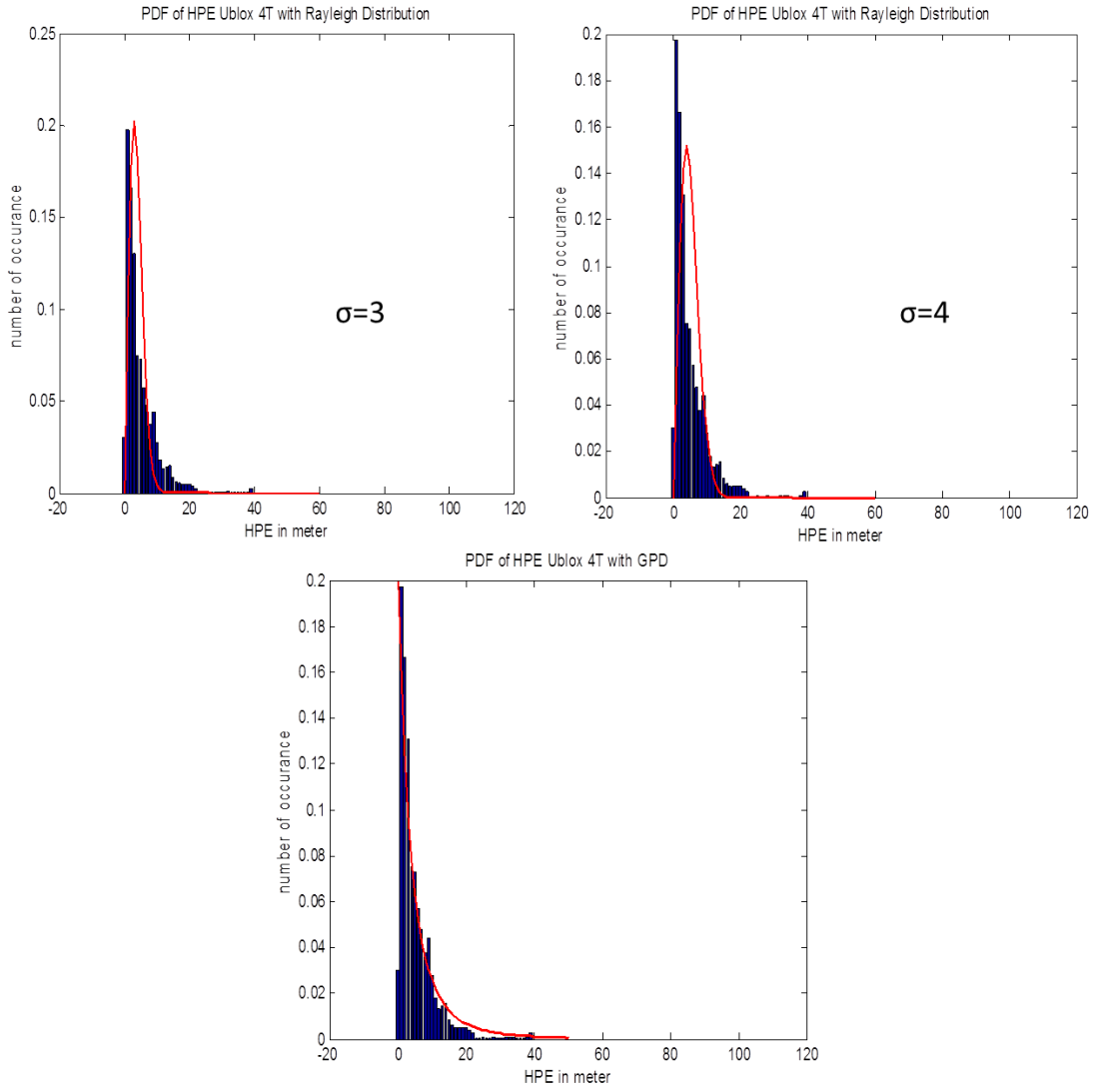

FIGURE 6.3: PDF comparison in urban environment

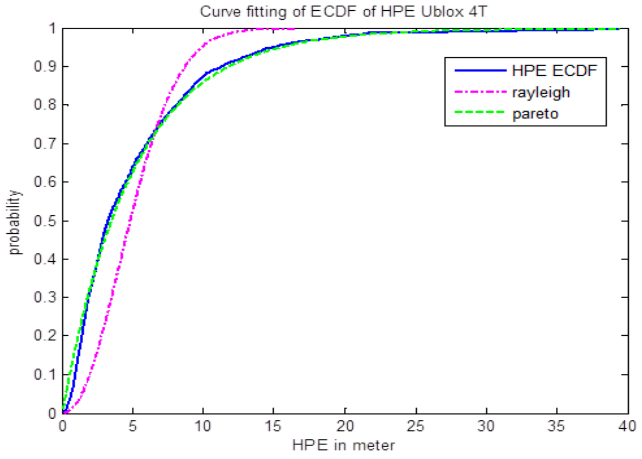

FIGURE 6.4: CDF in urban environment

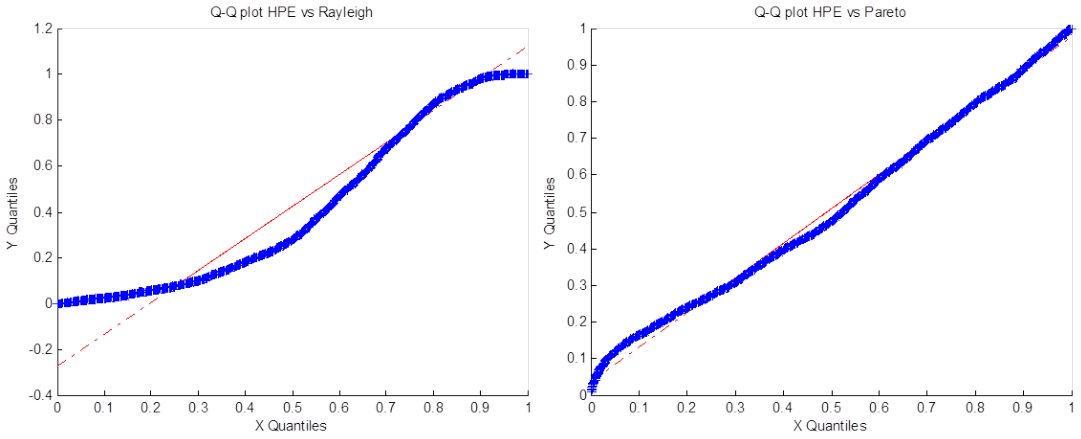

FIGURE 6.5: Q-Q plots comparing HPE vs Rayleigh Distribution and HPE vs Generalized Pareto distribution (urban environment)

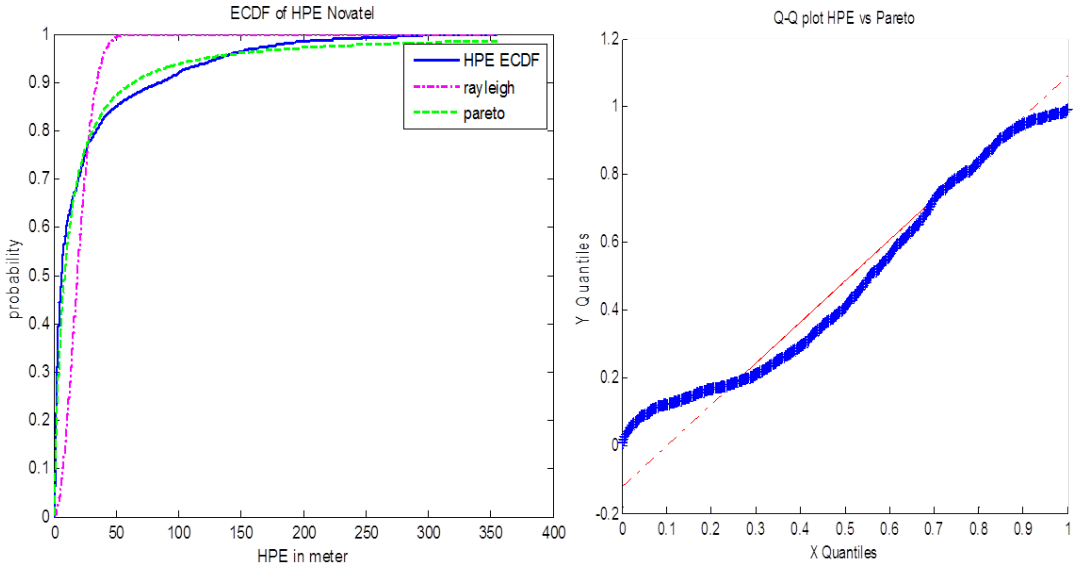

FIGURE 6.6: CDFs and Q-Q Plot for Novatel receiver in urban environment

$\sigma = 4$ (top right figure). On the other hand, the comparison with generalized Pareto tracing (bottom figure) shows a better fitting of the heavy tail of the HPE PDF.

From the HPE CDF in figure 6.4, the accuracy of the positioning is about 11 meters at 90% confidence and 15 meters at 95% confidence. This increase of error and the change of distribution shape are mainly due to the biases from multipath and NLOS in urban environment. In term of curve fitting, the CDF plots show that the GPD has better fitting than Rayleigh. In the Q-Q plots of figure 6.5, it can be observed also that the Pareto distribution has a better fitting with the HPE than the Rayleigh distribution when in urban environment.

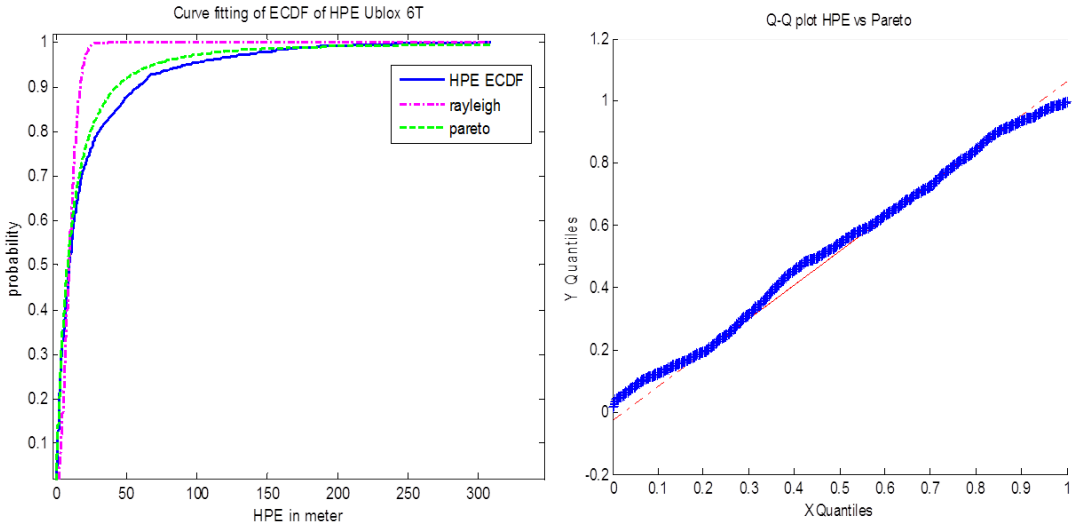

FIGURE 6.7: CDFs and Q-Q Plot for Ublox 6T receiver in urban environment

Figure 6.6 shows the curve fitting of the HPE CDF for a Novatel receiver in urban environment. In this case, the generalized Pareto distribution also has a good fitting as compared to the Rayleigh distribution, as can be seen in the CDF plots, and the Q-Q plot of the GPD. Good fitting of the HPE CDF with Pareto CDF in urban environment is also observed for the Ublox 6T receiver (figure 6.7).

The observed results from the 3 receivers (Ublox 4T, Novatel, and Ublox 6T) suggest that generalized Pareto distribution is suitable to model the HPE distributions in urban environment.

6.3.4 Along-street and across-street error distributions in urban environments

In the urban environment, apart from the radial HPE characterization, the position errors are also observed in terms of "along the street" and "across the street" errors. For some land navigation applications (such as lane keeping), this along street (forward) errors and across street (lateral) errors characterization could be a more suitable alternative to the HPE in the radial form. The geometric configuration affects differently for these errors in two directions depending on the street orientation in space.

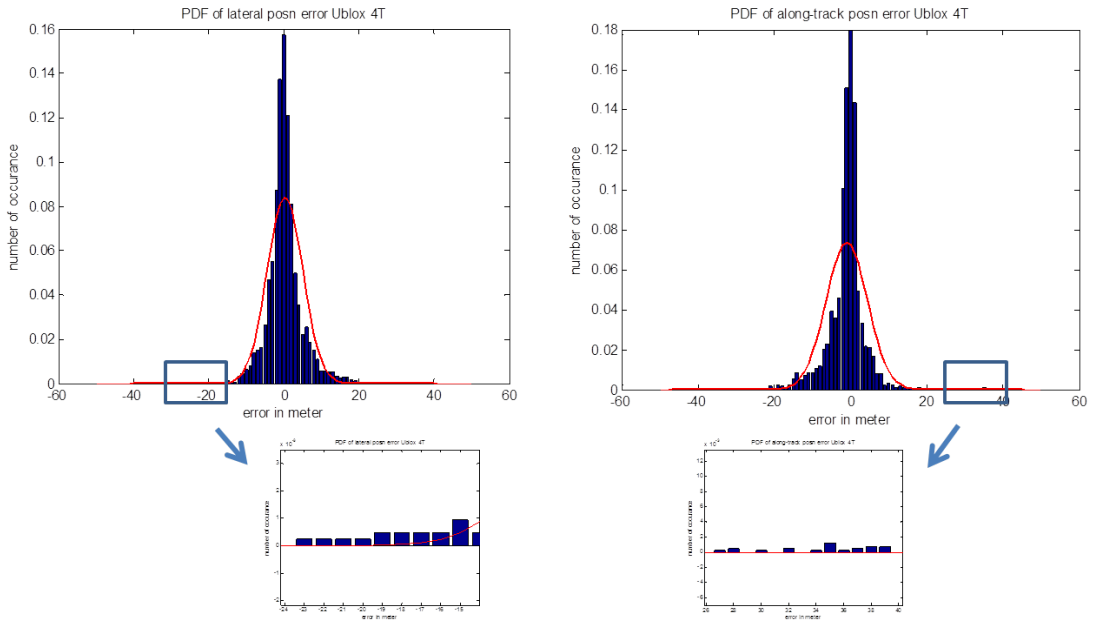

FIGURE 6.8: PDFs of lateral and along-track position errors

In order to convert the E_{east} and E_{north} to E_{fwd} and $E_{lateral}$, $\mathbf{E}_{pos}$ is multiplied with a rotational matrix $\mathbf{R}$ [230]. Therefore,

$$\mathbf{E}_{fwd,lat} = \begin{bmatrix} E_{fwd} \\ E_{lateral} \end{bmatrix} = \mathbf{R}.\mathbf{E}_{pos} \tag{6.7}$$

where

$$R = \begin{bmatrix} \cos\theta & \sin\theta \\ -\sin\theta & \cos\theta \end{bmatrix}, \quad \theta = atan2(ref_{\Delta N}, ref_{\Delta E})$$

$ref_{\Delta N}$ is the distance of 2 consecutive referenced positions in the North direction

$ref_{\Delta E}$ is the distance of 2 consecutive referenced positions in the East direction

Figure 6.8 shows the PDF plots of the along-track position errors and the lateral position errors in urban environment using a Ublox 4T receiver. In this case, the position errors have both positive and negative value range. Generally, both PDFs have heavy tails as compared to standard Gaussian distribution as shown in Figure 4a.

In figure 6.9, their CDF plots are fitted with a normal CDF, Student-T CDF and Pareto CDF for comparison. It can be seen that the Pareto has the best fit for both along-track error and lateral error CDFs.

Figure 6.10 and 6.11 respectively show the lateral and along track errors using a Novatel

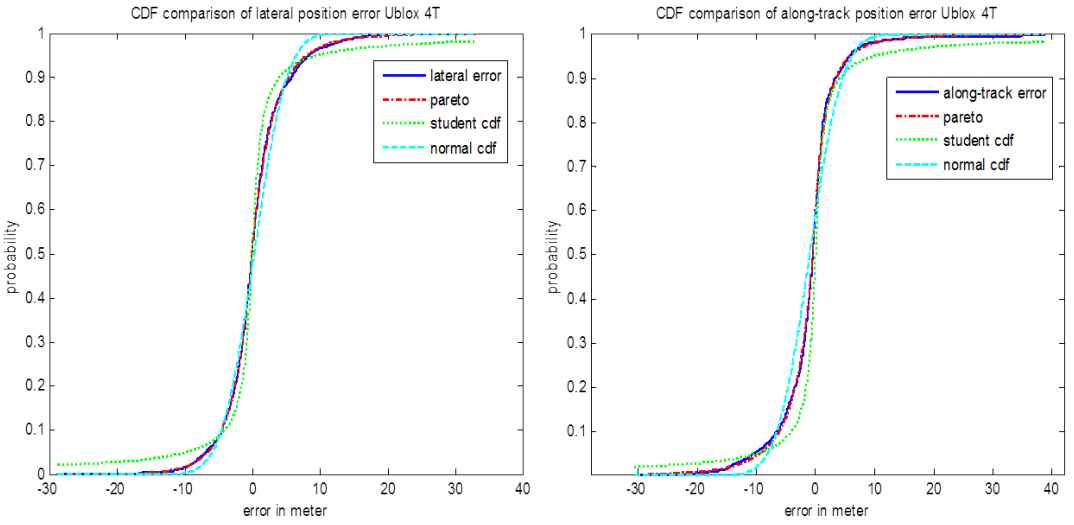

FIGURE 6.9: CDF curve fitting for lateral and along-track position errors for Ublox 4T receivers

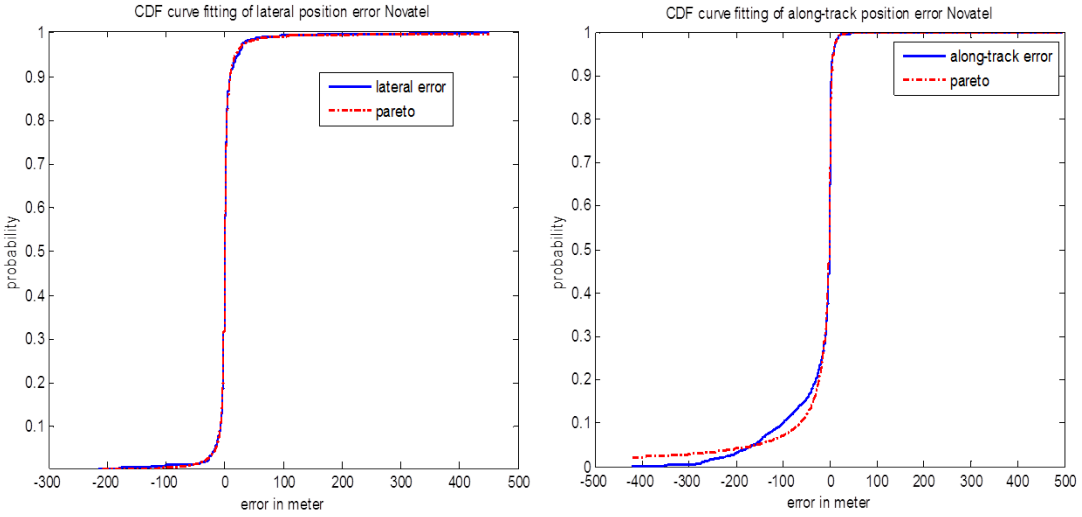

FIGURE 6.10: CDF curve fitting for lateral and along-track position errors for Novatel receivers

and a Ublox 6T receivers that are being fitted by the Pareto distribution. From the plots, the GPD shows good fitting with the CDF of the lateral and along track errors.

Alternatively, the along-track and lateral position error could also be represented in their squared values. Figure 6.12 shows their CDF plots. In this form, their CDF can also be well fitted by the Pareto CDF as shown.

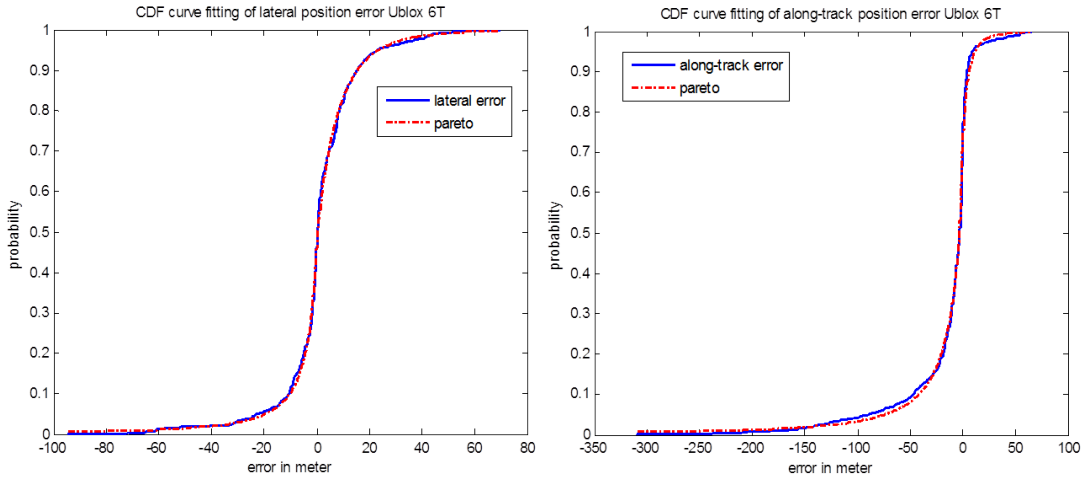

FIGURE 6.11: CDF curve fitting for lateral and along-track position errors for Ublox 6T receivers

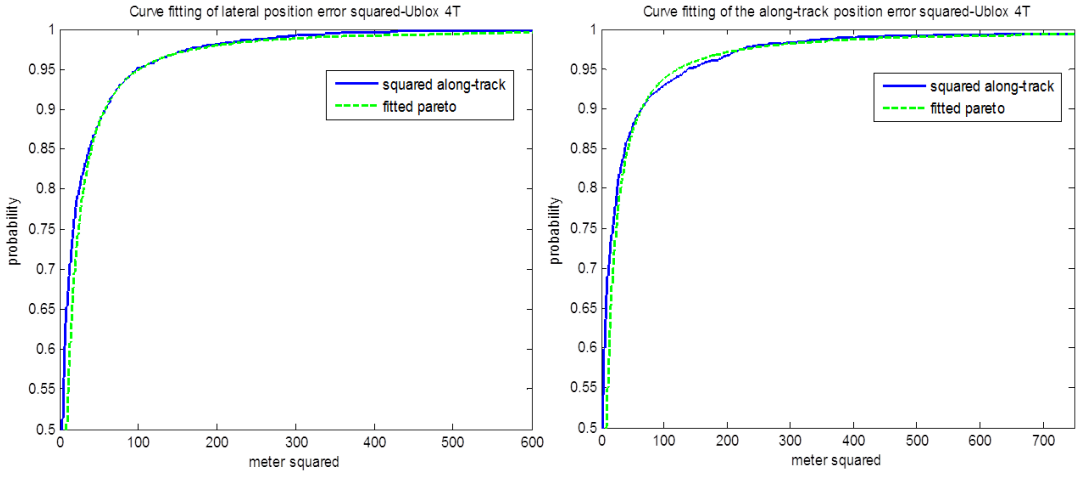

FIGURE 6.12: CDF curve fitting for lateral squared and along-track squared position errors for Ublox 4T receivers

6.4 Direct position domain overbounding using generalized Pareto CDF

Error ellipse is related to the positioning confidence level or integrity by the HPE cumulative distribution function. Once the CDF of the HPE is estimated, a protection radius of integrity can be computed from the inverse of the CDF.

The two-dimensional horizontal position error (HPE) may be represented in a form of a radial error or an error ellipse, R_{emp}. Then, this error ellipse is related to the positioning confidence level or integrity, P_b, by the HPE cumulative distribution function. Once the

CDF of the HPE is estimated, an overbounding HPL can be computed from the inverse of the CDF [179].

$$F_R(R_{emp}) = Prob(position\,error \leqslant R_{emp}) = P_b = 1 - P_{HMI} \tag{6.8}$$

therefore,

$$R_{emp} = F_R^{-1}(P_b) = Inverse\,CDF(P_b) \tag{6.9}$$

As has been shown earlier in section 6.3.3 the HPE of a certain receiver in urban environment may be characterized by a Generalized Pareto Distribution (GPD) CDF. Therefore, by implementing the concepts of direct position domain and CDF overbounding (described in chapter 3), the GPD is used to overbound the HPE. This approach of positioning error characterization allows the calculation of HPL from the CDF based on the required probability of highly misleading information (P_{HMI}).

The CDF of a GPD has the following form:

$$CDF_{GPD} = 1 - [1 + \xi(\frac{x-\mu}{\sigma})]^{\frac{-1}{\xi}}\ for\ x \geqslant \mu \tag{6.10}$$

where the scale parameter σ affects the size and slope of the distribution, the shape parameter ξ affect the shape of the tail of the distribution and the location parameter μ is related to the value of x when the CDF = 0.

Once the generalized Pareto CDF overbound the CDF of the HPE, the Horizontal Protection Level can be calculated from its inverse. Given,

$$CDF_{GPD} = 1 - [1 + \xi(\frac{x-\mu}{\sigma})]^{\frac{-1}{\xi}} = Prob(position\ error \leqslant x) \tag{6.11}$$

Let R_p be the PL of position error. Equating the CDF to integrity probability P_B,

$$1 - [1 + \xi(\frac{R_p-\mu}{\sigma})]^{\frac{-1}{\xi}} = (1 - P_{HMI}) = P_B \tag{6.12}$$

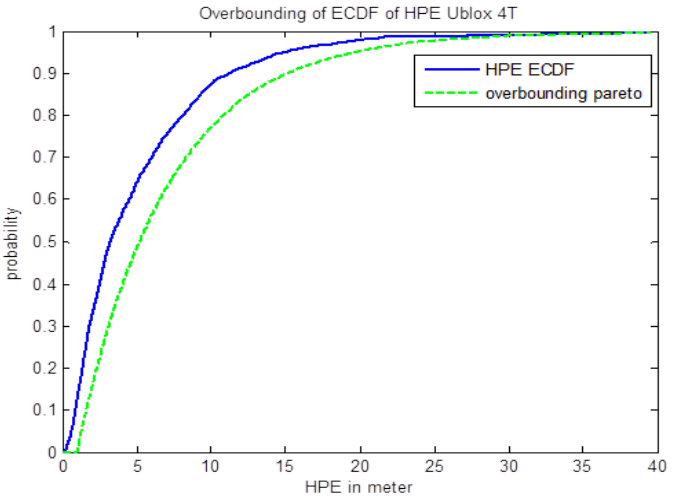

FIGURE 6.13: Overbounding of the HPE by GPD

To obtain the HPL, solve for R_p,

$$\begin{aligned}
[1+\xi(\frac{R_p-\mu}{\sigma})]^{\frac{-1}{\xi}} &= 1-P_B \\
\frac{-1}{\xi} ln[1+\xi(\frac{R_p-\mu}{\sigma})] &= ln(1-P_B) \\
ln[1+\xi(\frac{R_p-\mu}{\sigma})] &= -\xi ln(1-P_B) \\
[1+\xi(\frac{R_p-\mu}{\sigma})] &= (1-P_B)^{-\xi} \\
\xi(\frac{R_p-\mu}{\sigma}) &= (1-P_B)^{-\xi}-1
\end{aligned}$$

Hence,

$$HPL = R_p = \frac{\sigma}{\xi}[(1-P_B)^{-\xi}-1]+\mu \tag{6.13}$$

Figure 6.13 shows the overbounding of the HPE by the generalized Pareto CDF for the case of Ublox 4T receiver. It can be seen that it complies with the CDF overbounding requirement. For the result in this experiment, the HPL for 90% integrity is 15 meters (HPE at 12 meters) and for 95% integrity is 20 meters (HPE at 15 meters). The tightness of the overbounding may be considered reasonable. While tighter overbound will improve availability in general, specific application requirements must also be taken into consideration especially for those which need ample safety distance.

6.5 Position Integrity Monitoring for Urban Environments

In real time positioning, the true position error is not accessible. Therefore, for monitoring the position integrity, some test statistic is used and this test statistic has to be calculated based on some observable measurements. In this work, the integrity of the estimated positions in urban environments is monitored based on the horizontal position residual.

In this approach, the observable horizontal position residual is calculated using least square (LS) estimation, and then matched to the HPE overbound which is characterized a priori by the GPD CDF. This way, the test statistic is able to represent the overbound of the HPE. The mapping of the position residual space to the overbounding position error space may be described by the principle of random variable transformation.

6.5.1 Horizontal Position Residual Calculation

The position residual vector, $\delta\hat{x}$ is calculated using the Least Square (LS) estimation. Consider the following linear pseudorange model:

$$\Delta Y = H.\Delta X + E \tag{6.14}$$

For Least Square estimation,

$$\Delta\widehat{X} = G.\Delta Y \tag{6.15}$$

where

- $G = (H^T H)^{-1} H^T$
- $\Delta\widehat{X}$ is the estimated position
- ΔY is the measured PRs

The PR residual is:

$$\delta\rho = \Delta Y - H\Delta\widehat{X} \tag{6.16}$$

Hence, the position residual is:

$$\delta\hat{x} = G.\delta\rho \tag{6.17}$$

Then, the horizontal position residual, $HPE_{\delta\hat{x}}$ is calculated by taking the norm of the $\delta\hat{x}$ in the north and east directions:

$$HPE_{\delta\hat{x}} = \sqrt{\delta\hat{x}_{east}^2 + \delta\hat{x}_{north}^2} \tag{6.18}$$

6.5.2 Calculation of the matching parameters

Fitting the CDF of $HPE_{\delta\hat{x}}$, denoted as HPE_R to Generalized Pareto Distribution gives the relation,

$$HPE_R = \frac{\sigma}{\xi}[(1 - P_B)^{-\xi} - 1] + \mu \tag{6.19}$$

$$HPE_R = \frac{\sigma}{\xi}[(P_{HMI})^{-\xi} - 1] + \mu \tag{6.20}$$

The HPE_R parameters: σ, ξ and μ are determined from curve fitting of experimental data from the same trajectory which the HPE were calculated.

In order to calculate the matching parameters, the CDF parameters of the horizontal position residual, HPE_R, is matched to the predetermined CDF parameters that overbound the HPE which have been calculated off line.

The bounding GPD CDF of the characterized horizontal position error used for HPL calculation is,

$$HPL = \frac{\sigma_o}{\xi_o}[(P_{HMI})^{-\xi_o} - 1] + \mu_o \tag{6.21}$$

Then, what is desired: $Matched\ HPE_R = HPL$

So let,

$$A\sigma = \sigma_o,\ B\xi = \xi_o,\ \mu + C = \mu_o$$

Therefore,

$$Matched\ HPE_R = \frac{\sigma.A}{\xi.B}[(P_{HMI})^{-\xi.B} - 1] + \mu + C \tag{6.22}$$

and the matching parameters are:

$$A = \frac{\sigma_o}{\sigma},\ B = \frac{\xi_o}{\xi},\ C = \mu_o - \mu \tag{6.23}$$

6.5.3 Test statistic derivation

The $Matched\ HPE_R$ provides the basis to calculate the test statistic for position integrity checking. For monitoring the position integrity, the test statistic is calculated based on the observable $HPE_{\delta\hat{x}}$:

$$Matched\ HPE_R = \frac{\sigma.A}{\xi.B}[P_{HMI})^{-\xi.B} - 1] + \mu + C \tag{6.24}$$

Rearrange the equation and substitute,

$$\begin{aligned}
Matched\ HPE_R - (\mu + C) &= \frac{\sigma.A}{\xi.B}[(P_{HMI})^{-\xi.B} - 1] \\
Matched\ HPE_R - (\mu + C) &= \frac{\sigma}{\xi}[(1 - P_B)^{-\xi} - 1]\frac{A}{B}[\frac{(P_{HMI})^{-\xi.B} - 1}{(P_{HMI})^{-\xi} - 1}] \\
Matched\ HPE_R - (\mu + C) &= (HPE_R - \mu)\frac{A}{B}[\frac{(P_{HMI})^{-\xi.B} - 1}{(P_{HMI})^{-\xi} - 1}] \\
Matched\ HPE_R &= (HPE_R - \mu)\frac{A}{B}[\frac{(P_{HMI})^{-\xi.B} - 1}{(P_{HMI})^{-\xi} - 1}] + \mu + C
\end{aligned} \tag{6.25}$$

Therefore

$$Test\ Statistic = (HPE_{\delta\hat{x}} - \mu)\frac{A}{B}[\frac{(P_{HMI})^{-\xi.B} - 1}{(P_{HMI})^{-\xi} - 1}] + \mu + C \tag{6.26}$$

$$Test\ Statistic = Matched\ HPE_{\delta\hat{x}}$$

Once the matching parameters A,B and C are determined, positioning integrity can be monitored by calculating the test statistic on line and comparing it against the threshold.

As a summary (figure 6.14), the process to develop the proposed integrity monitoring scheme is as follows. First, the data of the actual position errors and the position residuals are gathered at the same time along a certain trajectory in an urban environment. From the collected data of the position errors, the ECDF of the HPE is determined and then, it is bounded by a generalized Pareto CDF. In this work, this overbounding CDF is denoted as HPL. Subsequently, the horizontal position residual ($HPE_{\delta\hat{x}}$) is determined and modelled also by a generalized Pareto distribution (denoted as HPE_R). After that, in order for the HPE_R to represent the overbound of the HPE (i.e. the HPL), the HPE_R has to be matched to the HPL by tuning or adjusting the values of the HPE_R parameters as described in section 6.5.2. Once the matching parameters are

Step 1	**Select a route in an urban environment.**
Step 2	**Take the PRs and positions measurements and also the reference (actual) positions along the route at the same time.**
Step 3	**Determine positioning errors by taking the difference between measured positions and reference positions.**
Step 4	**From the position errors, calculate the horizontal position errors (HPE) and determine the CDF of the HPE.**
Step 5	**Determine the overbound of the HPE CDF. This overbound is modelled using Pareto CDF and designate as HPL.**
Step 6	**From the PRs and positions measurements, determine the position residuals along the route. Then, calculate the CDF of the position residuals and denote as HPE$_R$. This HPE$_R$ is also modelled using Pareto CDF.**
Step 7	**Match the HPE$_R$ to the HPL. In this process, the matching parameters are determined.**
Step 8	**By matching the HPE$_R$ to the HPL, we have the values of the HPE$_R$ that correspond to the values of the HPL .**
Step 9	**The HPL can be used as an integrity indicator for positioning but we cannot monitor the HPL in real time since there is no reference position.**
Step 10	**However, we can monitor the HPE$_R$ in real time. Therefore, since we have matched the HPE$_R$ to the HPL, we can indirectly monitor the HPL values by monitoring the HPE$_R$.**

FIGURE 6.14: Summary of integrity monitoring process

obtained, the matched horizontal position residual ($Matched\ HPE_{\delta\hat{x}}$) can be used as a test statistic to monitor the integrity of the positioning.

The proposed integrity monitoring scheme for urban environment is shown in Figure 6.15. First, The HPL is calculated based on the required probability of hazardous misleading information, P_{HMI}. This HPL is compared against the HAL for the intended application to determine whether the integrity monitoring is available. If the required HAL is less than the HPL, the integrity cannot be monitored. Then, the integrity checking is performed by comparing a test statistic to the threshold. As long as the test statistic is not more than the threshold, the positioning integrity is considered to

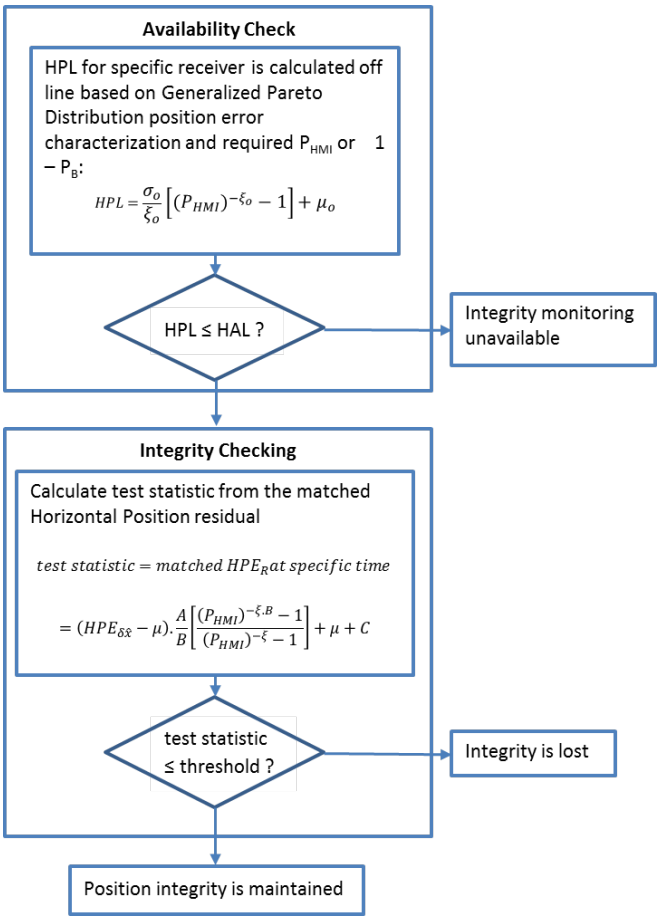

FIGURE 6.15: Integrity monitoring scheme for urban environments

be maintained. The threshold can be set depending on the required P_{HMI} which then gives the maximum HPL as the threshold using equation 6.21.

Note that in this approach, the observable distribution is matched to the overbounding HPL. As a consequence, unlike the traditional RAIM, the test statistics distribution is matched to ensure similar conservative overbounding of the HPE like the HPL.

6.6 The Composite Approach in Monitoring Integrity

In dealing with non-zero mean error distribution, two approaches have been generally developed to calculate the PL. In one approach, the biases are considered as a multiple of noise and formulated as PL for the errors. Largely known as the sigma inflation approach, this method is the one implemented with the SBAS and GBAS. The rms PRs errors are inflated to accommodate the biases which result in the PL as a probabilistic

bound for the sum of noises and biases. Further description of this approach can be found for example in [16, 19, 231].

The other approach is the composite approach, where biases are treated independent of noise. It is assumed in this method that the noise can be modelled as a zero-mean Gaussian distribution. Even though this approach has not been adopted by the civil aviation authorities, many studies pertaining to the concept have been done and available for example in [16–19].

In composite approach, the PL can be formulated as a sum of a noise component, PL_n plus a bias component, PL_b:

$$PL = PL_n + PL_b \tag{6.27}$$

The calculation for the case of zero mean Gaussian noise PL:

$$PL_n = K_n \sigma_p \tag{6.28}$$

with

$$\sigma_p = \sqrt{\sum_{i=1}^{N} S_i^2 \sigma_i^2}$$

and

$$K_n = \sqrt{2} erfc^{-1}(P_{HMI})$$

σ_p is the root of the sum squares of the weighted range-domain sigmas for each of the total N observed satellites, and K_n describes the inverse cumulative distribution that associate the sigma with the integrity probability, P_b which is equal to $1 - P_{HMI}$ [175, 180]. Let μ_i be the bias of each PR, then PL_b is the total bias expressed as:

$$PL_b = \sum_{i=1}^{N} S_i \mu_i \tag{6.29}$$

In civil aviation, specific sources and effects of the bias have been considered and modelled. Some of these models such as the absolute bias model, sigma-relative bias model and piecewise-linear bias model are described in [19]. However, in urban environments, the biases are mainly due to NLOS and multipath receptions which are difficult to model,

hence it is very difficult to come up with an expression of PL_b. In the open-sky environment, the main advantage of treating the noise and bias separately is the final net decrease of the PL [232]. This is due to the much smaller noise bound and typically, this reduction is more than the increase in the bias bound.

6.6.1 Position error decomposition and characterization

In order to implement the composite approach for position integrity monitoring in urban environments, the HPE need to be decomposed into the bias component and the Gaussian noise component and then characterized. While there are several techniques exist in the error distribution decomposition, in this work we choose the autoregressive (AR) model to estimate the HPE time-series since it is suitable and quite straight forward to decompose the errors into Gaussian noise and bias components.

$$HPE = AR(p) + \epsilon \tag{6.30}$$

The first order $AR(1)$ can be written as:

$$x_t = \phi x_{t-1} + \epsilon_t \tag{6.31}$$

where ϵ_t $N(0, \sigma^2)$

For the order p, the $AR(p)$ is given as:

$$x_t = \phi_1 x_{t-1} + \phi_2 x_{t-2} + \cdots + \phi_p x_{t-p} + \epsilon_t \tag{6.32}$$

rearrange the equation,

$$\epsilon_t = x_t - \phi_1 x_{t-1} - \phi_2 x_{t-2} - \cdots - \phi_p x_{t-p} \tag{6.33}$$

Therefore, it can be seen that this model decomposes the error into a Gaussian noise component ϵ_t and other regressive components which can be representative of bias. Several techniques can be used in estimating the AR coefficients such as the Yule-Walker solution, forward-backward approach and Burgs method. In this work, 4th order AR

is used and Burgs method is selected because it always produces causal models and provides higher Gaussian likelihood more often than the Yule-Walker method [20].

The next step is to extract the noise from the bias so that they can be characterized separately. This can be done by filtering the time series accordingly. The filter transfer function in the z-transform is given by:

$$Y(z) = (1 - \phi_1 z^{-1} - \cdots - \phi_p z^{-p})X(z) \tag{6.34}$$

where $Y(z)$ is the z-transform of ϵ_t. Since ϵ_t is assumed to be a zero-mean Gaussian noise, it can be characterized by its variance, σ_ϵ^2.

Once the ϵ_t is obtained, $bias_t$ is calculated by:

$$bias_t = HPE_t - \epsilon_t \tag{6.35}$$

Unlike in the open sky environment, bias in the urban environments are mainly due to MP and NLOS receptions which make their modelling to be very complex deterministically. Hence in this work, the bounding of the bias will be done using the statistical approach where the bias distribution will be bounded by a Gaussian distribution. As such, the bounding distribution of bias can be characterized as [19]:

$$HPE_{bias} = \mu_b + \sigma_b\sqrt{2}erf^{-1}(2P_b - 1) \tag{6.36}$$

where P_b is the integrity probability. In a simplified notation,

$$HPE_{bias} = \mu_b + \sigma_b K_H \tag{6.37}$$

The values of μ_b and σ_b are obtained a priori from the bounding curve fitting of the HPE bias ECDF.

6.6.2 The calculation of composite HPL

It has been established that in real operations, the actual HPE cannot be assessed. As a solution, a statistical measure on the HPE, such as the HPL, is used to represent the

positioning performance. For the composite approach, the HPL needs to be calculated for the bias and the noise components.

a. HPL for the noise component

Unlike the augmentation systems such as SBAS and GBAS, land vehicle positioning in urban environment does not have references. Hence the noise variance to be used for calculating the HPL is obtained from the PR variance model. In this work, the PR variance of the CNo-Elevation model [21] is adopted:

$$\sigma_i^2 = k \times \frac{10^{(-0.1 \times CNo_{measured})}}{\sin^2(\theta_i)} \tag{6.38}$$

where k equal to 1 for LOS signal and changes for NLOS signal.

Equation 6.28 shows the HPL for a zero-mean Gaussian distribution. However, in the implementation, there exist some elements of uncertainty since the estimation of the noise distribution from the HPE is not perfect and σ_p is obtained from a PR variance model which is different from the σ_ϵ of the estimated HPE noise. Therefore, as commonly practised in the civil aviation, the sigma needs to be inflated to compensate for these uncertainties and ensure that the HPL noise bounds the HPE noise.

In [233], the inflation factor f (to inflate σ_i) is incorporated in the VPL as follows:

$$VPL_{inflated} = K_{ffmd}\sqrt{\sum_{i=1}^{N} S_i^2 (f.\sigma_i)^2} \tag{6.39}$$

Whereas in [232], the VPL is inflated in the position domain with inflation factor ξ such that:

$$VPL_{inflated} = \xi K_V \sigma_p \tag{6.40}$$

In this work, the inflation of the HPL noise is implemented in the position domain with an inflation factor A such that:

$$HPLnoise_{inflated} = A.K_H \sigma_p \tag{6.41}$$

To estimate A, we equate the $HPLnoise_{inflated}$ to the bounding distribution of ϵ_t so that:

$$A.K_H\sigma_p = K_H\sigma_\epsilon \tag{6.42}$$

and therefore

$$A = \frac{\sigma_\epsilon}{\sigma_p} \tag{6.43}$$

where σ_ϵ is the std. div. of HPE noise and σ_p is the std. div. of predicted position error based on PRs variance model.

b. HPL for the bias component

The HPL for bias is based on the position residual (which is observable in real time) and then inflated/matched statistically to bound the empirical CDF of HPE decomposed bias. The CDF matching is done using the CDF parameters transformation similar to the sigma inflation approach in CDF bounding.

The position residual CDF is:

$$HPE_r = \mu_r + K_H\sigma_r \tag{6.44}$$

Inflating the HPE_r becomes:

$$HPLbias_{inflated} = \mu_r + B + C.K_H\sigma_r \tag{6.45}$$

Rearrange and substitute 6.44 into 6.45,

$$HPLbias_{inflated} = HPE_r - K_H\sigma_r + B + C.K_H\sigma_r \tag{6.46}$$

$$HPLbias_{inflated} = HPE_r + B + (C-1).K_H\sigma_r \tag{6.47}$$

To estimate parameters B and C, let

$$\mu_r + B = \mu_b$$

and

$$C.K_H\sigma_r = \sigma_b K_H$$

where μ_b and σ_b are parameters from 6.37. Hence,

$$B = \mu_b - \mu_r \tag{6.48}$$

i.e, the mean of $HPLbias_{inflated}$ is shifted to match the mean of $HPEbias$, and

$$C = \frac{\sigma_b}{\sigma_r} \tag{6.49}$$

i.e, the sigma of $HPLbias_{inflated}$ is inflated to match the sigma of $HPEbias$.

6.7 Equipment, Data Collection and Testing

The data for the experiments were collected along the trajectories in downtown Toulouse for both parts of the works(Figure 6.16). The reference data along the trajectory are provided by the SPAN Novatel GPS/IMU-FSAS system with decimeter level of accuracy. For the work on GPD, the GPS signals are measured using u-blox LEA-4T receiver.

The collected data were sampled at 1 Hz. The duration and the number of the gathered samples depends on the trajectory. For Trajectory 1, 2, 3 and 4, the collected data are 4257, 3278, 5098 and 4852 samples respectively. The duration taken varies from about 1 hour to 1.5 hours.

However, the samples need to be independent. The issue with MP and NLOS signals is that they are correlated. In order to attenuate this effect, the collected data is further re-sampled. In this work, we down-sample the data at the 10th sample after the previous sample (i.e we skip 9 samples in between the selected samples). Based on the difference between referenced positions and measured positions, the CDF of the horizontal position errors were determined empirically along 4 designated trajectories. Then, each of these respective HPE CDFs was overbound by a generalized Pareto distribution. The position residuals were calculated from the measured PRs using the LS approach as described earlier.

There are two parts of the test. The first one is to determine how well the position residual can be matched to the overbounding GPD CDF and to see if it overbounds the HPE. The results are analyzed based on the CDF plots comparison.

FIGURE 6.16: Example of the trajectory for data collection in downtown Toulouse

In the second part of the test, the performance of the proposed test statistic was observed. Based on the set threshold, the integrity of positioning was monitored and the Probability of Missed Detection (P_{MD}) and the probability of False Alert (P_{FA}) were calculated to compare with the selected integrity requirement. In this work, the probabilities are defined as:

$$P_{FA} \sim \%\text{test statistic} > \text{threshold; HPE} \leqslant \text{HAL}$$

$$P_{MD} \sim \%\text{test statistic} \leqslant \text{threshold; HPE} > \text{HAL}$$

As for the work on the composite approach, the receivers used are the Ublox 4T, Novatel and Septentrio AsteRx4 receivers. The Ublox 4T and Novatel used the same trajectory with 5,098 samples at 1Hz sampling rate (about 1.5 hours) . The Septentrio AsteRx4, which is a multi-constellation receiver, used a different trajectory with 12,447 samples at 0.5 Hz sampling rate (about 1 hour and 40 minutes). The collected data are also down sampled similarly like the previous data to attenuate the correlation effect. In order to obtain the positioning errors, the measured positions are compared along the trajectories to the reference positions which were also obtained from a high grade navigation system (SPAN Novatel GPS/iMAR IMU).

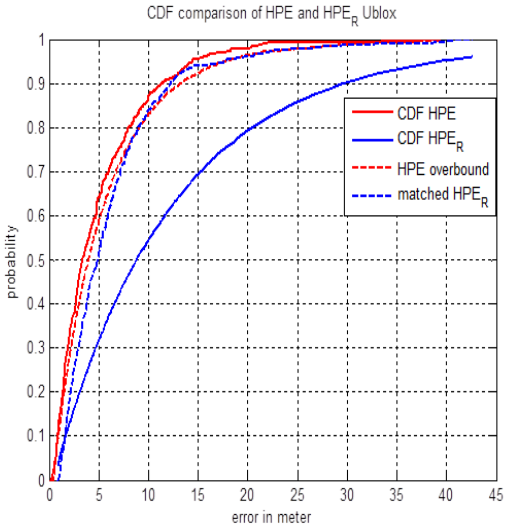

FIGURE 6.17: Result of matching position residual to overbounding CDF (Trajectory 1)

6.8 Results and analysis

6.8.1 Results on GPD

a. Matching of Horizontal Position Residuals to the Overbounding CDF

Each Figure 6.17, 6.18, 6.19 and 6.20 plots HPE CDF (solid red), its overbounding CDF (dashed red), position residual CDF (solid blue) and the matched position residual CDF (dashed blue) for each trajectory 1, 2, 3 and 4. Overall, it can be seen in each figure that, the matched position residual CDF does overbound the HPE CDF. However, in term of matching with the overbounding GPD CDF, trajectory 1 and 2 performed better than trajectory 3 and 4. This situation occurred depending on how well is the curve fitting of the position residual CDF which is then used to determine the matching parameters A, B and C (shown in Table 6.1). In a worse case situation, this bad matching may even cause the matched position residual CDF not to overbound the HPE CDF. However, this situation can be overcome by tuning these parameter values in order to achieve a better matching.

From Table 6.1, it can be observed also that each trajectory has different sets of matching parameter values. In this work, each trajectory has only a few thousands of samples. When dealing with statistical distributions, the assumption of ergodicity and stationarity are usually made. However, most real life situations do not meet exactly the ergodicity or

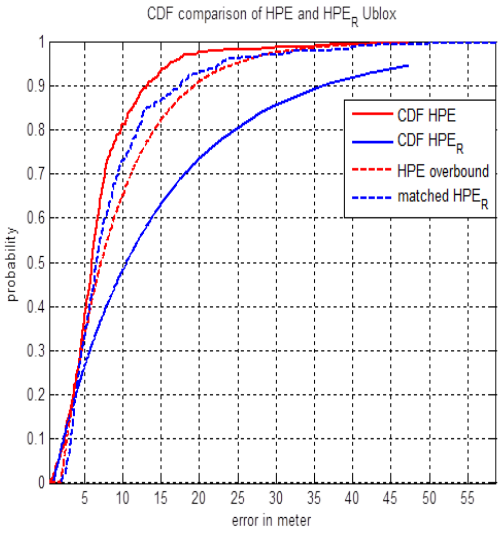

FIGURE 6.18: Result of matching position residual to overbounding CDF (Trajectory 2)

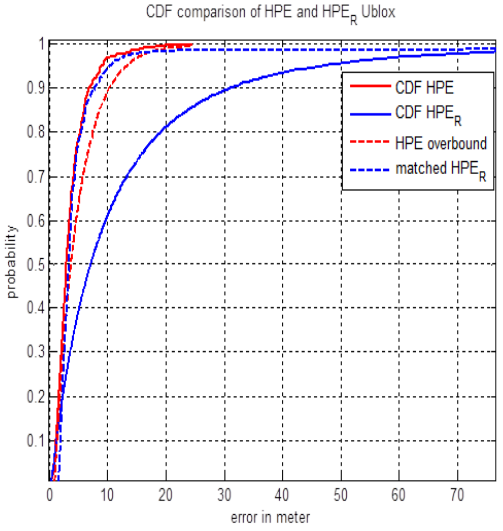

FIGURE 6.19: Result of matching position residual to overbounding CDF (Trajectory 3)

	A	B	C
Trajectory 1	0.4133	1.7821	0.4159
Trajectory 2	0.5785	-0.1594	1.1226
Trajectory 3	0.4693	0.0220	1.1050
Trajectory 4	0.4884	-0.3049	2.3476

TABLE 6.1: Matching parameters

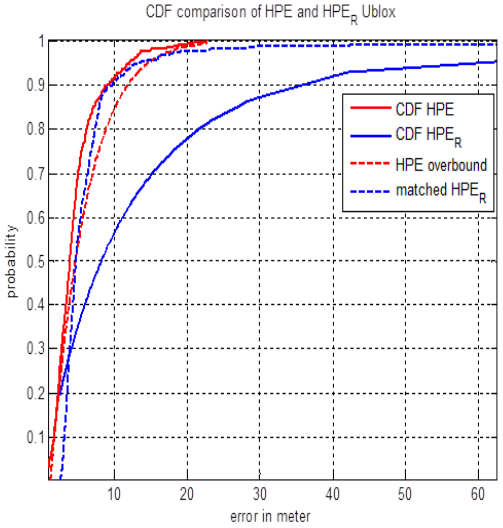

FIGURE 6.20: Result of matching position residual to overbounding CDF (Trajectory 4)

stationarity criteria. As has been described earlier in section 3.6, by using a conservative overbounding on the actual error distributions, the navigation community aimed to have enough margins to take into account the risk of any non-modelled errors which would cause the variations of the statistical properties, hence non-stationarity. Therefore, in this work it is perceivable that if more samples are obtained from various trajectories and combined, 1 set of matching parameters can be calculated and tuned to match the overbounding CDF with enough margins for conservative bounding. Indeed further studies and analysis with more data can be pursued in this interest.

The number of available independent samples also affects the acceptable confidence level of the probability of integrity, P_B or the P_{HMI}. As a "rule of thumb", at least 10^n independent samples are needed for $10^{-(n-1)}$ level of P_{HMI}. For example, 10^4 independent samples are required when characterizing the P_{HMI} at 10^{-3}. Hence, this is another reason to have more data for further analysis.

b. Position integrity monitoring analysis Table 6.2 shows the calculated P_{FA} and P_{MD} when the test statistic was used to monitor the positioning integrity along the 4 trajectories. For comparison purposes, the error probabilities were also calculated using the non-inflated position residual, $HPE_{\delta\hat{x}}$ as test statistic. In setting the threshold, the P_{HMI} was set at 0.05.

The P_{FA} calculated using the proposed test statistic are generally a lot smaller than the ones calculated based on $HPE_{\delta\hat{x}}$. These low percentages of P_{FA} increase the availability

	Threshold (m)	$Inflated\ HPE_{\delta\tilde{x}}$		$HPE_{\delta\hat{x}}$	
		P_{FA} (%)	P_{MD} (%)	P_{FA} (%)	P_{MD} (%)
Trajectory 1	18.08	4.23	2.33	20.72	1.69
Trajectory 2	24.35	3.84	1.64	15.07	1.37
Trajectory 3	13.64	2.65	1.94	21.16	0.01
Trajectory 4	15.83	4.07	1.85	23.89	0.18

TABLE 6.2: Positioning integrity monitoring performance

and continuity of the positioning system. In term of the P_{MD}, the calculated values are slightly larger than those of the $HPE_{\delta\hat{x}}$ but more importantly, are still less than the set P_{HMI} of 5%. As such, these results not only show that the integrity requirement is met but also indicate that the proposed test statistic is able to balance between the P_{FA} and P_{MD} and hence optimize the position integrity monitoring and continuity in urban canyon areas.

Based on the presented results, the proposed scheme is capable of monitoring position integrity. However, it is worth noted that since this scheme adopted the direct position domain approach, it cannot identify the faulty measurements. On the other hand, this approach enables to monitor the integrity of any type of receiver without the need to know the positioning estimator algorithms as long as we have the characterized position error of the receiver.

6.8.2 Results on composite approach

a. Noise and bias characterization results from AR model decomposition. The results of the horizontal position errors decomposition into the noise and bias components are plotted in Figures 6.21 and 6.22 for the Ublox, Figures 6.23 and 6.24 for the Novatel and Figures 6.25 and 6.26 for the Septentrio receivers. For each receiver, the first part of the plots shows the time series of the decomposed noise in the left plot and the right plot shows the decomposed bias (blue) compared to the total HPE (red). The unit of the time series is second and the unit for HPE, noise and bias is in meter.

In the second part, the QQ plots of the distributions of HPE, the decomposed noise and bias with respect to the standard normal distribution are shown. These QQ plots are used to observe the similarity/difference of the distribution of interest (in this case

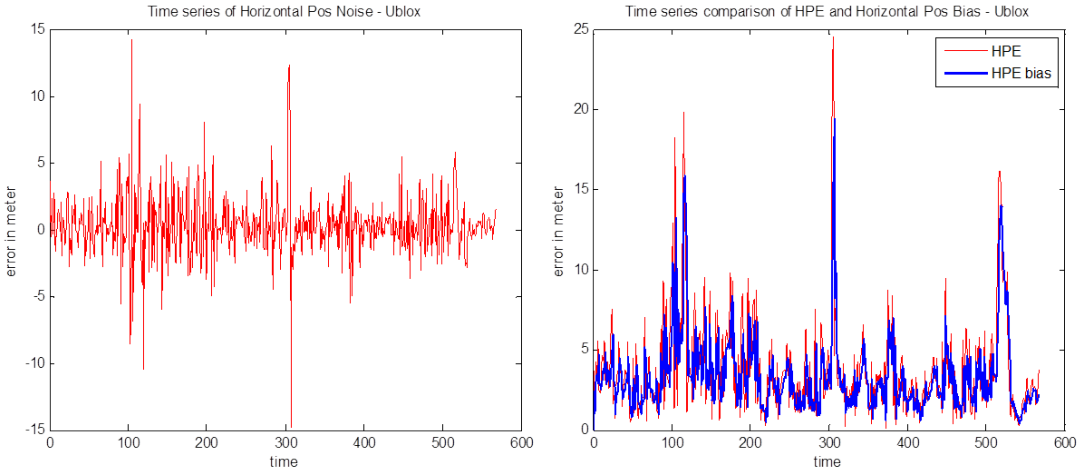

FIGURE 6.21: Decomposed noise and bias from Ublox receiver HPE

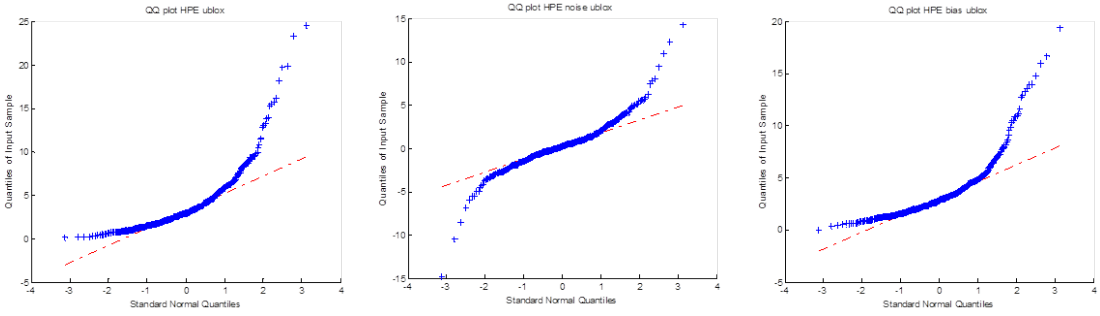

FIGURE 6.22: QQ plots of the Ublox receiver HPE, decomposed noise and bias

HPE, noise and bias) to the standard Gaussian distribution which is represented by the red dotted straight line in the plots. If the distribution of interest is also Gaussian distributed, it will follow and overlap with the red dotted straight line. Otherwise, it will deviate from the red dotted straight line. In all of the time series results, extracted noise appears to be random. In term of the position error, as expected, it can be seen that the multi-constellation high performance Septentrio receiver is able to perform better than the single constellation receivers in the deep urban environment. Only at a few very severe locations in deep urban area that the Septentrio experienced more than 10 meters of positioning error.

However, as shown in the QQ plots, the extracted noise seems to follow the Gaussian distribution but with some heavy tails. The quantile at which the tail starts to become heavy differs among the receivers. For Septentrio, the extracted noise follows Gaussian distribution almost up to the 3rd quantile, while for Ublox is about up to the 2nd quantile and for Novatel is only up to the 1st quantile. These situations indicate that

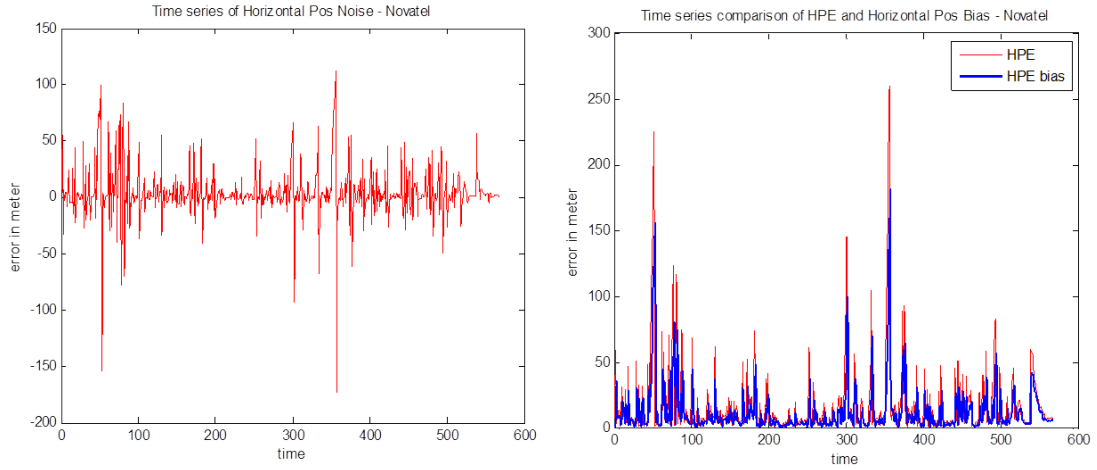

FIGURE 6.23: Decomposed noise and bias from Novatel receiver HPE

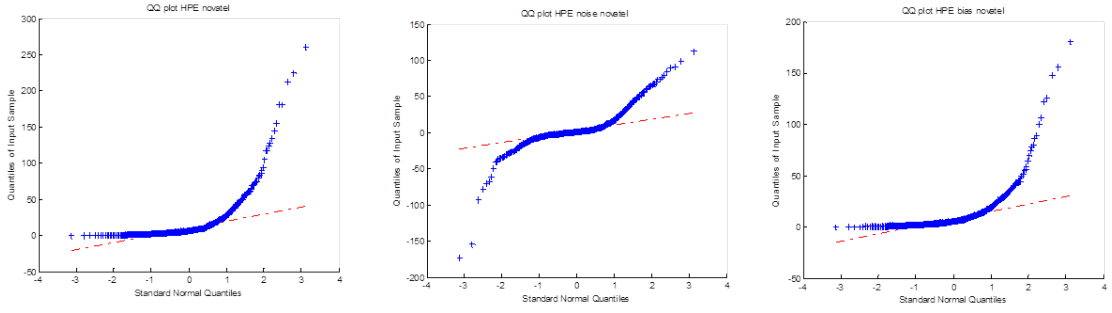

FIGURE 6.24: QQ plots of the Novatel receiver HPE, decomposed noise and bias

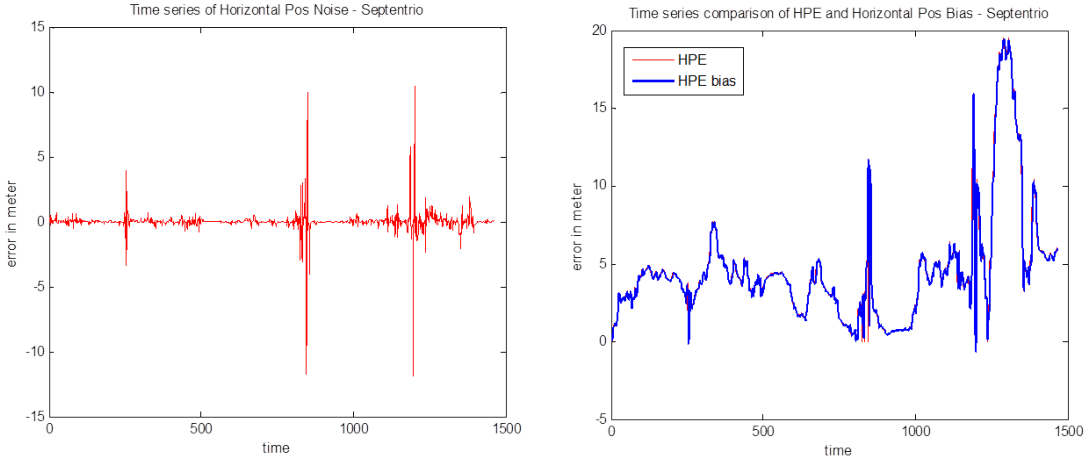

FIGURE 6.25: Decomposed noise and bias from Septentrio receiver HPE

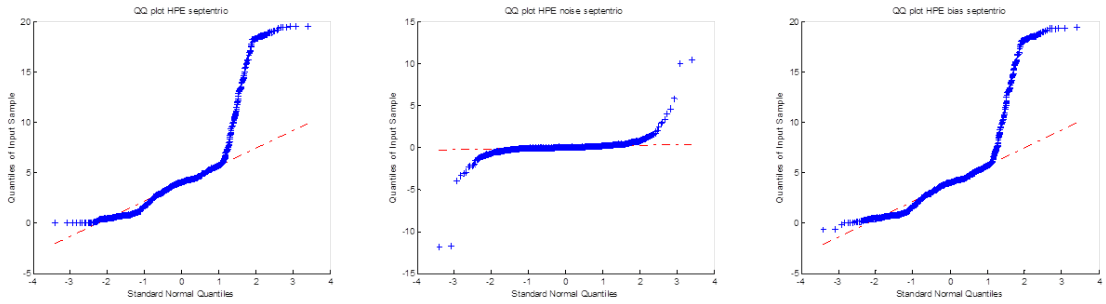

FIGURE 6.26: QQ plots of the Septentrio receiver HPE, decomposed noise and bias

the AR model approach used in this work to extract the Gaussian noise from HPE is not effective to totally suppress the heavy tail and extract only a white Gaussian noise from the HPE. The extend to what quantile that the noise distribution follows a Gaussian distribution will effect how much inflation is needed to bound the noise distribution and the acceptable maximum confidence level of the bound. However, considering that for a multi-constellation receiver such as Septentrio suffers heavy tails only after the third quantile, the composite HPL bound based on Gaussian distribution can still be effective if the accepted P_{HMI} is not too small (for example in the range of 10^{-2}). Therefore, even though there are some elements of heavy tails, the usability of this technique depends on the AL, threshold or P_{HMI} that is required for the intended applications. If the heavy tail is at the very extreme value and the AL threshold is before reaching the heavy tail region, then this technique is still possible.

b. Inflated HPL noise bounding. Figures 6.27, 6.28 and 6.29 respectively show the plots of the inflated HPL bounding the CDFs of the noises for Ublox, Novatel and Septentrio receivers. In the plots, the inflated HPL is represented by a dashed blue line. The initial CDF observed from the variance model is represented by the solid blue line. The CDF of the noise distribution is represented in solid red while its bound is plotted by a dotted red line. In all three plots, it is observed that the inflated HPL is able to bound the CDF of the noise distribution.

In the case of Ublox (Figure 6.27) and Novatel (Figure 6.28), the initial CDF obtained from the variance model (solid blue) do not bound the noise CDF (solid red). After the sigma inflation/matching, the variance model CDF is transformed into the inflated HPL and able to bound the noise CDF.

In the case of Septentrio (Figure 6.29), the initial variance model CDF does bound the

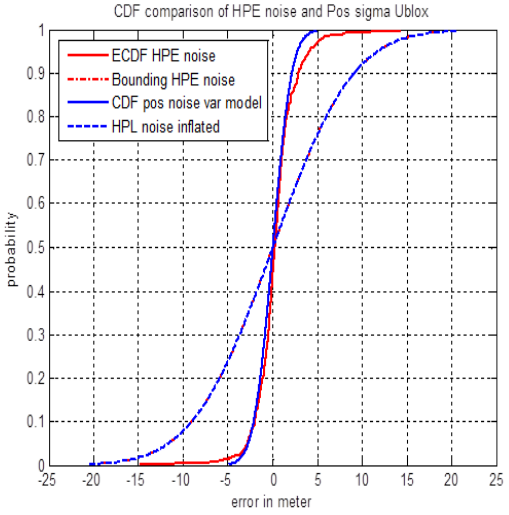

FIGURE 6.27: Inflated CDF bounding of the noise (Ublox)

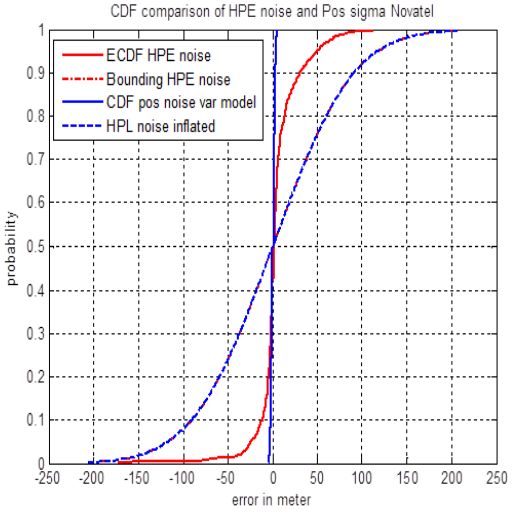

FIGURE 6.28: Inflated CDF bounding of the noise (Novatel)

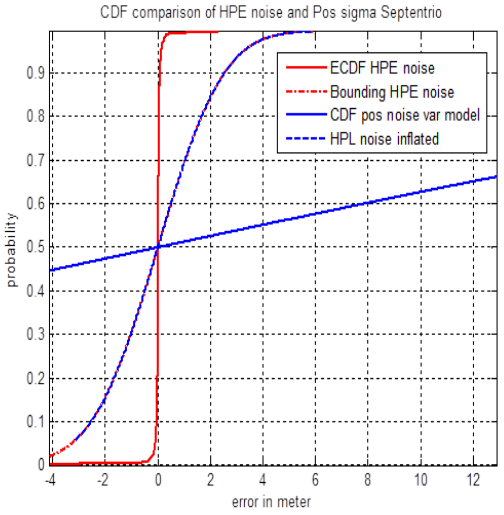

FIGURE 6.29: Inflated CDF bounding of the noise (Septentrio)

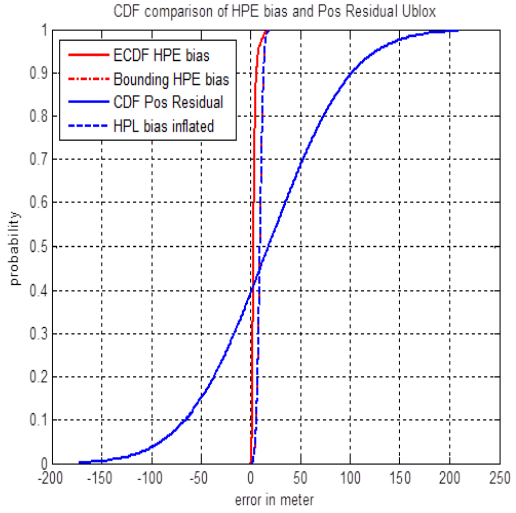

FIGURE 6.30: Inflated CDF bounding of the bias (Ublox)

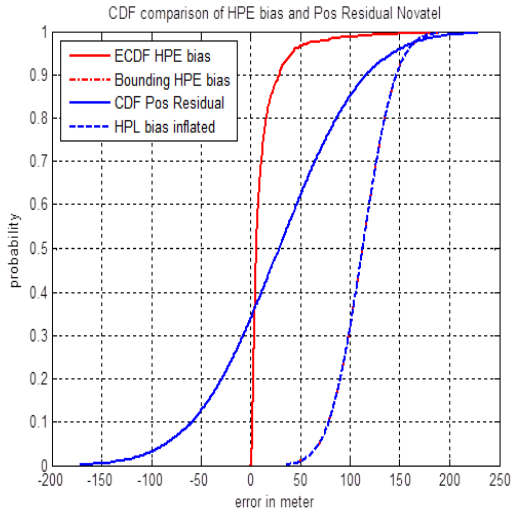

FIGURE 6.31: Inflated CDF bounding of the bias (Novatel)

noise CDF but it is too conservative. With the inflation/matching of the sigma parameter, the inflated HPL is calculated and able to bound the noise CDF more optimally.

c. Inflated HPL bias bounding. The inflated HPL bounding for the CDFs of the biases for the case of Ublox, Novatel and Septentrio receivers are shown in Figures 6.30, 6.31 and 6.32 respectively. First of all, it should be highlighted that since the HPE is defined as a norm of a 2D errors, the values are always positive. Hence, even though the extracted noise has both positive and negative values, the remaining biases in the HPE remain in positive value. Therefore, unlike the noise CDF bounding which concerns on both positive and negative sides of the CDF, the bias bounding will only concern with the positive side of the CDF. From the plots in Figures 6.30, 6.31 and

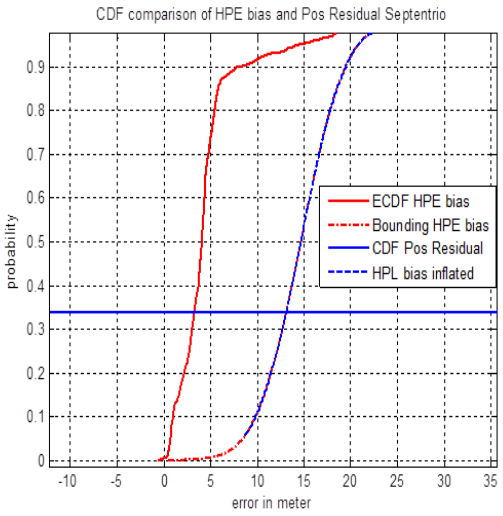

FIGURE 6.32: Inflated CDF bounding of the bias (Septentrio)

6.32, after the inflation, the bias distributions are bounded by their respective inflated HPL. It is interesting to note that while the multi-constellation receiver Septentrio has better accuracy in urban environments, its integrity performance due to bias is not that much different than that of the ublox receiver. At 90% confidence, the inflated HPL for Septentrio is about 19 meter while for the ublox is about 13 meter. Therefore, it shows that the effect of bias depends on the environment rather than the accuracy of the receiver.

6.9 Conclusion

Implementing classical RAIM for integrity monitoring in harsh environment is not effective due to the non-Gaussian error distribution characteristics of the measurements and positioning. By using the generalized Pareto distribution as the overbounding position error characteristic and relating the position residual space to the overbounded position error space, this work derives a novice test statistic for positioning integrity monitoring in urban environments. This direct position domain approach of integrity checking allows the monitoring of positioning confidence without the need to know the positioning algorithm implemented by the receiver.

In term of the HPE characterization in urban environments, the generalized Pareto distribution seems to be able to fit the HPE CDF quite well. However, it is not a perfect fit as can be seen from the results. This is expected because the distribution

characteristic of position errors in the urban environments is very complex. Therefore, a parametric distribution inherently tends to face some limitation in modelling the position error distribution in urban environment. Nevertheless, achieving a perfect fit of the distribution model is not exactly of a concern in this work because the distribution model is intended as an overbound to the actual position error distribution.

Other than implementing the GPD as the HPE CDF overbound and using the observable position residual as the matched HPL to monitor the positioning integrity in urban environments, this work also investigates the composite approach in the HPL computation for position integrity monitoring in urban environments. In order to be able to compute the composite HPL autonomously, inflated or matched error variance (based on C/No) is used to calculate the noise component HPL and the position residual is used to calculate the bias component HPL. CDF bounding techniques in direct position domain are also used here to bound the noise and bias CDFs.

AR filtering is used to extract the noise from the HPE in order to decompose the noise and bias. However, the results indicate that AR approach is not effective enough because the extracted noise is not totally Gaussian distributed but still have some heavy tails. With the aim to use a simple and straight forward distribution, Gaussian CDF is used as the overbound in this composite approach. However, since the noise and also the bias components are heavy tailed, tight bounding is difficult to achieve due to high parameter inflation. In worse case, the bounding of the tail region by Gaussian distribution may not be effective especially for applications that require very small P_{MD}.

In obtaining the HPE CDF overbound, the direct position domain approach is able to bypass the difficulties and complexity of modelling the PR errors in urban environments that the range domain overbounding has to face. However, there is a limitation in this direct position domain approach in that each satellite channel is not monitored. Therefore, even when enough satellites are available (i.e. more than 5 satellites), fault detection and exclusion (FDE) cannot be readily implemented using this approach. On the other hand, if the multiple biases of the measured PR combined with the geometry in such a way that the PRs residual remain small but the position error becomes large, only the position domain approach would detect the error and not in the range domain. As such, a combination of both range-domain (such as the proposed approach in Chapter 5) and position domain approaches could be implemented as a multi-layered integrity

monitoring concept described in Chapter 5. Alternatively, a parallel systems can be implemented where several position estimations are calculated at the same time with each one having 1 of the PR excluded. This way, it is also possible to identify which PR is causing the unacceptable error in the positioning.

One of the pertinent overbounding issue in the aviation sector is the sparse data at the extreme tail of the error distribution. When striving for a P_{HMI} value at 10^{-7}, the number of samples at the extreme tail region are statistically not enough to validate the overbounding criteria. Hence, extrapolation techniques such as the Extreme Value Theory has been implemented to deal with the issue. However, this issue could be relaxed a little in the land applications because not all applications would require such a small P_{HMI} value. For example, a P_{HMI} of 10^{-2} may already be acceptable for some of the land applications.

In addition, this exercise of characterizing position errors of the receivers in urban environment may also benefit the effort to categorize and certify the receivers. By having the HPE characteristics of the receivers, the receivers can be classified into several performance grades and this shall allow a proper selection of a suitable receiver for a certain type of land applications.

Chapter 7

Conclusions and perspectives

This thesis addresses the challenges in reliability monitoring of GNSS aided positioning for land vehicle applications in urban environments. The main objective of this research is to develop methods of trusted positioning using GNSS measurements and confidence measures for the user in constrained urban environments. Essentially, positioning confidence is defined with the ability to trust the estimated position.

In these land-based applications, the GNSS receiver is usually a sub-system providing positioning, velocity and time (PVT) information that would be used as subsequent inputs by the next module in the application system as a whole. In fact, the GNSS is not the only technology included in the positioning module when hybrid solution is implemented. In such case, the GNSS technology is complemented by other sensors, for instance inertial or odometric, in order to improve the performance of the PVT solution. Because of these arrangements, there is a need to choose a suitable receiver type and to know its minimum performances so that the final applications requirement at the user level will be met. For this purpose, the characterization of positioning error is needed to provide the final user with the level of confidence needed by his application which uses the technical requirements of the GNSS solution. Since many of the services involve financial, legal and potentially safety-of-life repercussions, these applications would need compliance with safety and reliability requirements.

Many factors affect the end performance of a GNSS receiver. Some of them are related to the inherent quality of the receiver and its antenna (sensitivity, quality of signal processing, resilience to interference and jamming, etc.), while some are related to the

atmospheric layers which the signals pass through and finally some are related to the receiver environment of reception. The local reception environment (masks, multipath, diffraction, etc.) including the dynamics of mobile objects has crucial effects on the signal quality resulting on serious degradation and challenges on the performance characterization. Indeed, along with the emergence and innovation of new land applications, many of the demands and challenges on their performances come from urban environments where the processing needs of the received signals are extensively more complex than in open sky environments.

Reliable GNSS positioning is difficult to be achieved in dense urban areas because in these environments the satellites signals are often obscured or reflected by buildings and receiver-surrounding objects, which distort measurements and bias the calculated position. Diffracted and reflected signals received together with the direct signal can result in ten-meter-order positioning errors, and hundreds of meters of positioning error can be present in non-line-of-sight (NLOS) signals situations. As these issues hinder or slow down the adoption of GNSS in applications which require high service availability or a good level of confidence in PVT information for usage in urban environments, effective and timely solutions are very much sought after. For all these reasons, we chose to work on monitoring the reliability of GNSS aided positioning for land vehicle applications in urban environments.

In the civil aviation framework, integrity monitoring is mostly accomplished by Receiver Autonomous Integrity Monitoring (RAIM) techniques which use Fault Detection and Exclusion (FDE) algorithms to reject outliers from measured data and also by augmentation systems like Ground Based Augmentation System (GBAS) and Satellite Based Augmentation System (SBAS) that relay integrity information to aircrafts to compute Protection Level (PL) associated to an integrity risk. These techniques are designed for aeronautics applications where high redundancy of data exists, mature performance standards for each phase of navigation are available, measurement and position errors are assumed to be Gaussian distributed and only a single fault is expected.

Algorithms for positioning integrity and reliability monitoring are usually based on statistical inference and hypothesis testing. Since actual position error cannot be known or measured in real time, RAIM calculates a measurable scalar parameter that provides information about pseudorange measurement errors (which can be linked to the position

error). This measurable parameter is called test statistic. It is a random variable with known distribution. For example, in Least Square RAIM, the test statistic is calculated from PR residuals, which are the difference between the measured PR and the PR derived from the estimated navigation solution. In RAIM, failure detection is achieved by comparing a test statistic against a detection threshold. For implementation in urban settings, the test statistic has to be formulated to detect errors in the measurements like outliers coming from NLOS and MP effects. The challenge is to be able to characterize the test statistic in this kind of non-Gaussian environments.

In the SBAS approach, whenever the monitored PL is less than the Alert Limit (AL), the positioning is considered to be within the integrity requirement. However, for land applications especially in urban settings, simple or direct adaptation from the civil aviation approach of integrity monitoring is not possible due to the challenging signal degradation characteristics. Because of the circumstances posed by the urban settings, the developed approaches for open sky environments are not effective in ensuring reliability in restricted environments. The main challenge in these harsh urban environments is the difficulty to have a reliable model of the received measurements, from which most of performance and integrity metrics are usually formulated as in the case of civil aviation applications.

In the first part of the research, the NLOS errors in urban settings are characterized by means of a 3D model of the urban surrounding. In an environment with limited number of visible satellites, excluding degraded signals could result in not having enough number of acceptable measurements for a position fix or adversely affect the satellites geometry. Therefore, if the degraded signal can be identified, and if its bias error can be known, the signal can be corrected and effectively used for positioning. For this purpose, a GNSS simulator is used together with the 3D model in order to identify NLOS signals and to predict their biases. From this prediction, NLOS signals are corrected and used to improve the accuracy and integrity of the estimated positions. The ability of the 3D model to predict the signal reception state either in LOS or NLOS was found to be encouraging. Nevertheless, due to the limitations of the 3D model in terms of geometrical and morphological factors, the ability to predict the NLOS bias was deemed modest and not concluding for the short processed data. Even so, when the predicted biases were utilized for PR corrections in position estimation, the result showed that the positioning

errors are generally almost similar to those calculated using the measured bias computed from the reference trajectory.

In this thesis, the second part of the work proposes a reliability monitoring technique in the range domain for urban environment using a trusted velocity sensor. The approach takes on pseudorange (PR) prediction using hybridization with other sensors to maintain positioning continuity even under the situation of reduced number of satellite visibility. Single odometer and gyro are used as the DR sensors that are loosely coupled with the GNSS receiver to obtain a reference position for reliability checking of GNSS pseudorange. By using the hybrid approach, residuals are generated and test statistic are calculated, and tested against a threshold. A few forms of residuals were derived based on several observables, namely the PR, the range rate and the velocity. For the velocity residual, the odometer was investigated as a reference sensor. The result of the PR residual representation of the actual range errors varies from satellite to satellite. The residual has good representation for the satellites with large fault value. Since this is the case, the PR residuals were able to perform its function to detect the faulty measurements before they are accepted as valid measurements for positioning. In this sense, the PR residual can be used as the first layer in the multiple layers of reliability monitoring metrics. Similar potential has also been demonstrated by the FDE technique based on the range rate residual. However, its drawback in this work as compared to the PR residual based approach is that it cannot be implemented to correct or replace the faulty measurement. On the other hand, it was found that it is quite difficult for the velocity based residual to be related to positioning error. Rather, it would be useful for velocity error detection. We looked at the 3D model and other sensors because we are convinced that in harsh environments, the integrity monitoring needs additional information other than from the GNSS.

The research in this thesis has also led to a development of a novel experimental scheme in integrity monitoring for positioning in urban environments. Working directly in the position domain, the distributions of Horizontal Position Errors (HPE) are characterized using generalized Pareto Distribution. Then, a test statistic is derived based on position residuals (rather than pseudorange residuals) which CDF are mapped or inflated to match the characterized overbounding position error CDF. By monitoring the test statistic against a specific threshold, the positioning integrity and continuity are met

at a certain level of confidence. The results using data collected in Toulouse downtown areas show that the technique is quite promising.

The method is then extended to autonomously compute the Horizontal Protection Level (HPL) in urban environments using a composite approach. The decomposition of the HPE distributions into its noise and bias components was implemented with an AR filter. Aiming for simplicity and straight forward implementation, Gaussian distribution is used as the CDF bounds for both the noise and bias distributions. While heavy tails issue was faced in this approach, its applicability is potentially higher for multi-constellation receivers as indicated in the results.

Several perspectives are noticeable resulting from the works of this thesis. Among them, the following ones present a special interest:

- To use more measurement samples obtained from various cities for the analysis. With such data, further assessment on the robustness of the generalized Pareto Distribution overbounding approach for positioning integrity monitoring in urban environments may be conducted. Other types of distribution that can deal with heavy tail are also potentially worth to be investigated for this purpose.
- To identify and pursue a more effective technique to extract the random Gaussian noise from HPE distribution. This will contribute to a more effective bounding of the noise in the composite approach of HPL computation for urban environments.
- To identify and develop techniques that can optimally combine the heuristic methods, range domain and position domain approaches in an integrity monitoring metrics. It could be in multiple layers, to be executed sequentially or in parallel, or selectively based on specific situations.
- To investigate further on the effectiveness of the velocity residual technique in monitoring velocity based applications. It could be interesting also to search for methods to link the velocity residual to positioning so that it may be used for positioning monitoring.
- To pursue possible techniques that use non-parametric approaches to model or bound the errors either in the range or in the position domain.

Bibliography

[1] International Civil Aviation Organization. International standards and recommended practices - annex 10 to the convention on international civil aviation - aeronautical telecommunications - volume i, radio navigation aids, 6th edition (with amendment 85), July 2006.

[2] GPS Directorat. Global Positioning System Standard Positioning Service Performance Standard (GPS SPS PS). http://www.gps.gov/technical/ps, September 2008. Acessed:22/4/2015.

[3] P. Misra and P. Enge. *Global Positioning System: Signals, Measurements and Performance*. Ganga-Jamuna Press, 2001.

[4] U.S. Department of Defense. Global positioning system, standard positioning service, performance standard, 4th edition, 2008.

[5] A. Simsky and F. Boon. Carrier phase & Doppler-based algorithms for real-time standalone positioning. In *Proceedings of GNSS*, Graz, 22-25 April 2003.

[6] B.H. Lee and G.I. Jee. Performance Analysis of Doppler Aided GPS/QZSS precise positioning for land vehicles. *Annual of Navigation*, 20:85–96, 2013.

[7] OKTAL-SE. Synthetic environment. http://www.oktal-se.fr. Accessed: 01/04/2013.

[8] A. Bourdeau, M. Sahmoudi, and J-Y. Tourneret. Prediction of GNSS signal bias using a 3D model in urban environments. In *The Europeen Navigation Conference, ENC*, Vienna, Austria, 23-25 April 2013.

[9] N. Viandier, D.F. Nahimana, J. Marais, and E. Duflos. GNSS Performance Enhancement in Urban Environment Based on Pseudo-range Error Model. *Position, Location and Navigation Symposium (PLANS),IEEE/ION*, pages 377–382, 5-8 May 2008.

[10] M. Spangenberg, V. Calmettes, O. Julien, J.Y. Tourneret, and G. Duchateau. Detection of Variance Changes and Mean Value Jumps in Measurement Noise for Multipath Mitigation in Urban Navigation. *NAVIGATION*, 57(1):35–52, 2010.

[11] A. Wieser, M. Gaggl, and H. Hartinger. Improved positioning accuracy with high sensitivity GNSS receivers and SNR aided integrity monitoring of pseudo-range observation. *Proceedings of the 18th International Technical Meeting ION GNSS 2005*, pages 1545–1554, 2005.

[12] H. Kuusniemi. *User-Level Reliability and Quality Monitoring in Satellite-Based Personal Navigation*. PhD thesis, Tempere University of Technology, Findland, 2005.

[13] J.F. Liao and B.S. Chen. Robust Mobile Location Estimator with NLOS Mitigation using Interacting Multiple Model Algorithm. *IEEE Trans. on Wireless Com.*, 5(11), November 2006.

[14] P.J.G. Teunissen and P.F. de Bakker. Single-receiver single channel multi-frequency GNSS integrity: outliers, slips, and ionospheric disturbances. *Journal of Geodesy*, 87(2), February 2013.

[15] H-G. Büsing, U. Haak, and P. Hecker. Odometer-aided Instantaneous Signal Reacquisition for Automotive GNSS Receivers. In *Proceedings of the 24th International Technical Meeting of The Satellite Division of the Institute of Navigation*, pages 954–959, Portland, OR, September 2011.

[16] B. DeCleene. Defining Pseudorange Integrity - Overbounding. In *Proceedings of the 13th International Technical Meeting of the Satellite Division of The Institute of Navigation*, pages 1916–1924, Salt Lake City, UT, September 2000.

[17] T. Walter, J. Blanch, P. Enge, B. Pervan, and L. Gratton. Shaping Aviation Integrity-Two RAIM for Safety. *GPS World*, 19(4):42–49, 2008.

[18] R. Suddapalli. Aircraft position integrity for Differential Satellite-based Navigation in the presence of both bias and noise errors. Ma thesis, Ohio University, 2008.

[19] J. Rife and S. Pullen. The Impact of Measurement Biases on Availability for CAT III LAAS. *NAVIGATION: Journal of the Institute of Navigation*, 52(4):215–228, 2005-2006.

[20] X. Luo. *GPS Stochastic Modelling - Signal Quality Measures and ARMA Processes*. PhD thesis, Karlsruhe Institute of Technology, Germany, 2012.

[21] S. Tay and J. Marais. Weighting models for GPS Pseudorange observations for land transportation in urban canyons. In *6th European Workshop on GNSS Signals and Signal Processing*, Munich, 2013.

[22] GSA. GNSS Market Report Issue 3. Technical report, GSA, October 2013.

[23] European Union Road Federation(ERF). ERF Discussion paper Intelligent Roads: What can the Road community expect from GALILEO? Technical report, International Road Federation(IRF) Brussel Programme Centre, April 2006.

[24] Toll Collect, Germany. Service on the road. http://www.toll-collect.de/en/home.html. Accessed: 24/10/2014.

[25] SKYTOLL, Slovakia. Electronic tolling system. http://www.skytoll.sk/index-en.html. Accessed: 24/10/2014.

[26] TODAY (2 October 2014). LTA calls for tender to develop satellite-based ERP system. http://www.todayonline.com/singapore/lta-calls-tender-develop-satellite-based-erp-system. Accessed: 22/10/2014.

[27] J. Giraud, M-L. Mathieu, J.P. Boyero Garrido, and I. Fernandez Hernandez. Pushing Standardisation of GNSS-based Location Systems to Support Terrestrial Applications Development. *ION GNSS*, September 2013.

[28] M. Lu, K. Weavers, and R. Ven der Heijden. Technical feasibility of advance driver assistance systems (ADAS) for road traffic safety. *Transportation Planning and Technology*, 28(3):167–187, 2005.

[29] K. Aichhorn, P. Khalsa, J. Seybold, and F. Dini. GNSS-based metering for vehicle applications and value added road services. *8th ITS European Congress 2011, Lyon, France*, 2011.

[30] J. Cosmen-Schortmann, B. Grush, C. Hamilton, M. Azaola-Sáenz, and M.A. Martínez-Olagüe. The need for standard performance definitions for GNSS road use metering. *ITS World Congress, Stockholm*, 2009.

[31] E. Kaplan and C. Hegarty. *Understanding GPS: Principles and Application*. Artech House, 2nd edition, 2006.

[32] B. Parkinson and J.J. Spilker. *Global Positioning System: Theory and Application*, volume 1. American Institute of of Aeronautics and Astronautics, Washington, D.C., 1996.

[33] United States Government. Official u.s. government information about the global positioning system (gps) and related topics. http://www.gps.gov. Acessed:30/10/2014.

[34] C. Hegarty and E. Chatre. Evolution of the Global Navigation Satellite System (GNSS). *Proceedings of IEEE*, 96(12):1902–1917, 2008.

[35] Y. Urlichich, V. Subbotin, G. Stupak, V. Dvorkin, A. Povalyaev, S. Karutin, and R. Bakitko. GLONASS Modernization. *GPS World*, pages 34–39, November 2011.

[36] China Satellite Navigation Office. Beidou navigation satellite system open service performance standard (version 1.0), 2013.

[37] China Satellite Navigation Office. Beidou navigation satellite system signal in space interface control document - open service signal (version 2.0), 2013.

[38] Inside GNSS. BEIDOU: China's Rapidly Emerging GNSS. *Inside GNSS*, pages 30–31, May/June 2013.

[39] Indian Space Research Organization. Navigation satellites. http://www.isro.org/satellites/navigationsatellites.aspx. Acessed:21/10/2014.

[40] GPS World. India Launches Third Navigation Satellite, IRNSS-1C. *GPS World*, October 16 2014.

[41] Quasi-Zenith Satellite System Service. http://www.qzs.jp/en/. Acessed:21/10/2014.

[42] Electronic Navigation Research Institute (Japan). Development of qzss. http://www.enri.go.jp/~sakai/qzss_e.htm. Acessed:21/10/2014.

[43] L.R. Weill M. S. Grewal and A.P. Andrews. *Global Positioning Systems, Inertial Navigation, and Integration*. John Wiley & Sons, Inc., 2 edition, 2007.

[44] D. Borio, N. Sokolova, and G. Lachapelle. Doppler measurements and velocity estimation: A theoretical framework with software receiver implementation. In *Proc., ION/GNSS*, volume 9, pages 304–316, 2009.

[45] S. Gleason and D. Gebre-Egziabher. *GNSS Applications and Methods*. Artech House, 2009.

[46] RTCA Inc. Minimum operational performance standards for global positioning system/wide area augmentation system airborne equipment. RTCA DO-229D, December 13 2006.

[47] *ICAO-Global Navigation Satellite System(GNSS) Manual*. ICAO, first edition, 2005.

[48] W. Baarda. A testing procedure for use in geodetic networks. New Series 2 4, Netherland Geodetic Commission, 1968.

[49] P.J.G. Teunissen and A. Kleusberg. *GPS for Geodesy*. 2nd edition.

[50] D. Jong and P. J. G. Teunissen. Minimal detectable biases of GPS observations for a weighted ionosphere. *Earth Planets Space*, 52:857–862, 2000.

[51] S. Hewitson and J. Wang. GPS Receiver Autonomous Integrity Monitoring (RAIM) performance analysis. *GPS Solutions*, 10:155–170, 2006.

[52] R. Brown and P. McBurney. Self-Contained GPS Integrity Check using Maximum Solution Separation. *NAVIGATION*, 35(1), 1988.

[53] Y. Lee. Analysis of Range and Position comparison methods as a means to provide GPS Integrity in the user receiver. In *US Institute of Navigation Annual Meeting*, pages 1–4, 1986.

[54] K. Sheridan. Service requirement document (SRD) for vehicle performance and emissions monitoring system (VPEMS). *Project Development Document (PDD) by Centre for Transport Studies*, London,UK: Dept. Civil. Eng., Imperial College London,2001.

[55] T. Walter and P. Enge. Weighted RAIM for precision approach. *ION GPS, Palm Springs, CA,*, 1995.

[56] Z. Jiang, P.D. Groves, W.Y. Ochieng, S. Feng, C.D. Milner, and P.G. Mattos. Multi-Constellation GNSS Multipath Mitigation Using Consistency Checking. *Proceedings of the 24th International Technical Meeting of The Satellite Division of the Institute of Navigation (ION GNSS 2011), Portland OR, September 19-23, 2011*, pages 3889–3902, September 2011.

[57] A.C. Escher, C. Macabiau, N. Martin, B. Roturier, and V. Vogel. GNSS/IRS Hybridization: Fault Detection and Isolation of more than one range failure. *Proceedings of ION GPS 2002*, pages 2619–2629, USA.

[58] S. Feng and W.Y. Ochieng. User Level Autonomous Integrity Monitoring for Seamless Positioning in All Conditions and Environments. *European Navigation Conference GNSS 2006*, Mancherter, UK.

[59] C. Macabiau, B. Gerfault, I. Nikiforov, L. Fillatre, B. Roturier, and E. Chatre. RAIM Performance in Presence of Multiple Range Failures. *Proceedings of ION NTM 2005*, pages 779–791, San Diego, CA.

[60] N.A. Tmazirte, M. E. El Najjar, J. A. Al Hage, C. Smaili, and D. Pomorski. Fast multi fault detection and exclusion approach for GNSS integrity monitoring. In *17th International Conference on Information Fusion, Fusion 2014*, pages 1–6, July 2014.

[61] R.G. Brown. A Baseline GPS RAIM Scheme and a Note on the Equivalence of Three RAIM Methods. *NAVIGATION: Journal of the Institute of Navigation*, 39 (3), Fall 1992.

[62] L. Wang, P.D. Groves, and M.K. Ziebart. Multi-Contellation GNSS Performance Evaluation for Urban Canyons Using Large Virtual Reality City Models. *Journal of Navigation*, 65(3):459–476, 2012.

[63] L. Wang M.K. Ziebart P.D. Groves, Z. Jiang. Intelligent Urban Positioning using Multi-Constellation GNSS with 3D Mapping and NLOS Signal Detection. *Proceeding of the 25th ITM ION GNSS 2012, Nashville*, pages 458–427, September 2012.

[64] J. Cosmen-Schortmann, M. Azaola-Saenz, M.A. Martinez-Olague, and M. Toledo-Lopez. Integrity in urban and road environments and its use in liability critical applications. *Position, Location and Navigation Symposium, 2008 IEEE/ION*, pages 972–983, May 2008.

[65] D. Salos, C. Macabiau, A. Martineau, B. Bonhoure, and D. Kubrak. Nominal GNSS pseudorange measurement model for vehicular urban applications. *Position Location and Navigation Symposium (PLANS), 2010 IEEE/ION*, pages 806–815, May 2010.

[66] V. Drevelle. *Étude de méthodes ensemblistes robustes pour une localisation multisensorielle intègre: Application à la navigation des véhicules en milieu urbain.* Phd thesis, lUniversité de Technologie de Compiègne (UTC), France, 2011.

[67] National Aeronautics and Space Administration. Nasa technical standard (software safety standard), nasa-std-8719.13b w/change 1 july 8, 2004. Technical report, NASA, 2004.

[68] B. Grush and P. Khalsa. A New Paradigm for using GNSS for Road Tolling. *Proceedings of the 2009 International Technical Meeting of The Institute of Navigation, Anaheim CA*, pages 617–622, January 2009.

[69] G. Toulminet, J. Boussuge, and C. Laurgeau. Comparative synthesis of the 3 main European projects dealing with cooperative systems (CVIS, SAFESPOT and COOPERS) and description of COOPERS demonstration site 4. *Proceedings of the 11th International IEEE Conference on Intelligent Transportation Systems 2008, Beijing*, pages 809–814, 2008.

[70] J. Ibaez-Guzmán. *Automotive Informatics and Communicative Systems: Principles in Vehicular Networks and Data Exchange.* Information Science Reference, 2009.

[71] S.G. Lanza, C.B. Gutierrez, and J.C. Schortmann. GINA -GNSS for innovative road applications-: EGNOS/Galilello for road user charging and Value

Added Services. *9th International Conference on Intelligent Transport Systems Telecommunications,(ITST),20-22 Oct 2009*, pages 348–352, October 2009.

[72] K. Sheridan, D. Wells, C. Botteron, J. Leclère, F. Dominici, and A. Defina. An Assisted-GNSS Solution for Demanding Road Applications using the EGNOS Data Access System (EDAS). *Toulouse Space Show'10, Toulouse, France, June 8-11, 2010.*

[73] E. Wasle, M. Lytvyn, P. Berglez, C. Mongredien, and A. Kahmann. Automotive Urban Assist Enabled by Satellite Navigation Technology. *Proceedings of the 24th International Technical Meeting of The Satellite Division of the Institute of Navigation (ION GNSS 2011), Portland, OR, September 2011*, pages 349–355, September 2011.

[74] TACOT. Tacot project presentation. http://www.corte.be/Inc/DocumentFromDatabase.asp, 2012. Accessed:21/10/2014.

[75] P. Bonnifait. Contribution à la localisation dynamique d'automobiles. Application à l'aide à la conduite. Synthèse scientifique présenteée pour l'obtention de l'habilitation à diriger des recherches, Université de Technoligie Compiègne, France, Décembre 2005.

[76] Umar Iqbal Bhatti. *Improved integrity algorithms for integrated GPS/INS systems in the presence of slowly growing errors.* Phd thesis, Imperial College London, London, United Kingdom, 2007.

[77] R. Toledo-Moreo, D. Betaille, and F. Peyret. Lane-Level Integrity Provision for Navigation and Map Matching With GNSS, Dead Reckoning, and Enhanced Maps. *IEEE Transactions on ITS 2010*, 11(1):100–112, March 2010.

[78] Olivier Le Marchand. *Approche autonome pour la localisation et la surveillance de lintégrité dun véhicule automobile en environnement complexe.* Phd thesis, lUniversité de Technologie de Compiègne (UTC), France, 2010.

[79] J. Marais, E. Duflos, N. Viandier, D.F. Nahimana, and A. Rabaoui. Advanced signal processing techniques for multipath mitigation in land transportation environment. In *Intelligent Transportation Systems (ITSC), 2010 13th International IEEE Conference on*, pages 1480–1485. IEEE, 2010.

[80] C. Cappelle, Maan E. El Najjar, F. Charpillet, and D. Pomorski. Virtual 3D City Model for Navigation in Urban Areas. *Journal of Intelligent & Robotic Systems*, 66(3):377–399, 2012.

[81] D. Btaille, F. Peyret, M. Ortiz, S. Miquel, and L. Fontenay. A new modelling based on urban trenches to improve GNSS positioning Quality of Service in cities. *IEEE Intelligent Transportation Systems Magazine*, 5(3), Fall 2013.

[82] J. Marais, D.F. Nahimana, N. Viandier, and E. Duflos. GNSS accuracy enhancement based on pseudo range error estimation in an urban propagation environment. *Expert systems with applications*, 40(15):5956–5964, 2013.

[83] B. Grush. A Performance Assessment Framework for GNSS Tolling Systems. *16th International Road Federation World Meeting 2010, Lisbon, Portugal,25 - 28 May 2010*, 2010.

[84] Carlos Daniel Salós Andrés. *Integrity monitoring applied to the reception of GNSS signals in urban environment.* PhD thesis, INP Toulouse, 2012.

[85] A.J. Van Dierendonck. Theory and Performance of Narrow Correlator Spacing in a GPS Receiver. *NAVIGATION, Journal of Institute of Navigation*, 39(3):265–283, Fall 1992.

[86] L. Garin and J. Rousseau. Enhanced Strobe Correlator Multipath Rejection for Code & Carrier. In *Proceedings of the 10th International Technical Meeting of the Satellite Division of the Institute of Navigation, ION-GPS 97*, pages 559–568, Kansas City, Missouri, 1619 September 1997.

[87] R.D.J. van Nee, J. Siereveld, P.C. Fenton, and B.R. Townsend. The multipath estimating delay lock loop: approaching theoretical accuracy limits. In *Position Location and Navigation Symposium, 1994., IEEE*, pages 246–251, Apr 1994.

[88] B. Townsend and P. Fenton. A Practical Approach to the reduction of pseudorange multipath errors in a L1 GPS receivers. In *Proceedings of the 7th International Technical Meeting of the Satellite Division of the Institute of navigation, ION-GPS*, volume 1, pages 143–148, 1994.

[89] L.R. Weill. Multipath Mitigation Using Modernized GPS Signals: How Good Can it Get? In *Proceedings of ION-GPS*, Portland, OR, 2002.

[90] P.C. Fenton and J. Jones. The theory and performance of NovAtel Inc.s Vision Correlator. In *Proceedings of ION GNSS*, pages 2178–2186, Long Beach, USA, 2005.

[91] M. Sahmoudi and R. J. Landry. Multipath mitigation techniques using maximum-likelihood principle. *Inside GNSS*, pages 24–29, November/December 2008.

[92] M.Z.H. Bhuiyan and E.S. Lohan. *Global Navigation Satellite Systems: Signal, Theory and Applications*, chapter Multipath Mitigation Techniques for Satellite-Based Positioning Applications. InTech, 2012.

[93] F. Van Diggelen. *A-GPS: Assisted GPS, GNSS, and SBAS*. Artech House, Boston, 2009.

[94] J. Bickerstaff, R. Frayling-Cork, and T. Haddrell. Capture, Analysis and Mitigation of Multipath in a High Sensitivity GPS Receiver. In *Proceeding of ION-GNSS*, Fort Worth, TX, 26-29 September 2006.

[95] J.B. Bullock et al. *Understanding GPS Principles and Applications*, chapter Integration of GPS with Other Sensors and Network Assistance, pages 459–558. Artech House, Norwood, MA, 2nd edition.

[96] M. Monnerat. AGNSS standardization the path to success in location-Based services. *Inside GNSS*, pages 22–33, July/August 2008.

[97] I. Kraemer and B. Eissfeller. A-GNSS: A Different Approach. *InsideGNSS*, pages 52–61, September/October 2009.

[98] J.K .Ray, M.E. Cannon, and P. Fenton. Mitigation of Static Carrier Phase Multipath Effects Using Multiple Closely-Spaced Antennas. In *Proceedings of the Institute of Navigation (ION-GPS 98)*, Nashville, September 1998.

[99] V. Filippov, D. Tatarnicov, J. Ashjaee, A. Astakhov, and I. Sutiagin. The First Dual-Depth Dual-Frequency Choke Ring. In *Proceeding of ION/GPS*, 1998.

[100] J. Jones, P. Fenton, and B. Smith. Theory and performance of the pulse aperture correlator. NovAtel Document, 2004.

[101] C. Bartone and F. Van Graas. Ranging Airport Pseudolite for Local Area Augmentation. In *Proceeding of IEEE PLANS*, Palm Springs, CA, April 1998.

[102] P.D. Groves, Z. Jiang, B. Skelton, P. A. Cross, L. Lau, Y. Adane, and I. Kale. Novel Multipath Mitigation Methods using a Dual-polarization Antenna. In *Proceedings ION GNSS 2010*, 2010.

[103] M. H. Keshvadi, A. Broumandan, and G. Lachapelle. Analysis of GNSS Beamforming and Angle of Arrival Estimation in Multipath Environments. In *Proceedings of ION ITM*, pages 427–435, San Diego, CA, January 2011.

[104] J. Marais, M. Berbineau, and M. Heddebaut. Land Mobile GNSS Availability and Multipath Evaluation Tool. *IEEE Transactions on Vehicular Technology*, 54(5): 1697–1704, 2005.

[105] J. Meguro, T. Murata, J. Takiguchi, Y. Amano, and T. Hashizume. GPS Multipath Mitigation for Urban Area Using Omnidirectional Infrared Camera. *IEEE Transactions on Intelligent Transportation Systems*, 10(1):22–30, 2009.

[106] N. Viandier, J. Marais, A. Rabaoui, and E. Duflos. GNSS pseudorange error density tracking using Dirichlet Process Mixture. In *13th Conference on Information Fusion, FUSION 2010, Edinburgh, UK, July 26-29, 2010*, pages 1–7, 2010.

[107] B. W. Parkinson and P. Axelrad. Autonomous GPS Integrity Monitoring Using the Pseudorange Residual. *NAVIGATION*, 35(2):255–274, 1988.

[108] Z. Jiang, P.D. Groves, W.Y. Ochieng, S. Feng, C.D. Milner, and P.G. Mattos. GNSS NLOS and Multipath Error Mitigation using Advanced Multi- Constellation Consistency Checking with Height Aiding. *Proceedings of ION GNSS*, 2012.

[109] P. D. Groves and Z. Jiang. Height Aiding, C/No Weighting and Consistency Checking for GNSS NLOS and Multipath Mitigation in Urban Areas. *Journal of Navigation*, 66(5):653–659, 2013.

[110] M. Obst, S. Bauer, and G. Wanielik. Urban Multipath Detection and mitigation with Dynamic 3D Maps for Reliable Land Vehicle Localization. *Proceedings of IEEE/ION PLANS 2012.*

[111] S. Peyraud et al. About Non-Line-Of-Sight Satellite Detection and Exclusion in a 3D Map-Aided Localization Algorithm. *Sensors*, 13:829–847, 2013.

[112] D.E. Gustafson, J.M .Elwell, and J.A. Soltz. Innovative Indoor Geolocation Using RF Multipath Diversity. In *Proceedings of IEEE/ION PLANS*, pages 904–912, San Diego, CA, April 2006.

[113] A. Soloviev and F. V. Graas. Use of deeply integrated GPS/INS architecture and laser scanners for the identification of multipath reflections in urban environments. *IEEE Journal of Selected Topics in Signal Processing*, 3(5):786–797, October 2009.

[114] A. Bourdeau, M. Sahmoudi, and J.Y. Tourneret. Tight Integration of GNSS and a 3D City Model for Robust Positioning in Urban Canyons. *Proceedings of the ION GNSS 2012, Nashville, TN, USA*, September 2012.

[115] R. Kumar and M.G. Petovello. A Novel GNSS Positioning Technique for Improved Accuracy in Urban Canyon Scenarios Using 3D City Model. In *Proceedings of the 27th International Technical Meeting of The Satellite Division of the Institute of Navigation (ION GNSS+ 2014)*, pages 2139–2148, Tampa, FL, September 2014.

[116] X. Zhang, Q. Wang, and D. Wan. Map-matching in road crossings of urban canyons based on road traverses and linear heading change model. *IEE Trans. Instrumentation and Measurement*, 56(6):2795–2803, 2007.

[117] I. Skog and P. Händel. In-Car Positioning and Navigation Technologies - A Survey. *IEEE Trans. on Intelligent Transportation Systems*, 10(1), March 2009.

[118] M. Millera, M. Uijt de Haag, A. Soloviev, M. Veth, J. Raquet, T. Klausutis, and J. Touma. Navigation in GPS Denied Environmetn: Feature-Aided Inertial Syatems. *Low Cost Navigation Sensors and Integration Technology*, NATO RTO EN SET 116(2011), 2011.

[119] G. Welch and G. Bishop. An introduction to the kalman filter. Technical Report TR 95-041, University of North Carolina, Chapell Hill, Chapell Hill, July updated:2006.

[120] R.E Kalman. A new approach to linear filtering and prediction problems. *Trans. ASME, J. Basic Eng*, 82(Series D):35–45, 1960.

[121] E. Wan and R. Van der Merwe. The unscented kalman filter for nonlinear estimation. In *IEEE Symposium on Adaptive Systems for Signal Processing, Communication and Control*, pages 153–158, 2000.

[122] S. Julier and J. Uhlmann. A new extension of the Kalman filter to nonlinear systems. In *International Symposium on Aerospace/Defense Sensing, Simulation andControls*, pages 182–193, 1997.

[123] F. Gustafsson, F. Gunnarsson, N. Bergman, U. Forssell, J. Jansson, R. Karlsson, and P. Nordlund. Particle filters for positioning, navigation, and tracking. *IEEE Trans. Signal Process*, 50:425–437, 2002.

[124] P. D. Groves. *Principles of GNSS, Inertial, and Multi-sensor Intgrated Navigation Systems*. Artech House Inc., Boston-London, 2008.

[125] B. Barshan and H.F Durant-White. Inertial Navigation Systems for Mobile Robots. *IEEE Transactions on Robotics and Automation*, 11(3), 1995.

[126] T. Li, M. G. Petovello, G. Lachapelle, and C. Basnayake. Ultra-tightly Coupled GPS/Vehicle Sensor Integration for Land Vehicle Navigation. *Journal of Institute of Navigation*, 54(4):263–274, 2010.

[127] D.M. Bevly and S. Cobb. *GNSS for Vehicle Control*. GNSS technology and applications series. Artech House, 2010. ISBN 9781596933026. URL http://books.google.fr/books?id=y2z8q-sfL9YC.

[128] M.M. Atia, A. Noureldin, and M. Korenberg. Gaussian process regression approach for bridging GPS outages in integrated navigation systems. *Electronics Letters*, 47 (1):52–53, January 2011.

[129] A. Angrisano. *GNSS/INS Integration Methods*. Phd thesis, UNIVERSITA DEGLI STUDI DI NAPOLI, Napoli, 2010.

[130] U. Iqbal, A.F. Okou, and A. Noureldin. An integrated reduced inertial sensor system – riss / gps for land vehicle. In *Position, Location and Navigation Symposium, IEEE/ION*, pages 1014–1021, May 2008.

[131] J. Gao. *Development of a Precise GPS/INS/On-Board Vehicle Sensors Integrated Vehicular Positioning System*. Phd thesis, THE UNIVERSITY OF CALGARY, Calgary, Alberta, June 2007.

[132] X. Niu, S. Nasser, C. Goodall, and N. El-Sheimy. A Universal Approach for Processing any MEMS Inertial Sensor Configuration for Land-Vehicle Navigation. *Journal of Navigation*, 60(2):233–245, 2007.

[133] R. Carlson, J. Gerdes, and J. Powell. Practical position and yaw rate estimation with GPS and differential wheelspeeds. In *Proc. 6th Int. Symp. AVEC*, Hiroshima, Japan, September 2002.

[134] R. Carlson, J. Gerdes, and J. Powell. Error sources when land vehicle dead reckoning with differential wheelspeeds. *Navig.*, 51(1):13–27, 2004.

[135] M.A. Quddus, W.Y. Ochieng, and R.B. Noland. Current map-matching algorithms for transport applications: state-of-the art and future research directions. *Transportation Research Part C: Emerging Technologies*, 15(5), 12-328 2007. October.

[136] N. R. Velaga, M. A. Quddus, and A. L. Bristow. Developing an enhanced weight based topological map-matching algorithm for intelligent transport systems. *Transportation Research Part C: Emerging Technologies*, 17(6):672–683, December 2009.

[137] N. Tradisauskas, J. Juhl, H. Lahrmann, and C.S. Jensen. Map matching for intelligent speed adaptation. *IET Intell. Transp. Syst.*, 3(1):57–66, March 2009.

[138] W.Y. Ochieng, M.A. Quddus, and R.B. Noland. Map-matching in complex urban road networks. *Brazilian Journal of Cartography*, 55(2):1–18, 2004.

[139] C. White, D. Bernstein, and A. L. Kornhauser. Some map matching algorithms for personal navigation assistants. *Transp. Res. C, Emerg. Technol.*, 8(1):91–108, February 2000.

[140] N.R. Velaga, M.A. Quddus, A.L. Bristow, and Y. Zheng. Map-Aided Integrity Monitoring of a Land Vehicle Navigation System. *IEEE Transaction on Intelligent Transportation Systems*, 13(2), June 2012.

[141] C. Fouque and P. Bonnifait. On the use of 2D navigable maps for enhancing ground vehicle localization. In *IEEE/RSJ International Conference on Intelligent Robots and Systems 2009. IROS 2009.*, pages 1885–1890, Oct 2009.

[142] F. Peyret, D. Bétaille, C. Pinana, and R. Toledo-Moreo. GNSS Autonomous Localization: NLOS Satellite Detection Based on 3-D Maps. *IEEE Robotics & Automation Megazine*, pages 57–63, March 2014.

[143] M. A. Sturza. Navigation System Integrity Monitoring Using Redundant Measurements. *NAVIGATION*, 35(4):69–87, Winter 1988-1989.

[144] Anaïs Martineau. *Performance of Receiver Autonomous Integrity Monitoring (RAIM) for Vertical Guided Approaches*. PhD thesis, l'Institut National Polytechnique de Toulouse, Toulouse, France, 2008.

[145] P. B. Ober. Ways to Improve RAIM/AAIM Availability Using Position Domain Performance Computations. In *Proceedings of the 1997 National Technical Meeting of The Institute of Navigation*, pages 485–497, Santa Monica, CA., 1997.

[146] R.G. Brown and G.Y. Chin. GPS RAIM: Calculation of Thresholds and Protection Radius Using Chi-Square Methods - A Geometric Approach. *Global Positioning System*, v:155–179, 1997.

[147] M. Brenner. Integrated GPS/Inertial detection availability. *Journal of The Institute of Navigation*, 43(2), Summer 1996.

[148] A. Angrisano, S. Gaglione, and C. Gioia. Performance assessment of GPS/-GLONASS single point positioning in an urban environment. *Acta Geodaetica et Geophysica*, 48(2):149–161, June 2013.

[149] GPS Directorat. Global Positioning System Standard Positioning Service Performance Standard (GPS SPS PS). http://www.gps.gov/technical/ps, October 2001. Acessed:22/4/2015.

[150] M. Joerger, F-C. Chan, S. Langel, and B. Pervan. RAIM Detector and Estimator Design to Minimize Integrity Risk. In *Proceedings of 25th International Technical Meeting of The Satellite Division of the Institute of Navigation*, pages 2785–2807, Nashville, TN, September 2012.

[151] S. Hewitson and J. Wang. Receiver Autonomous Integrity Monitoring (RAIM) for Multiple Outliers, 2004. Accessed: 26/11/2014.

[152] Y. Wang. FDE and Positioning Performance in a Multi-Fault Scenario Using GPS and Galileo. In *Proceedings of the 18th International Technical Meeting of the Satellite Division of The Institute of Navigation*, pages 1772–1780, Long Beach, CA, September 2005.

[153] P.J.G. Teunissen and A. Kleusberg. *GPS for Geodesy*. Springer-Verlag, 2nd edition, 1998.

[154] I. Martini and G.W. Hein. An integrity monitoring technique for multiple failures detection. In *Proceedings of IEEE/ION PLANS 2006*, pages 450–467, San Diego, CA, April 25-27 2006.

[155] B. Vassileva and B. Vassilev. A new technique for SBAS availability improvement. *Int. Journal of Microwave and Wireless Technologies Special Issue 02*, 4(2):217–221, April 2012.

[156] M. Azaola and J. Cosmen. Autonomous Integrity An Error Isotropy-Based Approach for Multiple Fault Conditions. *Inside GNSS*, 4(1):28–36, 2009.

[157] E. Kang. *Radar System Analysis, Design and Simulation.* Artech House, 2008.

[158] P.A. Boysen and H. Zunker. Low Cost Sensor Hybridisation and Accurancy Estimation for Road Applications. *ESA Conference Navitec 2004. Noordwijk, The Netherlands*, December 2004.

[159] R. Toledo-Moreo, J. Santa, M. Zamora, B. Úbeda, and A. Skarmeta. A study of integrity indicators in outdoor navigation systems for modern road vehicle applications. *Proceedings of IEEE/RAS 2nd Workshop on Planning, Perception and Navigation for Intelligent Vehicles, Nice, 2008*, 2008.

[160] O. Le Marchand, P. Bonnifait, J. Ibanez-Guzman, and D. Betaille. Vehicle Localization Integrity Based on Trajectory Monitoring. *IEEE/RSJ International Conference on Intelligent Robots and Systems, St. Louis, USA*, 2009.

[161] D. Salós, A. Martineau, C. Macabiau, B. Bonhoure, and D. Kubrak. Receiver Autonomous Integrity Monitoring of GNSS Signals for Electronic Toll Collection. *IEEE Tran on Intelligent Transportation System*, 15(1):94–103, February 2014.

[162] D. Kubrak and G. Carrié. Toward a new definition of a PNT trust level in a challenged multi frequency / multi-constellation environment. In *Proceedings of the 27th International Technical Meeting of the ION Stellite Division, ION GNSS+ 2014*, pages 2310–2316, Tampa, Florida, 8-12 September .

[163] G. Carrie, D. Kubrak, M. Monnerat, and J. Lesouple. Toward a New Definition of a PNT Trust Level: Comparing Concept in Challanged Multi Frequency / Multi-Constellation Environment. In *NAVITEC*, Noordwijk, The Netherlands, 3-5 December 2014. ESA/ESTEC.

[164] F.M. Shubert, J. Wandel, F. Soualle, M. Mink, S. Carcanague, R. Ioannides, P. Crosta, and M. Crisci. Integrity of Navigation for Land Users: Study Concept and Simulator Architecture. In *NAVITEC*, Noordwijk, The Netherlands, 3-5 December 2014. ESA/ESTEC.

[165] R.G. Brown. Solution of the two-failure GPS RAIM problem under worst-case bias conditions: Parity space approach. *NAVIGATION*, 44(4):425–432, Winter 1997-1998.

[166] Y.C. Lee. Performance of Receiver Autonomous Integrity Monitoring (RAIM) in the presence of simultaneous multiple satellite faults. In *Proceedings of the 60th Annual Meeting of the Institute of NAvigation*, pages 687–697, Dayton, OH, June 7-9 2004.

[167] J.E. Angus. RAIM with multiple faults. *NAVIGATION*, 53(4):249–257, Winter 2006.

[168] J. Liu, M. Lu, X. Cui, and Z. Feng. Theoretical analysis of RAIM in the occurrence os simultaneous two-satellite faults. *IET Radar, Sonar and Navigation*, 1(2):92–97, 2007.

[169] P.Y. Hwang. Applying NIORAIM to the Solution Separation Method for Inertially-Aided Aircraft Autonomous Integrity Monitoring), booktitle = Proceedings of ION NTM, year = 2005, editor = , volume = , number = , series = , pages = 992–1000, address = San Diego, CA, month = , organization = , publisher = , note = , abstract = , keywords = ,.

[170] P. Madonna, S. Viola, and L. Sfarzo. NIORAIM algorithm applied to a multiconstellation GNSS: Analysis of integrity monitoring performances in various phases of flight. In *Position Location and Navigation Symposium (PLANS)IEEE/ION*, pages 1258–1263, May 4-6 2010.

[171] A. Ene. *Utilization of Modernized Global Navigation Satellite Systems for Aircraft-Based Navigation Integrity.* PhD thesis, Stanford University, California, USA, 2009.

[172] T. Walter, P. Enge, and B. DeCleene. Integrity lessons from the WAAS integrity panel (WIPP). *ION GPS*, 2002.

[173] J. Rife and S. Pullen. *GNSS Applications and Methods*, chapter Aviation application. Artech House, 2009.

[174] J. Blanch, T. Walter, and P. Enge. RAIM with Optimal Integrity and Continuity Allocations Under Multiple Failures. *IEEE Trans. on Aerospace and Electronic Systems*, 46(3):1235–1247, July 2010.

[175] J. Rife, T. Walter, and J. Blanch. Overbounding SBAS and GBAS error distributions with excess-mass functions. In *Proc. International Symposium on GPS/GNSS*, Sydney, 6-8 Dec 2004.

[176] J. Rife, S. Pullen, B. Pervan, and P. Enge. Core Overbounding and its Implications for LAAS Integrity. In *Proceedings of ION GNSS*, pages 2810–2821, 2004.

[177] J. Rife, S. Pullen, B. Pervan, and P. Enge. Paired overbounding for nonideal LAAS and WAAS error distributions. *IEEE Trans. Aerospace and Electronic Systems,*, 42(4):1386–1395, 2006.

[178] J. Rife and D. Gebre-Egziabher. Symmetric overbounding of correlated errors. *NAVIGATION*, 54(2):109–124, 2007.

[179] C. Tiberius and D. Odijk. Does the HPL bound the HPE. In *Proceedings of NaviTec08 workshop. ESA-Estec*, pages 10–12, The Netherlands, December 2008.

[180] B. Roturier, E. Chatre, and J. Ventura-Traveset. The SBAS Integrity Concept Standardized by ICAO. Application to EGNOS. *GNSS Conference*, May 2001.

[181] P.B. Ober, L. de Haan, D. Li, A. van den Berg, and R. Farnworth. Statistical Validation of SBAS Integrity. In *Proceedings of the European Navigation Conference*, Rotterdam, Netherlands, 16-19 May 2004.

[182] J. Lee, S. Pullen, and P. Enge. Sigma Overbounding using a Position Domain Method for the Local Area Augmentation of GPS. *IEEE Transactions on Aerospace and Electronic Systems*, 45(4):1262–1247, Oct 2009.

[183] O. Osechas and J. Rife. Tightening DGNSS Protection Levels Using Direct Position-Domain Bounding. In *Proceedings of ION GNSS+ 2013*, pages 1329–1340, Nashville, TN, September 2013.

[184] R. Braff and C. Shively. A Method of Over Bounding Ground Based Augmentation System (GBAS) Heavy Tail Error Distributions. *The Journal of Navigation*, 58: 83–103, 2005.

[185] Z. Xing. *Over-bounding Integrated INS/GNSS Output Errors.* PhD thesis, Dept. of Aerospace Engineering and Mechanics, University of Minnesota, Twin City Campus, Oct 2010.

[186] J. Rife. The Effect of Uncertain Covariance on a Chi-Square Integrity Monitor. *NAVIGATION: Journal of the Institute of Navigation*, 60(4):249–324, 2013.

[187] P.B. Ober, R. Farnworth, E. Breeuwer, and D. van Willigen. SBAS Integrity Verification. In *Proceeding of ION GPS 2001*, pages 1805–1830, Salt Lake City, UT, September 2001.

[188] C. Shively and R. Braff. An overbound concept for pseudorange error from the lass ground facility. In *Proceedings of IAIN World Congress/ION 55th Annual Meeting*, pages 661–671, San Diego, CA, June 2000.

[189] Panagiotakopoulos D, A. Majumdar, and W.Y. Ochieng. Extreme value theory-based integrity monitoring of global navigation satellite systems. *GPS Solutions*, 18:133–145, 2014.

[190] J-M. Azais, S. Gadat, J-C. Lvy, B. Rols, C. Mercadier, C. Jordan, and N. Suard. GNSS Integrity Achievement by using Extreme Value Theory. In *Proceedings of the 22nd International Technical Meeting of The Satellite Division of the Institute of Navigation*, pages 1281–1287, Savannah, GA, September 2009.

[191] J. Bradbury. Prediction of Urban GNSS Availability and Degradation Using Virtual Reality City Models. In *Proceedings of ION GNSS*, Fort Worth, Texas, September 2007.

[192] F. Peyret, D. Bétaille, and F. Mougel. Non-Line-Of-Sight GNSS signal detection using an on-board 3D model of buildings. *11th International Conference on ITS Telecommunications (ITST)*, 23-25 August 2011.

[193] P.D. Groves, L. Wang, and M. Ziebart. Shadow Matching: improved GNSS accuracy in urban canyons. *GPS world*, 23(2):14–18, February 2012.

[194] S. Miura, S. Hisaka, and S. Kamijo. GPS Multipath Detection and Rectification using 3D Maps. In *16th International IEEE Annual Conference on Intelligent Transportation Systems (ITSC 2013)*, pages 1528–1534, The Hague, 6-9 October 2013.

[195] Y. Zhao. *Vehicle Location and Navigation Systems.* Artech House ITS Series, 1st edition, 1997.

[196] E. Abbot and D. Powell. Land-Vehicle Navigation Using GPS. *IEEE Proceedings of the Institute of Electrical and Electronics Engineer*, 87(1):145–162, January 1999.

[197] Y. Wu. Versatile Land Navigation using Inertial Sensors and Odometry: Self-calibration, In-motion Alignment and Positioning. In *Inertial Sensors and Systems-Symposium Gyro Technology (ISS-SGT)*, Karlsruhe, Germany, 16-17 September 2014.

[198] Jim Stephen. Development of a multi-sensor GNSS based vehicle navigation system. Msc thesis, University of Calgary, August 2000.

[199] A. Somieski, Ch. Hollenstein, E. Favey, and C. Schmid. Low-cost sensor fusion dead reckoning using a single-frequency GNSS receiver combined with gyroscope and wheel tick measurements. In *23rd International Technical Meeting of the Satellite Division of the Institute of NAvigation*, pages 1645–1652, Portland, OR, 21-24 September 2010.

[200] J. Farrell and M. Barth. *The Global Positioning System and Inertial Navigation.* McGraw-Hill, New York, 1998.

[201] D. Gingras. *Automotive Informatics and Communicative Systems Principles in Vehicular Networks and Data Exchange*, chapter Chapter 12 An overview of positioning and data fusion techniques applied to land vehicle navigation systems, pages 219–246. IGI Global, Hershey, PA, 2009.

[202] H. Sairo, D. Akopian, and J. Takala. Weighted dilution of precision as quality measure in satellite positioning. *Radar, Sonar and Navigation, IEE Proceedings*, 150(6):430–436, 2003.

[203] H. Sairo, H. Kuusniemei, and J. Takala. Combined performance of FDI and KDOP analysis for user-level integrity monitoring. In *11th IAIN World Congress*, Berlin, 21-24 October 2003.

[204] Hanna Sairo. *Error Detection in Personal Satellite Navigation.* Phd thesis, Tampere University of Technology, Finland, December 2006.

[205] E-H. Shin and N. El-Sheimy. Accuracy Improvement of Low Cost INS/GPS for Land Applications. In *Proceedings of the 2002 National Technical Meeting of The Institute of Navigation*, pages 146–157, San Diego, CA, 28-30 January 2002.

[206] M. Zribi, K. Touil, and M. Benjelloun. Vehicle Localization via Sensor Fusion using Evidence Theory. *NAVIGATION*, 56(1):23–33, Spring 2009.

[207] A. Dumitrache, Zamora M. A., R. Toledo-Moreo, and A.G. Skarmeta. Hybridized GPS/DR Positioning System with Unknown Initial Heading for Land Vehicles. In *11th International IEEE Conference on Intelligent Transportation Systems*, pages 974–979, Beijing, 12-15 October 2008.

[208] S. Rezaei and R. Sengupta. Kalman filter based integration of DGPS and vehicle sensors for localization. In *IEEE International Conference on Mechatronics and Automation*, pages 455–460, Ontario, Canada, August 2005.

[209] Ch. Hollenstein, E. Favey, C. Schmid, A. Somieski, and D. Ammann. Performance of a Low-cost Real-time Navigation System using Single-frequency GNSS Measurements Combined with Wheel-tick Data. In *ION GNSS ITM*, pages 1610–1618, Savannah, GA, 2008.

[210] L. Zhao, W.Y. Ochieng, M.A. Quddus, and R.B. Noland. An extended Kalman filter algorithm for integrating GPS and low cost dead reckoning system data for vehicle performance and emissions monitoring. *Journal of Navigation*, 56(2), 2003.

[211] M. St-Pierre and D. Gingras. Comparison between the unscented Kalman filter and the Extended Kalman filter for the position estimation module of an intgrated navigation information system. In *IEEE Intelligent Vehicles Conference*, Parma, Italy, June 2005.

[212] S. Arulampalam, S. Maskell, N. Gordon, and T. Clapp. A Tutorial on Particle Filters for Online Nonlinear/Non-Gaussian Baysian Tracking. *IEEE Transactions on Signal Processing*, 50(2):174–188, 2002.

[213] N. Yang, W. F. Tian, Z. H. Jin, and C. B. Zhang. Particle filter for sensor fusion in a land vahicle navigation system. *Measurement Science and Technology*, 16(3): 677–681, 2005.

[214] A. Y. Kibangou and A. Monin. GPS based land vehicle positioning using Gaussian sum filters. In *IEEE International Conference in Acoustic, Speech and Signal Processing (ICASSP)*, pages 3653–3656, 2008.

[215] M. St-Pierre and D. Gingras. Neural network based data fusion for vehicle positioning in land navigation system. In *Society of Automotive Engineering (SAE) Conference*, Detroit, USA, March 2004.

[216] M.A. Zamora, D. Bétaille, and F. Peyret. About the interest of Linearised Kalman Filter for low-cost GPS-based hybrid positioning system for land vehicles. In *13th World COnferencia and Exhibition on ITS and Services*, January 2006.

[217] J. F. Wagner and T. Wieneke. Integrating satellite and inertial navigation - conventional nd new fusion approaches. *Control Engineering Practice*, 11(5):543–550, 2003.

[218] R. Toledo-Moreo, D. Bétaille, F. Peyret, and J. Laneurit. Fusing GNSS, Dead-Reckoning, and Enhanced Maps for Road Vehicle Lane-Level Navigation. *IEEE Journal of Selected Topics in Signal Processing*, 3(5):798–809, October 2009.

[219] J. Georgy, A. Noureldin, M.J. Korenberg, and M.M. Bayoumi. Modeling the Stochastic Drift of a MEMS-Based Gyroscope in Gyro/Odometer/GPS Integrated Navigation. *IEEE Trans. On Intel. Trans. Systems*, 11(4):856–872, December 2010.

[220] G. Strang and K. Borre. *Linear Algebra, Geodesy, and GPS*. Wellesly-Cambridge Press, 1997.

[221] B. Hofmann-Wallenhof, H. Lichtenegger, and J. Collins. *Global Positioning System: Theory and Practice*. Springer, 5th rev. edition, 2001.

[222] B. Grush, J. Cosmen-Shortmann, C. Hamilton, and M.A. Martinez-Olagüe. GMAR standard performance definitions for GNSS road user metering. In *ITS World Congress*, Stockholm, 2009.

[223] S. Langel, S. Khanafseh, and B. Pervan. Bounding Integrity Risk in the Presence of Parametric Time Correlation Uncertainty. In *Proceedings of ION ITM*, pages 1666–1680, Manassas, VA, 2012.

[224] B. Sayim, I. amd Pervan, S. Pullen, and P. Enge. LAAS Ranging Error Overbound for Non-zero Mean and Non-Gaussian Multipath Error Distributions. In *Proceedings of the ION Annual Meeting*, pages 490–499, Albuquerque, New Mexico, 2003.

[225] T. Walter, J. Blanch, and J. Rife. Treatment of Biased Error Distributions in SBAS. *Journal of Global Positioning Systems*, 3(1-2):265–272, 2004.

[226] R.G. Brown. *Receiver Autonomous Integrity Monitoring*, volume II, chapter Chapter 5, pages 143–165. AIAA Inc., Washington, D.C., 1996.

[227] P. B. Ober. *Integrity prediction and monitoring of navigation systems*. Integricom Publishers, Netherlands, 2003.

[228] C. Walck. *Handbook on statistical distribution for experimentalists*. Internal Report SUF-PFY/06-01, Stockholm, 2007. p.139.

[229] N. L. Johnson, S. Kotz, and N. Balakrishnan. *Continuous Univariate Distributions*, volume 1. Wiley, New York, 2nd edition, 1994.

[230] H. Goldstein, C. Poole, and J. Safko. *Classical Mechanics*. Addison Wesley, San Francisco, 3rd edition, 2002.

[231] B. Pervan, S. Pullen, and I. Sayem. Sigma Estimation, Inflation and Monitoring in the LAAS Ground System. In *ION GPS 2000*, pages 1234–1244, Salt Lake City, UT, 19-22 Sept 2000.

[232] D. Bruckner, F. van Grass, and T. Skidmore. Statistical characterization of composite protection levels for GPS. *GPS solution*, 15:263–273, 2011.

[233] J. Lee. LAAS Position Domain Monitor Analysis and Test Results for CAT II/III Operations. In *Proc. ION GNSS*, pages 2786–2796, Long Beach, CA, September 2004.

Université de Toulouse (ISAE SUPAERO)

RÉSUMÉ DES TRAVAUX EN FRANÇAIS

par

Khairol Amali bin Ahmad

Supervisor: Mohamed SAHMOUDI (ISAE-SUPAERO),

Christophe MACABIAU (ENAC)

DRAFT

June 2015

RÉSUMÉ DES TRAVAUX EN FRANÇAIS

Introduction

Les services des systèmes globaux de positionnement par satellite (GNSS) pour les applications terrestres sont devenus très utiles et populaires que son marché devrait croître encore d'une façon exponentielle les années à venir. Les applications terrestres actuelles avec de nombreuse services potentielles couvrent une large gamme d'applications telles que le tarification basée sur la localisation, "pay-as-you-drive" (PAYD), la tarification routière, le suivi de voiture spécifique (les courses, les assurances, les criminels, etc.) et rapports de géolocalisation. En outre, les applications pour le système d'assistance au conducteur (ADAS) comme le suivi de la voie, l'évitement de collision etc. font également l'utilisation du système de positionnement par GNSS.

Dans ces applications terrestres, le récepteur GNSS est généralement un sous-système qui permet de calculer la position, la vitesse et l'heure (PVT) qui seront utilisées comme entrées ultérieures par le module suivant dans le système global de l'application. En fait, le GNSS n'est pas la seule technologie incluse dans le module de positionnement lorsque une solution hybride est mis en œuvre. Dans ce cas, la technologie GNSS est complétée par d'autres capteurs, par exemple inertiel ou odométrie, afin d'améliorer les performances de la solution PVT. En raison de ces dispositions, il est nécessaire de choisir un type de récepteur approprié et de connaître ses performances minimales de sorte que l'exigence des applications finales au niveau de l'utilisateur sera atteinte. A cet effet, la caractérisation de l'erreur de positionnement est nécessaire pour fournir à l'utilisateur final avec le niveau de confiance requis par son application qui utilise les exigences techniques de la solution GNSS. Comme un bon nombre des services impliquent des engagements financiers, juridiques et potentiellement des répercussions de sécurité de la vie, ces applications doivent se conformer avec les exigences de sécurité et de fiabilité.

De nombreux facteurs affectent la performance finale d'un récepteur GNSS. Certains d'entre eux sont liés à la qualité intrinsèque du récepteur et de son antenne (sensibilité, la qualité du traitement du signal, la résilience aux interférences et de brouillage, etc.), tandis que certains sont liés aux couches atmosphériques qui les signaux passent à travers et enfin certains sont lié à l'environnement de réception du récepteur. L'environnement de réception locale (masquage, multi-trajets, diffraction, etc.), y compris la dynamique des objets mobiles a des effets décisifs sur la qualité du signal résultants de la dégradation subie ce qui implique une dégradation des performances de positionnement du récepteur.

En effet, avec l'émergence et l'innovation de nouvelles applications terrestres, la plupart des exigences et des défis sur leurs performances proviennent de milieux urbains où les besoins de traitement des signaux reçus sont beaucoup plus complexes que dans les environnements à ciel ouvert.

Une localisation fiable par GNSS est difficile à atteindre dans les zones urbaines denses parce que dans ces environnements les signaux satellites sont souvent masqués ou réfléchis par les bâtiments et les objets environnants le récepteur, qui faussent les mesures et biaisent la position calculée. Les signaux réfractés et réfléchis reçus avec le signal direct peut entraîner des erreurs de positionnement de dix mètres d'ordre, et des centaines de mètres d'erreur de positionnement peuvent être présents quand les signaux reçus en la configuration non-line-of-sight (NLOS). Comme ces problèmes empêchent ou ralentissent l'adoption du GNSS dans les applications qui nécessitent une haute disponibilité de service ou un bon niveau de confiance dans l'information PVT pour une utilisation dans des environnements urbains, des solutions efficaces et opportunes sont très recherchés. Pour toutes ces raisons, nous avons choisi de travailler sur le contrôle de la fiabilité du positionnement GNSS pour les applications de véhicules terrestres dans les milieux urbains.

Positionnement par satellite

Un récepteur GNSS calcule la pseudo-distance (PR) à partir d'un satellite sur la base de l'estimation du temps de propagation du signal de satellite multiplié par la vitesse de la lumière. Dans la pratique, les récepteurs GNSS ne sont pas synchronisés avec le temps GNSS. Par conséquent, la PR est basée sur la durée de transition du signal et de la différence de temps entre l'horloge du récepteur et celle du satellite.

Les mesures de PR réelles sont également affectés par diverses erreurs de propagation et du système et d'environnement. En tenant compte de ces bruits et des erreurs, PR peut être représentée par l'équation [1]:

$$\rho_i = d_i + c.dt_r - c.dt_s + I_i + T_i + \epsilon_i \tag{1}$$

où

- d_i est la distance en ligne droite entre le récepteur et le satellite
- $c.dt_i$ est le décalage de l'horloge du satellite
- $c.dt_r$ est le décalage de l'horloge du récepteur

- I_i est le retard ionosphérique
- T_i est le retard troposphérique
- ϵ_i représente le bruit du récepteur, les multi-trajets et NLOS

En milieu urbain, l'erreur dans ϵ_i est dominé par les multi-trajets et NLOS qui sont connus pour être dépendant de l'environnement local, non-gaussien, non stationnaire et peut être temporellement corrélés. Par conséquent, la propagation par multi-trajets et les biais NLOS sont très difficiles à estimer et en effet devenu l'un des sujets ciblés dans cette thèse.

Une fois les PR sont mesurées, on obtient un ensemble d'équations non linéaires à quatre inconnues, appelé l'équation de navigation. Dans un système de coordonnées cartésiennes,

$$\rho_i = d_i + c.dt_r \tag{2}$$

où

$$d_i = \sqrt{(x_i - x)^2 + (y_i - y)^2 + (z_i - z)^2} \tag{3}$$

Au moins quatre mesures de PR sont nécessaires pour estimer les 4 inconnues (x, y, z et dt_r). Les positions des satellites sont calculées en utilisant les paramètres de Kepler démodulés obtenus à partir d'un message de navigation par satellite. La position est calculée et ensuite transformée en un système de coordonnées en longitude, latitude et altitude ellipsoïdale. Le système le plus couramment utilisé est de coordonnées WGS84 (World Geodetic System 1984) [2]. Le modèle de mesures standard liant les measures PR, données dans le vecteur Z, du vecteur d'état à estimer, X, est donné par:

$$\mathbf{Z} = \mathbf{HX} + \varepsilon \tag{4}$$

En utilisant les mesures de PR, plusieurs algorithmes différents peuvent être utilisés pour calculer diverses solutions, par exemple; position, biais d'horloge, la vitesse, le temps et l'accélération. Les algorithmes de navigation les plus couramment utilisés sont les moindres carréés pondéré et le filtre de Kalman. Outre les mesures de PR, la solution de navigation peut également exploiter d'autres mesures GNSS comme des mesures de l'effet Doppler (DR) ou des mesures de la phase des porteuses (CP) pour lisser la solution dans le domaine de mesures ou dans le domaine de la position. Les méthodes de lissage existantes utilisent les CP et DR pour profiter de la caractéristique de haute précision de la CP et de la DR, afin d'améliorer la précision de la PVT [3, 4].

Contrôle de l'intégrité

Dans le domain de l'aviation civile, le contrôle de l'intégrité est souvent accompli par les techniques de contrôle autonome de l'intégrité par le récepteur (RAIM) qui utilisent les algorithmes de détection et d'exclusion des défauts (FDE) pour rejeter les valeurs aberrantes à partir des données mesurées et aussi par les systèmes d'augmentation comme l'augmentation basée sur des systèmes sol (GBAS) et l'augmentation basée sur des satellites (SBAS) qui transmettent des informations d'intégrité aux avions pour calculer le niveau de protection (PL) associée à un risque d'intégrité. Ces techniques sont conçues pour les applications aéronautiques où la haute redondance des données existe, des normes de performance matures pour chaque phase de la navigation sont disponibles, les erreurs de mesure et de position sont modélisées par une distribution gaussienne et un seul défaut est attendu à un instant du traitement.

Les algorithmes d'intégrité de positionnement et de surveillance de la fiabilité sont généralement basés sur l'inférence statistique et tests d'hypothèses. En raison de réelle erreur de position ne peut pas être connue ou mesurée en temps réel, RAIM calcule un paramètre scalaire mesurable qui fournit des informations sur les erreurs de mesure de pseudo-distance (qui peut être lié à l'erreur de position). Ce paramètre mesurable est appelée statistique de test. C'est une variable aléatoire de distribution connue. Par exemple, dans Least Square RAIM, la statistique de test est calculée à partir de résidus de pseudodistance (PR), qui sont la différence entre le PR mesuré et le PR dérivé de la solution de navigation estimée. Dans RAIM, détection de défaut est obtenue en comparant une statistique de test contre un seuil de détection. Pour la mise en œuvre en milieu urbain, la statistique de test doit être formulée pour détecter les erreurs dans les mesures aberrantes comme provenant de NLOS et des effets multi-trajets. La difficulté est de pouvoir caractériser la statistique de test dans ce type d'environnement non gaussiens.

Dans l'approche SBAS, chaque fois que le PL surveillée est inférieure à la limite d'alerte (AL), le positionnement est considéré comme étant dans la condition d'intégrité. Cependant, pour les applications terrestres en particulier en milieu urbain, l'adaptation directe ou simple de contrôle de l'intégrité de l'approche de l'aviation civile n'est pas possible en raison des caractéristiques de dégradation du signal. En raison de circonstances posées par les milieux urbains, les approches développées pour les environnements à ciel ouvert ne sont pas efficaces en assurant la fiabilité de positionnement dans des environnements restreints. Le principal défi dans ces environnements difficiles en milieu urbain est la difficulté d'avoir un modèle fiable des mesures reçues, l'outil de base pour la plupart des méthodes d'analyse des performances et d'intégrité, comme dans le cas des applications de l'aviation civile.

Contributions Scientifiques de la Thèse

NLOS: caractérisation en milieu urbain à l'aide d'un modèle 3D

Dans la première partie de la thése, les erreurs NLOS en milieu urbain sont caractérisées par un modèle 3D de l'environnement urbain. Dans un environnement avec un nombre limité de satellites visibles, l'exclusion des signaux dégradés pourrait entraîner ne pas avoir assez de mesures acceptables pour une solution de position ou nuire à la géométrie des satellites. En utilisant un simulateur GNSS avec le modèle 3D, les signaux NLOS sont identifiés et leurs biais sont estimés. Grâce à cette prédiction, les signaux NLOS sont corrigés et utilisés pour améliorer l'exactitude et l'intégrité des positions estimées.

A cet effet, ce travail combine le modèle de variance sigma-ε avec un saut de moyenne (biais NLOS) pour modéliser les erreurs de pseudodistances. Tout d'abord, un modèle 3D de l'environnement est utilisé pour détecter l'état de réception NLOS et de prédire le biais NLOS liées au phénomène de retard excès. Pour un positionnement fiable, un ajustement de la variance des PR en LOS basé sur les valeurs du C/No est mis en œuvre. En outre, le biais est soustrait des NLOS PR lors de l'étape de trilatération du calcul de la position. Les biaises NLOS ont été obtenus à priori pour chaque satellite en mesurant la différence entre les PR mesurées et les PR référencées lorsque l'état de réception est déterminé en situation NLOS par le modèle 3D. La performance du système proposé est évaluée à l'aide des données réelles et comparée à un filtre de Kalman standard sans les informations aidant du simulateur 3D.

Prédiction des conditions des signaux GNSS via un modèle 3D

Dans ce travail, le logiciel SE-NAV [5] est utilisé pour prédire la réception du signal des systèmes GNSS comme le GPS dans des scènes virtuelles 3D de zones urbaines connues. La propagation de signaux est basée sur un algorithme de traçage de rayon qui calcule les effets d'ombrage et de multi-trajets. SE-NAV utilise l'optique géométrique pour calculer les rayons réfléchis, diffractés et transmis. Basé sur ces multiples rayons qui atteignent le récepteur, l'état de réception LOS ou NLOS d'un satellite est fourni. Afin de caractériser les biais a priori, la position des satellites et le récepteur doivent être connus. Les positions des satellites sont calculées sur la base des données d'éphémérides alors que les positions le long de la trajectoire sont obtenues à partir du récepteur.

Nous précisons que le modèle 3D représente seulement une approximation de la réalité de la propagation et que la reconstruction parfaite des signaux réels reçus reste très difficile. Tout d'abord, il existe une variabilité non quantifié de la vie réelle de l'environnement qui

entoure le récepteur par rapport à la représentation virtuelle de l'environnement statique de réception. Par exemple, il ya des objets non-permanents tels que les véhicules et les personnes qui peuvent affecter la propagation du signal, mais ne sont pas inclus dans le modèle 3D. Au fil du temps, même le feuillage de la végétation change et ainsi les attributs de surface du bâtiment. En fait, pour acquérir la modélisation de la précision des structures et des matériaux de construction en termes de leurs effets sur les signaux GNSS est en soi une tâche difficile.

La complexité de la propagation du signal électromagnétique pose encore une autre contrainte sur le modèle 3D. Les modèles déterministes basés sur l'optique géométrique (GO) et la théorie uniforme de la diffraction (UTD) exigent des informations géométrique et morphologique détaillée sur l'environnement de propagation. Dans les scénarios urbains, la propagation des rayons est affectée par de multiples interactions avec les diffuseurs. Chaque fois qu'un rayon est modélisée avec une réflexion ou diffraction, il ya une erreur associée à la prédiction du modèle en raison de la représentation inexacte de propriétés du matériau ou les dimensions des objets dans l'environnement. Pour les rayons qui sont modélisés par de multiples réflexions, ces erreurs ont tendance à s'accumuler, ce qui rend les prédictions du modèle encore moins précis. En outre, l'effet de l'antenne réelle et le modèle du récepteur sur le signal reçu, le plus souvent, sont indisponibles pour être inclus dans le modèle 3D. Tout cela introduit des erreurs dans la prédiction de la PR par un modèle 3D.

Pour tous les raisons ci-dessus, dans le travail de [6], les auteurs ont étudié la validité de l'aide d'un modèle de simulation 3D GNSS, en particulier SE-NAV, de prévoir les mesures de PR biais. De la comparaison entre les biais de la PR mesurée à l'aide de la position de référence et les biais prédites en utilisant le modèle SE-NAV 3D, le travail conclut que les erreurs de PR simulées sont tout à fait compatibles avec les veritables erreurs avec une correspondance qui peut atteindre 80% pour certains recépteur.

En dehors de prédire l'état de réception, le modèle 3D est également utilisé pour prédire le biais statistique NLOS, qui doit être utilisé pour les corrections de PR. Dans ce cas, la différence entre la valeur du biais simulé et du biais NLOS mesuré affectera la qualité de la position finale calculée. Le biais NLOS mesuré est calculé à partir de la différence entre la PR mesurée et la PR réfrencée lorsque l'état de réception est dèterminé en NLOS par SE-NAV. Considérant que, le biais NLOS prédit est obtenu à partir du retard de trajet du signal calculé par SE-NAV en utilisant les estimations de position calculées par le récepteur lorsque l'état de réception est déterminé en NLOS par SE-NAV.

Chaque fois qu'il y a de nombreuses composantes réfléchies d'un signal, SE-NAV fournit les retards des trajets multiples. Dans le cas d'un signal LOS, la valeur du retard de la composante directe du signal est fourni en 0. Dans le cas d'une réception NLOS, toutes

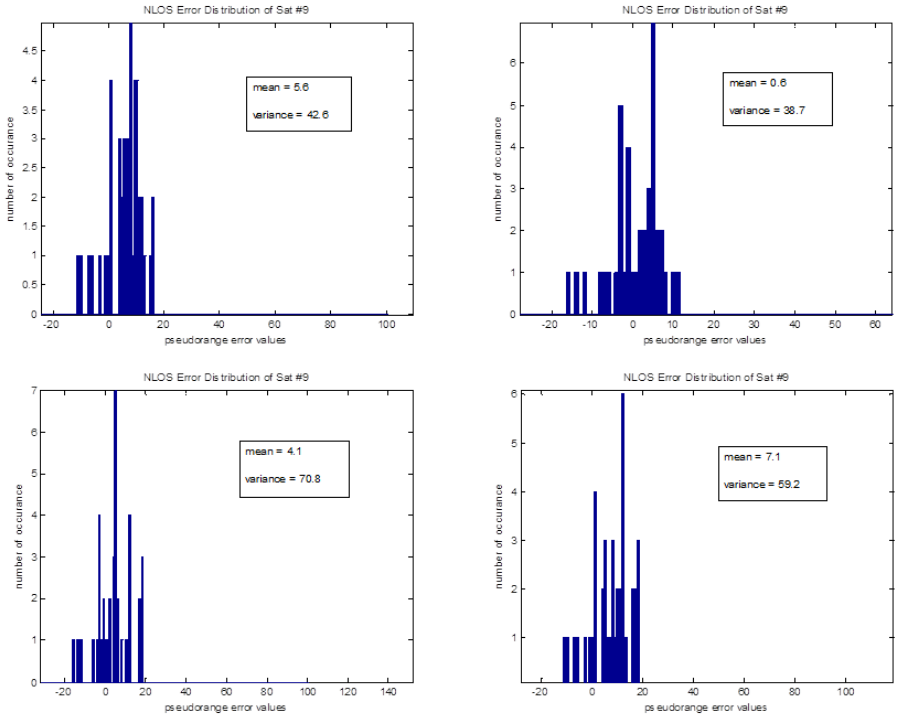

FIGURE 1: Distributions d'erreur de PR en milieu urbain (le Capitole, Toulouse) obtenues à partir d'un même satellite dans diverses périodes de 40 secondes

les composantes du signal devraient arriver en retard puisqu'il n'y a aucune composante directe du signal. Dans ce travail, quand il y a plus d'un trajet réfléchi dans le cas NLOS, une perspective optimiste est choisi au moment de décider de la valeur du biais prévu à la réception NLOS. Il est supposé que le récepteur va acquérir la composante non-direct avec le plus court délais, car il est probable que la composante qui correspond au plus court délai aura la plus grande puissance, à savoir la moins atténuée quand il arrive sur le récepteur et donc celle qui affecte plus le traitement de récepteur.

L'approche proposée pour le positionnement avec des signaux NLOS

Au cours d'une fenêtre d'observation relativement longue, l'erreur de mesure NLOS peut être modèlisée par une distribution non gaussienne et peut être approximée par un mélange de distributions gaussiennes [7]. Cependant, pour une courte fenêtre d'observation, l'approche la plus courante consiste à modéliser l'erreur de pseudodistances par une distribution gaussienne avec une moyenne non-nulle et une variance adaptive [8], comme illustré dans la figure 1. Ici, les distributions d'erreur du même satellite sont présentés sur différentes 40 secondes fenêtres où on peut observer les variations de la moyenne et de la variance. Dans le cas NLOS, la présence de signaux réfléchis introduit seulement un saut sur la valeur moyenne en raison de la distance supplémentaire. Dans le cas d'un trajet LOS dégradé, une variation supplémentaire est présenté comme une augmentation

de l'incertitude sur le trajet direct. En conséquence, ces effets du bruit du signal LOS dégradé et le biais NLOS sur l'erreur des mesures de PR sont modélisés séparément.

Pour le cas de la réception en LOS avec un multitrajet dégradé, la mise en œuvre du modèle de la variance basée sur le rapport signal-sur-bruit, dit SIGMA-ε, permettrait d'améliorer la précision de positionnement dans l'environnement urbain [9, 10]. La matrice de covariance de l'observation peut être réalisé sous la forme $\mathbf{R} = diag(\sigma_1^2, \sigma_2^2, \ldots, \sigma_k^2)$ où

$$\sigma_k^2 = a + b.10^{\frac{-C/No}{10}} \tag{5}$$

et σ_k^2 est la variance de la k^{eme} observation. Les constantes a et b sont déterminés en fonction de l'environnement et de l'équipement de l'utilisateur, qui peut être calculées à priori hors ligne à l'aide des erreurs de mesures des PR et leur C/No sur une certaine époque.

Pour chaque satellite, la pseudodistance ρ_k peut être exprimée par,

$$\rho_k = d_k + c.dt_k^{sat} + c.dt_k^{rcv} + atmo_k + m_k + \epsilon_k \tag{6}$$

avec $c.dt$ représente décalage d'horloge (par satellite ou récepteur), $atmo$ représente à la fois les retards ionosphériques et troposphériques. Le terme m_k est le retard de propagation par multitrajets tandis que ϵ_k représente le bruit du récepteur. En milieu urbain, m_k est la principale contributrice de l'erreur et pourrait représenter des conditions LOS/NLOS mixtes. Une fois les troposphériques, ionosphériques et horloge erreurs sont compensées, le modèle est réduit à l'expression suivante,

$$\rho_k = d_k + m_k + \epsilon_k \tag{7}$$

Pour illustrer plus en détail les conditions LOS/NLOS dans la propagation par multitrajets, nous pouvons réécrire l'équation comme [11]:

$$\rho_k = d_k + m_k + b_k w_k \tag{8}$$

où

$$m_k = \begin{cases} 0, \text{ en condition LOS} \\ m_{NLOS}, \text{ en condition NLOS} \end{cases} \tag{9}$$

$$b_k = \begin{cases} \sigma, \text{ en condition LOS} \\ \sqrt{\sigma^2 + \sigma_{NLOS}^2}, \text{ en condition NLOS} \end{cases} \tag{10}$$

et w_k est la moyenne nulle du bruit blanc gaussien $\mathcal{N}(0, 1)$. En d'autres termes, le terme NLOS est caractérisé par sa moyenne, m_{NLOS}, et sa variance, σ_{NLOS}^2. Ainsi, dans le cas

du NLOS, pour corriger la pseudo-distance du biais de NLOS, la mesure affectée devient

$$\rho'_k = \rho_k - m_{NLOS} = d_k + b_k w_k \tag{11}$$

et

$$b_k = \sqrt{\sigma^2 + \sigma^2_{NLOS}} \tag{12}$$

Le biais estimé en utilisant le modèle 3D est soustrait des PR qui sont utiliss dans l'estimation de la PVT par un filtre de Kalman étendu. L'équation d'état peut être fournie par:

$$\mathbf{X_{k+1}} = \mathbf{F}\mathbf{X_k} + \mathbf{v_k} \tag{13}$$

où $\mathbf{X}$ est le vecteur d'état, $\mathbf{F}$ est la matrice de transition d'état et $\mathbf{v}$ est le bruit de processus de distribution gaussienne de moyenne nul.

En supposant un modèle de vitesse presque constante, le vecteur d'état cosidéré est:

$$\mathbf{X_k} = [p_k, \dot{p}_k, ct_k, \dot{ct}_k]^T \tag{14}$$

où p_k est le x_k, y_k, z_k coordonnées de position, $\dot{p}_k$ sont les vitesses, ct_k est le biais d'horloge et $\dot{ct}_k$ est la dérive d'horloge.

La matrice de transition d'état est donné par:

$$\mathbf{F} = \begin{bmatrix} \mathbf{I} & T_s\mathbf{I} & 0 & 0 \\ 0 & \mathbf{I} & 0 & 0 \\ 0 & 0 & 1 & T_s \\ 0 & 0 & 0 & 1 \end{bmatrix} \tag{15}$$

où $\mathbf{I}$ est la matrice d'identité 3×3 et T_s est la période d'échantillonnage.

Le bruit de processus en temps discret est donné par:

$$\mathbf{v_k} \sim \mathcal{N}(0, diag(\mathbf{Q_1}, \mathbf{Q_2})) \tag{16}$$

où

$$\mathbf{Q_1} = \begin{bmatrix} \frac{T_s^3}{3}\sigma_a^2\mathbf{I} & \frac{T_s^2}{2}\sigma_a^2\mathbf{I} \\ \frac{T_s^2}{2}\sigma_a^2\mathbf{I} & T_s\mathbf{I} \end{bmatrix} \tag{17}$$

et

$$\mathbf{Q_2} = \begin{bmatrix} \sigma_b^2 T_s + \frac{T_s^3}{3}\sigma_d^2 & \frac{T_s^2}{2}\sigma_d^2 \\ \frac{T_s^2}{2}\sigma_d^2 & T_s\sigma_d^2 \end{bmatrix} \tag{18}$$

La variance de biais d'horloge σ_b^2 et la variance de dérive d'horloge σ_d^2 dépendra de la qualité du récepteur, tandis que la variance de l'accélération σ_a^2 dépend du mouvement du récepteur.

Si la PR mesurée est prévue en tant que signal LOS, sa covariance est adaptée à la valeur selon l'équation 5. Si la mesure est prévue une réception NLOS, le biais NLOS m_{NLOS} est prédit à partir de SE-NAV où il fournit la distance retardée du ray tracing NLOS par rapport à la distance en ligne droite entre le satellite et le récepteur. Ensuite, le biais est soustraite de la mesure de la PR et la variance de NLOS σ_{NLOS}^2 est inclus dans la covariance comme décrit par les équations 8 et 11. Par conséquent, l'équation d'observation peut être formulée sous la forme,

$$\mathbf{z_k} = \mathbf{h}(\mathbf{X_k}) + \mathbf{m_k} + \mathbf{b_k w_k} \tag{19}$$

où $\mathbf{h}$ décrit la dépendance non-linéaire des observations en fonction de l'état. La covariance d'observation est,

$$\mathbf{b_k w_k} \sim \mathcal{N}(0, \mathbf{R}) \tag{20}$$

où $\mathbf{R}$ dépend de la condition LOS/NLOS de l'état de réception de la mesure PR.

Résultats et analyse

Afin de mettre en œvre le modèle SIGMA-ε de la variance comme dans l'équation 5, les valeurs des paramètres a et b devront être déterminés en ajustant l'écart-type $\sigma_k = \sqrt{a + b.10^{\frac{C/No}{10}}}$ d'erreurs absolues des pseudodistances en fonction des valeurs de C/No. Figure 2 montre un exemple de la courbe obtenue et le tableau 1 liste tous les a et b valeurs déterminées par satellite visible lors de la collecte de données. Il a été observé que pour plusieurs satellites, il y a des valeurs négatives de la constante b, ce qui indique une dégradation de sigma pour C/No. Cette situation confirme la question de la difficulté d'utiliser uniquement C/No tant qu'indicateur de la qualité de la mesure dans les environnements urbains en particulier avec ce court données. La réception de signaux GNSS dans les environnements urbains sont dégradés par multitrajets et NLOS, donc il est possible pour un signal réfléchi d'avoir une valeur C/No élevée.

La prédiction LOS/NLOS par SE-NAV est comparée à la valeur C/No des mesures PRs. Les C/No de valeurs de seuil de 40, 38 et 30 dB-Hz sont utilisées pour cette comparaison. On peut voir dans le tableau 2 que le seuil < 40 dB-Hz a le plus d'accord entre la prédiction SE-NAV et le critère du C/No. Ces valeurs C/No peuvent également être comparé avec l'angle d'élévation des satellites (figure 3) puisque les signaux des satellites de basse altitude sont plus susceptibles d'être reçu comme NLOS en milieu

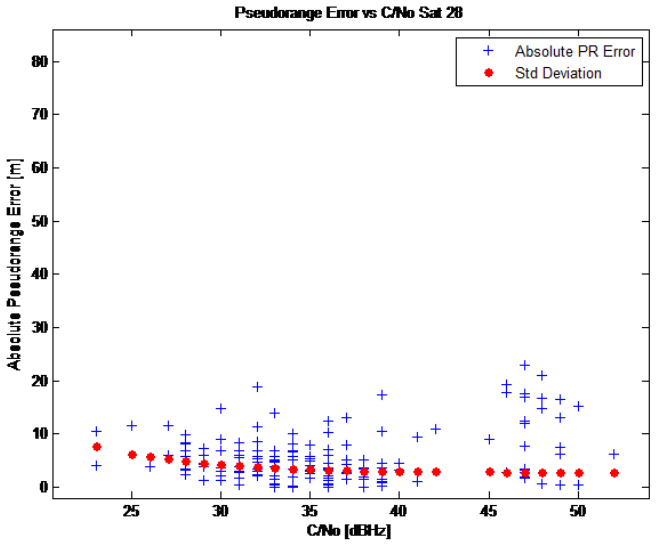

FIGURE 2: Erreurs de Pseudodistances en fonction C/No

Sat #	Number of samples	*a*	*b*
5	164	164	-1 x 10^4
8	127	115	1 x 10^4
9	152	127	3336
10	132	171	2 x 10^4
15	165	136	-1 x 10^4
17	24	325	1339
18	114	48	2 x 10^4
24	18	982	- 4649
26	161	55	-1 x 10^4
27	155	29	-7603
28	162	8	1 x 10^4

TABLE 1: Liste des paramètres du modèle de la variance (C/No) obtenu par ajustement de la courbe des erreurs de PR absolues

Sat PRN, Elevation	Threshold < 40 dB-Hz	Threshold < 38 dB-Hz	Threshold < 30 dB-Hz
5, 35°	61 %	45 %	2 %
8, 26°	98 %	95 %	48 %
9, 26°	89 %	87 %	54 %
10, 12°	86 %	82 %	75 %
15, 65°	64 %	47 %	5 %
17, 9°	100 %	100 %	62 %
18, 17°	100 %	100 %	72 %
24, 4°	100 %	100 %	100 %
26, 43°	91 %	80 %	14 %
27, 40°	94 %	93 %	38 %
28, 48°	93 %	83 %	15 %
Total	**89 %**	**83 %**	**44 %**

TABLE 2: La conformité entre la prédiction SE-NAV LOS/NLOS et le critère sur le C/No

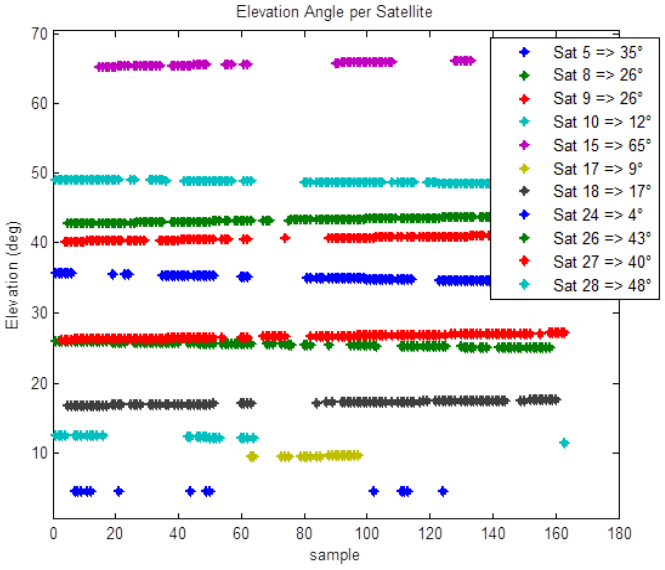

FIGURE 3: L'angle d'élévation par satellite

urbain par rapport à ceux avec une altitude plus élevée. Dans le tableau 2, pour les satellites dotés de moins de 26^o élévation, la prédiction LOS/NLOS par SE-NAV est parfaitement en accord avec la métrique du C/No. Autrement dit, la prédiction de la réception LOS/NLOS par le modèle 3D est plus semblable à la prédiction basée sur C/No lorsque l'élévation des satellites est basse par opposition quand l'élévation du satellite est plus élevé.

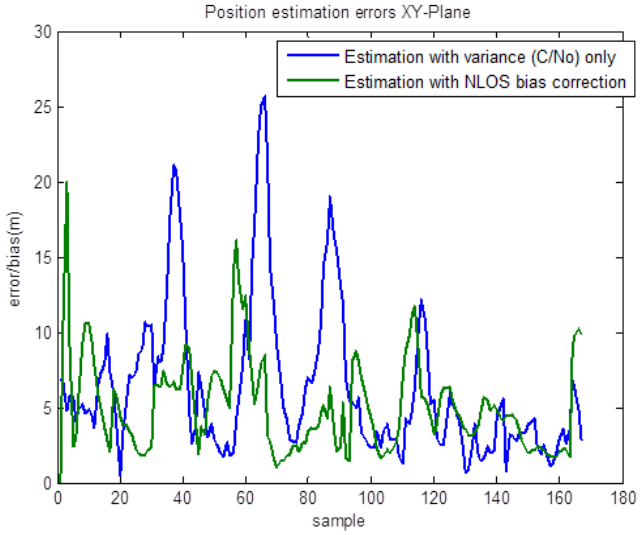

FIGURE 4: Erreur d'estimations de position dans le plan XY

La figure 4 compare les erreurs de position 2D entre l'estimation de position avec correction du biais NLOS et estimation de position en utilisant le C/No modèle de variance (sans tenir compte LOS/NLOS réception). On peut voir que l'estimation avec correction de biais NLOS était généralement meilleur que l'estimation de position en utilisant seulement le C/No modèle de variance. L'estimation avec correction du biais a été en mesure de réduire les grandes erreurs qui existent dans l'estimation, plus que dans le cas avec le modèle de la variance (autour de la 37ème, 66ème et 87ème échantillons) basée sur le C/No.

La figure 5 montre la comparaison du biais mesurée contre le biais prédit pour les satellites 5, 8 et 28. La comparaison montre que bien qu'il y ait une certaine similitude dans les profils, les valeurs des biais sont très différents entre eux. Autres recherches pourraient être poursuivie afin d'améliorer le prédiction de biais NLOS par le modèle 3D. Malgré la différence entre leurs valeurs de biais, leurs performances de positionnement dans le plan X-Y (figure 6) sont assez semblables en général. Cet effet est dû à la projection des biais de distance dans le domaine de position qui est également influencée par la géométrie de la constellation des satellites. La différence des biais de mesure et prédits peut également être impacté par d'autres objets réels dans les environs du récepteur qui ne sont pas pris en compte dans le modèle 3D (voiture et personnes de passage, arbre, etc).

La capacité du modèle 3D pour prédire LOS/NLOS est encourageant en comparaison avec d'autres indicateurs tels que C/No et l'angle d'élévation par satellite. D'autre part, la capacité du modèle 3D à prédire le biais NLOS a été jugé modeste et non concluante pour les données traitées, relativement de courte durée. Plus de recherches

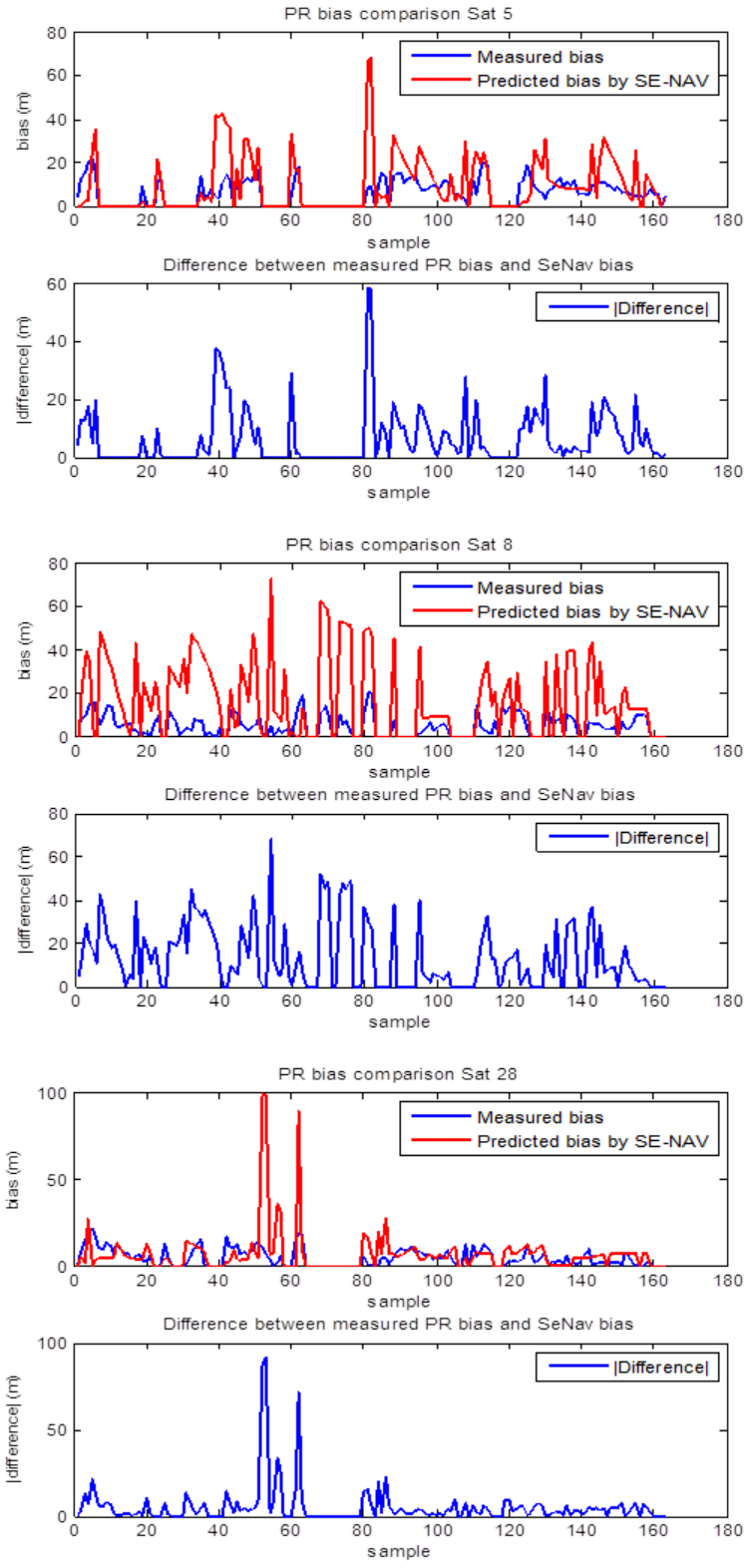

FIGURE 5: Comparaison des biais NLOS mesurés contre les biais prédits

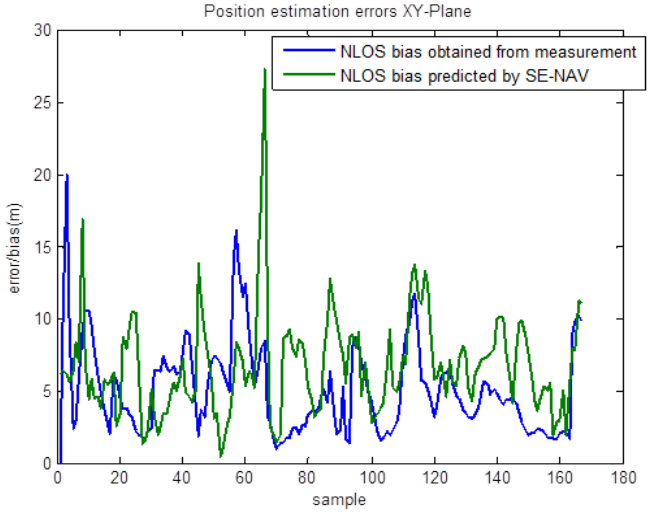

FIGURE 6: Les erreurs de position - biais NLOS mesurés contre le biais NLOS prédit par SE-NAV

et des analyses sont nécessaires pour valider la qualité des prédictions par modèle 3D. De même, quand les biais prédits ont été utilisés pour les corrections de PR dans l'estimation de position, les résultats ont montré que les erreurs de positionnement sont généralement presque similaires à celles calculées en utilisant la biais mesurée calculée à partir de la trajectoire de référence. Même si la prédiction n'est pas parfaite, les incertitudes associé sont absorbée par le filtre de Kalman et donc ce sont des informations utiles. Par conséquent, en terme de la prédiction de biais, d'autres techniques d'exploiter mieux les informations 3D doivent être développées.

Fiabilité de la mesure par prédiction de pseudodistances en utilisant une approche hybride

Dans la deuxième partie de la thèse, nous avons proposé une technique de surveillance de la fiabilité dans le domaine des mesures GNSS pour l'environnement urbain en utilisant un capteur de vitesse fiable. L'approche prévoit les pseudodistances (PR) par hybridation avec d'autres capteurs. Un odomètre et gyroscope sont utilisés pour obtenir une position de référence pour la vérification de la fiabilité de la pseudodistance. En utilisant l'approche hybride, les résidus sont générés pour former une statistique de test qui est testée contre un seuil. Quelques formes de résidus ont été calculées sur la base de plusieurs observables, qui sont la PR, la variation de la distance et la vitesse.

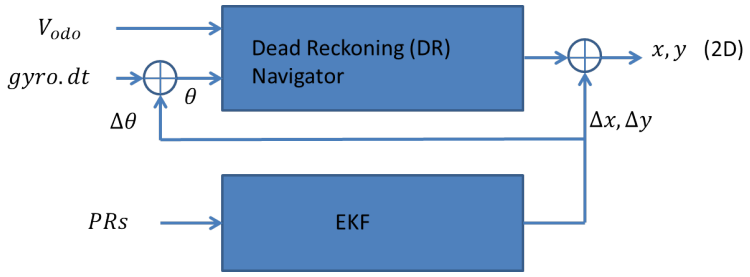

FIGURE 7: Le schéma de principe du filtre de navigation hybride

GNSS/Odomèter/Gyroscope Intégration des mesures pour la prédiction des PRs

Le filtre d'intégration de navigation à l'estime utilise un seul odomètre pour mesurer le déplacement et un gyroscope pour mesurer la direction (i.e. le cap) du véhicule. La figure 7 montre le filtre de navigation mis en œuvre dans cette recherche qui a une configuration d'une fusion lâche du GPS, gyroscope et odomètre. Nous utilisons une approche standard de navigation à l'estime pour prédire la position 2D du véhicule sur la base des mesures obtenues à partir de l'odomètre et du gyroscope. En même temps, l'EKF du GNSS fournit des corrections à la sortie du navigateur à l'estime et également à l'entrée de lacet du gyroscope. Par conséquence, lorsque les signaux satellites sont bons, ils vont corriger la sortie de navigateur à l'estime. Le positionnement hybride dans ce travail est réalisé par la formulation suivante:

$$\hat{x}_{user}(k) = \hat{x}_{user}(k-1) + V_{odo}.\cos\theta.dt + \Delta x \quad (21)$$

$$\hat{y}_{user}(k) = \hat{y}_{user}(k-1) + V_{odo}.\sin\theta.dt + \Delta y \quad (22)$$

$$\theta(k) = \theta(k-1) + gyro.dt - b_{gyro}.dt \quad (23)$$

où:

- $\hat{x}_{user}(k)$ est la position de l'utilisateur dans les coordonnées x
- $\hat{y}_{user}(k)$ est la position de l'utilisateur dans les coordonnées y
- V_{odo} est la vitesse linéaire mesurée par l'odomètre
- $\theta(k)$ est l'angle du cap
- $gyro$ est la vitesse angulaire du cap fournie par la gyroscope
- b_{gyro} est le biais estimé de la vitesse angulaire du cap de la gyroscope
- Δx est la correction de la position estimée de coordonnée x
- Δy est la correction de la position estimée de coordonnée y

Le vecteur d'état d'erreur mis en œuvre pour la EKF dans ce travail est:

$$\mathbf{x} = \begin{bmatrix} \delta x \\ \delta y \\ \delta\theta \\ b_{gyro} \\ b_c \\ d_c \end{bmatrix} \tag{24}$$

où

- δx : erreur de position sur l'axe des x
- δy : erreur de position sue l'axe des y
- $\delta\theta$: erreur du cap
- b_{gyro} : biais du gyroscope
- b_c : biais d'horloge récepteur GNSS
- d_c : dérive de l'horloge récepteur GNSS

La matrice de transition d'état, $\mathbf{F}$, est donnée par:

$$\mathbf{F} = \begin{bmatrix} 1 & 0 & V_{odo}.\cos(\theta)dt & 0 & 0 & 0 \\ 0 & 1 & -V_{odo}.\sin(\theta)dt & 0 & 0 & 0 \\ 0 & 0 & 1 & -dt & 0 & 0 \\ 0 & 0 & 0 & 1 & 0 & 0 \\ 0 & 0 & 0 & 0 & 1 & dt \\ 0 & 0 & 0 & 0 & 0 & 1 \end{bmatrix} \tag{25}$$

L'odomètre utilisé dans les expériences de ce travail est le capteur iMWS-V2 de iMAR, qui est un capteur de roue montée sur le véhicule de l'ISAE sur une bande magnétique. Pour obtenir l'angle du cap, le gyroscope iMAR de la contrôle IMU-FSAS a été utilisée. Les signaux GPS sont mesurés à l'aide d'un récepteur u-blox LEA-4T. Les données de référence, le long de la trajectoire, sont fourni par un système NovAtel SPAN.

Le résultat de la figure 8 montre que la vitesse mesurée par l'odomètre a une ressemblance très proche de la vitesse de référence avec un coefficient de corrélation de 0,987. Cette très forte corrélation indique que l'odomètre peut être un bon capteur de référence. Cependant, il existe certaines zones mortes pour la sortie de l'odomètre, soit lorsque la vitesse du véhicule est faible, l'odomètre ne délivre pas une information de vitesse valide.

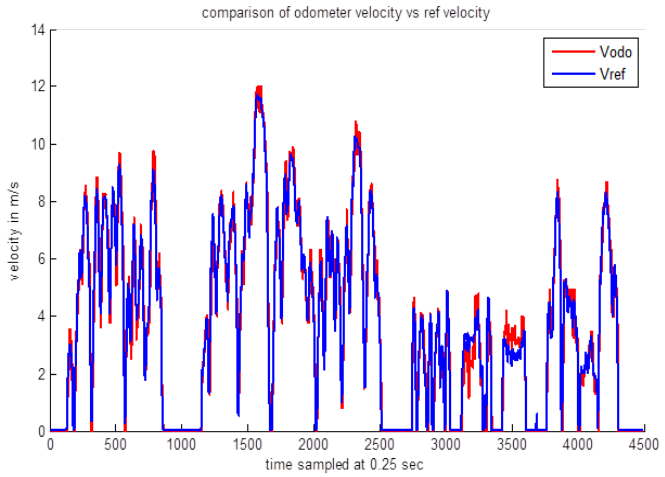

FIGURE 8: Comparaison de la vitesse odomètre avec une vitesse de référence

Métriques de fiabilité

Trois formes de résidus (PR, de vitesse et de taux de distance) ont été pris en compte afin d'analyser leur capacité à surveiller la fiabilité des mesures qui sont utilisées pour calculer les solutions PVT.

a. Test de fiabilité des pseudodistances GNSS. L'objectif de cette approche consiste à utiliser un capteur d'aide d'une manière tel que la relation de la mesure du capteur de référence pour le positionnement par GNSS peut fournir une procédée de contrôle de la fiabilité. L'algorithme que nous avons utilisé est basé sur les résidus de pseudodistances qui est la différence entre la mesure et la pseudodistance prédite. À chaque instant k et pour chaque satellite i, le résidu de PR est:

$$r^i(k) = PR^i_{measured}(k) - PR^i_{predict}(k) \tag{26}$$

Les PR prédites sont calculées à partir des positions des satellites, $\mathbf{X}_{sat}$ et les positions estimées de l'utilisateur, $\hat{\mathbf{X}}_{user}$

$$PR^i_{predict}(k) = |\mathbf{X}_{sat} - \hat{\mathbf{X}}_{user}| + c\Delta t(k) \tag{27}$$

où $c\Delta t$ est le biais d'horloge. Pour calculer le $PR^i_{predict}(k)$, les valeurs de $\hat{\mathbf{X}}_{user}$ sont calculés en utilisant des mesures hybrides à partir d'un odomètre, un gyroscope, et toutes les PR qui sont disponibles à l'instant k (à l'exception du $PR^i_{measured}(k)$ qui est à tester). Ainsi, le $PR^i_{predict}(k)$ est prédite sans l'influence de $PR^i_{measured}(k)$. Si aucun des signaux satellites sont disponibles, la PR est estimée à la base des capteurs de navigation à l'estime seulement.

La formulation globale du résidu est donc donnée par,

$$r^i(k) = |y^i(k) - (\sqrt{[(X^i_{sat}(k) - \hat{X}_{user}(k))^2 + (Y^i_{sat}(k) - \hat{Y}_{user}(k))^2 + (Z^i_{sat}(k) - \hat{Z}_{user}(k))^2]} + c\Delta t(k))| \tag{28}$$

où:

- $y^i(k)$ est la pseudodistance mesurée à partir de satellite i à l'instant k
- $c\Delta t(k)$ est le biais d'horloge. Il est ici dans l'équation de souligner que ce biais existe encore dans la pseudo-distance prédite
- $\hat{X}_{user}(k), \hat{Y}_{user}(k), \hat{Z}_{user}(k)$ sont des positions d'utilisateur dans le cadre de ECEF à chaque période de temps

Afin d'identifier les pseudodistances défectueuses, une statistique de test T, est comparée à une valeur de seuil pour rejeter ou accepter la $PR^i_{measured}(k)$. Pour calculer la statistique de test pour chaque PR, une métrique de chi-deux pondérée est utilisée:

$$T = r^t.Z^{-1}.r \tag{29}$$

où r est le résidu de la PR caracterisé par sa variance:

$$Z = cov(r) = var(PR^i_{measured}) + var(PR^i_{predict}) \tag{30}$$

La variance de $PR^i_{measured}$ peut être déterminée à partir du modèle de variance qui est principalement liée à son C/No ou l'angle d'élévation [12]. Ici, le modèle SIGMA-ε [9] est utilisé.

D'autre part, la variance de la $PR^i_{predict}$ peut être obtenue avec la norme euclidienne du vecteur de ligne de vue et de la loi de propagation de l'erreur [13]:

$$var(PR^i_{predict}(k)) = e_{sat,user}(k).P_{user}(k).e^t_{sat,user}(k) \tag{31}$$

où:

$$e_{sat,user}(k) = \frac{x^i_{sat}(k) - \hat{x}_{user}(k)}{\|x^i_{sat}(k) - \hat{x}_{user}(k)\|} \tag{32}$$

$$P_{user}(k) = \begin{bmatrix} \sigma^2_x & \sigma_{xy} & \sigma_{xz} \\ \sigma_{yx} & \sigma^2_y & \sigma_{yz} \\ \sigma_{zx} & \sigma_{zy} & \sigma^2_z \end{bmatrix} \tag{33}$$

Pour la matrice de covariance de la position de l'utilisateur $P_{user}(k)$, on suppose la non-corrélation entre x, y et z, seuls les éléments diagonaux ont un intérêt ici. En outre, étant

donné que le positionnement est en 2D, σ_z^2 peut être mis à zéro. La matrice $P_{user}(k)$ n'est pas accessible directement à partir du navigateur hybride utilisé dans ce projet.

Cependant, les variances σ_x^2 et σ_y^2 peut être calculées en utilisant la règle de combinaison de la variance et de la loi de propagation de la variance. Une fois σ_x^2 et σ_y^2 sont calculées, la $cov(r)$ peut être déterminée par la mise en œuvre des équations 30, 31, 32 et 33. Le seuil est fixé par le niveau de confiance appliqué à la distribution de chi-deux avec 1 degré de liberté, $r^t.Z^{-1}.r \sim \chi_1^2$.

Figures 9 et 10 montrent les courbes qui comparent les résidus des PR calculées (tracées en rouge) contre les erreurs réelles de distance des satellites (tracées en bleu). La performance du résidu de PR varie pour différents satellites en fonction de la précision de la position estimée par rapport à la position du récepteur réel. La figure **??** indique le nombre de satellites visibles (bleu) contre le nombre de satellites "non-défectueux" (rouges) après la mise en œuvre du procédé de détection de défaut et d'identification. Dans cette expérience, le seuil est fixé à 2,706 (99% de niveau de confiance). Le résultat montre que dans une partie de la trajectoire, les satellites non-défectueux ont été réduits à 4 ou même moins. Dans ce cas, l'algorithme RAIM traditionnelle ne peut être mise en œuvre car il a besoin d'au moins 5 satellites visibles. Ensuite, la figure 12(a) montre l'erreur de position 2D avant (vert) et après (rouge) l'exclusion des mesures défectueuses en utilisant un filtre hybride GPS/odomètre/gyroscope tandis que la figure 12(b) est le résultat de l'utilisation de seulement GPS pour le positionnement. Le résultat montre que le filtre hybride GPS/odomètre/gyroscope améliore le positionnement. En outre, la détection de défaut et l'exclusion (FDE) pour véhicule terrestre en milieu urbain peuvent être effectuées mieux quand l'odomètre et gyroscope est hybridé avec le GPS par rapport au cas du GPS seul. Figure 13(a) montre le résultat de la détection d'erreur de PR, l'identification et l'adaptation (DIA) qui a été mis en œuvre sur le navigateur hybride à l'aide du contrôle de l'intégrité de la mesure (la technique proposée dans cette thèse). L' adaptation a été réalisée en remplaçant les PR défectueuses identifiées avec leurs PR prédites. En d'autres termes, les PR défectueuses ont été corrigées. D'autre part, la figure 13(b) montre que cette approche de la correction d'erreur de PR ne pourrait être atteint que lorsque le signal GPS a été utilisé dans le positionnement sans l'intégration de l'odomètre et du gyroscope.

b. Test de fiabilité de la vitesse de l'utilisateur. Avec la vitesse de satellite connue, la vitesse de l'utilisateur peut être déterminée à partir des mesures Doppler selon l'équation suivante,

$$D = -\frac{L1}{c}[e_{sat,user}.(V_{user} - V_{sat}) + d_t] + \varepsilon \tag{34}$$

où:

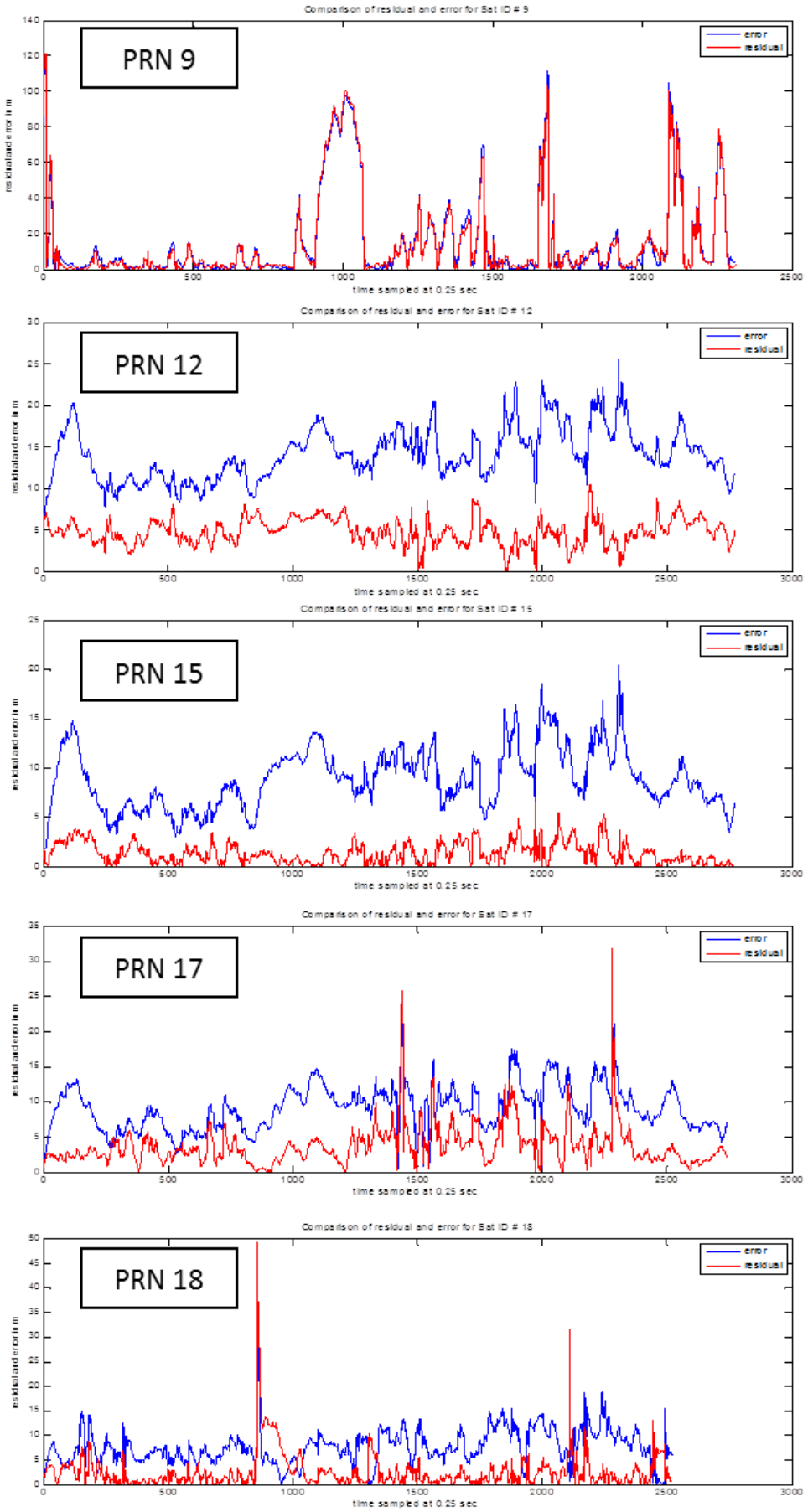

FIGURE 9: Comparaison des résidus de PR contre l'erreurs de pseudo-distance par satellite (predites en utilisant les références)

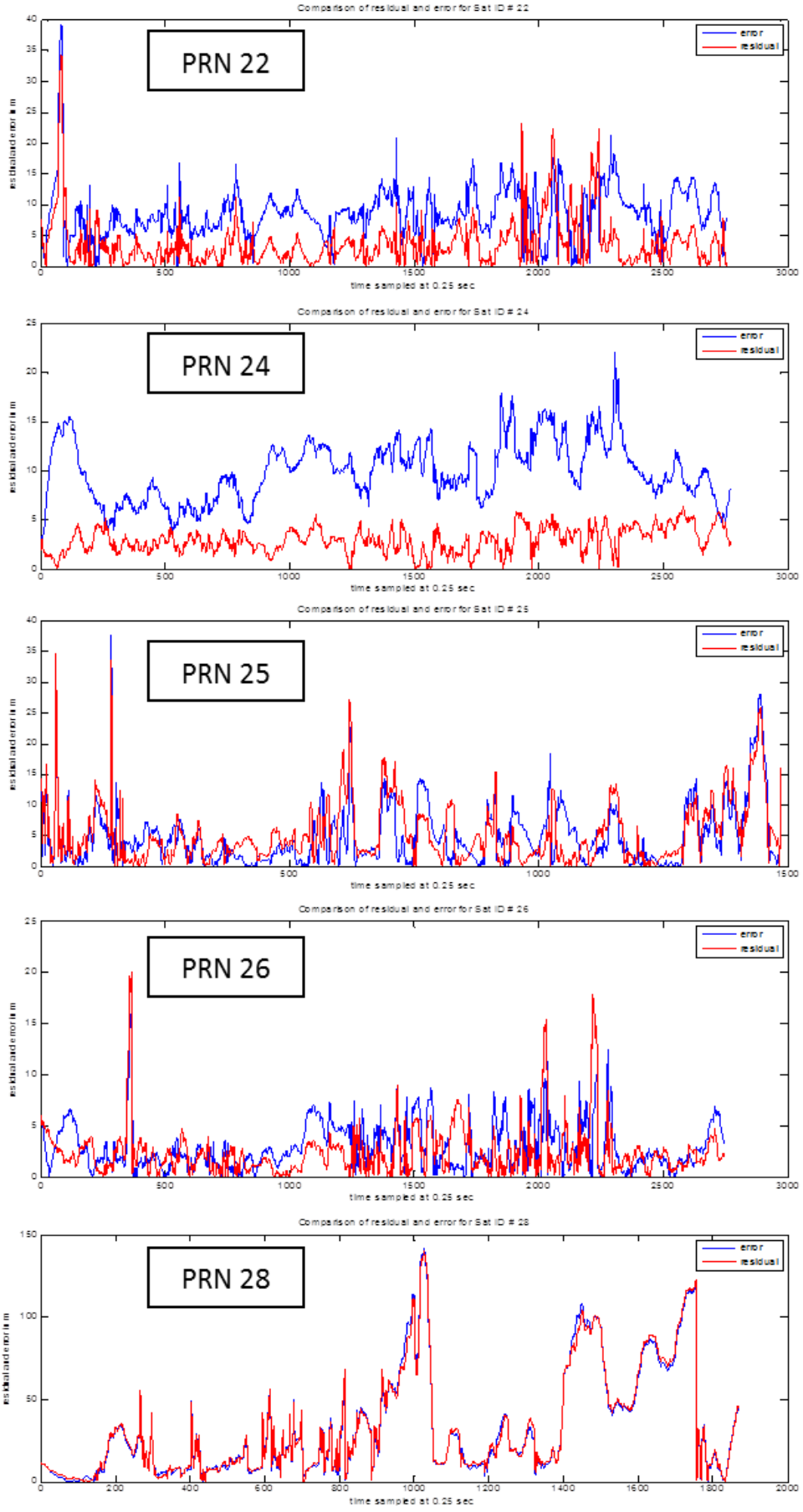

FIGURE 10: Comparaison des résidus de PR contre l'erreurs de pseudo-distance par satellite (predites en utilisant les références)

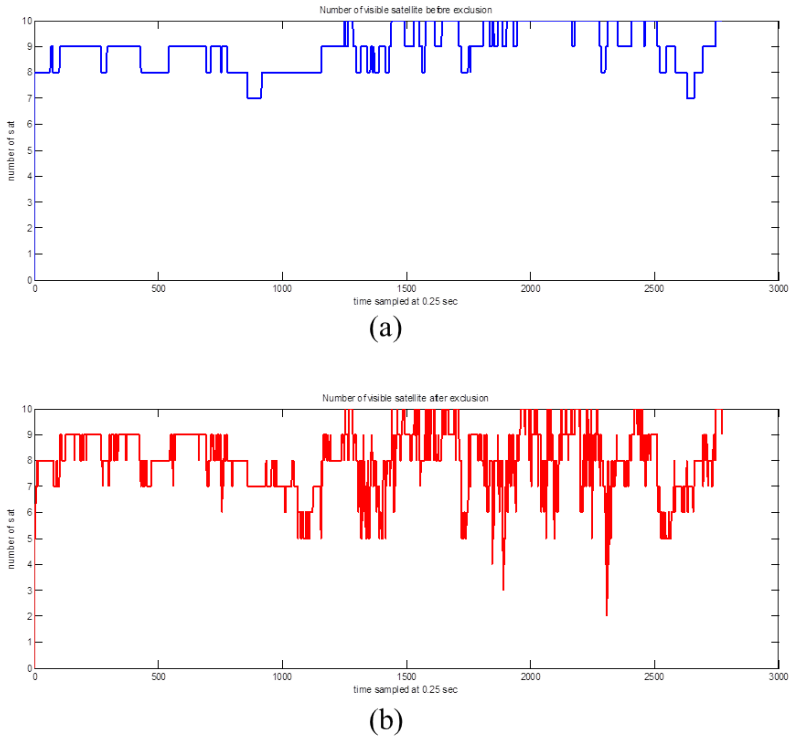

FIGURE 11: Comparaison du nombre de satellites visibles par rapport au nombre de satellites non-défectueux

- D est la mesure de l'effet Doppler en Hz
- $L1$ est la fréquence de la porteuse
- c est la vitesse de la lumière
- $e_{sat,user}$ est la vecteur unité de la ligne de vue entre le satellite et le récepteur
- V_{user} est le vecteur de vitesse de l'utilisateur
- V_{sat} est le vecteur de vitesse du satellite
- d_t est la dérive d'horloge du récepteur
- ε est le bruit de mesure

On peut envisager de tester la position estimée en générant un résidu, r_V en utilisant la différence entre la vitesse de l'utilisateur et la vitesse prédite.

$$r_V = |V_{user} - V_{predict}| \tag{35}$$

Dans cette thèse, nous proposons de calculer la vitesse prédite à partir de V_{odo}. La vitesse de l'utilisateur, V_{user} est déterminée à partir des données GPS. Par conséquent,

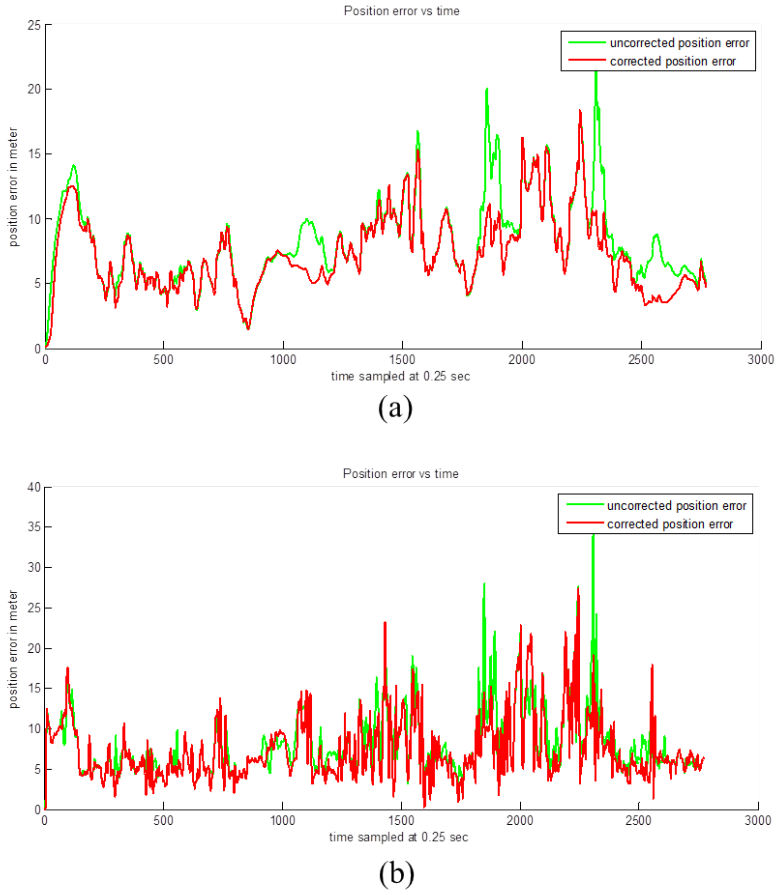

FIGURE 12: Comparaison d'erreur de position après l'exclusion de défaut (a)filtre hybride avec exclusion (b)GPS seulement

ici, V_{odo} est totalement un capteur de référence externe et ne contribue pas à la solution de positionnement. Par conséquent, le résidu de vitesse est défini par,

$$r_V = |V_{GPS} - V_{odo}| \tag{36}$$

La figure 14 montre la performance du test du résidu de vitesse. Comme on peut le voir dans la courbe, il est difficile d'établir une relation directe entre le résidu de vitesse (bleu) et l'erreur de position (rouge). Autres recherches et analyses sont nécessaires afin de l'utiliser pour le contrôle d'intégrité.

c. Test de fiabilité en utilisant le taux de la distance.

L'équation du taux de la distance est donnée par

$$\begin{aligned} \dot{\rho} &= -\frac{c}{L1}D = e_{sat,user}.(V_{user} - V_{sat}) + d_t + \varepsilon \\ &= \dot{r} + d_t + \varepsilon \end{aligned} \tag{37}$$

où:

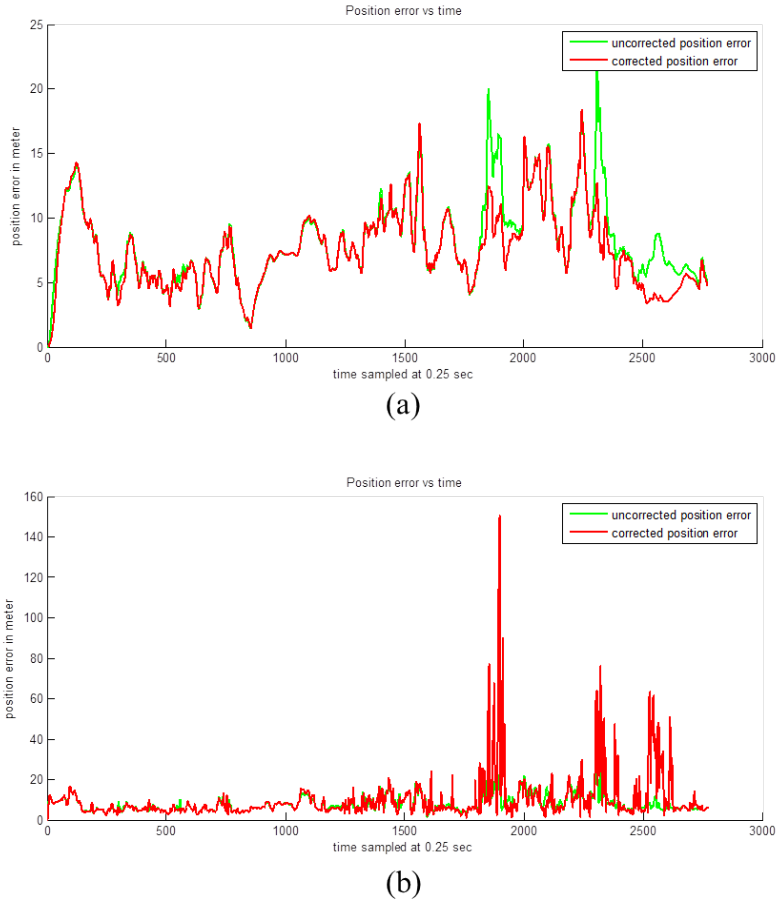

FIGURE 13: Comparaison d'erreur de position après correction de défaut (a)filtre hybride avec correction (b)GPS seulement

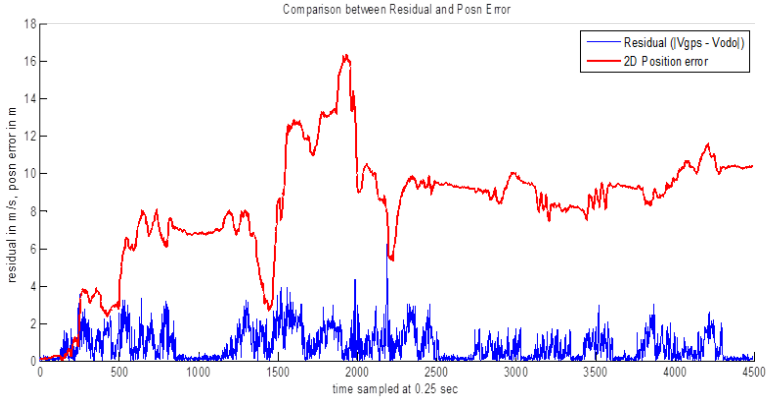

FIGURE 14: Comparaison du résidu de vitesse (bleu) contre l'erreur de position 2D (rouge)

- $\dot{\rho}$ est le taux de variation de la pseudodistance
- $\dot{r}$ est le taux de la distance géométrique entre le récepteur et le satellite

Le résidu p, est calculé en utilisant les valeurs prédites et mesurées de $\dot{\rho}$,

$$p = |\dot{\rho}_{measured} - \dot{\rho}_{predict}| \tag{38}$$

où:

$$\dot{\rho}_{measured} = \frac{PR(k) - PR(k-1)}{dt} \tag{39}$$

et

$$\dot{\rho}_{predict} = e_{sat,user}.V_{user}(k) - e_{sat,user}.V_{sat}(k) + d_t \tag{40}$$

où la $V_{sat}(k)$ est calculée à partir des données d'éphémérides et $V_{user}(k)$ obtenue à partir du filtre de Kalman en fonction de V_{odo} et l'angle de cap θ. La statistique de test, $T = p^t.Z^{-1}.p$ est utilisée pour ce résidu. Ici, la covariance, Z, est déterminée *a priori* à partir des données observées.

Figure 15 montre le résultat de la mise en œuvre l'un FDE fondée sur des résidus du taux de distance. Comme le résidu de la PR , l'erreur de positionnement peut également être améliorée en utilisant la FDE basée sur les résidus du taux de distance.

Les résultats de ces différents modes pour la réalisation de test des résidus suggèrent que le résidu basé sur les PR a l'avantage d'effectuer le contrôle d'intégrité dans le domaine de distance même si quand il y a moins de 5 satellites disponibles. Cependant, pour les applications de l'utilisateur qui nécessitent la surveillance de la vitesse, le résidu basé sur la vitesse semble être plus approprié. Bien sûr, il y a une possibilité de les combiner comme multi-indicateurs pour surveiller la fiabilité du récepteur. Toutefois, d'autres études sont nécessaires pour déterminer la performance de chaque test des résidus pour les environnements environnants et les comportements dynamiques de l'utilisateur. Cette connaissance est cruciale pour le développement d'un algorithme approprié pour le récepteur de décider à partir de plusieurs indicateurs, en particulier chaque fois qu'il y a une certaine contradiction entre eux.

La confiance du positionnement GNSS dans des environnements urbains en utilisant la majoration de la CDF des HPE

Enfin, nous avons développé une nouvelle approche expérimentale de surveillance de l'intgrité pour le positionnement en milieu urbain. En travaillant directement dans le domaine de la position, des erreurs de position horizontale (HPE) sont caractérisées en

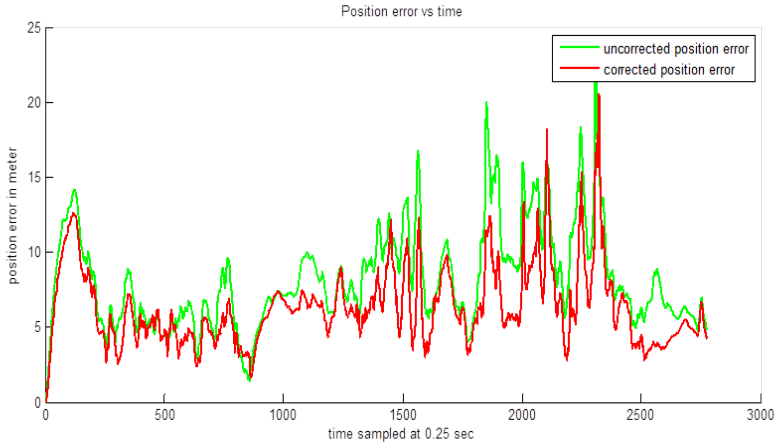

FIGURE 15: Erreur de position après correction de défaut en utilisant le résidu de taux de la distance

utilisant la distribution de Pareto généralisée. Puis, une statistique de test est dérivée basée sur les résidus de position (plutôt que des résidus de pseudodistance) où son CDF est estimée et gonflée pour correspondre à la CDF des erreurs liés à la position caractérisée. En surveillant de la statistique de test contre un seuil spécifique, l'intégrité et la continuité de positionnement sont remplies à un certain niveau de confiance. En outre, le calcul du niveau de protection horizontale (HPL) en utilisant une approche composite a également été proposée.

La caractérisation de l'erreur de position

Dans ce travail, la caractérisation de l'erreur de position du récepteur en utilisant la distribution de HPE est obtenue à partir de l'erreur de position sur les composantes nord et est. Les erreurs sont calculées sur la base de la différence entre les positions mesurées et les positions référencées. Puisque l'erreur horizontale 2D a deux composantes nord et est, la HPE peut être représentée comme une erreur radiale, définie par:

$$HPE = \sqrt{E_{east}^2 + E_{north}^2} \tag{41}$$

Dans les environnements degagés, en général, les erreurs de pseudodistance mesurées ont tendance à être distribués selon une loi normale. Dans l'estimation de la position du récepteur en utilisant les PR mesurées, ces erreurs gaussiennes de PR sont combinées et propagées au domaine de la position par l'intermédiaire qui est la matrice d'estimation linéaire pour former des erreurs avec une distribution gaussienne ègalement. Autrement dit l'E_{est} et l'E_{nord} ont tendance à avoir une distribution gaussienne aussi. Théoriquement, en supposant des conditions idéales où les distributions de E_{est} et E_{nord}

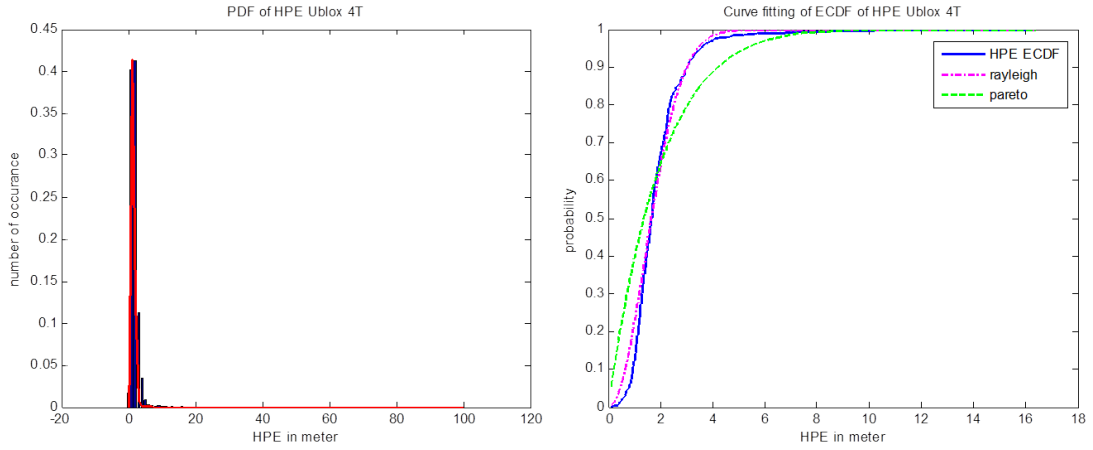

FIGURE 16: PDF et CDF d'HPE dans la zone degagée

sont aussi de moyenne nulle et indépendante, la distribution de leur norme, qui est l'HPE, aurait une distribution de Rayleigh. Selon cette hypothèse, le PDF et CDF de l'HPE sont calculées en utilisant les données empiriques et tracées dans la figure 16. Les résultats de ces expériences indiquent que la distribution de HPE dans des environnements degagés peut être représentée par une distribution de Rayleigh.

Dans le cas de milieux urbains, il a été montré que les distributions des erreurs de PR peuvent être non gaussienne en raison des biais multi-trajets et NLOS du signal. Pour cette raison, l'ajustement de courbe pour l'HPE en milieu urbain est réalisé en utilisant la distribution de Pareto. En général, cette distribution est adaptée pour les distributions à queue lourde, comme c'est le cas de l'erreur de positionnement en milieu urbain où on trouve des large valeurs d'erreurs avec une faible probabilité. La CDF de la distribution de Pareto généralisée est égale à:

$$F(x) = \begin{cases} 1 - (1 + \frac{\xi(x-\mu)}{\sigma})^{\frac{-1}{\xi}} & \text{pour } \xi \neq 0 \\ 1 - exp(-\frac{x-\mu}{\sigma}) & \text{pour } \xi = 0 \end{cases} \tag{42}$$

La figure 17 montre la PDF de l'HPE d'un récepteur uBlox 4T dans un environnement urbain. La comparaison entre la PDF d'HPE et un tracé de distribution de Rayleigh (figure de gauche) montre que les deux distributions sont différentes significativement. Par contre, la comparaison avec la distribution de Pareto généralisé (figure de droite) montre un meilleur ajustement avec la queue lourde. Dans la figure 18, le tracé de CDF montre également que la GPD correspond mieux que la Rayleigh à la CDF d'HPE. Dans ce travail, les résultats analysées à partir des données des trois récepteurs différents (uBlox 4T, Novatel, et uBlox 6T) indiquent que la distribution de Pareto généralisée est mieux adapté pour modéliser les distributions d'HPE en milieu urbain.

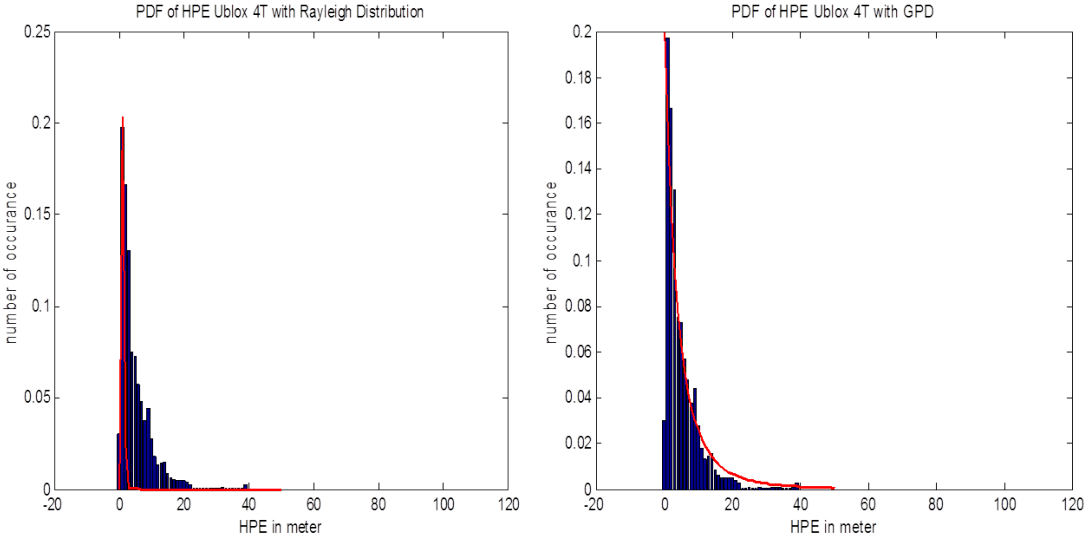

FIGURE 17: Comparaison de PDF en milieu urbain

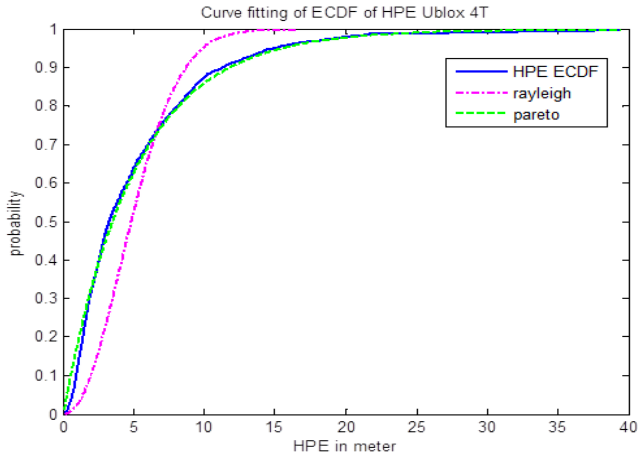

FIGURE 18: CDF en milieu urbain

La majoration de CDF d'HPE par Pareto généralisée dans le domaine de position directe

La CDF d'une GPD a la forme suivante:

$$CDF_{GPD} = 1 - [1 + \xi(\frac{x-\mu}{\sigma})]^{\frac{-1}{\xi}} \ for\ x \geqslant \mu \tag{43}$$

où le paramètre d'échelle σ agit sur la taille et la pente de la distribution, le paramètre de forme ξ affecte la forme de la queue de la distribution et le paramètre de localisation μ est associ'ee à la valeur de x lorsque le CDF $= 0$.

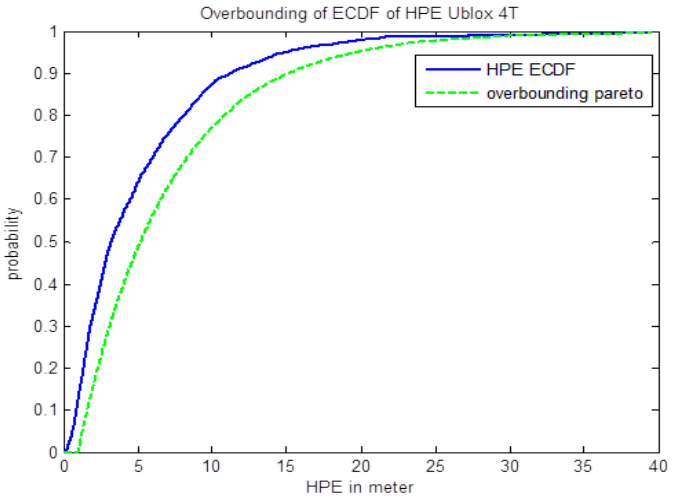

FIGURE 19: La majoration de l'HPE par GPD

Une fois que la CDF Pareto généralisée borne la CDF de l'HPE, le niveau de protection horizontale (HPL) peut être calculé à partir de son inverse, de la manière suivante:

$$CDF_{GPD} = 1 - [1 + \xi(\frac{x-\mu}{\sigma})]^{\frac{-1}{\xi}} = Prob(erreur\ de\ position \leqslant x) \tag{44}$$

Soit R_p le PL d'erreur sur la position. Assimillons la CDF à la probabilité de l'intgrité P_B,

$$1 - [1 + \xi(\frac{R_p-\mu}{\sigma})]^{\frac{-1}{\xi}} = (1 - P_{HMI}) = P_B \tag{45}$$

Pour obtenir le HPL, on résout les équations d'inconnue R_p,

$$\begin{aligned}
[1 + \xi(\frac{R_p-\mu}{\sigma})]^{\frac{-1}{\xi}} &= 1 - P_B \\
\frac{-1}{\xi} ln[1 + \xi(\frac{R_p-\mu}{\sigma})] &= ln(1 - P_B) \\
ln[1 + \xi(\frac{R_p-\mu}{\sigma})] &= -\xi ln(1 - P_B) \\
[1 + \xi(\frac{R_p-\mu}{\sigma})] &= (1 - P_B)^{-\xi} \\
\xi(\frac{R_p-\mu}{\sigma}) &= (1 - P_B)^{-\xi} - 1
\end{aligned}$$

Ainsi,

$$HPL = R_p = \frac{\sigma}{\xi}[(1 - P_B)^{-\xi} - 1] + \mu \tag{46}$$

La figure 19 montre la majoration de l'HPE par la CDF de Pareto généralisée dans le cas du récepteur uBlox 4T. Dans ce cas, l'HPL de l'intégrité à 90 % est de 15 mètres (HPE à 12 mètres) et l'intgrité à 95 % est de 20 mètres (HPE à 15 mètres).

Contrôle d'intégrité de positionement en milieu urbain

La vraie valeur de l'erreur sur la position n'est pas connue en temps réel. Par conséquent, pour le contrôle de l'intégrité de position, un test statistique est utilisé et ce test doit être calculé en utilisant des mesures observables. Dans ce travail, l'intégrité des positions estimées dans les milieux urbains est surveillé en fonction de le résiduel gonflé de la position horizontale. Le résiduel de la position horizontale observé est calculé en utilisant une estimation des moindres carrés (LS), puis gonflé pour correspondre à la borne d'HPE qui est caractérisé a priori par la GPD CDF. De cette façon, la statistique du test est en mesure pour représenter la limite de l'HPE. L'appriement de l'espace résiduel de position avec l'espace de délimitation d'erreur de position peut être décrite par le principe de transformation variable aléatoire.

a. Calcul du résidu de la position horizontale. Le vecteur des résidus de la position, $\delta\hat{x}$ est calculé en utilisant l'estimation des moindres carrés. Nous considérons le modèle de pseudodistance linéaire suivant:

$$\Delta Y = H.\Delta X + E \tag{47}$$

Pour l'estimation des moindres carrés,

$$\Delta\widehat{X} = G.\Delta Y \tag{48}$$

où

- $G = (H^T H)^T H^T$
- $\Delta\widehat{X}$ est la position estimée
- ΔY est les PR mesurées

Le résidu de la PR est:

$$\delta\rho = \Delta Y - H\Delta\widehat{X} \tag{49}$$

Par conséquent, le rèsidu de la position est:

$$\delta\hat{x} = G.\delta\rho \tag{50}$$

Ensuite, le résidu de position horizontale, $\mathrm{HPE}_{\delta\hat{x}}$ est obtenu en caculant la norme de la $\delta\hat{x}$ dans les directions nord et est:

$$HPE_{\delta\hat{x}} = \sqrt{\delta\hat{x}^2_{east} + \delta\hat{x}^2_{north}} \tag{51}$$

b. Calcul des paramètres d'inflation. En assimilant la CDF d'$HPE_{\delta\hat{x}}$, qui est désigné comme HPE_R, à la distribution de Pareto genéralisée, nous avons les équations,

$$HPE_R = \frac{\sigma}{\xi}[(1-P_B)^{-\xi}-1]+\mu \tag{52}$$

$$HPE_R = \frac{\sigma}{\xi}[(P_{HMI})^{-\xi}-1]+\mu \tag{53}$$

Les paramètres de HPE_R: σ, ξ et μ sont déterminés à partir de l'ajustement de courbe des données empiriques de la même trajectoire que l'HPE ont été calculés.

Afin de calculer les paramètres de l'inflation, les paramètres du résidu de CDF de la position horizontale, HPE_R, est adaptée aux paramètres de CDF prédéterminés qui délimitent l'HPE qui ont été calculées hors ligne.

La GPD CDF qui borne l'erreur de position horizontale caractérisé qui est utilisé pour le calcul de l'HPL est,

$$HPL = \frac{\sigma_o}{\xi_o}[(P_{HMI})^{-\xi_o}-1]+\mu_o \tag{54}$$

Ensuite, ce que l'on souhaite: $Inflated\ HPE_R = HPL$

Alors nous laissons,

$$A\sigma = \sigma_o,\ B\xi = \xi_o,\ \mu + C = \mu_o$$

En conséquence,

$$Inflated\ HPE_R = \frac{\sigma.A}{\xi.B}[(P_{HMI})^{-\xi.B}-1]+\mu+C \tag{55}$$

et les paramètres de l'inflation sont:

$$A = \frac{\sigma_o}{\sigma},\ B = \frac{\xi_o}{\xi},\ C = \mu_o - \mu \tag{56}$$

c. Dérivation du test statistique. Pour le contrôle de l'intégrité de position, le test statistique est calculé en fonction de l'$HPE_{\delta\hat{x}}$:

$$Inflated\ HPE_R = \frac{\sigma.A}{\xi.B}[P_{HMI})^{-\xi.B}-1]+\mu+C \tag{57}$$

En réorganisant et en substituant l'équation,

$$\begin{aligned} \textit{Inflated } HPE_R - (\mu + C) &= \frac{\sigma.A}{\xi.B}[(P_{HMI})^{-\xi.B} - 1] \\ \textit{Inflated } HPE_R - (\mu + C) &= \frac{\sigma}{\xi}[(1 - P_B)^{-\xi.B} - 1]\frac{A}{B}[\frac{(P_{HMI})^{-\xi.B} - 1}{(P_{HMI})^{-\xi} - 1}] \\ \textit{Inflated } HPE_R - (\mu + C) &= (HPE_R - \mu)\frac{A}{B}[\frac{(P_{HMI})^{-\xi.B} - 1}{(P_{HMI})^{-\xi} - 1}] \\ \textit{Inflated } HPE_R &= (HPE_R - \mu)\frac{A}{B}[\frac{(P_{HMI})^{-\xi.B} - 1}{(P_{HMI})^{-\xi} - 1}] + \mu + C \end{aligned} \quad (58)$$

Par conséquent

$$\textit{Test Statistique} = (HPE_{\delta\hat{x}} - \mu)\frac{A}{B}[\frac{(P_{HMI})^{-\xi.B} - 1}{(P_{HMI})^{-\xi} - 1}] + \mu + C \quad (59)$$

$$\textit{Test Statistique} = \textit{Inflated } HPE_{\delta\hat{x}}$$

Une fois que les paramètres d'inflation A, B et C sont déterminés, l'intégrité de positionnement peut être surveillée en calculant le test statistique et en le comparant contre du seuil. Dans cette approche, la distribution observée est adaptée à la borne d'HPL. En conséquence, contrairement à la RAIM traditionnelle, la distribution des statistiques de test est gonflé pour assurer que l'HPE a le même majoration comme l'HPL.

Chaque figure 20, 21, 22 et 23 montre les courbes de la CDF d'HPE (rouge solide), la CDF de sa délimitation (pointillé rouge), la CDF du résidu de la position (bleu solide) et la CDF du résidu gonflé de la position (en pointillés bleu) pour chaque trajectoire 1, 2, 3 et 4. En général, on peut voir sur chaque figure que la CDF du résidu gonflé est en mesure de borner la CDF d'HPE. Cependant, en terme de correspondance avec la délimitation de CDF du GPD, les trajectoires 1 et 2 ont performé mieux que les trajectoires 3 et 4.

Le tableau 3 montre l'P_{FA} et l'P_{MD} calculées lorsque la statistique de test a été utilisé pour surveiller l'intégrité de positionnement le long des quarte trajectoires. Aux fins de la comparaison, les probabilités d'erreur ont été calculées également en utilisant le résidu de la position (sans inflation), $HPE_{\delta\hat{x}}$ comme la statistique de test. La P_{HMI} a été fixé à 0,05.

Ces résultats montrent que l'exigence d'intégrité est respectée et la statistique de test proposée est en mesure d'équilibrer entre la P_{FA} et la P_{MD} et donc d'optimiser la surveillance de l'intégrité et la continuité de positionnement en milieux urbains. La technique proposée est capable de surveiller l'intégrité de positionnement. Cependant, puisque ce régime a adopté l'approche directe de domaine de position, il ne peut pas identifier les mesures erronées. D'autre part, cette approche est capable de surveiller l'intégrité de

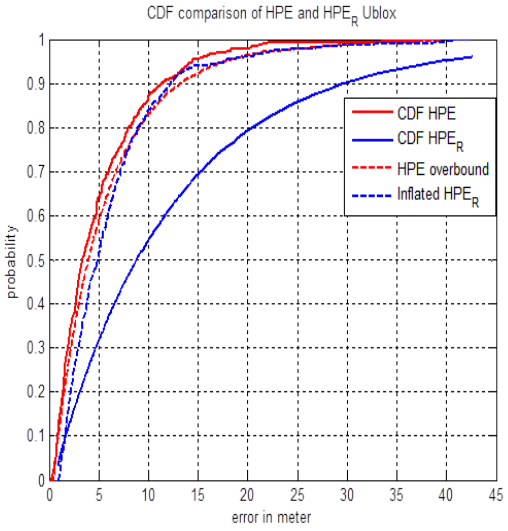

FIGURE 20: Résultat de la correspondance de la position résiduelle gonflée à l'CDF majorée (Trajectoire 1)

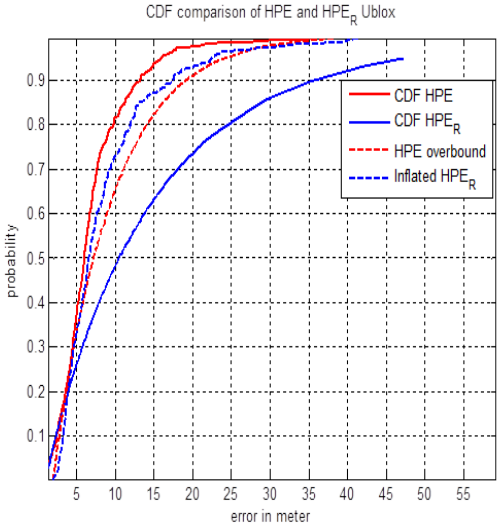

FIGURE 21: Résultat de la correspondance de la position résiduelle gonflée à l'CDF majorée (Trajectoire 2)

	Threshold (m)	***Inflated*** $HPE_{\delta\hat{x}}$		$HPE_{\delta\hat{x}}$	
		P_{FA} (%)	P_{MD} (%)	P_{FA} (%)	P_{MD} (%)
Trajectory 1	18.08	4.23	2.33	20.72	1.69
Trajectory 2	24.35	3.84	1.64	15.07	1.37
Trajectory 3	13.64	2.65	1.94	21.16	0.01
Trajectory 4	15.83	4.07	1.85	23.89	0.18

TABLE 3: Performances de surveillance de l'intégrité de positionnement

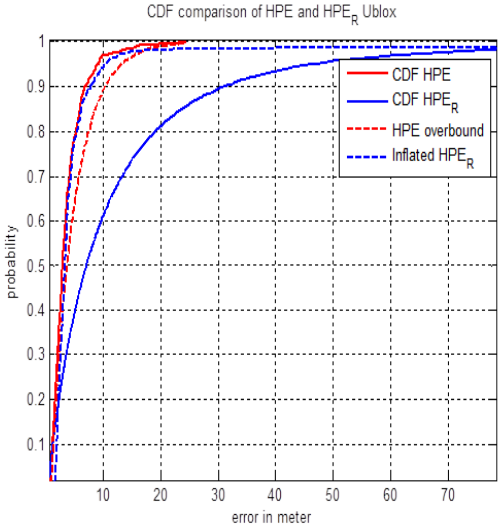

FIGURE 22: Résultat de la correspondance de la position résiduelle gonflée à l'CDF majorée (Trajectoire 3)

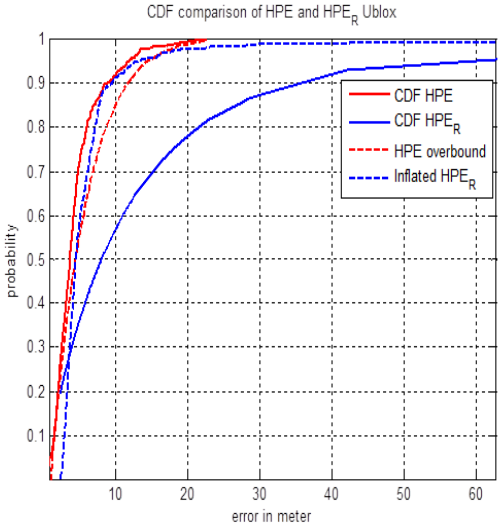

FIGURE 23: Résultat de la correspondance de la position résiduelle gonflée à l'CDF majorée (Trajectoire 4)

tout type de récepteur sans la nécessité de connaître les algorithmes d'estimation de positionnement tant que nous avons l'erreur de position caractérisé du rècepteur.

L'approche composite pour la surveillance de l'intégrité

Dans l'approche composite, le PL peut être formulé comme une somme de composante de bruit, PL_n, plus une composante de biais, PL_b [14–17]:

$$PL = PL_n + PL_b \tag{60}$$

Dans le domaine d'aviation civile, les sources et les effets du biais spécifiques ont été considérés et bien modélisés. Par contre, dans les milieux urbains, les biais sont principalement à cause de NLOS et multi-trajets réceptions qui sont difficiles à modéliser, donc il est très difficile d'arriver à une expression pour le PL_b.

Afin de mettre en œuvre l'approche composite pour surveillance de l'intégrité de la position en milieu urbain, l'HPE besoin d'être décomposé en la composante de biais et en la composante de bruit gaussien et ensuite à caractériser. À cet effet, dans ce travail, nous choisissons le modèle autorégressif (AR) pour estimer le séries chronologiques de l'HPE, car il est convenable et assez simple pour décomposer les erreurs dans les components du bruit et du biais.

$$HPE = AR(p) + \epsilon \tag{61}$$

Le 1^{er} ordre $AR(1)$ peut être écrite comme:

$$x_t = \phi x_{t-1} + \epsilon_t \tag{62}$$

où ϵ_t $N(0, \sigma^2)$

Pour l'ordre p, le $AR(p)$ est donné par:

$$x_t = \phi_1 x_{t-1} + \phi_2 x_{t-2} + \cdots + \phi_p x_{t-p} + \epsilon_t \tag{63}$$

En réarrangeant l'équation,

$$\epsilon_t = x_t - \phi_1 x_{t-1} - \phi_2 x_{t-2} - \cdots - \phi_p x_{t-p} \tag{64}$$

Par conséquent, on peut voir que ce modèle décompose l'erreur en une composante de bruit gaussien ϵ_t et d'autres composantes régressives qui peut être le représentant de biais. Dans ce travail, la 4ème ordre AR est utilisé et la méthode de Burg est choisie parce qu'elle produit toujours des modèles causaux et elle fournit la probabilité de gaussienne plus forte et plus souvent que la méthode de Yule-Walker [18].

Dans la prochaine étape, le bruit est séparé du biais de sorte qu'ils peuvent être caractérisés séparément. Cela peut être fait par filtration de la série chronologique. La fonction de transfert de filtre dans la transformée en z est donnée par:

$$Y(z) = (1 - \phi_1 z^{-1} - \cdots - \phi_p z^{-p}) X(z) \tag{65}$$

où $Y(z)$ est la la transformée en z de ϵ_t. Etant donné que ϵ_t est supposé être un bruit gaussien de moyenne nulle, il peut être caractérisé par sa variance, σ_ϵ^2.

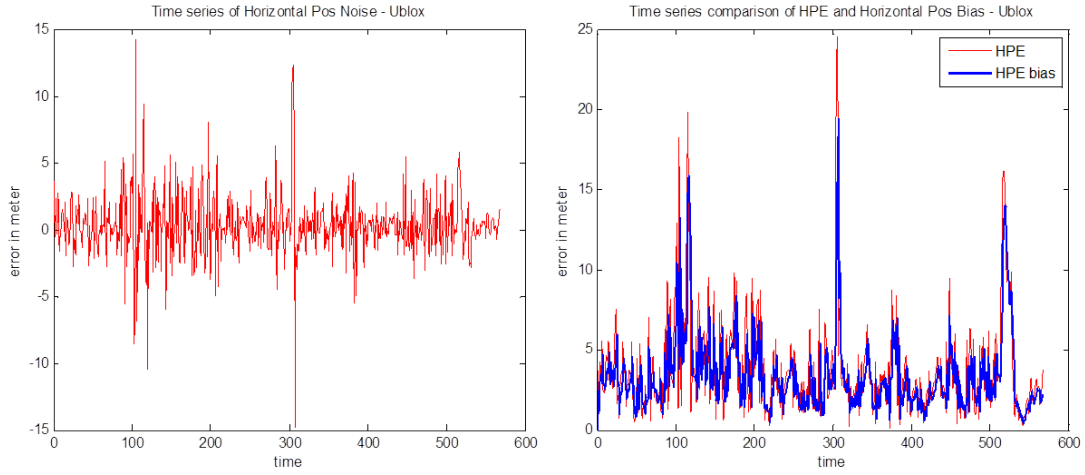

FIGURE 24: le bruit et le biais décomposés de l'HPE du récepteur uBlox

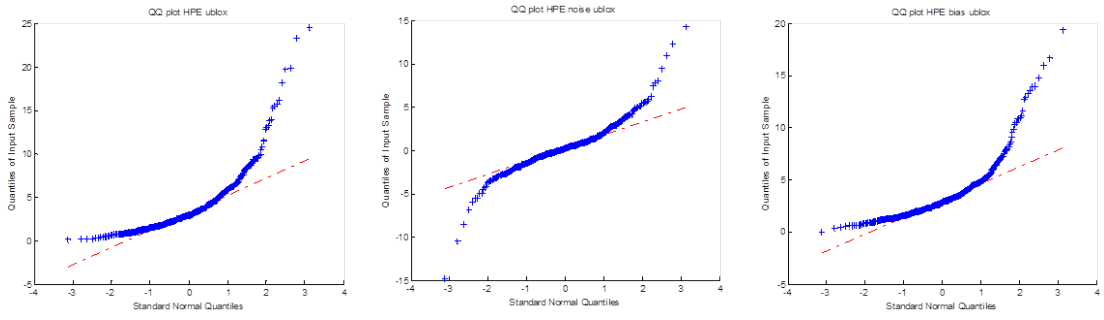

FIGURE 25: Diagramme Q-Q de l'HPE de récepteur uBlox, le bruit et le biais décomposés

Une fois le ϵ_t est obtenu, le $bias_t$ est calculé par:

$$bias_t = HPE_t - \epsilon_t \tag{66}$$

Les résultats de la décomposition de l'HPE dans les composantes de bruit et de biais sont tracées dans les figures 24 et 25 pour le récepteur uBlox, les figures 26 et 27 pour le récepteur Novatel et les figures 28 et 29 pour le récepteur Septentrio. Comme indiqué dans les diagrammes Q-Q, le bruit extrait semble suivre la distribution gaussienne mais avec des queues lourdes. Le quantile à laquelle la queue commencent à devenir lourdes diffère entre les récepteurs. Ces situations indiquent que l'approche de modèle AR utilisée dans ce travail pour extraire le bruit gaussien d'HPE n'est pas efficace pour supprimer totalement la queue lourde et extraire uniquement un bruit blanc gaussien de l'HPE. Cependant, même si il y a certains éléments de queues lourdes, l'utilité de cette technique dépend de l'AL, le seuil et la P_{HMI} qui sont requis pour les applications visées.

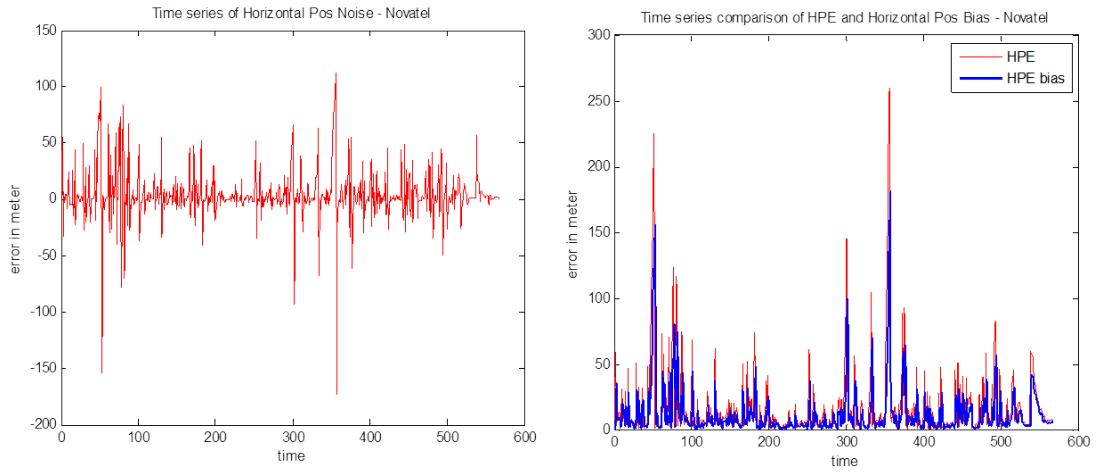

FIGURE 26: le bruit et le biais décomposés de l'HPE du récepteur Novatel

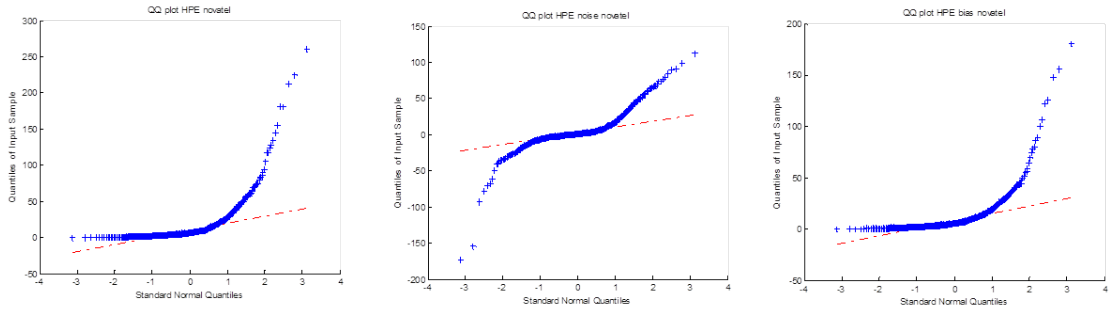

FIGURE 27: Diagramme Q-Q de l'HPE de récepteur Novatel, le bruit et le biais décomposés

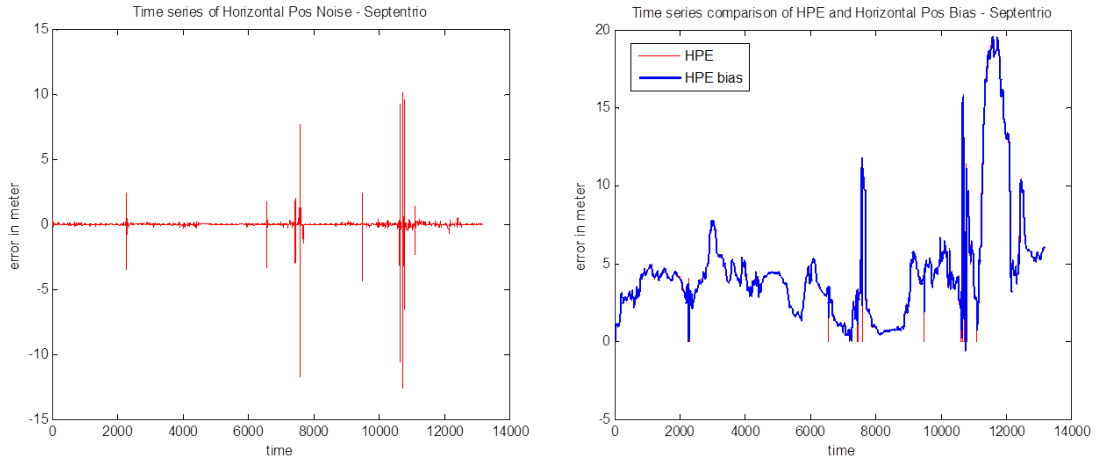

FIGURE 28: le bruit et le biais décomposés de l'HPE du récepteur Septentrio

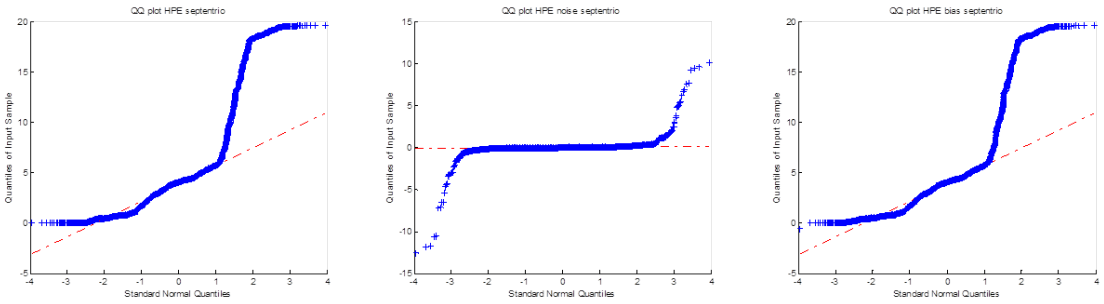

FIGURE 29: Diagramme Q-Q de l'HPE de récepteur Septentrio, le bruit et le biais décomposés

Contrairement à l'environnement à ciel ouvert, un biais dans les environnements urbains sont principalement dues à les réceptions multi-trajets et NLOS qui font leur modélisation déterministe d'être très complexe. Ainsi, dans ce travail, la délimitation de la biais a été fait en utilisant l'approche statistique où la distribution de biais est délimitée par une distribution gaussienne. En tant que tel, la distribution de délimitation de biais peut être caractérisée comme [17]:

$$HPE_{bias} = \mu_b + \sigma_b \sqrt{2} erf^{-1}(2P_b - 1) \tag{67}$$

où P_b est la probabilité d'intégrité. En une notation simplifiée,

$$HPE_{bias} = \mu_b + \sigma_b K_H \tag{68}$$

Les valeurs de μ_b et σ_b sont obtenus *a priori* en ajustant la courbe de la borne de CDF empirique (ECDF) du biais d'HPE.

Comme cela a été établi, il est l'HPL qui est utilisé pour surveiller l'intégrité de positionnement. Pour l'approche composite, l'HPL doit être calculé pour les deux la composante de biais et la composante de bruit.

a. HPL pour la composante de bruit. Contrairement aux systèmes d'augmentation tels que SBAS et GBAS, positionnement de véhicule terrestre en milieu urbain n'a pas de références. Ainsi la variance du bruit qui est utilisée pour le calcul de l'HPL est obtenue à partir du modèle de la variance de PR. Dans ce travail, le modèle de la variance du CNo-élévation de PR [19] est adopté:

$$\sigma_i^2 = k \times \frac{10^{(-0.1 \times CNo_{measured})}}{\sin^2(\theta_i)} \tag{69}$$

où k égale 1 pour le signal LOS et il change pour le signal NLOS.

Dans la mise en œuvre, il existe certains éléments d'incertitude car l'estimation de la distribution du bruit de l'HPE n'est pas parfait et σ_p est obtenu à partir d'un modèle de variance de PR qui est différente de la σ_ϵ du bruit d'HPE estimé. Par conséquent, le sigma doit être gonflé pour compenser ces incertitudes et de veiller à ce que le bruit d'HPL délimite le bruit d'HPE.

Dans ce travail, l'inflation du bruit HPL est mis en œuvre dans le domaine de position avec un facteur d'inflation A tel que:

$$HPLnoise_{inflated} = A.K_H\sigma_p \tag{70}$$

Pour estimer l'A, nous égalons l'$HPLnoise_{inflated}$ à la distribution de délimitation de ϵ_t de sorte que:

$$A.K_H\sigma_p = K_H\sigma_\epsilon \tag{71}$$

et donc

$$A = \frac{\sigma_\epsilon}{\sigma_p} \tag{72}$$

où σ_ϵ est l'écart-type du bruit de HPE et σ_p est l'écart-type de l'erreur de la position prédite basé sur le modèle de la variance de PR.

b. HPL pour la composante du biais. L'HPL de biais est basé sur le résidu de la position (qui est observable en temps réel) et ensuite gonflé/adapté statistiquement afin de borner l'ECDF de biais d'HPE. L'adaptation de CDF est fait en utilisant des paramètres de transformation de CDF similaire à l'approche de l'inflation sigma dans le délimitation de CDF. La CDF du résidu de la position est:

$$HPE_r = \mu_r + K_H\sigma_r \tag{73}$$

En gonflant l'HPE_r:

$$HPLbias_{inflated} = \mu_r + B + C.K_H\sigma_r \tag{74}$$

En réorganisant et en substituant 73 en 74,

$$HPLbias_{inflated} = HPE_r - K_H\sigma_r + B + C.K_H\sigma_r \tag{75}$$

$$HPLbias_{inflated} = HPE_r + B + (C-1).K_H\sigma_r \tag{76}$$

Pour estimer les paramètres B et C, nous laissons

$$\mu_r + B = \mu_b$$

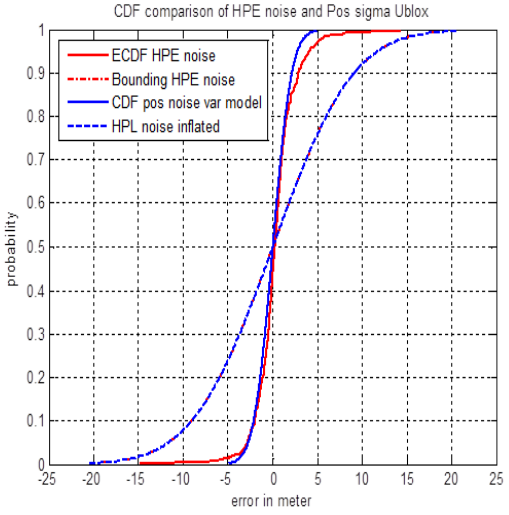

FIGURE 30: Délimitation gonflé de CDF du bruit (Ublox)

et

$$C.K_H\sigma_r = \sigma_b K_H$$

où μ_b et σ_b sont des paramètres de 68. De ce fait,

$$B = \mu_b - \mu_r \tag{77}$$

ce qui signifie que, la moyenne de $HPLbias_{inflated}$ est réglé pour correspondre à la moyenne de $HPEbias$, et

$$C = \frac{\sigma_b}{\sigma_r} \tag{78}$$

ce qui signifie que, le sigma de $HPLbias_{inflated}$ est gonflé pour correspondre au sigma de $HPEbias$.

Les figures 30, 31 et 32 sont le tracé de l'HPL gonflé délimitant les CDF des bruits pour les récepteurs uBlox, Novatel et Septentrio, respectivement. Dans les tracés, l'HPL gonflé est représenté par une ligne pointillée bleue. La CDF initiale observée à partir du modèle de la variance est représentée par la ligne bleue. La CDF de la distribution de bruit est représentée en rouge solide alors que sa limite est tracée par une ligne rouge pointillée. Dans tous les trois figures, on constate que l'HPL gonflé est en mesure de borner la CDF de la distribution du bruit.

La délimitation des CDF des biais par l'HPL gonflé dans le cas des récepteurs uBlox, Novatel et Septentrio sont présentées dans les figures 33, 34 et 35 respectivement. Parce que l'HPE est défini comme une norme des erreurs 2D, les biais de l'HPE restent en valeur positive. Par conséquent, la délimitation de biais ne concerne que le côté positif de la CDF. Dans les figures 33, 34 et 35, après l'inflation, les distributions de biais

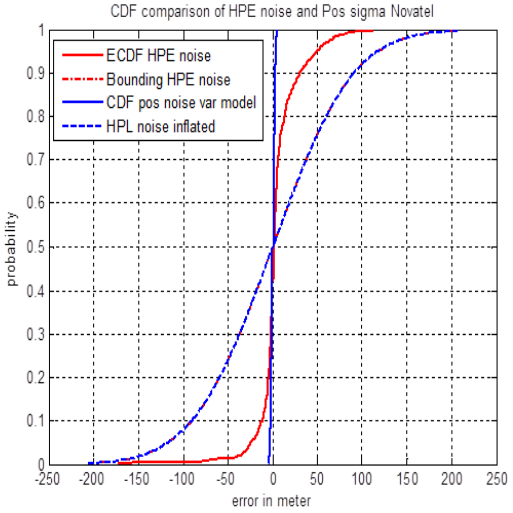

FIGURE 31: Délimitation gonflé de CDF du bruit (Novatel)

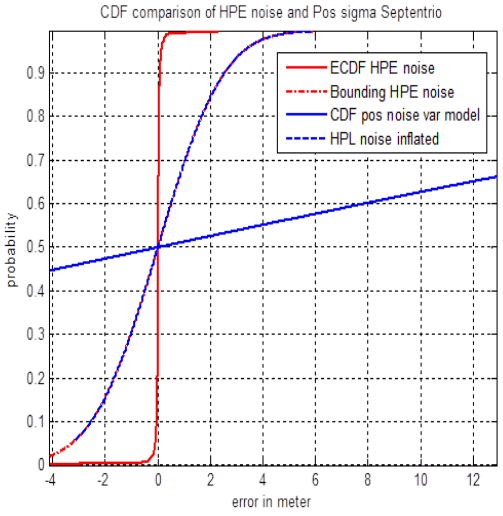

FIGURE 32: Délimitation gonflé de CDF du bruit (Septentrio)

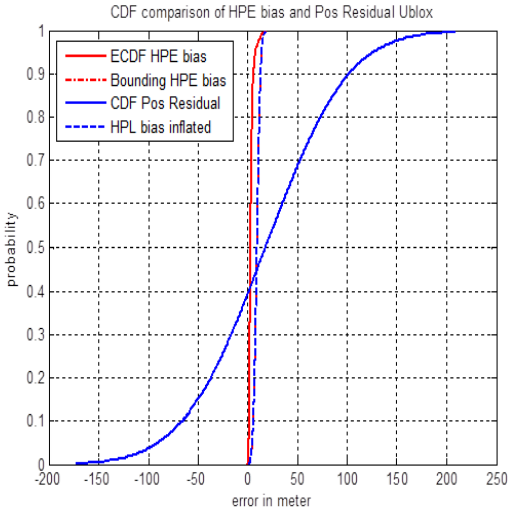

FIGURE 33: Délimitation gonflé de CDF du biais (Ublox)

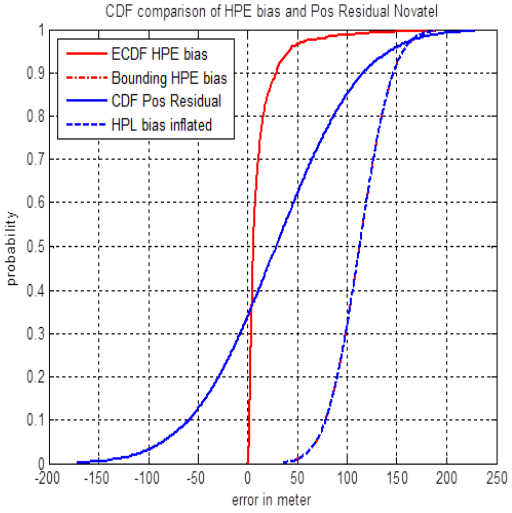

FIGURE 34: Délimitation gonflé de CDF du biais (Novatel)

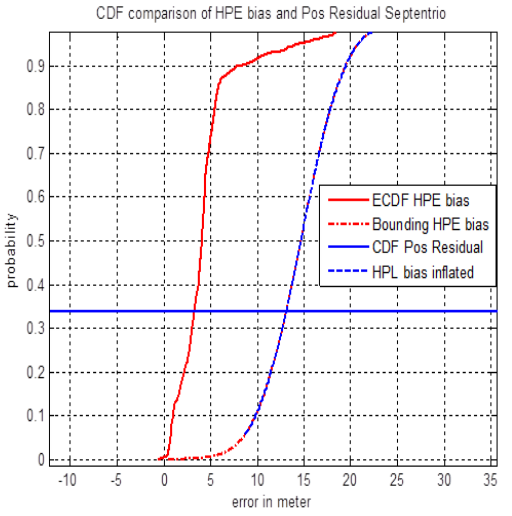

FIGURE 35: Délimitation gonflé de CDF du biais (Septentrio)

sont respectivement limitées par leur HPL gonflés. Il est intéressant de noter que tandis que le récepteur multi-constellation Septentrio a une meilleure précision dans des environnements urbains, sa performance d'intgrité en raison de biais n'est pas très différent que celui du récepteur uBlox. Au 90% de confiance, l'HPL gonflé pour Septentrio est d'environ 19 mètres alors que pour le uBlox est d'environ 13 mètres. Par conséquent, il montre que l'effet de biais dépend de l'environnement plutôt que la précision du récepteur.

En obtenant la majoration de CDF d'HPE, l'approche directe de domaine de position est en mesure de contourner les difficultés et la complexité de la modélisation des erreurs de PR dans les milieux urbains que la majoration dans le domaine de la distance doit

affronter. Cependant, il y a une limitation dans cette approche directe de domaine de position en ce que chaque canal de satellite n'est pas surveillé.

D'autre part, si les biais multiples de la PR mesurée combinés avec la géométrie dans une telle manière que les résidus de PR restent faibles, mais les erreurs de position devient grande, il est l'approche de domaine de position qui pourrait détecter l'erreur et pas dans la domaine de distance. En tant que tel, une combinaison de ces deux domaines de la distance et de position peut être mise en œuvre en tant que le concept de surveillance de l'intégrité multicouche.

En variante, des systèmes parallèles peuvent être mises en œvre où plusieurs estimations de position sont calculées en même temps avec chacun ayant une de la PR exclu. De cette façon, il est également possible d'identifier ce qui est la cause de la PR erreur inacceptable dans le positionnement.

Une des questions pertinentes de majoration d'erreur dans le secteur de l'aviation est la rareté des données observantes de la queue de la distribution d'erreur. Par conséquence, les techniques d'extrapolation tels que la théorie des valeurs extrêmes a été mis en œuvre pour faire face à le problème. Toutefois, cette question pourrait être détendit un peu dans les applications terrestres considérant que toutes les applications ne nécessiteraient une telle petite valeur de P_{HMI}. Par exemple, un P_{HMI} de 10^{-2} peut déjà être acceptable pour certaines des applications terrestres.

En outre, cet exercice de caractériser les erreurs de position des récepteurs différents en milieu urbain peut également bénéficier de l'effort de catégoriser et de certifier les récepteurs. En ayant les caractéristiques de HPE des récepteurs, les récepteurs peuvent être classés en différentes qualités de performance et cela doit permettre une sélection correcte d'un récepteur approprié pour un certain type d'applications terrestres.

Conclusions et Perspectives

Cette thèse porte sur les défis en matière de contrôle de la fiabilité de la navigation par GNSS pour les applications de véhicules terrestres dans les milieux urbains. L'objectif principal de cette recherche est de développer des méthodes de positionnement avec confiance en utilisant des mesures GNSS et d'autre mesures exterieurs pour l'utilisateur dans des environnements urbains contraintes. Essentiellement, la confiance de positionnement est identifiée avec la capacité de faire confiance à la position estimée.

Dans la première partie de nos travaux de recherche, les erreurs NLOS dans les milieux urbains sont caractérisés par l'aide d'un modèle 3D de l'entourage urbain. Dans un environnement avec un nombre limité de satellites visibles, l'exclusion des signaux dégradés pourrait aboutir à ne pas avoir assez de mesures acceptables pour une solution de position ou de nuire à la géométrie des satellites. Par conséquent, si le signal dégradé peut être identifié, et si son biais peut être estimé, le signal peut être corrigé et efficacement utilisé pour le positionnement. A cet effet, un simulateur de GNSS est utilisé conjointement avec le modèle 3D afin d'identifier les signaux NLOS et de prédire leurs biais. De cette prédiction, les signaux NLOS sont corrigées et utilisées pour améliorer la précision et l'intégrité des positions estimées. La capacité du modèle 3D à prédire l'état de réception du signal soit dans LOS ou NLOS a été jugée encourageante. Néanmoins, en raison des limites du modèle 3D en termes de la grande variabilité des facteurs géométriques et la capacité de prédire le biais NLOS instantan a été jugé modeste et pas concluante pour les données traitées. De même, quand les biais prédits ont été utilisées pour les corrections de PR dans le filtre de Kalman d'estimation de la position, les résultats ont montré que les erreurs de positionnement sont généralement presque similaires à celles calculées en utilisant le biais calculé à partir de la trajectoire de référence.

Dans cette thèse, la deuxième partie du travail propose une technique de surveillance de la fiabilité de les environnement urbain à l'aide d'un capteur de vitesse de confiance. L'approche prend une prédiction de pseudodistances déduites en utilisant l'hybridation avec d'autres capteurs pour maintenir la continuité de positionnement, même dans la situation de la réduction du nombre de satellites visibles. Un odomètre et un gyroscope sont utilisés comme des capteurs de DR qui sont couplés avec le récepteur GNSS pour obtenir une position de référence pour le contrôle de la fiabilité de la pseudodistance GNSS. En utilisant l'approche hybride, les résidus sont générés pour formuler un test statistique testé contre un seuil. Quelques formes de résidus ont été obtenues sur la base de plusieurs observables, à savoir le PR, le taux de la distance et la vitesse. Pour la vitesse résiduelle, l'odomètre a été étudié en tant que capteur de référence. Le résultat de la représentation résiduelle de la PR sur les erreurs varie d'un satellite à un autre. Le résiduel a une bonne représentation pour les satellites avec grande valeur de défaut. Puisque dans un tel cas, les résidus de PR ont été en mesure de détecter les erreurs de mesure avant qu'ils ne soient acceptés comme mesures valides pour le positionnement. En ce sens, le résiduel de PR peut être utilisé comme la première couche dans les couches multiples de métrique de surveillance de la fiabilité. Potentiel similaire a également été mise en évidence par la technique FDE qui est basé sur le résiduel de taux de la distance. Cependant, son inconvénient dans ce travail par rapport à l'approche basée sur PR résiduelle est qu'il ne peut pas être mis en œuvre pour corriger ou remplacer la mesure défectueuse. D'autre part, nous avons constaté qu'il est très difficile de lier

le résiduel de vitesse à l'erreur de positionnement. Au contraire, il serait utile pour la détection d'erreur de vitesse. Nous avons examiné le modèle 3D et d'autres capteurs parce que nous sommes convaincus que dans des environnements difficiles, la surveillance de l'intgrité a besoin d'informations supplémentaires autres que du GNSS.

La recherche dans cette thèse a également conduit au développement d'une nouvelle expérimentale de surveillance d'intégrité pour le positionnement dans les environnements urbains. Travailler directement dans le domaine de position, les distributions d'erreurs de position horizontale (HPE) sont caractérisés par la distribution de Pareto généralisée. Puis, une statistique de test est dérivée basée sur les résidus de position (plutôt que des résidus de pseudodistance) qui CDF sont adaptés ou gonflés pour correspondre à la majoration de CDF d'erreur de position caractérisée. En surveillant la statistique de test contre un seuil spécifique, l'intgrité et la continuité de positionnement sont remplies à un certain niveau de confiance. Les résultats à l'aide de données recueillies dans les zones du centre-ville de Toulouse montrent que la technique est assez prometteuse.

La méthode est ensuite étendue à calculer de manière autonome le niveau de protection horizontale (HPL) en milieu urbain à l'aide d'une approche composite. La décomposition des distributions HPE dans ses composantes de bruit et de biais a été mis en œuvre avec un filtre AR. En ciblant la simplicité et la mise en œuvre directe, la distribution gaussienne est utilisé comme les limites CDF tant pour le bruit et les distributions de biais. Alors que la question des queues lourdes a été confrontée dans cette approche, son application est potentiellement plus élevée pour les récepteurs multi-constellation, comme indiqué dans les résultats.

Plusieurs perspectives sont notables résultant des travaux de cette thèse. Parmi eux, les suivants présentent un intérêt particulier:

- Pour utiliser des échantillons de mesure obtenus dans de diverses villes pour l'analyse des performances. Avec ces données, une évaluation plus approfondie sur la robustesse de la distribution de surdélimitation de Pareto généralisée comme l'approche de l'intégrité de positionnement de surveillance en milieu urbain peut être effectuée. Autres types de distributions qui peuvent prendre en compte la queue lourde des erreurs peuvent être étudié pour caractériser les biais GNSS.
- Chercher une technique plus efficace pour extraire le bruit gaussien aléatoire de la distribution HPE. Cela contribuera à une délimitation plus efficace du bruit dans l'approche composite de HPL calcul pour les environnements urbains.
- Identifier et de développer des techniques qui peuvent combiner de manière optimale les méthodes heuristiques, des approches des domaines de mesures et des

domaines de la position dans une métrique de surveillance de l'intégrité. Il pourrait être en couches multiples, à exécuter de manière séquentielle ou en parallèle, ou de manière sélective en fonction des situations particulières.

– Pour étudier plus avant l'efficacité de la technique résiduelle de vitesse pour le suivi d'applications de vitesse. Il pourrait être également intéressant de rechercher des méthodes permettant de relier la vitesse résiduelle à la position de sorte qu'elle peut être utilisée pour le contrôle du positionnement.

– Étudier l'utilisation des approches statistiques non-paramétriques pour modéliser les erreurs soit dans le domaine de pseudo-distance ou dans le domaine de la position.

Bibliography

[1] P. Misra and P. Enge. *Global Positioning System: Signals, Measurements and Performance*. Ganga-Jamuna Press, 2001.

[2] U.S. Department of Defense. Global positioning system, standard positioning service, performance standard, 4th edition, 2008.

[3] A. Simsky and F. Boon. Carrier phase & Doppler-based algorithms for real-time standalone positioning. In *Proceedings of GNSS*, Graz, 22-25 April 2003.

[4] B.H. Lee and G.I. Jee. Performance Analysis of Doppler Aided GPS/QZSS precise positioning for land vehicles. *Annual of Navigation*, 20:85–96, 2013.

[5] OKTAL-SE. Synthetic environment. http://www.oktal-se.fr. Accessed: 01/04/2013.

[6] A. Bourdeau, M. Sahmoudi, and J-Y. Tourneret. Prediction of GNSS signal bias using a 3D model in urban environments. In *The Europeen Navigation Conference, ENC*, Vienna, Austria, 23-25 April 2013.

[7] N. Viandier, D.F. Nahimana, J. Marais, and E. Duflos. GNSS Performance Enhancement in Urban Environment Based on Pseudo-range Error Model. *Position, Location and Navigation Symposium (PLANS),IEEE/ION*, pages 377–382, 5-8 May 2008.

[8] M. Spangenberg, V. Calmettes, O. Julien, J.Y. Tourneret, and G. Duchateau. Detection of Variance Changes and Mean Value Jumps in Measurement Noise for Multipath Mitigation in Urban Navigation. *NAVIGATION*, 57(1):35–52, 2010.

[9] A. Wieser, M. Gaggl, and H. Hartinger. Improved positioning accuracy with high sensitivity GNSS receivers and SNR aided integrity monitoring of pseudo-range observation. *Proceedings of the 18th International Technical Meeting ION GNSS 2005*, pages 1545–1554, 2005.

[10] H. Kuusniemi. *User-Level Reliability and Quality Monitoring in Satellite-Based Personal Navigation.* PhD thesis, Tempere University of Technology, Findland, 2005.

[11] J.F. Liao and B.S. Chen. Robust Mobile Location Estimator with NLOS Mitigation using Interacting Multiple Model Algorithm. *IEEE Trans. on Wireless Com.*, 5(11), November 2006.

[12] P.J.G. Teunissen and P.F. de Bakker. Single-receiver single channel multi-frequency GNSS integrity: outliers, slips, and ionospheric disturbances. *Journal of Geodesy*, 87(2), February 2013.

[13] H-G. Büsing, U. Haak, and P. Hecker. Odometer-aided Instantaneous Signal Reacquisition for Automotive GNSS Receivers. In *Proceedings of the 24th International Technical Meeting of The Satellite Division of the Institute of Navigation*, pages 954–959, Portland, OR, September 2011.

[14] B. DeCleene. Defining Pseudorange Integrity - Overbounding. In *Proceedings of the 13th International Technical Meeting of the Satellite Division of The Institute of Navigation*, pages 1916–1924, Salt Lake City, UT, September 2000.

[15] T. Walter, J. Blanch, P. Enge, B. Pervan, and L. Gratton. Shaping Aviation Integrity-Two RAIM for Safety. *GPS World*, 19(4):42–49, 2008.

[16] R. Suddapalli. Aircraft position integrity for Differential Satellite-based Navigation in the presence of both bias and noise errors. Ma thesis, Ohio University, 2008.

[17] J. Rife and S. Pullen. The Impact of Measurement Biases on Availability for CAT III LAAS. *NAVIGATION: Journal of the Institute of Navigation*, 52(4):215–228, 2005-2006.

[18] X. Luo. *GPS Stochastic Modelling - Signal Quality Measures and ARMA Processes.* Phd thesis, Karlsruhe Institute of Technology, 2012.

[19] S. Tay and J. Marais. Weighting models for GPS Pseudorange observations for land transportation in urban canyons. In *6th European Workshop on GNSS Signals and Signal Processing*, Munich, 2013.